Non-equilibrium scaling behavior in stochastically driven biological assemblies

Federica Mura

München 2019

Non-equilibrium scaling behavior in stochastically driven biological assemblies

Federica Mura

A dissertation submitted
to the Faculty of Physics
of the Ludwig–Maximilians–Universität
München
for the degree of
DOCTOR RERUM NATURALIUM

Munich, 22.08.2019

First referee: Prof. Dr. Chase Broedersz
Second referee: Prof. Dr. Ulrich Gerland
Date of the oral examination: 18.10.2019

Zusammenfassung

Biologische Systeme arbeiten fern des thermodynamischen Gleichgewichts. Sie dissipieren kontinuierlich Energie auf molekularen Längenskalen und verletzen dabei die so genannte detailed balance-Bedingung. Die Verletzung von detailed balance kann jedoch auch als Zirkulation im Koordinatensystem eines Paares mesoskopischer Freiheitsgrade auftreten. Diese Dissertation konzentriert sich darauf, wie wir eine solche Zirkulation messen und daraus Informationen über die Nichtgleichgewichtsaktivität im System gewinnen können. Insbesondere schlagen wir die „cycling frequencies“ (Umlauffrequenzen) und „area enclosing rates“ als nichtinvasive Maße für Nichtgleichgewicht vor. Wir bauen ein Framework auf, mit dem theoretische Vorhersagen zum „spatial scaling“ (räumlichen Skalenverhalten) solcher Maßnahmen in biologischen Netzwerke abgeleitet werden können.
Diese Dissertation unterteilt sich in drei Hauptteile:

Teil I: Dieser Teil enthält die Einführung und Kapitel 1. Ziel dieses Teils ist die Motivation zu erklären, die uns bei unserer Arbeit geleitet haben, und die theoretischen Werkzeuge einführen, die in den nachfolgenden Kapiteln verwendet werden. In der Einführung konzentrieren wir uns auf ein toy model, das die Basis für die Definition des theoretischen Modells bildet, das wir in unserer Forschung verwendet haben, um biologische Netzwerke zu modellieren. Innerhalb dieses Modells führen wir auch die Nichtgleichgewichtsmaße ein, die wir in den nachfolgenden Kapiteln anwenden werden, wie auch die Beziehungen zwischen ihnen. In Kapitel 1 geben wir einen umfassenden Überblick über den Nachweis von Nichtgleichgewichtsaktivität in biologischen Systemen.

Teil II: Dieser Teil enthält das zweite Kapitel dieser Arbeit: “Non-equilibrium scaling behavior in driven biological assemblies“. Hier stellen wir ein einfaches, aber allgemeines Modell für biologisch aktive Netzwerke vor. In diesem Modell untersuchen wir, wie sich Nichtgleichgewichtsaktivität auf verschiedenen Längenskalen manifestiert. Wir stellen fest, dass unsere Nichtgleichgewichtsmaße ein Potenzverhalten als Funktion des Abstands zwischen zwei Messpunkten aufweisen. Wir stellen ein theoretisches Framework vor, das uns ermöglicht, einen analytischen Ausdruck für das Potenzverhalten abzuleiten. Darüber hinaus beziehen wir unsere Nichtgleichgewichtsmaße auf ein häufiger angewandtes Maß, die Entropieproduktionsrate. Wir zeigen, dass die cycling frequencies verwendet werden können, um eine Untergrenze für die Entropieproduktionsrate des Systems zu ermitteln.

Teil III: In diesem Teil untersuchen wir, welche Informationen über die Nichtgleichgewichtsaktivität im System durch Auswertung des Skalierungsverhaltens von Nichtgleich-

gewichtsmessungen ermittelt werden können. Während wir im vorangehenden Teil die Nichtgleichgewichtsaktivität nur mit stochastisch unkorrelierten Monopolkräften modelliert haben, betrachten wir hier mehrere Szenarien für die räumliche Struktur der internen Triebkräfte, die für biologische und synthetische Systeme relevant sein könnten. Zum Beispiel haben wir in unsere Modelle die Auswirkungen von Prozessen berücksichtigt, die normalerweise als Kraftdipole modelliert werden. Ein typisches Beispiel ist das aktive Gleiten von Myosin-filamenten in einem ActinMyosin Netzwerk, das zu Paaren gleicher und entgegengesetzter Kräfte führt. Hier betrachten wir auch korrelierte Aktivitäten, die durch die räumliche Organisation von Enzymen und molekularen Motoren entstehen können. Unsere Ergebnisse zeigen, dass solche Merkmale von Nichtgleichgewichtsaktivität sich auf das Langzeitskalenverhalten von Zweipunkt-Nichtgleichgewichtsmessungen auswirken können. Insgesamt legen unsere Untersuchungen nahe, dass die cycling frequencies und area enclosing rates ein guter Kandidat sind, um die Nichtgleichgewichtsaktivität in biologischen Systemen auf nicht-invasive Weise zu untersuchen.

Summary

Biological systems operate out of thermodynamic equilibrium, continuously dissipating energy and breaking detailed balance at the molecular scale. At larger scales, broken detailed balance may also manifest as circulation in the coordinates space of a pair of mesoscopic degrees of freedom. This thesis explores from a theoretical standpoint how it is possible to measure such a circulation and use it to extract information on the non-equilibrium activity in the system. In particular, we propose the cycling frequencies and area enclosing rates as non-invasive measures of non-equilibrium. We then build a framework which allows us to make theoretical predictions on the spatial scaling behavior of such measures in biological assemblies.
This thesis is organized in three main parts:

Part I: The first part of this thesis consists of the Introduction and Chapter 1. The goal is to provide the reader with the background needed to understand the motivations that guided our work and the theoretical tools that are employed in the rest of the thesis. In the introduction, we focus on a toy model that provides the basis for the definition of the theoretical model that we used to study biological assemblies. Within this toy model, we also introduce the non-equilibrium measures that we will employ in the rest of the thesis and the relations among them. In Chapter 1, we provide an extensive review about the detection of non-equilibrium in biological systems.

Related publications and contributors: The review work presented in Chapter 1 was carried out in collaboration with F. Gnesotto, J. Gladrow and under the supervision of Prof. C. P. Broedersz. This work was published in the review paper "*Broken detailed balance and non-equilibrium dynamics in living systems: a review*", *Rep. Prog. Phys.* **81**, 066601 (2018), reprinted in Chapter 1.

Part II: This part consists of the 2nd Chapter of this Thesis: "Non-equilibrium scaling behavior in driven biological assemblies". Here we introduce a simple yet general model that we employ to study biological assemblies, i.e. elastic networks that are driven out of equilibrium by active stochastic forces. Within this model, we investigate how non-equilibrium manifests at different length scales. To this end, we consider two probe particles in the network and employ two non-equilibrium measures defined in the space of the particles' coordinates: the cycling frequencies around the origin and area enclosing rates of the stochastic trajectories. We find that these two points non-equilibrium measures exhibit an average power law behavior as a function of the distance between

the probes. We present a theoretical framework that allows us to derive an analytical expression for such a power law. Furthermore, we relate our non-equilibrium measures to a direct measure of irreversibility in the system, the entropy production rate. We show that a measurement of the easily accessible cycling frequencies can be used to set a lower bound to the entropy production rate of the system.

Related publications and contributors: This research was realized in collaboration with G. Gradziuk, and under the supervision of Prof. C. P. Broedersz. This work resulted in two publications: "*Non-equilibrium scaling behavior in driven soft biological assemblies*", *Phys. Rev. Lett.* **121**, 038002 (2018), and "*Scaling behavior of non-equilibrium measures in internally driven elastic assemblies*", *Phys. Rev. E.* **99**, 052406, reprinted at the end of Chapter 2.

Part III: This part corresponds to the 3rd Chapter of this thesis: "Non-equilibrium measures reveal intrinsic features of the active driving". Here, we investigate what information on the non-equilibrium activity in the system can be recovered by looking at the scaling behavior of non-equilibrium measures. While in the previous part we modeled the non-equilibrium activity by means of stochastic uncorrelated monopole-forces, here we consider several scenarios for the spatial features of the internal driving that may be relevant in biological and synthetic systems. For instance, we included in our description the effects of processes that are usually modeled as force dipoles. A typical example is the active sliding of myosin minifilaments in actomyosin networks that gives rise to pairs of equal and opposite forces. Here, we also consider the case of spatially correlated activities, that may arise due to the spatial organization of enzymes and molecular motors. Our results show that such features of the active noise are reflected in the long-range scaling behavior of two-point non-equilibrium measures. Overall, our research suggests that the cycling frequencies and area enclosing rates are good candidates to explore non-equilibrium activity in biological systems, in a non-invasive way.

Related publications and contributors: This research was realized in collaboration with G. Gradziuk, and under the supervision of Prof. C. P. Broedersz. This work resulted in a manuscript: "*Mesoscopic non-equilibrium measures can reveal intrinsic features of the active driving*", currently submitted for publication, whose most recent version is reprinted at the end of Chapter 3.

Contents

Zusammenfassung **i**

Summary **iii**

Introduction **1**
I.0.1 Non-equilibrium dynamics in biological systems: a toolkit 2
I.0.2 Goals and significance of this thesis 9

1 Non-equilibrium in living systems: a review **11**
1.1 Publication in *Reports on Progress in Physics*: Broken detailed balance and non-equilibrium dynamics in living systems: a review 13

2 Non-equilibrium scaling behavior in driven biological assemblies **47**
2.1 Soft biological assemblies 48
2.2 Model 50
2.2.1 Non-equilibrium in a reduced subspace 52
2.3 Results 54
2.3.1 One dimensional chain 55
2.3.2 d-dimensional lattices 58
2.3.3 Lower bound for the entropy production rate 60
2.3.4 Chapter summary 62
2.4 Publication in *Phys. Rev. Lett*: Nonequilibrium Scaling Behavior in Driven Soft Biological Assemblies 65
2.5 Publication in *Phys. Rev. E*: Scaling behavior of non-equilibrium measures in internally driven elastic assemblies 77

3 Non-equilibrium measures reveal intrinsic features of the active driving **91**
3.1 Different scenarios for the non-equilibrium driving 92
3.2 Model 93
3.3 Results 94
3.3.1 Monopole and dipole activity 95
3.3.2 Correlated activities 101
3.3.3 Chapter summary 103
3.4 Publication preprint in *Arxiv*: Mesoscopic non-equilibrium measures can reveal intrinsic features of the active driving 105

Outlook **121**

Conclusions **125**

Acknowledgements **133**

Introduction

Living systems have always been a challenging target for Physics and Physicists. Newton introduced the term '*foci of activity*' to explain the mystery of life: the spontaneous generation of motion that didn't find justification in the mechanical philosophy. Whether these '*foci of activity*' were an intrinsic property of matter or were external to matter remained a matter of contention among philosophers for a long time [48]. Thanks to the striking developments of the twentieth century in the area of microscopy, the old abstract concept of '*foci of activity*' is becoming, more and more, a concrete, detailed picture available to us. For instance, nowadays, the spontaneous generation of motion is well understood as a result of the presence of molecular machines that convert chemical energy into mechanical forces and motion. Such a window into the panorama of living systems has brought to light the complexity of the mechanisms governing life. This raised the need of bringing together disciplines such as physics, chemistry, and biology in a new research field called 'Active Matter'.

The field of Active Matter studies systems composed of active agents. Each of these agents consumes energy to perform work, thereby driving the system out of thermodynamic equilibrium. Living systems carry out vital functions, by constantly dissipating energy at the molecular scale through enzymatic activity [26, 47, 55]. The action of these enzymes often results in complex behaviors which can be clearly identified as non-thermal processes because of their orderly and self-organized dynamics. Striking examples are cell migration, cell division or complex proteins patterns formed inside the cell, which orchestrate a variety of cellular processes [3, 13, 27, 43]. However, for many processes, it can be very challenging to say whether their dynamics differ significantly from those of a thermally driven one. For instance, the diffusion of catalytic enzymes may appear at first glance very similar to thermal diffusion, but it turns out to be different: the intensities of their fluctuations cannot be justified just in terms of thermal energy [19, 37, 45, 68, 86]. Also the erratic motion of biological assemblies, such as chromosomes [81], membranes [6, 7, 79], cytoskeleton [22, 25, 41, 47, 51, 59], may appear at first sight indistinguishable from a thermal process. Nevertheless, their dynamics are driven out of equilibrium at molecular scales by internal enzymatic processes. Non-equilibrium activity is certainly essential to maintain life, however, how to detect and characterize such non-equilibrium dynamics in biological systems is still an open question. The work presented in this thesis is devoted to address this question.

I.0.1 Non-equilibrium dynamics in biological systems: a toolkit

Several methods have been developed to discern between equilibrium and non-equilibrium dynamics. In this section we will give a brief overview of such methods, and we will shortly discuss some experimental results, that will lead us to define the goal of our research. A more detailed and extensive review on non-equilibrium in biological systems is included in Chapter 1.

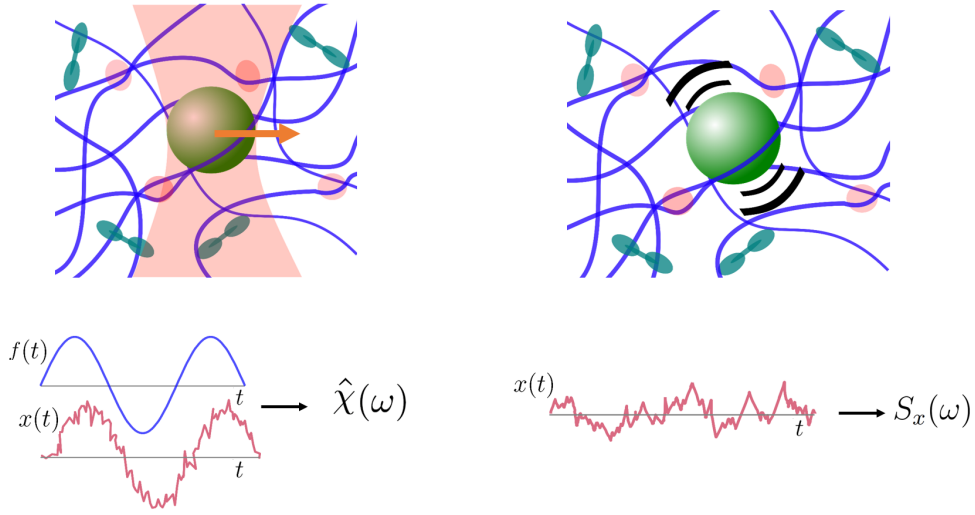

Figure I.1: Schematic of the approach to detect non-equilibrium, based on the FDT violation. The response function $\hat{\chi}(\omega)$ appearing in Eq. (I.2) can be measured by applying, via an optical tweezer, an external force to a particle embedded in biological environment. The power spectrum of the the particle fluctuations $S_x(\omega)$ can be measured from the trajectory of the freely diffusing particle. The estimated $\hat{\chi}(\omega)$ and $S_x(\omega)$ are then used to verify whether Eq. (I.2) holds.

Fluctuation-dissipation theorem violation One of the first approaches that has been used to quantify non-equilibrium activity is based on the violation of the fluctuation dissipation theorem (FDT). This theorem can be derived in the context of *linear response theory* [14]. Linear response theory deals with physical systems described by an observable quantity $x(t)$ that depends on a time-dependent field $f(t)$ through a linear response function $\chi(t)$ as:

$$\langle x(t)\rangle = \langle x(0)\rangle + \int_{-\infty}^{t} f(\tau)\chi(t-\tau)d\tau. \tag{I.1}$$

The FDT relates the power spectrum of the observable x, $S_x(\omega) = \langle \hat{x}(\omega)\hat{x}^*(\omega)\rangle$, to the imaginary part of the Fourier transform of the response function $\mathrm{Im}\hat{\chi}(\omega)$ [50]:

$$S_x(\omega) = \frac{2k_BT}{\omega}\mathrm{Im}\hat{\chi}(\omega), \tag{I.2}$$

where k_B is the Boltzmann constant. Eq. (I.2) is derived by assuming that the system is at thermal equilibrium at temperature T. A common procedure to verify whether a

system is out of equilibrium is to check for the violation of Eq. (I.2), by directly measuring the right and left hand-side of the equation. As practical example we can think of the position x of a particle, subject to an external time-dependent force $f(t)$. The linear response function χ can be estimated by measuring x while applying a small periodic perturbation $f(t)$ to the system. We can obtain $\hat{\chi}(\omega)$ from the Fourier transform of Eq. (I.1): $\hat{\chi}(\omega) = \langle \Delta\hat{x}(\omega) \rangle / \hat{f}(\omega)$. A direct measurement of the spontaneous fluctuations of $x(t)$ allows us to compute $S_x(\omega)$, the left hand-side of Eq. (I.2). In practice, in the case of active soft materials, these measurements can be carried out by embedding microscopic particles in the system. These particles can be used both as tracers and to impose external forces on the system, for example by using optical tweezers or magnetic fields (Fig. I.1).

The measure of the violation of the FDT has proven to be a useful method to asses the non-equilibrium nature of biological systems. It has been employed both in *in vitro* reconstituted systems and *in vivo*, for instance to prove the non-equilibrium dynamics of the cytoskeletal network, due to the activity of molecular motors as Myosin II [22, 25, 41, 47, 51, 59]. These motors, by converting ATP into mechanical work, play a major role in the active dynamics of the cytoskeleton. Examples of active dynamics, detected by observing the violation of FDT, are found also in two dimensional and one dimensional biological assemblies. The active fluctuations of red blood cell membranes have been detected by anchoring several probes to the cellular membrane. In this case, the active dynamics are generated by the actomyosin cortex situated beneath the membrane [7, 79]. To verify the violation of Eq. (I.2), it is not always necessary to embed artificial probes in the system. For instance, the active dynamics in bacterial chromosomes has been detected by fluorescently labeling multiple chromosomal loci [81], and the non-equilibrium dynamics of a reconstituted actomyosin network has been detected by measuring the bending modes of fluorescently labeled microtubules [9].

Even though the measurement of the FDT violation is a well established approach to quantify non-equilibrium, it requires the measurement of the system's response function which may be technically difficult especially in living systems. It requires to perturb the system, for example using optical tweezers. However, the detection of non-equilibrium processes does not always have to rely on invasive techniques. Recently, new non-invasive methods have been developed, which are based on the direct detection of irreversibility in the stochastic trajectories of the variables describing the system. We will discuss these methods in the following paragraphs.

Broken detailed balance An alternative and non-invasive method to detect non-equilibrium activity, based solely on the observation of the system dynamics, consists of detecting the breaking of the detailed balance condition. Put simply, this condition states that at equilibrium every elementary process in the system should be equilibrated by its reverse process, meaning that the two processes are equally likely (Fig. I.2). To formally introduce this principle in its most general form, we can consider a physical system described by a set of coordinates $\mathbf{x}$, which under time reversal transform as $x_i \to \epsilon_i x_i$, with $\epsilon_i = \pm 1$. For such system the detailed balance condition reads [30]:

$$p(\mathbf{x}', t+\tau; \mathbf{x}, t) = p(\epsilon\mathbf{x}, t+\tau; \epsilon\mathbf{x}', t), \tag{I.3}$$

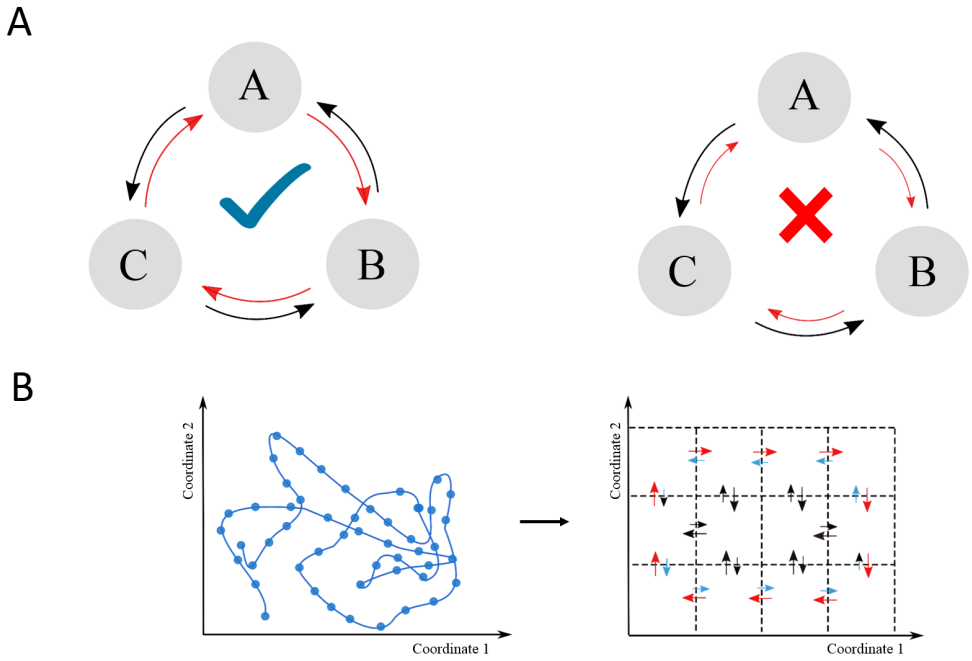

Figure I.2: A) Two systems with states A,B,C and forward and backward transitions. The left system obeys detailed balance (all arrows are of equal length), whereas the right system does not (net counterclockwise probability flux). B) When a stochastic trajectory (left) violates detailed balance, the transitions between different regions of the coordinate space are not balanced. A possible way to verify this condition is to discretize the coordinates space and count the number of transitions between first neighbour discrete states (right).

where we indicated with $p(x', t'; x, t)$ the joint probability density describing the system transition from $(\mathbf{x}, t)$ to $(\mathbf{x}', t')$, and we defined $\epsilon\mathbf{x} = (\epsilon_1 x_1, \epsilon_2 x_2, \ldots)$. A concrete example would be a gas of particles described by positions and velocities $(\mathbf{r}, \mathbf{v})$, which under time reversal transform as $(\mathbf{r}, \mathbf{v}) \to (\mathbf{r}, -\mathbf{v})$.

In this thesis we will focus on systems following Markovian dynamics, for which the probability density distribution $p(\mathbf{x}, t)$ fulfills a Fokker-Planck equation

$$\partial_t p(\mathbf{x}, t) = -\sum_i \partial_i \left[\mathbf{A}_i(\mathbf{x}) p(\mathbf{x}, t)\right] + \sum_{ij} \partial_i \partial_j \left[\mathbf{D}_{ij}(\mathbf{x}) p(\mathbf{x}, t)\right] := -\nabla \cdot \mathbf{j}(\mathbf{x}, t), \tag{I.4}$$

where $\mathbf{A}(\mathbf{x})$ and $\mathbf{D}(\mathbf{x})$ represent the drift term and the diffusion matrix respectively, and $\mathbf{j}(\mathbf{x})$ the probability density current. Within the Fokker Planck framework it is possible to show that, for a stationary Markov process, the detailed balance is equivalent to the following conditions [30]:

$$\epsilon_i \mathbf{A}_i(\epsilon\mathbf{x}) p_s(\mathbf{x}) = -\mathbf{A}_i(\mathbf{x}) p_s(\mathbf{x}) + 2\sum_j \partial_j \left(\mathbf{D}_{ij}(\mathbf{x}) p_s(\mathbf{x})\right), \tag{I.5}$$

$$\epsilon_i \epsilon_j \mathbf{D}_{ij}(\epsilon\mathbf{x}) = \mathbf{D}_{ij}(\mathbf{x}), \tag{I.6}$$

where $p_s(\mathbf{x})$ indicates the steady state solution of Eq. (I.4). For a set of coordinates which are all even under time reversal transformation ($\epsilon = 1$), Eq. (I.6) is trivially satisfied.

Instead, Eq. (I.5) reduces to:

$$\mathbf{A}_i(\mathbf{x})p_s(\mathbf{x}) - \sum_j \partial_j \left(\mathbf{D}_{ij}(\mathbf{x})p_s(\mathbf{x})\right) = \mathbf{j}_i = 0. \tag{I.7}$$

We immediately notice from Eq. (I.7) that the probability density current $\mathbf{j}$ vanishes under the condition of detailed balance. We can conclude that a non-zero probability current is equivalent to the condition of broken detailed balance, and therefore to a system out of equilibrium.

These results have been recently put to use to develop a non-invasive method for non-equilibrium detection in biological systems [5]. Broken detailed balance has been observed analyzing the stochastic fluctuations of primary cilia of Madin-Darby canine kidney cells. Primary cilia are microtubule-based organelles that act as microscopic sensors to perceive information on the environment surrounding the cell, while fluctuating with thermal like oscillations. The basal body of the cilium is anchored to the cell actomyosin cortex and is therefore subject to the action of myosin motor proteins, which can indeed induce non-equilibrium fluctuations. The work in [5] proved that the detection of broken detailed balance can be a helpful non-invasive method to asses whether stochastic fluctuations in biological systems are driven by non-equilibrium dynamics.

However, to fully exploit the potential of this technique, there are still open questions that require an answer. For instance, what are easily accessible measures that can be used to quantify broken detailed balance, going beyond the binary information on the system being or not at equilibrium? Recently, a lot of theoretical work has been devoted to answer this question, proposing various candidates for a reliable and informative measure of how far a system is from thermodynamic equilibrium. A natural and most commonly employed measure to quantify the time-irreversibility of a process is the entropy production rate, which can often be related to the energy dissipation in the system [8, 21, 28, 52, 65]. Alternative proposed measures are the average area enclosing rates [31, 38], and the average cycling frequencies of the stochastic trajectory in the coordinate space of two representative degrees of freedom [32, 33]. As we will see in the next section and in Chapter 2, all these measures are closely related.

Toy model: two stochastically driven coupled beads

In this section we discuss a very simple toy model which is ideal to provide some basic intuition for all the core concepts of this thesis. The model consists of two overdamped beads connected to each other and to the boundaries with springs of elastic constant k. The two beads are embedded in two independent thermal baths with respective temperatures T_1 and T_2, and viscous coefficient γ, as shown in Fig. I.3A. When $T_1 \neq T_2$ the system is clearly out of thermal equilibrium [5, 16, 52]. The overdamped equations of motion read

$$\frac{d\mathbf{x}(t)}{dt} = \mathbf{A}\mathbf{x}(t) + \eta(t), \tag{I.8}$$

where we indicated by $\mathbf{x} = (x_1, x_2)^{\mathrm{T}}$ the coordinates of the beads. The elastic interaction is described by the 2×2 matrix $\mathbf{A}$, which has elements $a_{ij} = (k/\gamma)\left(-2\delta_{ij} + (1 - \delta_{ij})\right)$.

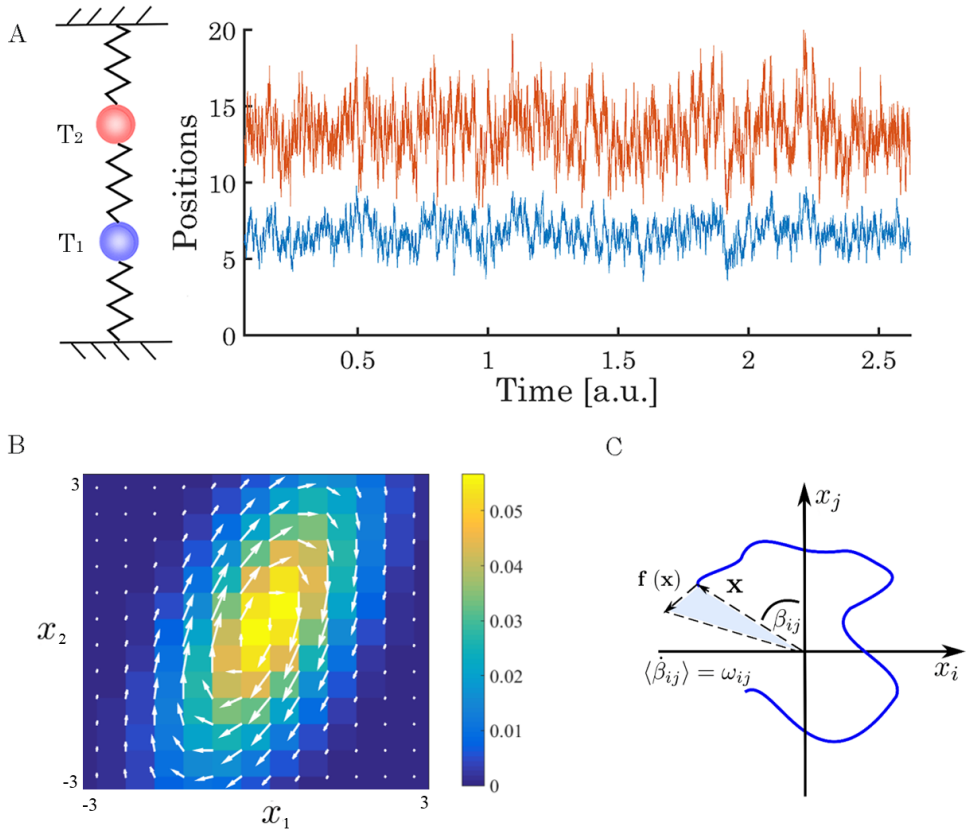

Figure I.3: A) Schematic of the two coupled beads system and simulated time series of the beads positions for $T_2 = 5T_1$. B) Probability distribution (color) and flux map (white arrows) obtained for $T_2 = 5T_1$. Adapted from [34]). C) Schematic trajectory in the coordinate space of two beads. The light blue area enclosed in the triangle represents $[\mathbf{x} \times \mathbf{f}(\mathbf{x})]/2\gamma$: the area enclosing rate obtained upon averaging over phase space. Here $\mathbf{f}(\mathbf{x})$ indicates the vector of elastic forces acting on the beads.

The stochastic noise is described by

$$\langle \eta_i(t)\eta_j(t')\rangle = \delta(t-t')\delta_{ij}\frac{2k_BT_i}{\gamma}. \tag{I.9}$$

where $\langle..\rangle$ indicates the ensemble average. Typical stochastic trajectories for such system can be obtained by numerically integrating Eq. (I.8), and are reported in Fig. I.3A. When we set $T_1 \neq T_2$ the system is not at thermal equilibrium, and as expected from the discussion in the previous section, this non-equilibrium activity manifests as a circulating current in the coordinate space of the two beads, as shown in Fig. I.3B.

The goal of this section is to clarify how such circulation relates to other non-equilibrium measures, such as cycling frequency, area enclosing rates, and entropy production rate. In this perspective, it is convenient to consider the Fokker Planck equation of this system

$$\partial_t p(\mathbf{x},t) = -\nabla\cdot[\mathbf{A}\mathbf{x}p(\mathbf{x},\mathbf{t})] + \nabla\cdot\mathbf{D}\nabla p(\mathbf{x},t) = -\nabla\cdot\mathbf{j}, \tag{I.10}$$

where the diffusion matrix $\mathbf{D}$ has entries $d_{ij} = \delta_{ij}\frac{k_BT_i}{\gamma}$, and the probability density current is defined as $\mathbf{j} = [\mathbf{A}\mathbf{x}p(\mathbf{x},\mathbf{t})] - \mathbf{D}\nabla p(\mathbf{x},t)$. The steady state solution $p_s(\mathbf{x})$ of Eq. (I.10) is a Gaussian distribution, with covariance matrix $\mathbf{C}$ solution of the Lyapunov equation:

$$\mathbf{A}\mathbf{C} + \mathbf{C}\mathbf{A}^{\mathrm{T}} = -2\mathbf{D}. \tag{I.11}$$

Therefore we have $\nabla p = -\mathbf{C}^{-1}\mathbf{x}p_s(\mathbf{x})$, and the steady state probability density current can be expressed as $\mathbf{j} = \mathbf{\Omega}\mathbf{x}p_s(\mathbf{x})$, with $\mathbf{\Omega} = \mathbf{A} + \mathbf{D}\mathbf{C}^{-1}$. An explicit calculation for $\mathbf{\Omega}$ yields:

$$\mathbf{\Omega} = \frac{k(T_1-T_2)}{\gamma c}\begin{pmatrix} 2(T_1+T_2) & -(7T_1+T_2) \\ (T_1+7T_2) & -2(T_1+T_2)\end{pmatrix}, \tag{I.12}$$

with $c = (T_1^2 + 14T_1T_2 + T_2^2)$. As expected, the flux vanishes at thermal equilibrium when $T_1 = T_2$. Such circulation can be directly measured from the beads trajectories by discretizing the coordinates space and counting the average number of transitions between neighbors cells [5], as shown in Fig. I.2B. However, instead of trying to infer the current field in full details, is it possible to avoid a discretization of the coordinates by defining some average quantities which are not space dependent, but still contain key information about the non-equilibrium dynamics of the system.

Cycling frequency The term cycling frequency refers to the average rate at which the trajectory revolves in the coordinate space. We have seen that the current density field can be expressed as $\mathbf{j} = \mathbf{\Omega}\mathbf{x}p_s(\mathbf{x})$. The average velocity of the trajectory in the phase space is described by the field $\mathbf{v} = \mathbf{\Omega}\mathbf{x}$. From Eq. (I.11) it is possible to show that the matrix $\mathbf{\Omega}$ has purely imaginary eigenvalues, $\lambda = \pm i\omega$, and therefore the velocity field $\mathbf{v}$ has an elliptical structure and gives rise to trajectories which revolve with angular velocity ω around the origin (Fig. I.3C).

In the particular case of the two beads system, the cycling frequencies measured in the coordinate space of the bead i and bead j are : $\omega_{ij} = \frac{\sqrt{3}k(T_i-T_j)}{\gamma\sqrt{c}}$. The cycling frequencies are indeed pseudo-scalar quantities, proportional to the temperature difference between the

beads, and they vanish when the system is at thermodynamic equilibrium. It is convenient to notice that:

$$\mathbf{\Omega} = \mathbf{A} + \mathbf{D}\mathbf{C}^{-1} = \frac{1}{2}\left(\mathbf{A}\mathbf{C} - \mathbf{C}\mathbf{A}^{\mathrm{T}}\right)\mathbf{C}^{-1}, \tag{I.13}$$

where in the second step we used Eq. (I.11). By taking the determinant on both sides of Eq. (I.13) we obtain

$$\det \mathbf{\Omega} = \omega_{ij}^2 = \frac{\left(\mathbf{C}\mathbf{A}^{\mathrm{T}} - \mathbf{A}\mathbf{C}\right)_{ij}^2}{4 \det \mathbf{C}}, \tag{I.14}$$

where we used the fact that $\left(\mathbf{A}\mathbf{C} - \mathbf{C}\mathbf{A}^{\mathrm{T}}\right) = -\left(\mathbf{A}\mathbf{C} - \mathbf{C}\mathbf{A}^{\mathrm{T}}\right)^{\mathrm{T}}$. In the next chapters we will see how Eq. (I.14) also applies to higher dimensional systems and will play a key role in our framework. Furthermore, Eq. (I.14) will also provide us with a direct connection to another non-equilibrium measure, the area enclosing rate, as we will see in the next paragraph.

Area enclosing rate The area enclosing rate is the mean area enclosed by the trajectory per unit time (Fig. I.3C), and is defined as:

$$\mathcal{A}_{ij} = \frac{1}{2}\langle \mathbf{x} \times \dot{\mathbf{x}} \rangle, \tag{I.15}$$

where $\langle \mathbf{x} \times \dot{\mathbf{x}} \rangle = \langle x_i \dot{x}_j - \dot{x}_i x_j \rangle$. For an overdamped system, $\dot{\mathbf{x}} = (A\mathbf{x} + \eta)$ where η is the vector of stochastic noises acting on the coordinates i and j. By noting that $\langle \eta_1 x_2 \rangle = \langle \eta_2 x_1 \rangle = 0$, we can replace $\langle \mathbf{x} \times \dot{\mathbf{x}} \rangle = (\mathbf{C}\mathbf{A}^{\mathrm{T}} - \mathbf{A}\mathbf{C})_{ij}$. Therefore, we obtain for the area enclosing rate

$$\mathcal{A}_{ij} = \frac{1}{2}\left(\mathbf{C}\mathbf{A}^{\mathrm{T}} - \mathbf{A}\mathbf{C}\right)_{ij} = \omega_{ij}\sqrt{\det \mathbf{C}}, \tag{I.16}$$

where in the last step we used Eq. (I.14) to relate $\mathcal{A}_{ij}$ to the cycling frequency ω_{ij}. Finally we will see in the next paragraph how these two non-equilibrium measures are closely related to another common measure of time irreversibility, the entropy production rate.

Entropy production rate The entropy production rate is the amount of entropy produced by an irreversible process per unit time. Here, starting from the Langevin framework, we will derive an expression for the average entropy production rate as defined in the Fokker Planck framework. Such an expression will be useful to connect the entropy production rate to the cycling frequency ω. To this end we will use some basic concepts of the theory of stochastic thermodynamics. For an extensive review on this topic the reader is referred to [74].

The framework of stochastic thermodynamics is based on defining the main concepts of classical thermodynamics, such as heat, work and entropy, as stochastic variables linked to the single stochastic trajectories. The average of such variables over the trajectories leads to the ensemble quantities we are used to deal with in classical thermodynamics theory. In the simple case of the two coupled beads, by single trajectory we mean therefore the trajectory resulting from a single realization of the stochastic variables η in Eq. (I.8). The

entropy change of the bath Δs_m during a single trajectory, from time 0 to t, can be written as

$$\Delta s_m = \frac{1}{T_1}\int_0^t \dot{x}_1(\tau) f_1(x_1(\tau)) d\tau + \frac{1}{T_2}\int_0^t \dot{x}_2(\tau) f_2(x_2(\tau)) d\tau, \tag{I.17}$$

where f_i indicate the force acting on the i_{th} bead. From Eq. (I.10) we obtain $\frac{\mathbf{f}}{\gamma} = \mathbf{v} + \mathbf{D}\nabla \ln p$. This leads to

$$\Delta s_m = k_{\mathrm{B}} \int_0^t \dot{\mathbf{x}}\mathbf{D}^{-1}\mathbf{v} d\tau + k_{\mathrm{B}} \int_0^t \dot{\mathbf{x}} \cdot \nabla \ln p. \tag{I.18}$$

The second term in Eq. (I.18) is associated to the change of entropy of the particles, $-\Delta s = k_{\mathrm{B}}(\ln p(\mathbf{x}, t) - \ln p(\mathbf{x}, 0))$, and then its ensemble average corresponds to the change in the common Gibbs entropy [73]. It is worth noting that in the limit of $t \to \infty$ the first term is proportional to the work performed by the viscous force and thus increases with the time t, while the second term does not. In such a limit we obtain for the total entropy change of the system $\Delta s_{tot} = \Delta s_m + \Delta s \simeq \Delta s_m$.

By taking the time derivative of the total entropy change in the system, and its ensemble average over the trajectories, we obtain the average entropy production rate Π

$$\Pi = \langle \partial_t \Delta s_{tot} \rangle = k_{\mathrm{B}} \int \frac{\mathbf{j}^{\mathrm{T}}(\mathbf{x})\mathbf{D}^{-1}\mathbf{j}(\mathbf{x})}{p(\mathbf{x})} d\mathbf{x}, \tag{I.19}$$

as usually defined within the Fokker Planck framework. Eq. (I.19) allows us to relate Π to the cycling frequency ω. In particular

$$\Pi = k_{\mathrm{B}} \int d\mathbf{x} (\mathbf{\Omega x})^{\mathrm{T}} \mathbf{D}^{-1} (\mathbf{\Omega x}) p(\mathbf{x}) = k_{\mathrm{B}} \mathrm{Tr}(\mathbf{\Omega}^{\mathrm{T}} \mathbf{D}^{-1} \mathbf{\Omega C}). \tag{I.20}$$

Since the entropy production is invariant under coordinate transformations, we can move to the coordinate system where $\mathbf{C} = \mathbb{1}$ (*'covariance-identity coordinates'*), such that $\mathbf{\Omega} = -\mathbf{\Omega}^{\mathrm{T}}$ [82]. Recalling that $\mathbf{\Omega}$ has eigenvalues $\lambda = \pm i\omega$, this yields to

$$\Pi = k_{\mathrm{B}} \omega^2 \mathrm{Tr}(\mathbf{D}^{-1}\mathbf{C}), \tag{I.21}$$

which is also invariant under coordinates transformation. The expression in Eq. (I.21) provides us with a direct relation between the average entropy production rate and the cycling frequency, and, as will become clear in Chapter 2, can be generalized to higher dimensional linear systems. By closing this paragraph we also close the circle of non-equilibrium measures that will be employed in the next chapters, and we are ready to discuss how these measures may actually be helpful in studying biological systems.

I.0.2 Goals and significance of this thesis

It is not surprising that living systems operate out of thermodynamic equilibrium. What is surprising is how the overlapping effects of a collection of different, complex and disordered non-equilibrium processes can lead to global dynamics that still explicitly break detailed balance. In fact, this broken detailed balance does not appear only at the length scales of

the processes responsible for its violation, but also at larger length scales, accessible with non-invasive microscopy techniques. For example, we have seen that the non-equilibrium dynamics which arise at the level of molecular motors can propagate to the much larger length scale of the primary cilia [5]. Finding a universal way to detect and characterize non-equilibrium in living systems is still a challenge, but once it is solved, it may have interesting applications. For instance, given that the intensity of the non-equilibrium activity of a cell is ultimately related to its metabolism, it may be possible to distinguish different cell types from non invasive and inexpensive measurements of their non-equilibrium activities [13, 62]. The study of non-equilibrium may also lead to progress in materials science: the internal driving characterizing biological soft materials can affect their macroscopic mechanical properties, and therefore a systematic non-equilibrium characterization might help to guide the development of engineered biomaterials [1].

There is still a long way to a comprehensive understanding of non-equilibrium processes in biophysics, and there are still many unanswered fundamental questions. The work presented in this thesis is devoted to make some progress in answering two of these questions. We have seen that the active nature of living matter on larger scales can be determined non-invasively by observing the breaking of the detailed balance condition in the dynamics of mesoscopic degrees of freedom, simply tracked with time-lapse microscopy experiments. However, it remains unclear how such non-equilibrium measures depend on the spatial scale at which the measurement is performed. A theoretical understanding of the spatial scaling behavior of broken detailed balance may reveal also how to extract quantitative information from measurable phase space currents to characterize the active nature of the system. Therefore, our research addresses the following questions:

How does non-equilibrium activity manifest at different length scales?

What details can we learn on the source of non-equilibrium dynamics at small scales, by measuring non-equilibrium at larger length scales?

To address these questions, we employed a simple yet general model to explore non-equilibrium in biological systems from a theoretical standpoint. In particular, we focus on studying biological assemblies, such as chromosomes, membranes or tissues, cytoplasm and cytoskeleton. The basic structure of this model consists of a d-dimensional elastic network of Brownian particles in a viscous medium, driven out of equilibrium by heterogeneously distributed stochastic forces, representing the internal enzymatic activity. Such a model can be seen as an extension of the two beads system discussed earlier. Within this model we develop a theoretical framework which allows to predict the behavior of various non-equilibrium measures. In particular, in Chapter 2 of this thesis, we focus on the first question and discuss how we can use our framework to make predictions about the spatial scaling of non-equilibrium measures. In Chapter 3, we focus on the second question, and explore how non-equilibrium measures can be informative on the properties of the active-noise in the system. Before jumping into the discussion of the results of our research we will report a review of the field of non-equilibrium detection in biological systems in Chapter 1.

Chapter 1

Non-equilibrium in living systems: a review

In this chapter is included the work of review carried out during my first year of Ph.D., in collaboration with my colleagues Federico Gnesotto, Jannes Gladrow, and under the guidance of Prof. Chase Broedersz. In this work, we reviewed the state of the art approaches to detect and characterize non-equilibrium in biological systems. Such a work helped us to formulate the questions of our research, and may provide a useful background for the reader interested in acquiring an overview of the field. However, this chapter is meant as an in-depth introduction with a particular focus on biological applications. The main concepts needed for the comprehension of the following Chapter 2 and Chapter 3 have already been presented in the introduction of this thesis.

Chapter abstract This review discusses the recent developments and efforts made to discern non-equilibrium fluctuations from thermal noise, mainly focusing on applications to biological systems. The first part focuses on the method to discern non-equilibrium dynamics based on the violation of the FDT. In particular, in section 2, it is discussed how a combination of active and passive microrheology can reveal the presence of active fluctuations in a system. Applications of such a method to reconstituted cytoskeletal networks, the cytoplasm of living cells, and cell membranes are reviewed. The second main block of the review discusses the alternative non-invasive method to detect non-equilibrium dynamics based on the detection of broken detailed balance at mesoscales. The details about the implementation of this technique are discussed in section 4 of the review, together with applications to biological systems. Additionally, we briefly discuss, in section 3, recent theoretical developments in stochastic thermodynamics and non-equilibrium statistical mechanics, and how these theories offer new perspectives to understand the physics of living systems.

1.1 Publication reprint

Broken detailed balance and non-equilibrium dynamics in living systems: a review

by

F. Gnesotto,*[1] F. Mura,*[1] J. Gladrow*[2] and C. P. Broedersz,[1]

* Contributed equally to this work
[1]Department of Physics, Arnold Sommerfeld Center for Theoretical Physics and Center for NanoScience, Ludwig-Maximilians-Universität München, Theresienstraße 37, 80333 München, Germany,
[2] Cavendish Laboratory, University of Cambridge, Cambridge CB3 0HE, United Kingdom

reprinted from

***Rep. Prog. Phys.* 81, 066601 (2018),**
doi:10.1088/1361-6633/AAB3ED.

IOP Publishing Reports on Progress in Physics
Rep. Prog. Phys. **81** (2018) 066601 (32pp) https://doi.org/10.1088/1361-6633/aab3ed

Review

Broken detailed balance and non-equilibrium dynamics in living systems: a review

F S Gnesotto[1,3], F Mura[1,3], J Gladrow[2,3] and C P Broedersz[1]

[1] Arnold-Sommerfeld-Center for Theoretical Physics and Center for NanoScience, Ludwig-Maximilians-Universität München, D-80333 München, Germany
[2] Cavendish Laboratory, University of Cambridge, Cambridge CB3 0HE, United Kingdom

E-mail: C.broedersz@lmu.de

Received 2 October 2017, revised 9 January 2018
Accepted for publication 5 March 2018
Published 18 April 2018

Corresponding Editor Professor Erwin Frey

Abstract

Living systems operate far from thermodynamic equilibrium. Enzymatic activity can induce broken detailed balance at the molecular scale. This molecular scale breaking of detailed balance is crucial to achieve biological functions such as high-fidelity transcription and translation, sensing, adaptation, biochemical patterning, and force generation. While biological systems such as motor enzymes violate detailed balance at the molecular scale, it remains unclear how non-equilibrium dynamics manifests at the mesoscale in systems that are driven through the collective activity of many motors. Indeed, in several cellular systems the presence of non-equilibrium dynamics is not always evident at large scales. For example, in the cytoskeleton or in chromosomes one can observe stationary stochastic processes that appear at first glance thermally driven. This raises the question how non-equilibrium fluctuations can be discerned from thermal noise. We discuss approaches that have recently been developed to address this question, including methods based on measuring the extent to which the system violates the fluctuation-dissipation theorem. We also review applications of this approach to reconstituted cytoskeletal networks, the cytoplasm of living cells, and cell membranes. Furthermore, we discuss a more recent approach to detect actively driven dynamics, which is based on inferring broken detailed balance. This constitutes a non-invasive method that uses time-lapse microscopy data, and can be applied to a broad range of systems in cells and tissue. We discuss the ideas underlying this method and its application to several examples including flagella, primary cilia, and cytoskeletal networks. Finally, we briefly discuss recent developments in stochastic thermodynamics and non-equilibrium statistical mechanics, which offer new perspectives to understand the physics of living systems.

Keywords: non-equilibrium, fluctuations, active living matter, fluctuation-dissipation theorem, detailed balance, cellular biophysics

(Some figures may appear in colour only in the online journal)

[3] These authors contributed equally.

Contents

1. Introduction 2
2. Non-equilibrium activity in biological systems and the fluctuation-dissipation theorem 3
   - 2.1. The violation of the FDT as a non-equilibrium measure 3
   - 2.2. Active and passive microrheology 4
   - 2.3. Activity in reconstituted gels 5
   - 2.4. Activity in cells 6
   - 2.5. ATP-dependent elastic properties and membrane fluctuations in red blood cells 8
   - 2.6. Simple model for ω^{-2} active force spectra in biological systems 10
3. Entropy production and stochastic thermodynamics 10
   - 3.1. Entropy production as a stochastic non-equilibrium measure 10
   - 3.2. Coordinate invariance in multivariate stochastic systems 13
   - 3.3. Energy-speed-accuracy trade-off in sensory adaption 14
   - 3.4. Current fluctuations in non-equilibrium systems 16
4. Detecting broken detailed balance in living systems 17
   - 4.1. Equilibrium, steady state, and detailed balance 17
   - 4.2. Probability flux analysis 18
     - 4.2.1. Estimating phase space currents 18
     - 4.2.2. Bootstrapping 19
     - 4.2.3. Toy model: two stochastically driven coupled beads 20
   - 4.3. Probe filaments to study broken detailed balance across scales in motor-activated gels 21
5. Outlook 25

Acknowledgments 25

References 26

1. Introduction

Living organisms are inherently out of equilibrium. A constant consumption and dissipation of energy results in non-equilibrium activity, which lies at the heart of biological functionality: internal activity enables cells to accurately sense and adapt in noisy environments [1, 2], and it is crucial for high-fidelity DNA transcription and for replication [3, 4]. Non-equilibrium processes also enable subcellular systems to generate forces for internal transport, structural organization and directional motion [5–9]. Moreover, active dynamics can also guide spatial organization, for instance, through nonlinear reaction-diffusion patterning systems [10–12]. Thus, non-equilibrium dynamics is essential to maintain life in cells [13].

Physically, cells and tissue constitute a class of non-equilibrium many-body systems termed *active living matter*. Importantly, cellular systems are not driven out of equilibrium by external forces, as in conventional active condensed matter, but rather internally by enzymatic processes. While much progress has been made to understand active behavior in individual cases, the common physical principles underlying emergent active behavior in living systems remain unclear. In this review, we primarily focus on research efforts that combine recent developments in non-equilibrium statistical mechanics and stochastic thermodynamics [14–16] (see section 3) together with techniques for detecting and quantifying non-equilibrium behavior [17] (see sections 2 and 4). For phenomenological and hydrodynamic approaches to active matter, we refer the reader to several excellent reviews [18–21].

A characteristic feature of living systems is that they are driven out of equilibrium at the molecular scale. For instance, metabolic processes, such as the citric acid cycle in animals and the Calvin cycle for carbon fixation in plants, generally involve driven molecular reaction cycles. Such closed-loop fluxes break detailed balance, and are thus forbidden in thermodynamic equilibrium (figures 1(A) and (B) [23]. Similar directed chemical cycles also power reaction-diffusion patterning systems in cells [11] and molecular motors, including myosins or kinesins [24]. Indeed, such molecular motors can generate mechanical force by coupling the hydrolysis of adenosine triphosphate (ATP) to conformational changes in a mechano-chemical cycle [24, 25]. The dissipation of this chemical energy drives unidirectional transitions between molecular states in this cycle. Such unbalanced transitions break detailed balance and result in directional motion of an individual motor.

One of the central theoretical challenges in the field of active living matter is to understand how the non-equilibrium dynamics of individual molecular components act in concert to drive collective non-equilibrium behavior in large interacting systems, which in general is made of both active and passive constitutents. Motor activity may drive sub-components of cells and tissue [17, 26, 27], but it remains unclear to what extent this activity manifests in the dynamics at large scales. Interestingly, even for systems out of equilibrium, broken detailed balance, for instance, does not need to be apparent at the supramolecular scale. In fact, at large scales, specific driven systems may even effectively regain thermodynamic equilibrium and obey detailed balance [28, 29].

There are, of course, ample examples where the dynamics of a living system is manifestly out of equilibrium, such as cell division or cell migration. In many cellular systems, however, one can observe stationary stochastic processes that appear at first glance thermally driven. Indeed, for many macromolecular assemblies in cells such as chromosomes [30], the nucleus [31], the cytoplasm [32–34], membranes [35–39], primary cilia [22, 40], and tissue [41] it has been debated to what extent non-equilibrium processes dominate their dynamics. Such observations raise the fundamental and practical question how one can distinguish non-equilibrium dynamics from dynamics at thermal equilibrium. To address this question, a variety of methods and approaches have been developed to detect and quantify non-equilibrium in biological systems. When active and passive microrheology are combined, one can compare spontaneous fluctuations to linear response functions, which are related to each other

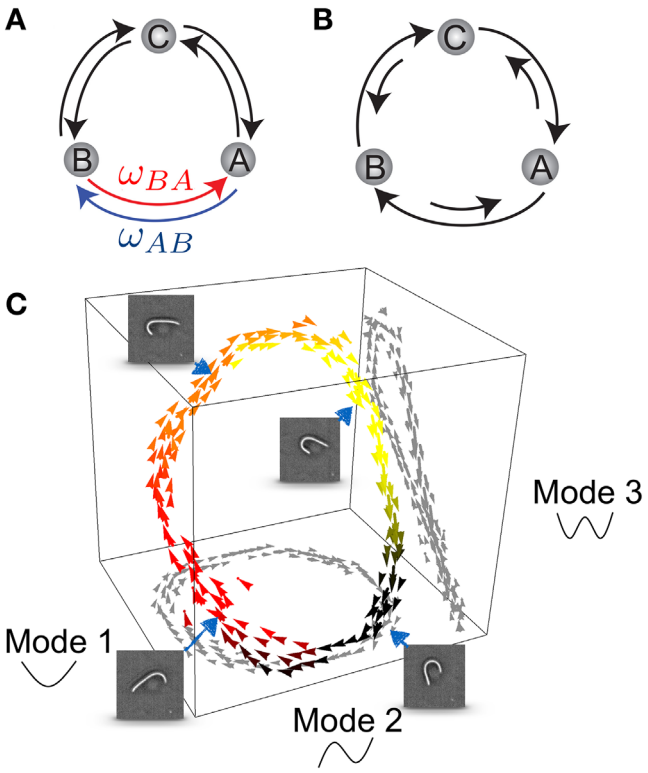

Figure 1. (A) In thermodynamic equilibrium, transitions between microscopic states are pairwise-balanced, precluding net flux among states. (B) Non-equilibrium steady states can break detailed balance and exhibit flux loops. (C) Snapshots of an isolated *Chlamydomonas* flagellum's beat cycle together with the 3D probability flux map of flagellar dynamics in a coarse grained phase space spanned by the first three modes. From [22]. Reprinted with permission from AAAS.

through the Fluctuation-Dissipation theorem (FDT) when the system is at thermal equilibrium [42–45]. Thus, the extent to which a system violates the FDT can provide insight into the non-equilibrium activity in a system. We will discuss this approach in detail in section 2. Other methods employ temperature or chemical perturbations to test the extent to which thermal or enzymatic activities primarily drive the behavior of a system, but such experiments are invasive and are often difficult to interpret. More recently, a non-invasive method to discriminate active and thermal fluctuations based on detecting broken detailed balance was proposed to study the dynamics of mesoscopic systems. This new approach has been demonstrated for isolated flagella (see figure 1(C)) and primary cilia on membranes of living cells [22]. The ideas underlying this method will be detailed in section 4 after briefly reviewing related work in stochastic thermodynamics in section 3.

Additional important insights on the collective effects of internal activity came from studies on a host of simple reconstituted biological systems. Prominent examples include a variety of filamentous actin assemblies, which are driven internally by myosin molecular motors. 2D actin-myosin assays have been employed to study emergent phenomena, such as self-organization and pattern formation [46, 47]. Moreover, actin-myosin gels have been used as model systems to study the influence of microscopic forces on macroscopic network properties in cellular components [43, 48–51]. Microrheology experiments in such reconstituted actin cytoskeletal networks have revealed that motor activity can drastically alter the rigidity of actin networks [52–54] and significantly enhance fluctuations [43, 55]. Importantly, effects of motor forces observed *in vitro*, have now also been recovered in their native context, the cytoplasm [34, 45, 55] and membranes [35, 36]. Further experimental and theoretical developments have employed fluorescent filaments as multiscale tracers, which offer a spectrum of simultaneously observable variables: their bending modes [56–58]. The stochastic dynamics of these bending modes can be exploited to study non-equilibrium behavior by looking for breaking of detailed balance or breaking of Onsager symmetry of the corresponding correlations functions [59, 60]. This approach will be discussed further in section 4.3.

2. Non-equilibrium activity in biological systems and the fluctuation-dissipation theorem

Over the last decades, a broad variety of microrheological methods have been developed to study the stochastic dynamics and mechanical response of soft systems. Examples of such systems include synthetic soft matter [61–65], reconstituted biological networks [26, 66–73], as well as cells, tissue, cilia and flagella [21, 22, 43, 71, 74–77]. In this section, we discuss how the combination of passive and active microrheology can be used to probe non-equilibrium activity in soft living matter. After briefly introducing the basic framework and the most commonly used microrheological techniques, we will discuss a selection of recent studies employing these approaches in conjunction with the fluctuation-dissipation theorem to quantify non-equilibrium dynamics.

2.1. The violation of the FDT as a non-equilibrium measure

Microscopic probes embedded in soft viscoelastic environments can not only be used to retrieve data about the spontaneous fluctuations of the surrounding medium, but can also be employed to measure the mechanical response of this medium to a weak external force. In the absence of an applied force, the average power spectrum $S_x(\omega) = \langle|\Delta x^2(\omega)|\rangle$ of fluctuations in the bead position $x(t)$ can be directly measured. The brackets here indicate an ensemble average. The same bead can, in principle, be used to extract the linear response function $\chi_x(\omega) = \langle\Delta x(\omega)\rangle/f(\omega)$ by measuring the average displacement induced by a small applied force $f(\omega)$. In systems at thermal equilibrium, these two quantities are related through the Fluctuation-Dissipation theorem (FDT), derived in the context of *linear response theory* [78, 79] (see figure 2). In frequency space, the FDT relates the autocorrelation function of position fluctuations of an embedded probe particle in the absence of external forces, to the imaginary part of the associated response function:

$$S_x(\omega) = \frac{2k_BT}{\omega}\chi_x''(\omega). \quad (1)$$

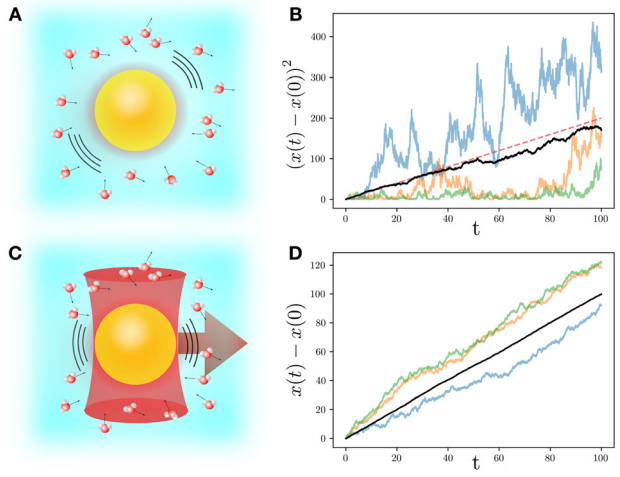

Figure 2. The fluctuation dissipation theorem implies a relation between thermal forces exerted by the molecules of the fluid on a Brownian bead and drag forces due to the viscosity of the fluid. (A) Cartoon of a freely diffusing Brownian particle. (B) Mean square displacement of the particle obtained by performing a Brownian simulation (black), and comparison with the analytical prediction $<(x(t)-x(0))^2>=2Dt$ (red). (C) Schematic of an external force f in the positive x direction applied on the particle via an optical tweezer. (D) The average displacement for the driven particle (black), obtained from Brownian dynamics simulation, increases linearly with time, as $<x(t)-x(0)>=\mu ft$, where μ is the mobility. In this simple cases, the FDT reduces to the Einstein relation: $D=\mu k_{\mathrm{B}}T$.

Importantly, a system that is actively driven into a non-equilibrium steady-state will typically not satisfy this equality; this fact can be used to our advantage to study activity in such a system. Indeed, the violation of the FDT has proven to be a useful method to assess the stochastic non-equilibrium nature of biological systems, for instance, by providing direct access to the active force spectrum in cells [45].

One of the first efforts to investigate deviations from the FDT in a biological system was performed on hair bundles present in the aural canal of a frog [80]. Hair bundles are thought to be primarily responsible for the capability of the ear to actively filter external inputs and emit sound [80, 81]. To trace the dynamics of the hair bundle, a flexible glass fiber was attached to the bundle's tip to measure both the position autocorrelation function and the associated response to periodic external stimuli. Interestingly, the magnitude of position fluctuations was observed to largely exceed the linear-reponse-based levels for a purely thermal system. This violation of the FDT indicates the presence of an internal energy source driving the system out of equilibrium.

A suggested measure of the degree of violation of the FDT is a frequency-dependent 'effective temperature' $T_{\mathrm{eff}}(\omega)$ [80, 82–86], defined as the ratio between fluctuations and dissipation: $T_{\mathrm{eff}}(\omega)\equiv\omega S_x(\omega)/2k_{\mathrm{B}}\chi_x''(\omega)$. For a system at thermal equilibrium $T_{\mathrm{eff}}=T$. However, this quantity can be drastically modified for an actively driven bundle: Close to its spontaneous oscillation frequency ω_0, the imaginary part of the response function of the hair bundle becomes negative. This implies that T_{eff} is frequency dependent and can also assume negative values.

Even though this example illustrates how the dimensionless quantity T_{eff}/T provides a simple metric for non-equilibrium, the concept of an effective temperature in this context remains a topic of debate [36, 37, 80, 87, 88]. Note, the existence of an effective temperature should not be mistaken for the existence of a physical mapping between an active system and an equilibrium system at a temperature T_{eff}. While there certainly are examples where such a mapping exists, this will not be the case in general. Furthermore, although it is not obvious how to interpret negative or frequency dependent effective temperatures, an interesting perspective is offered by Cugliandolo *et al* [82]. These authors demonstrated for a class of systems that the effective temperature can indicate the direction of heat flow and that this quantity can act as a criterion for thermalization [82]. In a more recent study, conditions were derived for systems in non-equilibrium steady states to be governed by a quasi-FDT: a relation similar to the equilibrium FDT, but with the temperature replaced by a constant $T_{\mathrm{eff}}>T$ [89]. These conditions entail that the intrinsic relaxation time of the system is much longer than the characteristic time scale of the active forces. However, these conditions may become more complicated in systems with a viscoelastic response governed by a spectrum of timescales for which the thermal force spectrum is colored [90]. Beyond being a simple way of measuring deviations from the FDT, the concept of an effective temperature may thus provide insight into active systems, but this certainly requires further investigation. Alternative measures for non-equilibrium have been the subject of more recent developments based on phase spaces currents and entropy productions rates, which are discussed in sections 3 and 4.

2.2. Active and passive microrheology

The successful application of the FDT in an active unidimensional context, as in the case of the hair bundle described above, paved the road for new approaches: microscopic probes were embedded into increasingly more complex biological environments to study the mechanics and to detect activity inside reconstituted cytoskeletal systems [26, 42, 43, 70] and living cells [42, 75, 91].

Probing violations of the FDT in such soft biological systems relies on high-precision microrheological approaches. Conventional single particle microrheology is divided into two categories: passive microrheology (PMR) [92] and active microrheology (AMR) [93–95]. PMR depends on the basic assumption that both the FDT and the generalized Stokes relationship apply. This assumption ensures that a measurement of the position fluctuation spectrum directly yields the rheological properties of the medium. Indeed, the generalized Stokes relation connects the force-response function to the viscoelastic response of the medium [92],

$$\chi_x(\omega)=\frac{1}{6\pi aG(\omega)}, \tag{2}$$

where a is the radius of the bead. This equation is valid in the limit of Stokes' assumptions, i.e. overdamped spherical

particle embedded in a homogeneous incompressible continuum medium with no slip boundary conditions at the particle's surface. Here, $G(\omega) = G'(\omega) + iG''(\omega)$ describes the complex shear modulus, where the the real part is the storage modulus G' describing the elastic component of the rheological response, and the imaginary part, G'', is the loss modulus accounting for the dissipative contribution. Under equilibrium conditions, the imaginary part of the response function χ_x'' is also related to the position power spectral density via the FDT (equation (1)). Thus, in PMR, the response function and the shear modulus are measured by monitoring the mean square displacement (MSD) $\langle \Delta x^2 \rangle(t) \equiv \langle (x(t) - \langle x \rangle)^2 \rangle$ of the embedded beads. By contrast, in AMR the mechanical response is directly assessed by applying an external force on an embedded probe particle, usually by means of optical traps or magnetic tweezers. Within the linear response regime, the response function can be measured as $\chi_x = \langle \Delta x(\omega) \rangle / f(\omega)$, and the complex shear modulus can then be determined from the generalized Stokes relation (equation (2)).

Although one-particle PMR has proven to be a useful tool to determine the equilibrium properties of homogeneous systems, biological environments are typically inhomogeneous. Such intrinsic inhomogeneity can strongly affect the local mechanical properties [96, 97], posing a challenge to determine the global mechanical properties using microrheology. To circumvent this issue, two-point particle microrheology is usually employed [42, 98]. This method is conceptually similar to one-point microrheology, but it is based on a generalized Stokes-Einstein relation for the cross-correlation of two particles at positions $\mathbf{r}_1$ and $\mathbf{r}_2$ with a corresponding power spectral density $S_{r_1,r_2}(R,\omega)$ with $R = |\mathbf{r}_2 - \mathbf{r}_1|$. This correlation function depends only on the distance between the two particles and on the macroscopic shear modulus of the medium. Thus, S_{r_1,r_2} is expected to be less sensitive to local inhomogeneities of the medium [98].

PMR has been extensively employed to assess the rheology of thermally driven soft materials in equilibrium, such as polymer networks [44, 62, 92, 99–104], membranes and biopolymer-membrane complexes [36, 105, 106], as well as foams and interfaces [107–109]. However, a PMR approach cannot be employed by itself to establish the mechanical properties of non-equilibrium systems, for which the FDT generally does not apply. If the rheological properties of the active system are known, the power spectrum of microscopic stochastic forces $\Delta(\omega)$—with both thermal and active contributions—can be extracted directly from PMR data for a single sphere of radius a [42, 44, 110]

$$\Delta(\omega) = 6\pi a\, S_x(\omega) |G(\omega)|^2 . \qquad (3)$$

The expression for the power spectrum of force fluctuations was justified theoretically [42, 111], considering the medium as a continuous, incompressible, and viscoelastic continuum at large length scales. The results discussed above laid out the foundations for a variety of studies that employed microrheological approaches to investigate active dynamics in reconstituted cytoskeletal networks and live cells, which will be discussed next.

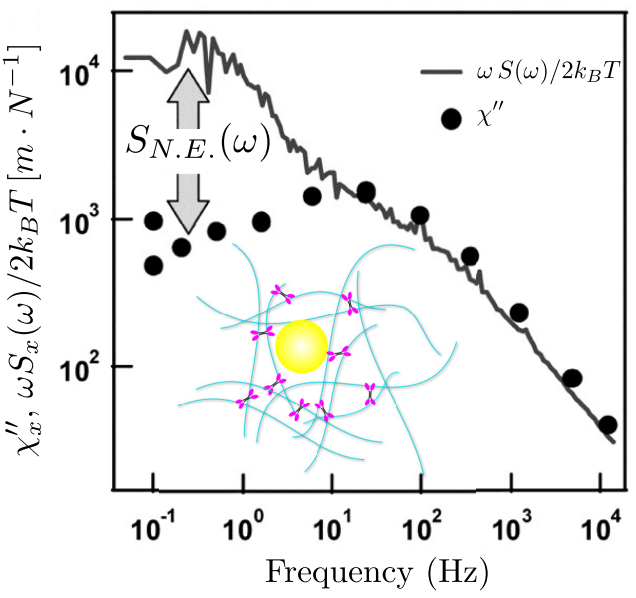

Figure 3. Violation of the FDT in reconstituted actin-myosin networks (inset). At frequencies below 10 Hz the response function estimated from spontaneous fluctuations of a probe bead via the FDT deviates significantly from the response χ'' measured directly using active microrheology (full circles). From [43]. Reprinted with permission from AAAS.

2.3. Activity in reconstituted gels

The cytoskeleton of a cell is a composite network of semiflexible polymers that include microtubules, intermediate filaments, F-actin, as well as associated proteins for cross-linking and force generation [6, 26, 112, 113]. The actin filament network is constantly deformed by collections of molecular motors such as Myosin II. These motors are able to convert ATP into directed mechanical motion and play a major role in the active dynamics of the cytoskeleton [8, 34, 43, 114, 115].

To develop a systematic and highly controlled platform for studying this complex environment, simplified cytoskeletal modules with a limited number of components were reconstituted *in vitro*, opening up a new field of study [26, 66, 116, 117]. Among these reconstituted systems, F-actin networks are perhaps the most thoroughly examined [20, 43, 68, 117–120]. Indeed, in the presence of motor activity, these networks display a host of intriguing non-equilibrium behaviors, including pattern formation [46–48, 121], active contractiliy and nonlinear elasticity [49, 52, 122–125], as well as motor-induced critical behavior [50, 53].

To study the steady state non-equilibrium dynamics of motor-activated gels, Mizuno *et al* constructed a three-component *in vitro* model of a cytoskeleton, including filamentous actin, an actin crosslinker, and Myosin II molecular motors [43]. The mechanical properties of the network were determined via AMR, while the activity-induced motion of an embedded particle was tracked via PMR. The measured imaginary component of the mechanical compliance, $\chi_x''(\omega)$, was compared to the response predicted via the FDT, i.e. $\omega S_x(\omega)/2k_BT$, as shown in figure 3. In the presence of myosin, the fluctuations in the low-frequency regime were

observed to be considerably larger than expected from the the measured response function and the FDT, indicating that myosin motors generate non-equilibrium stress fluctuations that rise well above thermally generated fluctuations at low frequencies.

These observations raise the question why motor-driven active fluctuations only dominate at low frequencies. This can be understood from a simple physical picture in which myosin motor filaments bind to the actin network and steadily build up a contractile force during a characteristic processivity time τ_p [126]. After this processivity time, the motor filament detaches from the actin polymers to which they are bound, producing a sudden drop in the force that is exerted locally on the network. Such dynamics generically generate a force spectrum $\Delta(\omega) \sim \omega^{-2}$ [111, 127], which can dominate over thermally driven fluctuations in an elastic network on time scales larger than the characteristic relaxation time of the network, but smaller than the processivity time of the motors (see section 2.6 for a more detailed discussion).

In addition to the appearance of non-equilibrium fluctuations, the presence of motors in the network led to a substantial ATP-dependent stiffening. It is well known that crosslinked semiflexible polymer networks stiffen under an external strain [67, 128–131]. Motors can effectively crosslink the network leading to stiffening, but they can also generate local contractile forces, and it is less clear how internal stress generation from such motor activity can induce large scale stresses and control network stiffness [54, 111, 123, 125, 132–136]. In a more recent experimental study, it was shown that motor generated stresses can induce a dramatic stiffening behavior of semiflexible networks [52]. This mechanism could be employed by cells and tissues to actively regulate their stiffness [132, 137–139].

An ensemble of beads dispersed in an active gel can not only be used to obtain fluctuation spectra, but also to infer the full probability distribution of the beads' displacements at a time-lag τ [88, 140, 141]. This distribution is typically observed to be Gaussian for a thermal systems, while non-Gaussian tails are often reported for an active system. In actin-myosin gels, for example, exponential tails in the particle position distributions are observed at timescales τ less than the processivity time of the motors. By contrast, at larger time lags, a Gaussian distributions is observed, in agreement with what was previously found for fluctuation spectra in frequency space [43]. Importantly however, non-Gaussianity is not a distinctive trait of non-equilibrium activity, since it can also appear in thermal systems with anharmonic potentials. In some cases, active systems are also governed by Gaussian distributions (see section 3.2).

The hallmarks of activity discussed above for actin-myosin gels are also observed in synthesized biomimetic motor-driven filament assemblies. For example, Betrand *et al* created a DNA-based gel composed of stiff DNA tubes with flexible DNA linkers [142]. As an active component, they injected FtsK50C, a bacterial motor protein that can exert forces on DNA. An important difference with the actin-based networks described above, is that here the motors do not directly exert forces on the DNA tubes, which constitute the filaments in the gel. Instead, the motors attach to long double-stranded DNA segments that were designed to act as cross-linkers between two stiff DNA tubes. Upon introduction of the motors, the MSD of tracer beads that were embedded in the gel was strongly reduced, even though the motors act as an additional source of fluctuations. This observation suggests a substantial stiffening of the gel upon motor activation. Furthermore, the power spectrum of bead fluctuations exhibited $\sim\omega^{-2}$ behavior, similar to results for *in vitro* actin-myosin systems and even for live cells, which we discuss next.

2.4. Activity in cells

The extensive variety of biological functions performed by living cells places daunting demands on their mechanical properties. The cellular cytoskeleton needs to be capable of resisting external stresses like an elastic system to maintain its structural integrity, while still permitting remodelling like a fluid-like system to enable internal transport as well as migration of the cell as a whole [113, 143]. The optimal mechanical response clearly depends on the context. An appealing idea is that the cell can use active forces and remodelling to dynamically adapt its (nonlinear) viscoelastic properties in response to internal and external cues [144–146]. In light of this, it is interesting to note that experiments on reconstituted networks suggest that activity and stresses can lead to responses varying from fluidization to actual stiffening [7, 52, 147]. Currently, however, it remains unclear how such a mechanical response plays a role in controlling the complex mechanical response of living cells [6, 143, 145, 148–151].

Important insights into the mechanical response of cells were provided by experiments conducted by Fabry *et al* via beads attached to focal adhesions near the cortex of human airway muscle cells. Their data indicate a rheological response where the loss and storage moduli are comparable, with a magnitude roughly in the range 100–1000 Pa around 1 Hz; also the moduli depend on frequency as a power law $|G(\omega)| \sim \omega^x$ with a small exponent $0.1 \leqslant x \leqslant 0.3$ [75], reminiscent of soft glassy rheology [84, 152–155].

The studies conducted by Lau *et al* [42] and Fabry *et al* [75] employed different probes at different cell sites for active and passive measurements, and determined a diffusive-like spectrum $\langle \Delta x^2 \rangle \sim \omega^{-2}$. A more recent assessment [74] was able to measure the cellular response and the fluctuation spectrum with the same probe and at the same cellular location. The rheological measurement of G was found to depend critically on the size of the engulfed magnetic beads and yielded a power law dependence on the applied torque-frequency $G(\omega) \sim \omega^{0.5-0.6}$. Furthermore, the conjuncted PMR and AMR assessments revealed a clear violation of the FDT, with the MSD of the beads increasing super diffusively with time. Measurements of the MSD of micron-size beads located around the nucleus of a living fibroblast also exhibited super-diffusive spectra, with a $\sim t^{3/2}$ dependence [156]. Upon depolymerization of the microtubule network, diffusive behavior was restored suggesting that the rectifying action of microtubule-related molecular motors might be responsible for the super diffusive behavior. Furthermore, when the motors were inhibited without perturbing the polymer

network, subdiffusive behavior was observed, in accordance to what is expected in equilibrium for a Brownian particle diffusing in a viscoelastic environment [110].

A systematic measurement of both active and passive cytoplasmic properties was carried out by Guo *et al* via submicron colloidal beads injected into the cytoplasm of live A7 Melanoma cells. The probe beads were conveniently employed to perform both PMR and AMR with the use of optical tweezers. The active microrheology experiments indicated a response with a shear modulus around 1 Pa, softer than measured near the cortex in [75], but with a similar power-law dependence of the complex shear modulus on frequency $|G(\omega)| \sim \omega^{0.15}$ [45]. Passive microrheology was employed to measure the mean square displacement (MSD) of position fluctuations in the cytoplasm under the same conditions (figure 4(A)). At short time-scales, the MSD is almost constant, as expected for a particle embedded in a simple elastic medium. By contrast, at long time scales, the system can relax, resulting in a MSD that increases linearly with time, as would be expected for simple diffusion-like behavior of a probe particle in a viscous liquid [91, 157].

Although these observations are deceptively close to the features of simple Brownian motion, this is clearly not the correct explanation for this phenomenon, given that the mechanical response of the system measured by AMR is predominantly elastic at these time scales. Furthermore, by treating cells with blebbistatin, an inhibitor of Myosin II, the magnitude of fluctuations notably decreased in the long time regime. While this suggests an important role for motor generated activity in driving the fluctuations of the probe particle, Myosin inhibition could also affect the mechanical properties of the cytoplasm, and thereby also the passive, thermally driven fluctuations of the probe particle. Nonetheless, by combining AMR and PMR it became clear that the system violates the FDT at these long time scales, implying that the system is not only out of equilibrium, but also that non-equilibrium activity can strongly alter the spectrum of force fluctuations.

The combination of AMR and PMR measurements was employed to infer the spectrum of force fluctuations using a method called force spectrum microscopy (FSM). This method makes use of the relation $\Delta(\omega) = |k(\omega)|^2 \langle \Delta x^2 \rangle(\omega)$, where the complex spring constant $k \equiv 1/\chi_x$ is related to G by $k = 6\pi G a$ (see equation (2)). The measured force spectrum exhibited two different power-law regimes: at high frequencies $\Delta(\omega) \sim \omega^{-0.85}$, while at low frequencies ($\omega \lesssim 10$ Hz), $\Delta(\omega) \propto \omega^{-2}$, in agreement with what is expected for typical molecular motor power spectra, as depicted in figure 4(B).

The observed high-frequency behavior is in accordance with predictions for particle fluctuations driven by thermal forces in a nearly elastic medium. In fact, if $G \sim \omega^{\beta}$, then $\langle \Delta x^2 \rangle(\omega) \sim \omega^{-(\beta+1)}$ at thermal equilibrium [42]. This implies that $\Delta(\omega) \sim \omega^{-0.85}$, with the measured $\beta = 0.15$. By contrast, an active model predicts $\langle \Delta x^2 \rangle(t) \sim t^{1+2\beta}$ if $\Delta(\omega) \sim \omega^{-2}$, which is consistent with what is observed in reconstituted motorized gels at timescales shorter than the processivity time τ_p [52, 55]. These experiments and others [34, 158] have thus established the active

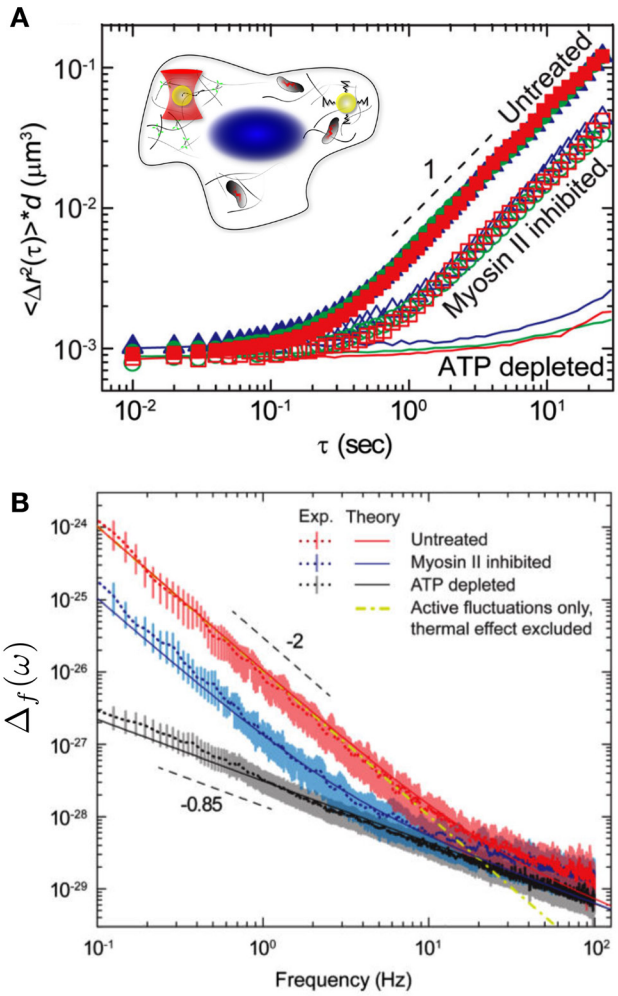

Figure 4. Fluctuations of probe particles inside living cells. (A) The MSD, $\langle \Delta x^2(\tau) \rangle$, of tracer beads rescaled by the particle diameter d, for untreated, Myosin inhibited, and ATP depleted cells. For untreated cells the MSD shows a plateau at short time scales, after which the MSD increases linearly with time. When Myosin is inhibited by blebbistatin, the power law does not change but the magnitude of the MSD is reduced. By depleting ATP in the cytoplasm, the dependence of the MSD on time becomes consistent with thermal motion in a viscoelastic environment at short times. A cartoon of AMR and PMR performed inside the cytoplasm is shown in the inset. (B) Measured force spectrum in the cytoplasm of untreated (red), blebbistatin treated (blue) and ATP-depleted (black) A7 cells. Adapted from [45], Copyright (2014), with permission from Elsevier.

nature and the characteristics of force spectra in the cytoplasm using embedded beads.

Various experiments employing PMR in live cells have been performed using alternative synthetic probes, such as nanotubes or embedded intracellular entities, including microtubules, vesicles, and fluorescently labeled chromosomal loci. In a recent study, Fakhri *et al* developed a new technology to investigate the stochastic dynamics of motor proteins along cytoskeletal tracks [34]. This cutting-edge method consists of imaging the near-infrared luminescence of single-walled carbon nanotubes (SWNT) targeted to kinesin-1 motors in live cells. Although traces of moving SWNT show long and relatively straight unidirectional runs, the dependence of the

tracers MSD on time exhibits several powerlaw regimes with an exponent that depends on the time range: At $t \approx 0.1$ s the exponent transitions from a value around 0.25 at short times to a value of 1 at larger times. By decomposing the MSD in motion along and perpendicular to the microtubule axis, it was shown that the dynamics of SWNT tracers originates from two distinct contributions: directed motion along the microtubules together with transverse non-directed fluctuations. The transverse fluctuations were attributed to bending fluctuations of the stiff microtubules, owing to motor-generated activity in the surrounding cytoskeleton, consistent with prior observations [158]. Indeed, the full time dependence of the MSD of traced kinesin motors could be described quantitatively with a model that assumes cytoskeletal stress fluctuations with long correlation times and sudden jumps. This is in agreement with a physical picture in which myosin mini-filaments locally contract the actin network during an attachment time set by the processivity time of the motors, followed by a sudden release.

Active bursts generated by Myosin-V are fundamental for nuclear positioning in mouse oocytes. In fact, active diffusion is here thought to create pressure gradients and directional forces strong enough to induce nuclear displacements [31, 159, 160]. As in the earlier studies discussed above, the FDT is sharply violated at low frequencies, while it is recovered at large ones [161].

To study the steady-state stochastic dynamics of chromosomes in bacteria, novel fluorescence-labelling techniques were employed on chromosomal loci in *E.Coli* cells. These experiments yielded sub-diffusive MSD behavior: $\langle \Delta x^2 \rangle(t) \sim t^{0.4}$ [30, 156, 162, 163]. Although purely thermal forces in a viscoelastic system, such as the cytoplasm or a nucleoid, can also generate sub-diffusive motion [164], Weber *et al* demonstrated a clear dependence of the MSD on ATP levels: When ATP was depleted from the cell, the MSD magnitude was reduced. Surprisingly however, the exponent, $\alpha = 0.4$, was not affected by varying ATP levels. Under the assumption that a change in the ATP level does not effect the dynamic shear modulus of the cytoplasm, this effect could be interpreted as resulting from active forces with a white noise spectrum and from a shear modulus that scales with frequency as $G \sim \omega^{0.7}$. While these results provide evidence for the existence of active diffusion by chromosomal loci, less invasive and more direct approaches are required to confirm and further study non-equilibrium behavior in the bacterial cytoplasm [165] and to understand the dynamics of the chromosome.

2.5. ATP-dependent elastic properties and membrane fluctuations in red blood cells

The elastic properties of cells play an important role in many biological systems. The unusually high deformability of red blood cells (RBCs) is a prominent example in this respect, lying at the heart of the cardiovascular system. RBCs have the astonishing capability to squeeze through micron-sized holes, which ensures seamless blood flow through tight capillaries. To explore how these astonishing properties emerge, a detailed understanding of passive and active behavior of the membrane enclosing RBCs and its connection to the underlying cytoskeleton is required.

The bending dynamics of membranes are largely determined by their curvature and their response to bending forces thus depends on their local geometry [166–169]. In flat membranes, the power spectral density of bending fluctuations is expected to scale as $\omega^{-5/3}$ for large ω [35, 169, 170]. A spectrum close to a $-5/3$-decay has indeed been reported in measurements of red blood cell membrane fluctuations [35]. Interestingly, the same experiments showed decreasing fluctuation amplitudes upon ATP-depletion, possibly indicating the role of non-equilibrium processes. The precise origin and nature of these processes, however, is difficult to determine due to the composite, ATP-dependent structure of erythrocyte membranes and cytoskeleton.

In addition, a flickering motion of RBC membranes observed in in microscopy experiments has sparked a discussion about the origin of these fluctuations. Indeed, the extent to which active processes determine the properties of RBCs is subject of intense research activity [35, 37, 171–177].

Although myosin is present in the cytoskeleton of human erythrocytes, mechano-chemical motors are not the only source of active forces in the cell. In the membrane of RBCs, actin forms triangular structures with another filamentous protein called spectrin. These structures are linked together by a protein known as 4.1R. Phosphorylation of 4.1R, an ATP-consuming process, causes the spectrin-actin complex to dissociate, which could lead to a softening of the cell. In accordance with this model, ATP-depletion was found to increase cell stiffness [38], and at the same time reduce membrane fluctuations on the $1-10$ s time scale. This is exemplified by the comparison between the green (ATP-depleted) and black (normal conditions) curves in figure 5(C).

In order to relate the magnitude of fluctuations to membrane stiffness κ and tension σ, Betz *et al* [35] employed a classical bending free-energy [178]

$$\mathcal{F}[h(r)] = \int \mathrm{d}^2 r \left[\frac{\kappa}{2} (\triangle h)^2 + \frac{\sigma}{2} (\nabla h)^2 \right]. \qquad (4)$$

A mode decomposition of the transverse displacement $h(\vec{q})$, evolving under thermal equilibrium dynamics of this energy functional leads to the correlator,

$$\langle h(\vec{q},t) h(\vec{q}\,',t') \rangle = \frac{(2\pi)^2 k_\mathrm{B} T}{\kappa q^4 + \sigma q^2} \delta(\vec{q} + \vec{q}\,') \mathrm{e}^{-\frac{|t-t'|}{\tau_q}}, \qquad (5)$$

which is reminiscent of the correlator derived for semiflexible filaments (see section 4.3). The decorrelation time τ_q is given by $\tau_q = 4\eta q/(\kappa q^4 + \sigma q^2)$. A Fourier transformation of the correlator yields the theoretical prediction for the power spectral density shown in figure 5. This model was also generalized to consider membrane fluctuations in the presence of active forces [169, 174, 177].

The observed stiffening of the membrane upon ATP-depletion, presented a dilemma: membrane stiffening at low ATP could be the cause of the reduction of thermally driven membrane flickering, as apposed to a picture in which membrane flickering is primarily due to stochastic ATP-driven

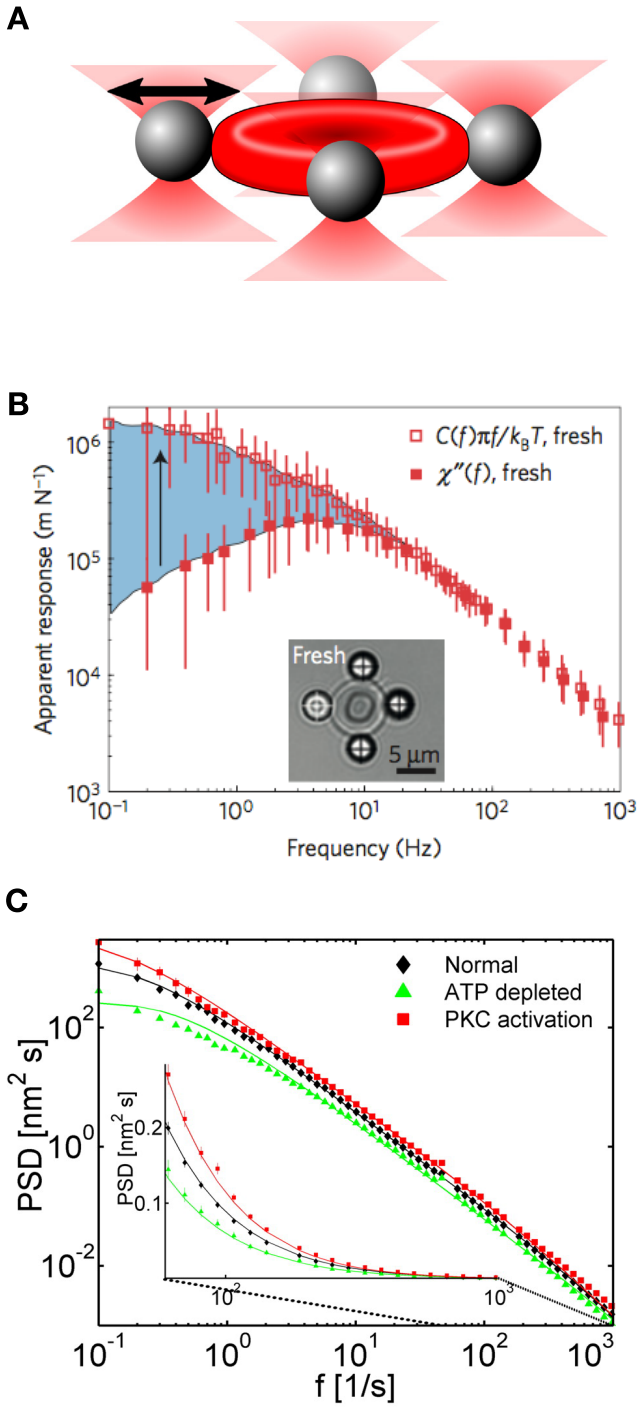

Figure 5. (A) Cartoon of a red blood cell whose membrane conformations and response are tracked via four attached microscopic beads. (B) The response and flickering spectrum of a red blood cell differ below 10 Hz, indicating a clear violation of the FDT. Adapted by permission from Macmillan Publishers Ltd: Nature Physics [36], Copyright (2016). (C) Power spectrum of RBC membrane fluctuations under normal conditions (black), after ATP-depletion (green) and after addition of a PKC (red). PKC stands for *protein kinase C*, which catalyzes the phosphorylation of 4.1R, leading to increased dissociation of actin-spectrin structures. Adapted from [35] with permission. Copyright © 2009 National Academy of Sciences.

processes. This conundrum was resolved in a subsequent study, in which RBC flickering motion was shown to violate the equilibrium FDT, providing strong evidence for an active origin of the flickering [36]. To demonstrate this, Turlier *et al* [36] attached four beads to live erythrocytes, three of them serving as a handle, while the remaining bead can either be driven by a force exerted by optical tweezers or the unforced bead motion can be observed to monitor spontaneous fluctuations. The complex response $\chi_x(\omega)$ is then obtained from the ratio of Fourier transformations of the position $x(\omega)$ and force $F(\omega)$. The equilibrium FDT in equation (1) relates these two quantities. The measured imaginary response $\chi_x''(\omega)$ is plotted together with the response calculated from equation (1) in figure 5(B). While the two curves exhibit stark differences at low frequencies, they become comparable for frequencies above 10 Hz. Thus, whatever the precise nature of active processes in erythocyte membranes is, the intrinsic timescales of these processes appear to be on the order of 1–10 Hz.

To explore the contributions to the mechanical properties of the membrane that arise specifically due to phosphorylation of 4.1R (and other molecules) in erythrocytes, the authors devised a semi-analytical non-equilibrium model for the elastic response of the membrane. Phosphorylation events are here modelled as on-off telegraph processes, which are added to an equilibrium description of membrane bending, such as in equation (4). The authors then decompose the membrane shape into spherical harmonic modes and calculate the single-mode power spectral density, which reads

$$S_x^{lm}(\omega) = \frac{2k_BT}{\omega}\chi_x^{lm}(\omega)'' + \frac{2\langle n_a\rangle\left(1-\langle n_a\rangle\right)\tau_a}{1+\omega\tau_a}\left|N^{lm}(\omega)\right|^2, \tag{6}$$

with $\tau_a = (k_a + k_i)^{-1}$ being the timescale, $n_a = k_a/(k_a + k_i)$ being the phosphorylation activity, and $N^{lm}(\omega)$ capturing the effects of tangential active noise on the membrane shape. The rate coefficients k_a and k_i characterize the simplified activate-inactivate (*a-i*) telegraph model, that the authors employ. The expression in equation (6) bears interesting similarities with the power spectrum of filament fluctuations (see section 4.3, equations (50) and (51)). The mode response here in equation (6) is also composed of independent thermal and non-equilibrium contributions. Interestingly, the model shows that the curvature of the membrane is crucial for it to sustain active flickering motions. Only a curved surface allows fluctuations of tangential stress to result in transversal motion. Modes that correspond to wavelengths too short to couple to tangential stresses also do not seem to be affected by non-equilibrium processes. The flickering therefore appears to be caused by a coupling of tangential stresses to transversal motion only within a certain window of spherical modes $2 \leqslant l \leqslant l^*$.

ATP-dependent fluctuations seem to contribute directly to the extraordinary mechanic properties of erythrocytes and may even help maintain their characteristic biconcave shape [175]. Recently, bending fluctuations of membranes have been implicated in general cell-to-cell adhesion [179]. The satisfactory agreement of theoretical and experimental fluctuation spectra in the examples discussed above highlights the merit of non-equilibrium statistical approaches to model and indeed explain properties of living biological matter.

In summary, the violation of the FDT is an elegant tool for the detection of activity in biological systems, as illustrated by the many examples discussed in the section above. That being said, for such a method to be applicable, the simultaneous

measurement of fluctuations *and* response is required. Even though this method gives information on the rheological properties of the system, its applicability can be challenging in contexts where the system is particularly delicate or poorly accessible such as chromosomes, the cytoskeleton, intracellular organelles, and membranes. Thus, in many cases a less invasive approach might be desired. These alternative approaches are further discussed in section 4.

2.6. Simple model for ω^{-2} active force spectra in biological systems

As illustrated by the examples discussed above, the mean square displacement of a probe particle in the cytoskeleton or in a reconstituted motor-activated gel has been widely observed to be surprisingly similar to a diffusive spectrum in a viscous medium: $\langle \Delta x^2 \rangle \sim t$. In a purely viscous environment, with only Brownian thermal forces, the force spectrum is well-described by white noise, which has a flat power spectrum over the whole frequency range by definition. The magnitude of the complex shear modulus for such a purely viscous fluid is $|G|^2 \sim \omega^2$. Such a simple rheological response, taken together with a white noise force spectrum, yields a displacement spectrum $\langle \Delta x^2 \rangle \sim \Delta / |G|^2 \sim \omega^{-2}$ *at all frequencies*. This mechanism, however, does not explain the effective diffusive behavior measured in cells below 10 Hz [7, 32, 34, 45, 88, 180]. Below, we illustrate with a simple model [111, 127, 180–182] that any active force with a sufficiently rapid decorrelation time can induce effective diffusive behavior of a bead in an elastic medium. The relevant range of time-scales is bound by the characteristic relaxation time of the network and by the processivity time of the motors.

Consider a particle moving in a simple viscoelastic solid with both active forces, f_A, and thermal forces, f_T. The stochastic motion of such a particle can be described by an overdamped Langevin equation [37, 42, 44, 65, 182–185]:

$$\gamma \dot{x}(t) = -kx(t) + f_T(t) + f_A(t)\,, \tag{7}$$

where k is the elastic stiffness and γ the friction coefficient of the gel, which is modelled as a Kelvin–Voigt medium [186]. For such a system, the thermal noise is described by:

$$\langle f_T(t) \rangle = 0\,,$$
$$\langle f_T(t') f_T(t) \rangle = 2\gamma k_B T \delta(t' - t).$$

By contrast, the independent active contribution, f_A, is modelled as a zero-average random telegraph process of amplitude f_0 [182, 187], whose autocorrelation function is

$$\langle f_A(t) f_A(s) \rangle = \frac{f_0^2}{4} \mathrm{e}^{-|t-s|/\tau}.$$

The inverse time constant $\tau^{-1} = \tau_{\mathrm{on}}^{-1} + \tau_{\mathrm{off}}^{-1} \ll k/\gamma$ is the sum of the switching rates of the motors between *on* and *off* states.

Suppose we perform a PMR experiment in which we only have access to the power spectral density of the position, we would measure

$$S_x(\omega) = \frac{\langle f_T^2 \rangle + \langle f_A^2 \rangle}{k^2 + \gamma^2 \omega^2} = \frac{2\gamma k_B T + \frac{f_0^2}{2} \frac{\tau}{(\omega\tau)^2 + 1}}{k^2 + \gamma^2 \omega^2}\,. \tag{8}$$

If we consider frequencies $\tau^{-1} \ll \omega \ll k/\gamma$ and assume that, in this frequency range, the magnitude of thermal fluctuations $2\gamma k_B T$ is negligible in comparison to the active force amplitude, the spectrum reduces to $S_x \approx f_0^2 \tau^{-1} / 2(k\omega)^2$. In other words, to observe the characteristic ω^{-2} spectrum, the frequency needs to be higher than the operational frequency of the motors $1/\tau$, but smaller than the characteristic frequency of the medium k/γ. Note that the functional dependence on frequency in this limit is identical to the case of purely Brownian motion in a simple liquid. For frequencies $\omega \ll 1/\tau$, $S_x \sim$ const., consistent with experiments (see figure 6(A) of [45]). Thus, this simple model illustrates how active forces with a characteristic correlation time can account for the characteristic features of active particle motion in viscoelastic solids.

3. Entropy production and stochastic thermodynamics

3.1. Entropy production as a stochastic non-equilibrium measure

Put colloquially, entropy is about disorder and irreversibility: transitions that increase the entropy of the universe are associated with an exchange of heat and should not be expected to spontaneously occur in reverse. Historically, this picture was shaped by experiments on the macroscopic scale, where temperature and pressure are well-defined variables. However, on length scales ranging from nanometers to microns, where most cellular processes occur, fluctuations matter. Entropy, once thought to increase incessantly, here becomes a stochastic variable with fluctuations around its norm. These ideas sparked many new developments in stochastic thermodynamics [14–16].

In this section, we briefly introduce and motivate several recent theoretical and experimental advances of this stochastic approach, which has extended thermodynamics to the realm of small systems. In particular, we will discuss a class of results known as '*fluctuation theorems*' (FTs), together with a selection of general developments that highlight the applications of these results to living systems. In section 3.2 we discuss aspects of entropy production that are specific to linear multidimensional system, and in section 3.3, we review a recent study that demonstrates how these concepts can be used to understand noisy control systems in cells. Finally, in section 3.4, we discuss a recently introduced fundamental lower bound for fluctuations around the currents of probability, which are associated with out-of-equilibrium systems.

A key idea of stochastic thermodynamics is to extend the classical notion of ensembles and define ensemble averages of variables, such as heat, work, and entropy over specific stochastic time trajectories of the system [188]. These trajectories can be seen as realizations of a common generating process, associated with a particular thermodynamic state.

The distribution $P(\delta)$ of fluctuations δ is often of interest. Fluctuation theorems are usually applicable far from equilibrium and constrain the shape of this distribution. Most FTs derived so far adhere to the following form

$$\frac{P(\delta)}{P(-\delta)} = \mathrm{e}^{\delta}, \tag{9}$$

which is always fulfilled for Gaussian probability distributions $P(\delta) \propto e^{-1/2(\delta-\theta)^2/\sigma^2}$ with a mean θ that equals the variance $\theta = \sigma^2/2$. Other distributions may of course also fulfill this theorem. The fluctuation theorem governing the amount of entropy produced after a time Δt, $S(\Delta t) = \pm\omega$, $P(\omega)/P(-\omega) = \mathrm{e}^{\omega}$ has received particular attention. This result underlines the statistical nature of the second law of thermodynamics: a spontaneous decrease in the entropy of an isolated system is not prohibited, but becomes exponentially unlikely. However, since the entropy is an extensive quantity, negative fluctuations only become relevant when dealing with small systems, such as molecular machines.

The first fluctuation theorems were derived in a deterministic context [189], then extended to finite time transitions between two equilibrium states [190], and finally to microscopically reversible stochastic systems [191]. Later, mesoscopic stochastic approaches based on a Langevin descriptions were proposed. These descriptions turn out to be especially suitable in an experimental biological context were typically only mesoscopic degrees of freedom are tracked [192–195].

Further physical intuition for entropy production can be obtained in the description provided by Seifert [195]. Here, the 1D overdamped motion of a colloidal particle is treated as a model system. The particle moves in a medium at fixed temperature T and is subject to an external force $F(x, \lambda)$ at position x, which evolves according to a protocol λ. The entropy production associated with individual trajectories, $\Delta s_{\mathrm{tot}} = \Delta s_m + \Delta s$, is given by the sum of two distinct contributions: the change of entropy of the medium Δs_m and the change of entropy of the system Δs. The former is related to the amount of heat dissipated into the medium, $\dot{q} = F(x, \lambda)\dot{x}$, as $\Delta s_m = \int \mathrm{d}t'\, \dot{q}/T$. The entropy change of the system is obtained from a trajectory-dependent entropy:

$$s(t) = -k_{\mathrm{B}} \ln(P(x(t), t)). \tag{10}$$

where $P(x(t), t)$ is the probability of finding the particle at $x(t)$ at time t. Taking the average of $s(t)$ naturally leads to the Gibbs entropy, $S = -k_{\mathrm{B}}\langle \ln(P(x(t), t))\rangle$. Within this framework, the integral fluctuation theorem (IFT) for Δs_{tot} can be derived [195], which reads

$$\left\langle \mathrm{e}^{-\frac{\Delta s_{\mathrm{tot}}}{k_{\mathrm{B}}}} \right\rangle = 1. \tag{11}$$

The IFT expresses a universal property of entropy production, which is valid if the process can be captured by a Langevin or master equation description. Note, that in this context this theorem also implies the second law, since it implies $\langle \Delta s_{\mathrm{tot}} \rangle \geqslant 0$. In steady-state, a similar approach leads to the steady-state fluctuation theorem (SSFT)

$$P(-\Delta s_{\mathrm{tot}})/P(\Delta s_{\mathrm{tot}}) = \mathrm{e}^{-\frac{\Delta s_{\mathrm{tot}}}{k_{\mathrm{B}}}}, \tag{12}$$

which is a stronger relation from which equation (11) follows directly. In early studies [192, 196] this theorem was obtained only in the long time limit, but it has been now extended to shorter timescales [195]. To experimentally validate the fluctuation theorems discussed, Speck *et al* studied a silica bead maintained in a NESS by an optical tweezer. In this study, a single silica bead is driven along a circular path by an optical tweezer [197]. The forces felt by the bead fluctuate fast enough to result in an effective force f, which is constant along the entire circular path. The entropy production calculated directly from trajectories indeed adhered to the SSFT described above.

The development of fluctuation theorems has given a fresh boost to the field of stochastic thermodynamics and has led to a number of interesting studies. For example, several conditions for thermodynamic optimal paths have been established [198–200]. These optimal paths represent a protocol for an external control parameter that minimizes the mean work required to drive the system between two equilibrium states in a given amount of time. These results could provide insight into thermodynamic control of small biological systems. Recently, a fundamental trade-off between the amount of entropy produced and the degree of uncertainty in probability currents has been derived, which was considered in the context of sensory adaptation in bacteria. This trade-off is discussed in section 3.4.

Another important connection between energy dissipation and the spontaneous fluctuations of a system in a non-equilibrium steady-state was found by Harada and Sasa [201]. When a system is driven out of equilibrium, the fluctuation dissipation theorem (FDT) is violated (see section 2). A natural question to ask is what the violation of the FDT teaches us about the non-equilibrium state of a system. Starting from a Langevin description for a system of colloidal particles in a non-equilibrium steady state, a relation was derived between the energy dissipation rate and the extent of violation of the equilibrium FDT [201],

$$\langle \dot{W} \rangle = \sum_{i=0}^{N-1} \gamma_i \left\{ \bar{v}_i^2 + \int_{-\infty}^{+\infty} \left[\tilde{S}_{v,ii}(\omega) - 2T\tilde{\chi}'_{v,ii}(\omega) \right] \frac{\mathrm{d}\omega}{2\pi} \right\} \tag{13}$$

where $\langle \dot{W} \rangle$ is the average rate of energy dissipation and γ_i denotes the friction coefficient for the i_{th}-coordinate; $\tilde{S}_{v,ii}(\omega)$ and $\tilde{\chi}_{v,ii}(\omega)$ are the Fourier transform of the velocity correlation function and response function respectively. A remarkable feature of this relation is that it involves experimentally measurable quantities such as the correlation function and the response function, thereby allowing a direct estimate of the rate of energy dissipation. The violation of FDT has been measured, for instance, for molecular motors such as F_1 ATPase or Kinesin. Using the Harada–Sasa relation, it has been possible to infer information on the dissipated energy and efficiencies of such biological engines [202, 203].

Intuitively, any experimental estimate of the entropy production rate will be affected by the temporal and spatial resolution of the observation. In [204] a coarse-grained description of a system in terms of mesostates was considered. With this approach, it was shown how the entropy

production obtained from the mesoscopic dynamics, gives a lower bound on the total rate of entropy production. Interestingly, in systems characterized by a large separation of timescales [205] where only the slow variables are monitored, the hidden entropy production arising from the coupling between slow and fast degrees of freedom, can be recovered using equation (13). Another interesting notion in this context is the *partial entropy production*, which refers to the fraction of entropy production that can be recovered from a partial observation of the system, i.e. when only a subset of degrees of freedom is accessible. This concept is illustrated and discussed in [206, 207], and a partitioning of the entropy production related to the observed and hidden variables with relative FTs is derived in [208].

The entropy production rate appears to be a good way of quantifying the breakdown of time reversal symmetry and energy dissipation. However, it is still unclear how this quantity is affected by the timescales that characterize the system. To address this, a system of active Ornstein–Uhlenbeck particles was considered [87]. This system can be driven out of equilibrium by requiring the self-propulsion velocity of each particle to be a persistent Gaussian stochastic variable with decorrelation time τ, thereby providing a simple, yet rich theoretical framework to study non-equilibrium processes. Interestingly, to linear order in τ, an effective equilibrium regime can be recovered: This regime is characterized by an effective Boltzmann distribution and a generalized FDT, even though the system is still being driven out of equilibrium. Indeed, the leading order contribution of the entropy production rate only sets in at $\sim \tau^2$.

In complex systems, we may sometimes face limited information about local or global thermodynamic forces. In such situations, the direction in which processes evolve, that is, the direction of time itself may in principle become unclear. Due to micro-reversibility, individual backward and forward trajectories are indistinguishable in equilibrium. Thus, it is natural to ask‘ how much information is needed to tell if a given trajectory runs forward or backward in time?

This question was studied by Roldan *et al* [209] using decision-theory, a natural bridge between thermodynamic and information-theoretic perspectives. Entropy production is here defined as $\Delta s_{\rm tot}(t) = k_{\rm B}\ln(P(X_t)/P(\tilde{X}_t))$ with X_t and $\tilde{X}_t$ denoting a forward trajectory and its time-reversed counterpart . The unitless entropy production, $\Delta s(t)/k_{\rm B}$ assumes the role of a log-likelihood ratio $\mathcal{L}(t)$ of the probability associated with the forward-hypothesis $P(X_t|H_{\rightarrow})$ and the backward-hypothesis $P(X_t|H_{\leftarrow})$, that is, $\mathcal{L}(t) = \ln P(X_t|H_{\rightarrow})/P(X_t|H_{\leftarrow})$. In a sequential-probability ratio test, $\mathcal{L}(t)$ is required to exceed a pre-defined threshold L_1 or subceed a lower threshold L_0, to decide which of the respective hypotheses H_1, H_0 is to be rejected. The log-likelihood ratio $\mathcal{L}(t)$ evolves over time as more and more information is gathered from the trajectory under scrutiny.

Interestingly, for decision-thresholds placed symmetrically around the origin $L_0 = -L$, $L_1 = L$, the observation time $\tau_{\rm dec}$ required for $\mathcal{L}(t)$ to pass either threshold turns out to be distributed independently of the sign of L, i.e.

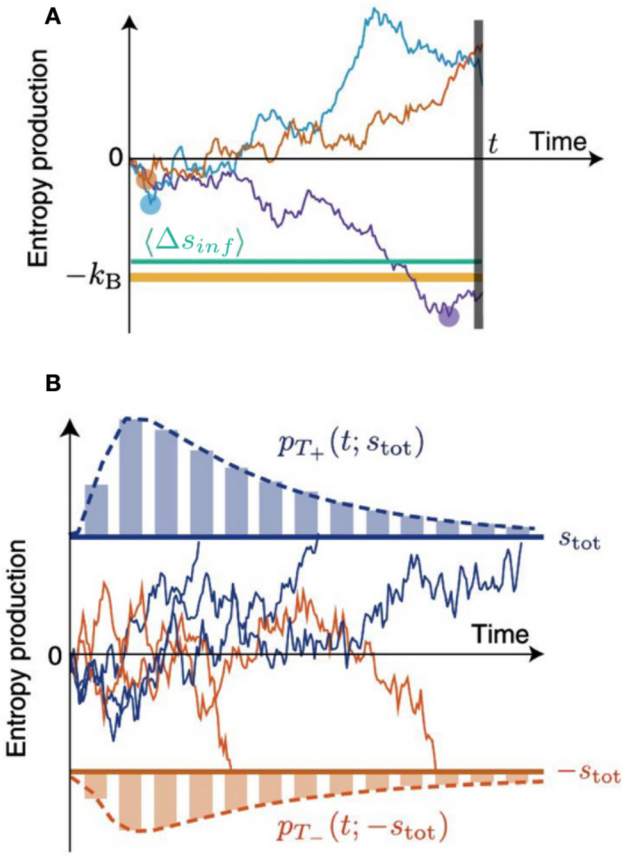

Figure 6. Entropy as a stochastic variable: illustration of the mean infimum inequality and the equivalence of entropy production stopping times. (A) The average of the minimum of an ensemble of entropy-trajectories (purple, red and blue) $\langle \Delta s_{\rm inf}(t) \rangle$ (cyan) is bound from below by $k_{\rm B}$ (thick yellow). (B) For entropy-bounds $\pm s_{\rm tot}$ that are symmetrically placed around 0 (thick red and blue), the stopping times T_+ and T_- share the same probability distribution (the figure shows unnormalized histograms). The stopping time T_+ (T_-) here is defined as the first-passage time of the entropy past the upper (lower) bound. Reproduced from [210].

$$P(\tau_{\rm dec}|\leftarrow) = P(\tau_{\rm dec}|\rightarrow). \tag{14}$$

From a thermodynamics perspective, this insight, implies that the average time it takes for a given process to produce a certain amount of entropy, must equal the average time it takes the same process to *consume* this amount of entropy. A process that consumes entropy takes up heat from the environment. This can only occur rarely, of course, so that the the second law is not violated.

In a related recent study, Neri *et al* [210] discuss the properties of ‘*stopping times*’ of entropy production processes using a rigorous mathematical approach. The stopping time here is defined as the time a process on average takes to produce or consume a certain amount of entropy relative to time t_0. This stopping time equivalence is sketched in figure 6(B). Importantly, stopping times are first passage times conditioned on the process actually reaching the threshold. The distribution of stopping times, therefore does not say anything about how probable it is for an observer to witness the process of reaching the threshold at all. Only *if* a trajectory reaches the

threshold, the conditional first passage time can be measured. Figure 6(A) depicts another property of the entropy $\Delta s(t)$: the average entropy is bounded from below by k_B.

These ideas were further illustrated by a few examples. The time a discrete molecular stepper, similar to the one illustrated in figure 9, would spend making N steps forward in a row, on average, is the same as it would spend making N steps backwards. This results from the way the entropy production for this system scales with the position, $\Delta s_{tot}(t) = -N(t)Fl/(k_B T)$, where F is the driving force and l denotes the step length. Related first-passage-time equivalences have been discussed in the context of transport [211], enzymes [212], molecular motors [213], and drift-diffusion processes [214]. Entropy stopping times, however, provide a unifying and fruitful perspective on first passage times of thermodynamic processes. Finally, we note that the properties of stochastic entropy production discussed above can also be derived from an Itô equation of the entropy that was recently derived [215].

Living systems form one of the most intriguing candidates to apply key concepts of stochastic thermodynamic. Several fluctuation relations have been experimentally verified for various biological processes[15, 216–222] and a stochastic thermodynamic description for chemical reaction networks have been developed [223] and applied, for instance, in catalytic enzymatic cycles [216]. A multitude of thermodynamic equalities and lower bound inequalities involving the entropy production have been used to investigate the efficiency of biological systems. This provides insight into the energy dissipation required for a system to perform its biological function at some degree of accuracy. Important contributions in this direction can be found, for instance, in [224] where the efficiency of molecular motors in transforming ATP-derived chemical energy into mechanical work is discussed. Following this line, we could ask how precise cells can sense their environment and use this information for their internal regulation. This was addressed in several works [1, 2, 225], highlighting a close connection between the amount of entropy produced by the cellular reaction network responsible for performing the 'measurement', and the accuracy of the final measured information (see section 3.3). In [226, 227] these concepts were further expanded and applied to more complex macroscopic systems, such as the self-replication of bacteria, whose description is not captured by a simple system of chemical reaction networks. Despite the system's complexity, insightful results were obtained by deriving the more general inequality:

$$\Delta S_m + \Delta S \geqslant -\ln \frac{\pi(II \to I)}{\pi(I \to II)}. \tag{15}$$

Here, the system's irreversibility, i.e the ratio of the probability of transition between two macrostates $\pi(II \to I)$ and the transition probability of the reversed process, represents a lower bound for the total entropy production: $\Delta S_m + \Delta S$, where ΔS is the internal entropy difference between the two macrostates and ΔS_m is the change of entropy of the bath. One can now identify the two macrostates I and II with an environment containing one and two bacterial cells respectively. Using probabilistic arguments it is then possible to express the probability ratio in equation (15) as a function of measurable parameters, which characterize the system's dynamics. With this approach, one can make a quantitative comparison between the actual heat produced by *E.coli* bacteria during a self-replication event and the physical lower bound imposed by thermodynamics constraints. These results may also have implications for the adaptation of internally driven systems, which are discussed in [227, 228].

3.2. Coordinate invariance in multivariate stochastic systems

Energy dissipation, variability, unpredictability are traits not exclusively found in biological systems. In fact, it was a meterologist, Edward Lorenz, who coined the term 'butterfly effect' to describe an unusually high sensitivity on initial conditions in what are now known as 'chaotic systems' [229]. In a fresh attempt to explain their large variability, stochastic models have been applied to periodically recurring meteorological systems. El-Niño, for example, is characterized by a slow oscillation of the sea surface temperature, which can cause violent weather patterns when the temperature is close to its maximum. Such a change in temperature can lead to new steady-states, in which the system is permanently driven out-of equilibrium under constant dissipation of energy and exhibits a rich diversity of weather 'states'. Out of equilibrium, transitions between states are still random, but certain transitions clearly unfold in a preferred temporal sequence.

Interestingly, in an effort to model meteorological systems stochastically, Weiss uncovered a direct link between energy dissipation and variability, which is intimately related to broken detailed balance [230]. More specifically, he found that out-of equilibrium systems can react more violently to perturbations than their more well-behaved equilibrium counterparts. This finding may be relevant in a much broader context, including biology, and we will therefore briefly summarize the main points here. Specifically, we will briefly explore this phenomenon of *noise amplification* from a perspective of coordinate-invariant properties [230].

In an open thermodynamic system in equilibrium, all state variables $\vec{x}$, are subject to the dialectic interplay of random forcing (noise) $\vec{\xi}$, relaxation, and dissipation. Consider an overdamped two-bead toy system at equilibrium, for example (see figure 12(A) and section 4.2.3), where the two beads are coupled by springs and are placed in contact with independent heat baths. Energy stored in the springs is permanently released and refuelled by the thermal bath, and flows back and forth between the two colloids in a balanced way. A sustained difference in temperature between the beads, $T_1 \neq T_2$, however, will permanently rectify the flow of energy and break this balance. Crucially, this temperature difference is a matter of perspective. If we set, for example, $T_1 = 0$, then bead 1 will not receive any noise any more and energy will flow to it from bead number 2. Interestingly, if we look at the normal coordinates of the beads $u_1(t) = (x_1(t) - x_2(t))/2$ and $u_2(t) = (x_1(t) + x_2(t))/2$, we find that their respective thermal noise has exactly the same temperature $T_2/2$. However,

if we could measure the fluctuations of noise in these coordinates, we would find that both noise terms correlate. Thus, in this case, mode 1 and 2 are driven not only by the same temperature, but by the very same white noise process.

Correlations amongst noise processes $\xi_1(t)$ and $\xi_2(t)$ exciting different variables $x_1(t)$ and $x_2(t)$ can, in principle, break detailed balance, even if the overall variance of the noise is equal in all directions, i.e. $\langle \xi_1^2 \rangle = \langle \xi_2^2 \rangle$. In other words, correlations in random forces in one coordinate system, result in differences in temperature in other coordinates and vice-versa. The simple temperature criterion $T_1 = T_2$ is thus insufficient to rule out broken detailed balance (see section 4.1); a comprehensive coordinate-invariant criterion is required.

Consider variables $\vec{x}(t)$ of a generic system, evolving stochastically according to a Langevin equation (16),

$$\frac{\mathrm{d}\vec{x}}{\mathrm{d}t}(t) = \mathbf{A}\vec{x}(t) + \mathbf{F}\vec{\xi}(t) \tag{16}$$

while the dynamics of the associated probability density $\rho(\vec{x}, t)$ is given by the corresponding Fokker-Planck equation (17).

$$\frac{\partial \rho}{\partial t}(\vec{x}, t) = -\nabla \cdot \left(\mathbf{A}\vec{x}\rho(\vec{x}, t) - \mathbf{D}\nabla\rho(\vec{x}, t)\right). \tag{17}$$

In the equations above, $\mathbf{F}$ denotes the forcing matrix, in which any noise variance is absorbed, such that $\vec{\xi}$ here has unit variance $\langle \vec{\xi}(t)\vec{\xi}^T(t') \rangle = \mathbf{1}\delta(t - t')$. The forcing matrix is directly related to the diffusion matrix $\mathbf{D} = \frac{1}{2}\mathbf{F}^T\mathbf{F}$, and the term $\mathbf{A}\vec{x}$ describes deterministic forces, and the matrix $\mathbf{A}$ therefore contains all relaxational timescales. Any linear system with additive, state-independent white noise $\vec{\xi}$ can be mapped onto these generic equations.

In an equilibrium system with independent noise processes, $\mathbf{D}$ is diagonal and fulfills the standard fluctuation-dissipation theorem $\mathbf{D} = k_\mathrm{B}T\mathbf{M}$, where $\mathbf{M}$ denotes the mobility matrix. In steady-state, the correlation matrix $\mathbf{C} = \langle \vec{x} \cdot \vec{x}^T \rangle$ both in and out of equilibrium, obeys the Lyanpunov equation $\mathbf{AC} + \mathbf{CA}^T = -2\mathbf{D}$, which can be thought of as a multidimensional FDT. The density ρ can therefore always be written as a multivariate Gaussian distribution $\rho(\vec{x}, t) = 1/\sqrt{|\mathbf{C}|}e^{-\frac{1}{2}\vec{x}^T\mathbf{C}^{-1}\vec{x}}$.

Apart from systems with temperature gradients, detailed balance is also broken in systems with non-conservative forces $\mathbf{A}\vec{x}$, which have a non-zero rotation $\partial_i (\mathbf{A}\vec{x})_j \neq \partial_j (\mathbf{A}\vec{x})_i$. Within our matrix framework, this condition simplifies to $A_{i,j} \neq A_{j,i}$ and thus requires $\mathbf{A}$ to be symmetric in equilibrium. In section 4.2.3 we give a detailed example for a 2D linear system of this framework and the bootstrapping technique discussed in section 4.2.2. In our example, $\mathbf{A}$ would represent a product between a mobility matrix and a stiffness matrix, both of which are symmetric resulting in a symmetric $\mathbf{A}$.

Note, this framework only applies to systems with dissipative coupling; reactive currents require a separate analysis. The two ways of breaking detailed balance in our case (temperature gradients and non-conservative forces) are reflected by a coordinate-independent commutation criterion for equilibrium [230]:

$$\mathbf{AD} - \mathbf{DA}^T = 0. \tag{18}$$

It was also argued that a system with broken detailed balance will sustain a larger variance than a similar system with the same level of noise, which is in equilibrium. This effect, referred to by Weiss as *noise amplification*, had previously been attributed to non-normality of the matrix $\mathbf{A}$, which is only true for diagonal $\mathbf{D}$. This type of noise amplification is now understood to be caused by broken detailed balance.

Although this amplification can be captured by different metrics, we here focus on the gain matrix $\mathbf{G} = \mathbf{1} + \mathbf{ACD}^{-1}$. The gain matrix is a measure of the variance of the system normalized by the amplitude of the noise input. To obtain a scalar measure, one can take, for example, the determinant of $\mathbf{G}$ which yields the gain g. It can be shown, that $g \geqslant g_0$ when detailed balance is broken, where g_0 is the gain of the same system in equilibrium. Finally, it is interesting to note, that the noise amplification matrix $\mathbf{G}$ is related to the average production of entropy in our generic model system. Let Π denote the production of entropy, then

$$\Pi = k_\mathrm{B}\,\mathrm{tr}\,(\mathbf{AG}), \tag{19}$$

providing a direct link between dissipation and increased variability in multivariate systems out of equilibrium.

3.3. Energy-speed-accuracy trade-off in sensory adaption

Energy dissipation is essential to various control circuits found in living organisms [231]. Faced with the noise inherent to small systems, cells are believed to have evolved strategies to increase the accuracy, efficiency, and robustness of their chemical reaction networks [232–234]. Implementing these strategies, however, comes at an energetic price, as is exemplified by Lan *et al* in the case of the energy-speed-accuracy (ESA) trade-off in sensory adaption [1, 235, 236]. This particular circuit is, of course, not the only active control in cell biology. The canonical example of molecular '*quality control*' is the kinetic proofreading process, in which chemical energy is used to ensure low error rates in gene transcription and translation [3]. Furthermore, fast and accurate learning and inference processes, which form the basis of sensing and adaptation, require some energy due to the inherent cost of information processing [2, 237–239]. A similar trade-off occurs in biochemical oscillations, which serve, for instance, as internal biological clocks. Here, the number of coherent cycles is linearly related to the energetic price that the system pays [240].

Sensory learning and adaptation at the cellular level involves chemical feedback circuits that are directly or indirectly driven by ATP hydrolysis, which provides energy input to break detailed balance. Examples of adaptation circuits are shown schematically in figures 7(B) and (C). These examples include the chemotactic adaption mechanism in *E. coli* (panel (B)), a well-established model system for environmental sensing. Common to all circuits is a three-node feedback structure, as depicted in figure 7(A). Conceptually, this negative feedback circuit aims to sustain a given level of activity a_0, independent of the steady amplitude of an external stimulus s, which here is assumed to be inhibitory. This adaptive behavior allows the circuit to respond sensitively to changes to the external stimulus over a large dynamic range in s.

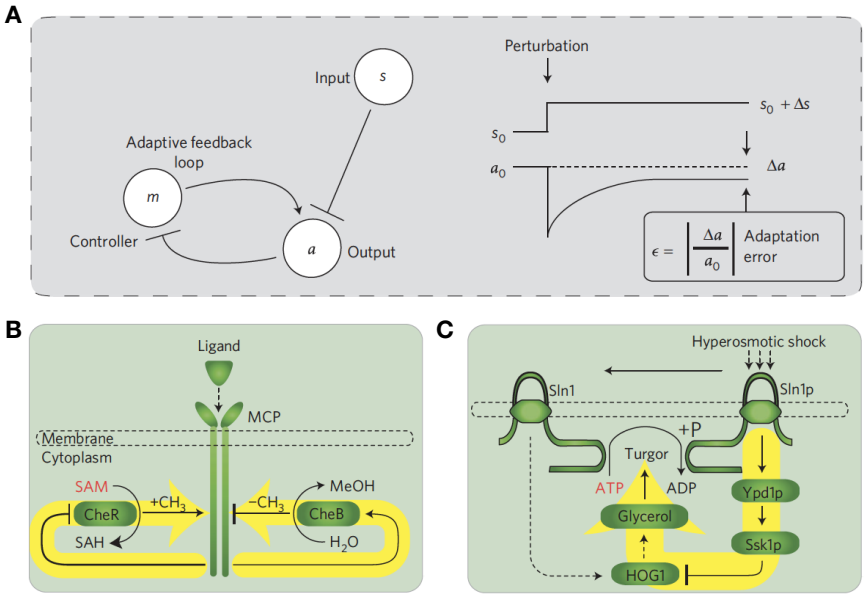

Figure 7. Models of adaptive feedback systems. (A) Simplified topology of a feedback circuit. The input s here is chosen to have an inhibitory effect. On the right the response of the output a is shown following a step in the input s. (B) Chemotactic circuit in *E. coli*. Ligand binding to a methyl-accepting-protein (MCP) causes further addition (mediated by CheR) or deletion (mediated by CheB) of methylgroups to MCP. This methylation counteracts the effects of ligand binding. (C) Osmotic sensing circuit in yeast. A reduction of osmolarity results in dephosphorylation of Sln1p→ Sln1, which activates the HOG1 (High osmolarity glycerol) mechanism. This mechanism acts to restore the tugor pressure inside the cell and eventually phosphorylates Sln1→Sln1p. Adapted by permission from Macmillan Publishers Ltd: Nature Physics [1], Copyright (2012).

The authors condense the dynamics of such a chemical network into a simple model (figure 7(A)) with abstract control $m(t)$ and activity $a(t)$ variables described by two coupled Langevin equations,

$$\dot{a} = F_a(a, m, s) + \xi_a(t) \tag{20}$$

$$\dot{m} = F_m(a, m, s) + \xi_m(t) \tag{21}$$

with F_a, F_m denoting the coarse-grained biochemical response and ξ_a, ξ_m being white-noise processes with different variances $2\Delta_a$ and $2\Delta_m$, respectively. Importantly, these biochemical responses do not fulfil the condition for conservative forces discussed in the previous section (above equation (18)). To function as an adaptive system with negative feedback, $\partial_m F_a$ and $\partial_a F_m$ must have different signs, which implies a breaking of detailed balance. Indeed, adaptation manifests in a sustained probability current $j = (j_a, j_m)$ in the phase space spanned by $a \times m$; the energetic cost to maintain this non-equilibrium steady-state is given by the amount of heat exchanged with the environment per unit time, which must equal the entropy production rate Π multiplied by the temperature T of the heatbath to which the system is coupled.

In general, a non-equilibrium system at steady-state that adheres to a Fokker-Planck equation produces entropy at a rate [14, 241],

$$\Pi = k_B \int \mathrm{d}\vec{x} \frac{1}{\rho(\vec{x}, t)} \vec{j}^T(\vec{x}, t) \mathbf{D}^{-1} \vec{j}(\vec{x}, t) \tag{22}$$

where $\rho(\vec{x}, t)$ is the probability density in phase space and $\mathbf{D}^{-1}$ is the inverse diffusion matrix. We note, that for linear systems equation (22) simplifies to equation (19).

Applying equation (22) to the model above for sensory adaption, yields the heat exchange rate $\dot{W} = \int \int \mathrm{d}m\mathrm{d}a \left[j_a^2/(\Delta_a \rho) + j_m^2/(\Delta_m \rho) \right]$. An assumed separation of timescales that govern the fast activity a and the slower control m, allows the authors to derive an *Energy-Speed-Accuracy* (ESA) relation, which reads

$$\dot{W} \approx (c_0 \sigma_a^2) \omega_m \log\left(\frac{\epsilon_0}{\epsilon}\right), \tag{23}$$

where, σ_a^2 represents the variance of the activity, and ϵ denotes the adaptation error defined as $\epsilon \equiv |1 - \langle a \rangle / a_0|$, while c_0 and ϵ_0 are constants that depend on details of the model. Here, ω_m parametrizes the rate of the control variable m. Therefore, an increase in ω_m or a reduction in ϵ requires an increased dissipation $\dot{W}$; put simply, swift and accurate adaptation can only be achieved at high energetic cost.

The authors argue that a dilution of chemical energy in living bacteria will mainly affect the adaptation rate, but leave the adaptation error unchanged. Starvation should therefore lead to lower adaptation rates to uphold the ESA relation. This prediction was tested in starving *E. coli* colonies under repeated addition and removal of MeAsp (see figure 8), an attractant which stimulates the chemotactic system shown in figure 7(B). The cells in this study were engineered to express fluorescent markers attached to two proteins involved in adaptation. Physical proximity between any of these two molecules is an indicator of ongoing chemosensing, and was measured using Foerster-resonance-energy transfer (FRET). Since the donor-acceptor distance correlates with the acceptor intensity, but anticorrelates with the donor intensity, the ratio of YFP (acceptor) and CFP (donor) intensities lends itself as a read-out signal to monitor adaptation. Indeed, after each addition/

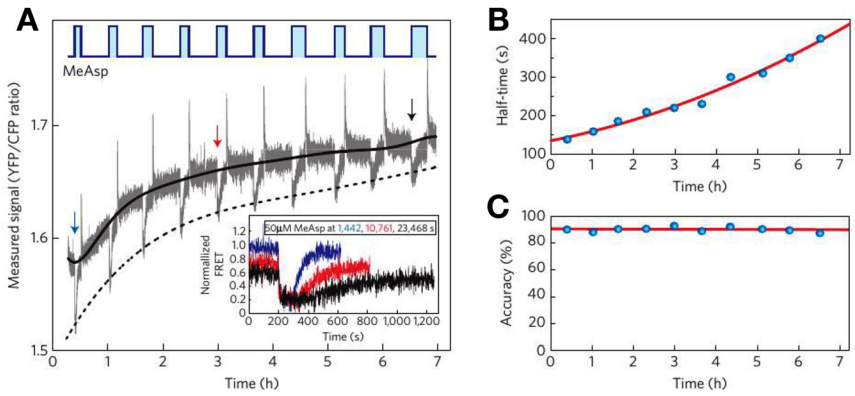

Figure 8. Experimental evidence for an energy-speed-accuracy (ESA) trade-off in *E. coli* chemotaxis. (A) Ratio of intensity of fluorescent reporters of adaptation. Changes in this signal are indicative of adaptation in the chemotatic circuit to external stimuli presented by the addition/removal of MeAsp. The inset illustrates the reduction of the FRET signal at the three different points in time indicated by arrows. (B) Half-times inferred from the responses to addition/removal cycles shown in (A). (C) Relative accuracies of adaptation. Adapted by permission from Macmillan Publishers Ltd: Nature Physics [1], Copyright (2012).

removal cycle of MeAsp, the signal recovers, albeit at a gradually decreasing pace, as is shown in the inset in figure 8(A). The decrease in the speed of adaptation is attributed to the progressing depletion of nutrition in the colony. In panels b and c, the adaptation half-time and relative accuracy are plotted. The graph in panel c clearly demonstrates the constancy of the accuracy of chemotatic system as nutrients are depleted over time, which is argued to be close to optimality.

3.4. Current fluctuations in non-equilibrium systems

Directed and chemically-specific transport of proteins, RNA, ions, and other molecules across the various membranes that foliate the cell is often achieved by active processes. A library of active membrane channel proteins has been described, which '*pump*' ions into and out of cells to control osmolarity, the electrical potential or the pH [242]. Furthermore, in eukaryotic cells, a concentration gradient of signalling molecules across the nuclear envelope causes messenger RNA (mRNA) molecules, expressed within the nucleus, to diffuse outwards through channels known as nuclear pore complexes (NPC) [112]. Outside of the nucleus, the mRNA is translated into proteins by the ribosomes, which are too large to traverse the NPCs. All these directed transport processes are essential to the cell. Thus, this raises the question of reliability of such processes [243, 244]. For example, how steady should we expect the supply of mRNA to the ribosomes to be [245]? Or, more generally, how predictable is the output rate of any given non-equilibrium process? Even active processes still endure fluctuations: molecular motors, at times, make a step backwards, or stall. Polymerizing filaments will undergo brief periods of sluggish growth or even shrinkage. Similarly, active membrane channels will sometimes transport more, and in other times fewer molecules. To illustrate this, an abstract example of such current fluctuations is depicted in figure 10, which will be further discussed below.

It seems intuitive, that predictability on the microscale always comes with an energy-price tag. In recent years, significant progress has been made to calculate the level of deviations from the average rate of a non-equilibrium process that is to be expected over finite times [199, 246–250]. More formally, a universal bound for finite-time fluctuations of a probability current in steady-state has been established. Such an uncertainty relation is perhaps best illustrated by the simple motor model discussed by Barato *et al* [247]: A molecular motor moves to the right at a rate k_+, and to the left at a rate k_-. The movement is biased, i.e. $k_+ > k_-$, driven by a free energy gradient $\Delta\mathcal{F} = k_\mathrm{B}T\log(k_+/k_-)$. A few trajectories for various values of k_+ are depicted in figure 9(A). As can be seen, the walker (shown in the inset), on average, moves with a constant drift $\langle x(t)\rangle = t(k_+ - k_-)$. Associated with this drift is a constant rate of entropy production $\Pi = (k_+ - k_-)\Delta\mathcal{F}/T$. Barato *et al* showed that the product of the total entropy produced $S(t) = \Pi t$ and the squared uncertainty $\epsilon^2 = \langle(x(t) - \langle x(t)\rangle)^2\rangle/\langle x(t)\rangle^2$ always fulfils the bound

$$TS(t)\epsilon(t)^2 \geqslant 2k_\mathrm{B}T. \tag{24}$$

For this particular model, the square uncertainty reads $\epsilon(t)^2 = (k_+ + k_-)/[(k_+ - k_-)^2 t]$, such that the product $TS(t)\epsilon(t)^2$ is constant in time. To further illustrate this point, we plotted the quantity $TS(t)\epsilon(t)^2$ for each choice of k_+ in figure 9(A), averaged over an ensemble of a hundred simulated trajectories in figure 9(B). Due to the finite ensemble size, the graphs fluctuate, but stay well above the universal lower bound of $2k_\mathrm{B}T$ for longer times t. So far, the theory underlying uncertainty relations was shown to be valid in the long time limit. Only recently, its validity has been extended to finite time scales [249, 250].

The bound in equation (24) can be generalized to any Markovian non-equilibrium steady-state [246, 248]. The four-node system in the inset in figure 10 is an example. Here, the integrated current $J_t = \int^t j(t')\mathrm{d}t'$ between any two nodes is distributed as $P(J_t = tj) \sim \mathrm{e}^{-tI(j)}$, with $I(j)$ denoting the large deviation function. This function therefore controls the variability of J_t. Interestingly, it can be shown that the large deviation function obtained in the linear response regime I_LR, is never exceeded by I, even far away from equilibrium [246]. Thus, an increase in currents is accompanied by an increase in the variability of these currents when a system is driven further

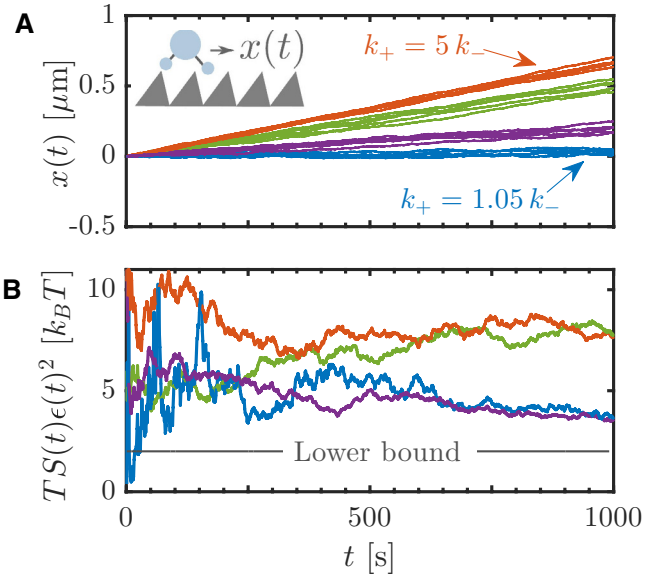

Figure 9. Variability of non-equilibrium steady states: (A) Example trajectories to show the spread in the average position $\langle x(t)\rangle$ after t steps. The inset depicts a simple model for a molecular motor in a sawtooth potential. (B) The products $TS(t)\epsilon(t)^2$ calculated over an ensemble of trajectories are bounded from below by the uncertainty relation. Despite the small size of the ensemble (100), equation (24) is fulfilled.

away from equilibrium. The relative uncertainty ϵ generalizes to $\epsilon^2 = \mathrm{var}(J)/\langle J\rangle^2$. The lower bound for this general ϵ^2 is similar in form to equation (24) and reads $2k_B/(\Pi t)$, i.e. $\Pi t\epsilon^2 \geqslant 2k_B$, where $\Pi = k_B \sum_{m<n} j_{(m,n)} \log[(p^{(s)}_{(m)} r_{(m,n)})/(p^{(s)}_{(n)} r_{(n,m)})]$ is the average entropy production rate in the system in steady-state [246]. The steady-state probability distribution is denoted here by $p^{(s)}_{(m)}$. The relation above is a bound for the uncertainty of the entire system. A similar relation also applies to any individual edge between two nodes n and m, $\langle (j_{(m,n)} - \langle j_{(m,n)}\rangle)^2\rangle/\langle j_{(m,n)}\rangle^2 \geqslant 2k_B/(\Pi_{(m,n)} t)$, where $\Pi_{(m,n)}$ denotes the entropy production associated with the edge (m,n). Recently, in an interesting connection to section 3, Gingrich *et al* [251] have found an uncertainty relation of the first-passage time T of a cumulative current J. More precisely, the time T it takes J to exceed a given threshold J_{thr} fulfils the relation

$$\frac{\mathrm{var}(T)}{\langle T\rangle}\Pi \geqslant 2k_B. \tag{25}$$

While the uncertainty relations discussed above appear abstract at first, they may soon prove useful in studying transport or control systems in cellular biology due to their general applicability. Reminiscent of Carnot's efficiency for macroscopic engines, one implication of equation (24) is that a reduction in uncertainty can only be achieved by dissipating more energy when the system is close to optimality.

4. Detecting broken detailed balance in living systems

Up to this point we discussed intrinsically invasive methods to probe biological systems for non-equilibrium dynamics.

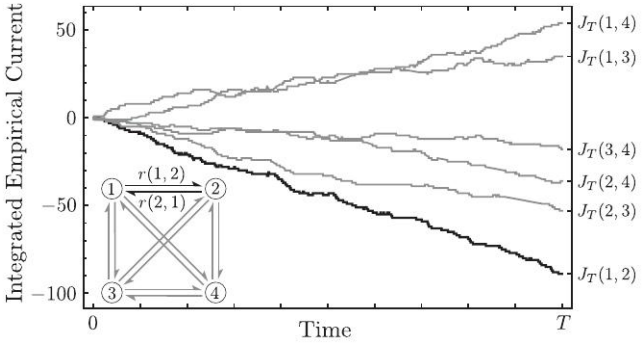

Figure 10. Variability of non-equilibrium steady states: Fluctuations of the cumulative probability current $J_T(m,n) = \int^T j_{m,n}(t)\mathrm{d}t$ along all nodes in the four state system shown in the inset. Fluctuations result in perturbations of the currents around their intrinsic rates $r(m,n)$. Adapted figure with permission from [246], Copyright (2016) by the American Physical Society.

For instance, to determine violations of the fluctuation-dissipation theorem a response function is required, which can only be measured by performing a perturbation in non-equilibrium systems (see section 2). Other methods that are used to probe for non-equilibrium involve thermal or chemical perturbations, and are therefore also inherently invasive. Such approaches are not ideal for investigating the stochastic dynamics of delicate sub-cellular system. Performing a controlled perturbation of such a system might not only be technically challenging, it may also be undesirable because of potential effects on the behavior or function of such a fragile system.

Ideally, we would like to avoid the technical and conceptual difficulties of invasive protocols to probe for non-equilibrium behavior. This raises the question: Could we perhaps measure a system's non-equilibrium behavior simply by looking at it? With this purpose in mind, we recently developed a method that indeed uses conventional video microscopy data of cellular and subcellular systems [22]. Detecting non-equilibrium behavior in the stochastic dynamics of mesoscopic coordinates of such systems can be accomplished by demonstrating that these dynamics break detailed balance. In this section, we will illustrate these ideas and discuss some recent related theoretical developments.

4.1. Equilibrium, steady state, and detailed balance

Suppose we can describe a system on a mesoscopic level by dividing phase space into small cells, such that the state of the system can be described by a state variable n. If the system is ergodic and irreducible, it will evolve towards a unique stationary solution $p^{(s)}_n$, which is constant in time. A necessary and sufficient requirement for such steady-state conditions is that the rate of transitions into any particular microstate, m, is balanced by the total rate of transitions from m to other microstates n:

$$\sum_n W_{n,m} = \sum_n W_{m,n}, \tag{26}$$

where $W_{n,m}$ describes the rate of transitions from state m to n. This result must hold for any system, at equilibrium or far

from equilibrium, that has reached steady state conditions. When the system is Markovian, equation (26) reduces to

$$\sum_n w_{nm} p_m^{(s)} = \sum_n w_{mn} p_n^{(s)}, \tag{27}$$

where w_{nm} describes the rate of transitions from state m to n, given that the system is in state m.

In thermodynamic equilibrium, it can be shown that a system must obey an even stronger condition: detailed balance. Classical closed ergodic systems are characterized by a time-independent Hamiltonian, which we will here restrict to be an even function of the momenta and independent of magnetic fields. The microscopic degrees of freedom of such a system obey deterministic dynamics described by Hamilton's equations, which are time reversal invariant. This has important implications also for the probability distribution of mesoscopic observables, which characterize the systems states at thermodynamic equilibrium. Consider, for instance, a mesoscopic variable y, which represents a generalized coordinate that either does not depend on the microscopic momenta, or that is an even functions of the microscopic momenta. Then, the transition between states must obey [187]

$$p_2^{(e)}(y_2, \tau; y_1, 0) = p_2^{(e)}(y_1, \tau; y_2, 0)\,. \tag{28}$$

Here we indicate with $p_2^{(e)}$ the two-point joint probability distribution. This result is referred to as the principle of detailed balance. Put simply, it means that the transitions between any two mesostates are pairwise balanced, and this result derives from the transition rates between any two microstates also being pairwise balanced. For Markovian systems we can write detailed balance more conveniently as

$$w(y_2|y_1)\, p^{(e)}(y_1) = w(y_1|y_2)\, p^{(e)}(y_2), \tag{29}$$

where the w's indicate the conditional rates between states. Finally, we note that if we add observables z, which are odd functions of the momenta, equation (28) needs to be generalized to

$$p_2^{(e)}(y_2, z_2, \tau; y_1, z_1, 0) = p_2^{(e)}(y_1, -z_1, \tau; y_2, -z_2, 0)\,. \tag{30}$$

It is important to note that for a system in steady state dynamics, broken detailed balance is direct evidence of non-equilibrium, but showing that a system obeys detailed balance in a subspace of coordinates is insufficient to prove equilibrium. Indeed, even for systems out of equilibrium, broken detailed balance is not necessarily apparent at the supramolecular scale [28, 29, 59, 60]. One can also often observe stationary stochastic processes in cells that, at first glance, appear to be thermally driven. Examples include the fluctuations of cytoskeletal filaments such as microtubuli, F-actin filaments or the fluctuations of intracellular organelles. These cases should be contrasted with obvious examples of mesoscopic non-equilibrium, non-stationary, irreversible processes such as cell growth, locomotion and mitosis. Thus, in general, it is unclear how and when broken detailed balance that realized on the molecular level also manifests at larger scales.

4.2. Probability flux analysis

In this section, we describe the basis and methodology that can be used to infer broken detailed balance from microscopy data. We consider a system, which is assumed to evolve according to stationary dynamics. This could, for instance, be a primary cilium or a flagellum [22]. In general, these systems exhibit stochastic dynamics, comprised of both a deterministic and a stochastic component. The dynamics of such systems can be captured by conventional video microscopy. To quantify this measured stochastic dynamics, we first need to parameterize the configuration of the system. The shape of a flagellum, for instance, could be conveniently decomposed into the dynamic normal modes of an elastic beam. In this example, the corresponding mode amplitudes represent time-dependent generalized coordinates of the system. Note, these mode amplitudes can be extracted from a single time frame and strictly represent configurational coordinates, which are independent of the microscopic momenta.

In general, a video microsocopy experiment can be used to extract time traces of D mesoscopic tracked coordinates $x_1, ..., x_D$, which represent the instantaneous configuration of the system. Clearly, this only represents a chosen subset of all coordinates that completely specify the whole system. Furthermore, only spatial or conformational degrees of freedom are considered in this discussion here. Indeed, fluctuations in momenta in a typical overdamped biological or soft-matter systems relax on very short time-scales, which are not resolved in typical video microscopy experiments. However, the basic methodology described below can readily be generalized to also include momentum-like variables.

We define a probability density, $\rho(x_1, ..., x_D, t)$, in terms of only the tracked degrees of freedom. This probability density can be obtained from the full joint probability density in terms of a complete set of variables, by integrating out all the untracked degrees of freedom. In the reduced configurational phase space of the tracked degrees of freedom, the dynamics of the system still obeys a continuity equation:

$$\frac{\partial \rho(x_1, ..., x_D, t)}{\partial t} = -\nabla \cdot \vec{j}(x_1, ..., x_D, t) \tag{31}$$

where $\vec{j}(x_1, ..., x_D, t)$ is the current density describing the net flow of transitions of the system in the D-dimensional configurational phase space. Here, we only consider systems with dissipative currents [90]. While at steady state the divergence of the current needs to vanish, in equilibrium any dissipative current itself must be identically zero.

4.2.1. Estimating phase space currents Here we discuss one way of estimating currents from a set of time-traces. To provide a simple illustration of this approach, we consider a system with a 2D configurational phase space, as illustrated in figure 11(A). The dynamics of the system is captured by a time trace in this configurational phase space. It is convenient to analyze these trajectories using a discretized coarse-grained representation of the 2D phase space. This coarse-grained phase space (CGPS) consists of a collection of equally sized,

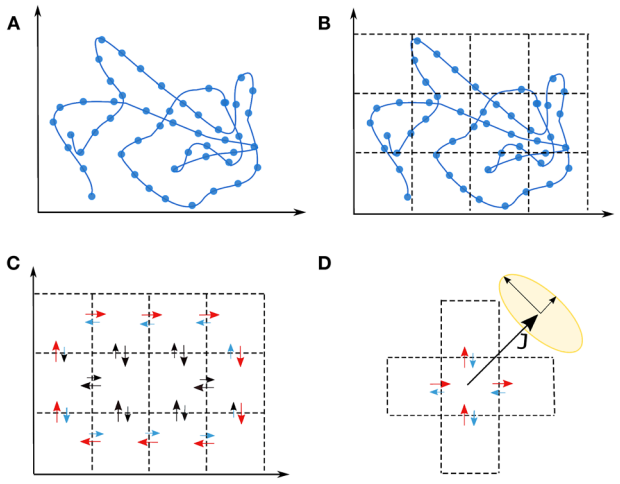

Figure 11. Schematic illustrating the coarse-graining procedure for the estimation of phase space currents and corresponding error bars. (A) Trajectory in continuous phase space. (B) Grid illustrating the discretization of the continuous phase space. (C) By counting transitions between first neighbour discrete states it is possible to estimate the currents (indicated by the arrows) across the boundaries. (D) Current error bars representation obtained through the bootstrapping procedure. From [22]. Reprinted with permission from AAAS.

rectangular boxes, each of which represents a discrete state figure 11(B). Such a discrete state in CGPS encompasses a continuous set of microstates, each of which belongs to a unique, discrete state. The primary reason for using this discretized representation of phase space is to be able to obtain informative results on experimental data with limited statistics.

In this 2D CGPS, a discrete state α has two neighboring states, respectively α_+ (larger x_i) and α_- (smaller x_i), along each direction x_i, resulting in four possible transitions. The dynamics of the system indeed satisfies the discrete continuity equation

$$\frac{\mathrm{d}p_\alpha}{\mathrm{d}t} = -\tilde{W}^{(x_1)}_{\alpha^-,\alpha} + \tilde{W}^{(x_1)}_{\alpha,\alpha^+} - \tilde{W}^{(x_2)}_{\alpha^-,\alpha} + \tilde{W}^{(x_2)}_{\alpha,\alpha^+}, \quad (32)$$

where $\tilde{W}_{\alpha,\beta} = W_{\alpha,\beta} - W_{\beta,\alpha}$ is the net rate of transitions from state β to α and p_α is the probability to be in discrete state α, which will become time independent when the system reaches steady-state conditions.

This probability p_α is related to the probability density $\rho(x_1, ..., x_2, t)$ defined above, and equation (32) can be obtained by integrating equation (31) on both sides over the volume of state α in CGPS. We can estimate this probability from a measured trajectory by using

$$p_\alpha = t_\alpha / t_{\text{total}}, \quad (33)$$

where t_α is the accumulated time that the system spends in state α and t_{total} is the total duration of the experiment.

The net rates $\tilde{W}$ in CGPS can be estimated from the measured trajectories simply by counting the net number of transitions per unit time:

$$\tilde{W}^{(x_i)}_{\alpha,\beta} = \frac{N^{(x_i)}_{\alpha,\beta} - N^{(x_i)}_{\beta,\alpha}}{t_{\text{total}}}. \quad (34)$$

Here $N^{(x_i)}_{\alpha,\beta}$ is the number of transitions from state β to state α along the direction x_i. In a mechanical system, the trajectories through phase space are continuous such that there can be only transitions between neighboring states. However, due to the discreteness in a measured time trajectory, it is possible that a transition between neighboring states is 'skipped', resulting in an apparent transition between non-neighboring states. In these cases, it is convenient to perform an interpolation of the time trace to estimate the intermediate transitions. It is important that this interpolation is performed in a time-symmetric way, so that the interpolation filter preserves time-reversal symmetry. In fact, this should be taken into account with any kind of filtering that is performed on measured time traces.

The currents in CGPS that describes back-and-forth transitions through all four boundaries of the box associated with a discrete state (figure 11(C)), can be defined by:

$$\vec{J}(\vec{x}_\alpha) = \frac{1}{2}\left(\tilde{W}^{(x_1)}_{\alpha^-,\alpha} + \tilde{W}^{(x_1)}_{\alpha,\alpha^+}, \tilde{W}^{(x_2)}_{\alpha^-,\alpha} + \tilde{W}^{(x_2)}_{\alpha,\alpha^+}\right). \quad (35)$$

Here, $\vec{x}_\alpha$ is the center position of the box associated with state α.

With this approach, prominent examples such as an isolated beating flagella of *Chlamydomonas reinhardtii* were examined [22] (see figure 1). Dynein motors drive relative axial sliding of microtubules inside the axoneme of the flagellum [77, 252, 253]. To quantify the non-equilibrium dynamics of this system, we decomposed the axoneme shapes measured using time-lapse microscopy into the dynamic normal modes of an elastic filament freely suspended in a liquid. Using this approach, we obtained the amplitudes of the projections coefficients for the first 3 modes. These amplitude time series were used to construct a trajectory in a phase space spanned by the three lowest-order modes, which were analyzed using PFA, as shown in figure 1(C). Here, the vector fields indicate the fluxes for the first three modes. Thus, this method can be used to quantify the non-equilibrium dynamics of the flagellum in a phase space of configurational degrees of freedom.

In addition, we considered primary cilia of Madin-Darby Canine Kidney (MDCK II) epithelial. Primary cilia are hair-like mechano and chemosensive organelles that grow from the periphery of certain eukaryotic cells [40, 254, 255]. At first glance the dynamics of the deflection angle and curvature of primary cilia appear to exhibit random fluctuations. Using probability flux analysis (PFA), however, it was demonstrated that there are significant circulating probability fluxes in a configurational phase space of angle and curvature, providing evidence for the non-equilibrium nature of primary cilia [22]. This approach is now gaining traction in variety of systems, ranging from the post translation Kai circadian clock [256] to motility phenotypes [257]. When the mobility of a system is known, a related approach can be used to estimate the heat dissipation [258]. However, in a non-equilibrium system, the mobility must be obtained by a perturbative measurement.

4.2.2. Bootstrapping. In practice, the finite length of experimental or simulated trajectories limits the accuracy with which we can estimate fluxes in phase space. This has an

important implication: even when considering a system at thermodynamic equilibrium, a measurement from finite data will typically result in apparent non-zero currents. In such a case we can not statistically distinguish the measured apparent current from a zero current. Therefore, it is important to asses if the estimated currents are statistically significant. Moreover, these current fluctuations may also be interesting to study in and of themselves (see section 3.4). In this section we briefly describe 'bootstrapping', a method that can be used to associate error bars to the measured currents.

The error bars on the probability flux can be determined by counting statistics of the number of transitions in equation (34). In general, however, there may be correlations between in-and-outward transitions for a given state, which renders it difficult to perform a simple estimate of the error-bar. A possible way around this, which naturally takes correlations into account, is to bootstrap trajectories from the experimentally measured or simulated trajectories.

To perform this bootstrapping procedure, we first determine all the transitions between discrete states in the CGPS from the measured trajectories. From this data, we construct a set A of n events, describing specific transitions of the system between two states, including the transition time. Given A, we can generate a new set of transitions, A', by randomly sampling n *single* events (with replacements) from A. This procedure, however, ignores possible correlations. To capture the effects of correlations on the accuracy of our current estimator, we bootstrap trajectories by randomly sampling a group of m consecutive events from A to construct a new set of transitions $A'_i(m)$ [259].

For each bootstrapped trajectory we calculate the current field and by averaging over all the realizations, we estimate the covariance matrix. To visualize the error bars (standard error of the mean) on the estimated currents, we depict an ellipse aligned with the principle components of this covariance matrix. The short and long axes of these error-ellipses are defined by the square roots of the small and large eigenvalues, respectively, of the covariance matrix, figure 11(D). Empirically, we found that the estimated error bars reduce substantially by including pairwise correlations, i.e. in going from $m = 1$ to $m = 2$, after which the error bars became largely insensitive to m. Such correlations can arise because of the coarse graining of phase space, which can introduce a degree of non-Markovianity.

4.2.3. Toy model: two stochastically driven coupled beads. To provide some basic intuition for stochastic non-equilibrium systems we next discuss a simple model, which can easily be solved both analytically and numerically. With this model, which was also studied in [260, 261], we illustrate how probability flux analysis (PFA) can be used on simulated data to obtain current densities in coarse grained phase space. The results are shown to be consistent with analytical calculations within error bars.

Consider a system consisting of two microscopic overdamped beads in a liquid connected to each other and to a rigid boundary by springs with elastic constant k, as depicted in figure 12(A). The two beads are assumed to be in contact with two independent heat baths, respectively at temperatures T_1 and T_2. The stochastic dynamics of this system is described by the overdamped equation of motion

$$\frac{\mathrm{d}\vec{x}}{\mathrm{d}t} = \mathbf{A}\vec{x} + \mathbf{F}\vec{\xi}, \tag{36}$$

where $\vec{x} = (x_1, x_2)^T$ represents the beads positions. The deterministic dynamics is captured by the matrix

$$\mathbf{A} = \frac{k}{\gamma}\begin{pmatrix} -2 & 1 \\ 1 & -2 \end{pmatrix}. \tag{37}$$

The drag coefficient γ, characterizing the viscous interactions between the beads and the liquid, is assumed to be identical for the two beads. The stochastic contribution, ξ_i, in the equation of motion is defined by

$$\langle\vec{\xi}\rangle = 0, \quad \langle\vec{\xi}(t)\otimes\vec{\xi}(t')\rangle = I\delta(t-t'), \tag{38}$$

and the amplitude of the noise is captured by the matrix

$$\mathbf{F} = \sqrt{\frac{2k_\mathrm{B}}{\gamma}}\begin{pmatrix} \sqrt{T_1} & 0 \\ 0 & \sqrt{T_2} \end{pmatrix}. \tag{39}$$

We can generate simulated trajectories for this system by numerically integrating equation (36). We will consider two exemplificative cases: (i) thermal equilibrium with $T_1 = T_2$, and (ii) non-equilibrium with $T_2 = 5T_1$. An example of the two simulated trajectories for this last case is shown in figure 12(A), where we note that the dynamics of individual trajectories appears to be, at first glance, indistinguishable from equilibrium dynamics. Interestingly however, the non-equilibrium nature of this system is revealed by applying PFA to these data, which gives coherently circulating probability fluxes in the phase space (figure 12(C)). By contrast, in the case of thermal equilibrium ($T_1 = T_2$) we find, as expected, that the flux vanishes, as shown in figure 12(B).

To compare these results of the estimated fluxes from simulations with analytical calculations, we next consider the time evolution for the probability density function $\rho(\vec{x}, t)$ of the system, which is described by the Fokker Planck equation:

$$\frac{\partial\rho(\vec{x},t)}{\partial t} = -\nabla\cdot[\mathbf{A}\vec{x}\rho(\vec{x},t)] + \nabla\cdot\mathbf{D}\nabla\rho(\vec{x},t), \tag{40}$$

where $\mathbf{D} = \frac{1}{2}\mathbf{F}\mathbf{F}^T$ is the diffusion matrix. The steady-state solution of this equation is a Gaussian distribution, with a covariance matrix, $\mathbf{C}$, which is found by solving the Lyapunov equation

$$\mathbf{A}\mathbf{C} + \mathbf{C}\mathbf{A}^T = -2\mathbf{D}. \tag{41}$$

The steady state probability flux density is given by $\vec{j} = \Omega\vec{x}\rho(\vec{x})$, where

$$\Omega = \frac{k(T_1 - T_2)}{\gamma c}\begin{pmatrix} 2(T_1+T_2) & -(7T_1+T_2) \\ (T_1+7T_2) & -2(T_1+T_2) \end{pmatrix} \tag{42}$$

with $c = (T_1^2 + 14T_1T_2 + T_2^2)$. As expected, the flux vanishes at thermal equilibrium when $T_1 = T_2$. In the near equilibrium regime, we can consider $T_1 = T$ and $T_2 = T + \epsilon$ with ϵ small. Within this limit, the current field can be written as

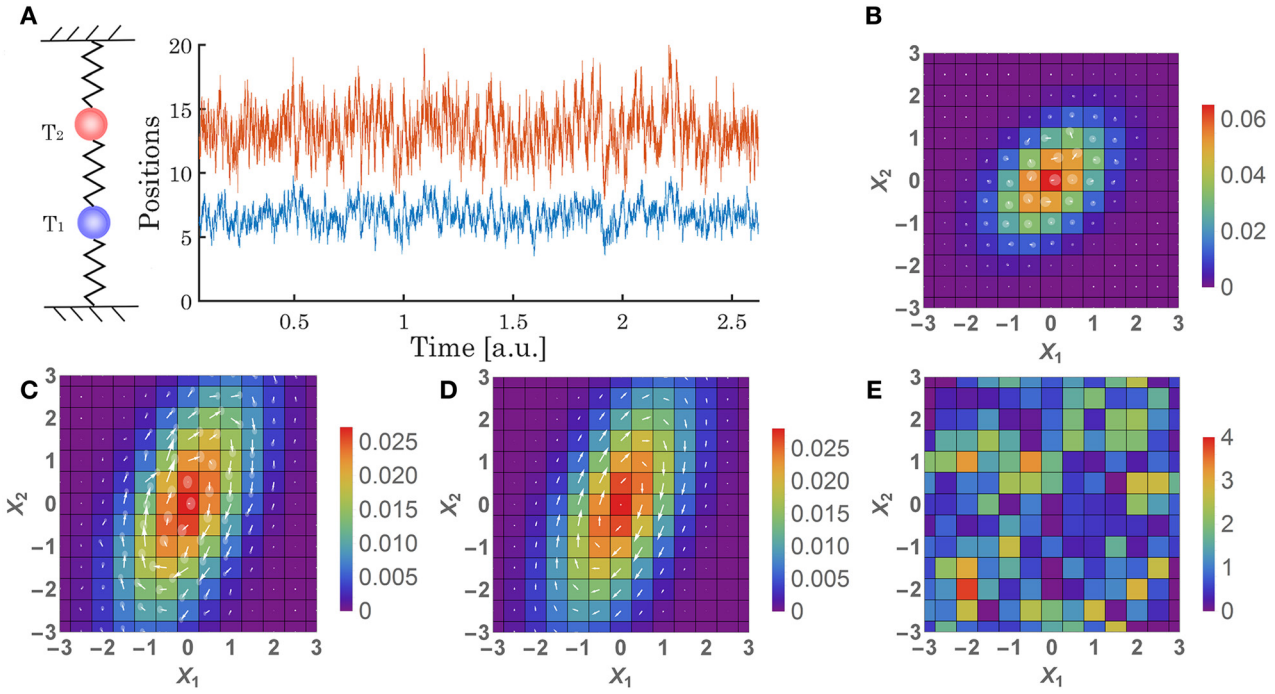

Figure 12. (A) Schematic of the two coupled beads system and simulated time series of the beads positions for $T_2 = 5T_1$. ((B) and (C)) Probability distribution (color) and flux map (white arrows) obtained by Brownian dynamics simulations at equilibrium ($T_1 = T_2$) (B) and non-equilibrium ($T_2 = 5T_1$) (C). Translucent discs represent a 2σ confidence interval for fluxes. (D) Analytical result for the probability distribution (color) and flux map (white arrows) obtained for a non-equilibrium case, ($T_2 = 5T_1$). From [22]. Reprinted with permission from AAAS. (E) Compatibility estimated from equation (45) between the estimated and theoretical second components of the currents.

$$\vec{j} \propto \frac{\epsilon}{T^2} e^{-\frac{k(x_1^2 - x_1 x_2 + x_2^2)}{k_B T}} \begin{pmatrix} x_1 - 2x_2 \\ -2x_1 + x_2 \end{pmatrix} + \mathcal{O}(\epsilon)^2 \qquad (43)$$

where we note how the amplitude and the direction of the flux are set by the ratio $\frac{\epsilon}{T^2}$, which vanishes at equilibrium. To gain some intuition on how the current decays with the distance in phase space, we can for example constrain equation (43) along the vertical direction ($x_1 = 0$),

$$\vec{j} \propto \frac{\epsilon}{T^2} e^{-\frac{kx_2^2}{k_B T}} \begin{pmatrix} -2x_2 \\ x_2 \end{pmatrix} + \mathcal{O}(\epsilon)^2. \qquad (44)$$

From equation (44) we can notice two opposite contributions to the amplitude, the linear dependence, dominant for small x_2 and the exponential dependence, dominant for larger x_2. This indicates an optimal distance from the origin at which the flux is maximum.

To compare the analytical expectation for the flux $\vec{j}$ with the results obtained using PFA on simulated trajectories, we calculate the compatibility $c_{ij,l}$ between the estimated $\hat{j}$ and the theoretical j values of the flux field in cell i, j, and in direction x_l:

$$c_{ij,l} = \frac{|\hat{j}_{ij,x_l} - j_{ij,x_l}|}{\sigma}, \qquad (45)$$

where σ is the error obtained from the bootstrapping analysis in PFA. The results for the second component of $\vec{j}$ yield an average compatibility of $\langle c_{ij} \rangle \simeq 1.02$ (figure 12(E)), indicating a good quantitative agreement between our estimation and the exact currents. A similar result is obtained in the equilibrium case ($T_1 = T_2$), for which the average compatibility is $\langle c_{ij} \rangle \simeq 0.95$. This concludes our analysis of probability fluxes in phase space for stochastic trajectories. These results illustrate how PFA can be used to infer accurate currents in coarse grained phase space from stochastic trajectories.

4.3. Probe filaments to study broken detailed balance across scales in motor-activated gels

While mesoscopic objects, such as cilia or flagella, can often be directly imaged, detecting non-equilibrium dynamics inside live cells on the microscale and below is more challenging. The cellular cytoskeleton, discussed in section 2, is a prominent example of active matter, which can best be described as a viscoelastic meshwork of biopolymers, activated by myosin motors [17, 21]. Random contractions of these myosin proteins fuelled by ATP hydrolysis can drive vigorous steady-state fluctuations in this polymer network. Such fluctuations can be quantified experimentally by embedding fluorescent probe particles. This technique has revealed multiple scaling regimes of the time dependence of the mean-squared displacement [32], which were attributed to a combination of the viscoelastic behavior of the network and the temporal dynamics of motor activity. In particular, endogenous embedded filaments such as microtubules, or added filaments such as single-walled carbon nanotubes have proved to be convenient probes [34, 55].

These experiments and others [45, 140, 262] have sparked a host of theoretical efforts [111, 185, 263–269] to elucidate the stochastic dynamics of probe particles and filaments in an active motorized gel. More recently, it has been suggested that

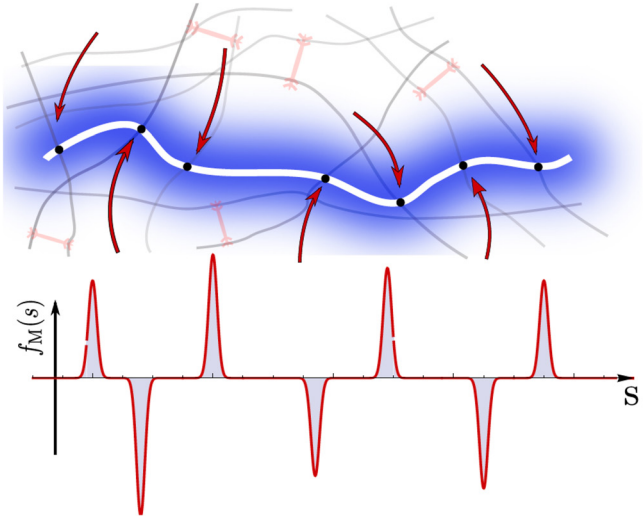

Figure 13. Fluctuations of a probe filament (blue) embedded in a viscoelastic actin (grey) network, driven out of equilibrium by random contractions of myosin (red, red arrows). Adapted figure with permission from [60], Copyright (2017) by the American Physical Society.

probe filaments can be also used as a multi-variable probe to discriminate active from thermal fluctuations using detailed balance [59, 60], and could be used to detect correlations in the profile of active forces along its backbone [58].

In the following, we lay out a framework to describe fluctuations of a semiflexible probe filament [56, 270–272], which is embedded in a motor-activated network [111, 127, 181]. We assume the probe filament to be weakly-bending, such that we can focus on the transverse coordinate $r_\perp(s,t)$, where the arclength $0 < s < L$ parametrizes the backbone, as shown in figure 13. The overdamped dynamics of such a probe filament is governed by a balance of (i) viscous and elastic forces of the surrounding viscoelastic medium, (ii) bending forces, (iii) thermal agitation, and (iv) motor-induced fluctuations, which read in this order as

$$\int_{-\infty}^{t} \mathrm{d}t'\, \alpha(t-t') r_\perp(s,t') + \kappa \frac{\partial^4 r_\perp}{\partial t^4}(s,t) = \xi(s,t) + f_M(s,t). \tag{46}$$

Terms on the left describe relaxation, while terms on the right contain stochastic contributions. For a predominantly elastic network, we can use the generalized Stokes equation, $\hat{\alpha}(\omega) = k_0 \hat{G}(\omega)$ to approximate the viscoelastic kernel on the left hand side as $\hat{G} = G_0 + i\eta\omega$, i.e. as a Kelvin–Voigt-type viscoelastic solid. The factor k_0 has a geometrical origin, and is given by $k_0 \approx 4\pi/\ln(L/d)$ for an infinitesimal rod segment of diameter d [126]. In a crosslinked actin network this approximation is reasonable for low frequencies typically below roughly 100 Hz, beyond which the network modulus exhibits a characteristic stiffening with frequency [45, 273, 274]. When the network is described as such a simple viscoelastic solid, the thermal noise is given by a Gaussian white-noise process $\xi(s,t)$, to which we add independent actively induced forces $f_M(s,t)$, specified in detail further below.

Bending forces can be conveniently studied from the perspective of bending modes of the probe filament. Following the approach in [59, 60], a description in terms of bending modes can be obtained from a decomposition of the backbone coordinates into orthogonal dynamic modes $r_\perp(s,t) = L\sum_q a_q(t) y_q(s)$ [56–58]. In this coordinate system, the multiscale character of probe filaments becomes apparent: each bending mode amplitude $a_q(t)$ is sensitive to a lengthscale corresponding to its wavelength. The precise form of bending modes, however, depends on the boundary conditions of the filament. The simplest case is a filament with zero transverse deflections at its end, where classical sine-modes $y_{q_m}(s) = \sqrt{2/L}\sin(q_m s)$ form an orthonormal set. Importantly, these modes are independent in equilibrium, due to their orthogonality. For fixed-end modes, mode number $m \in \{1,2,3,...\}$ and wave-vector q are related via $q(m) = m\pi/L$. The relaxational timescale of each mode is set by a balance between both elastic and viscous forces of the network and the bending rigidity of the filament. For inextensible filaments in purely viscous environments, this results in a strongly length-dependent decay

$$\tau_q = \frac{\eta}{\kappa q^4/k_0 + G_0}. \tag{47}$$

In the linear-response regime, we obtain the mode-response function to transverse deflections, $\chi_q(t)$, in fourier space $\hat{\chi}_q(\omega) = (\hat{\alpha}(\omega) + \kappa q^4)^{-1}$. This response function is related to mode variances in equilibrium via the mode fluctuation-dissipation theorem

$$\langle |\hat{a}_q(\omega)|^2 \rangle = \frac{2k_B T}{L^2 \omega} \hat{\chi}_q''(\omega). \tag{48}$$

Bending modes are thus ideally suited to not only detect motor activity, but also to measure their spatial and temporal characteristics. Perhaps for these reasons, bending mode fluctuations have been the subject of a number of studies in biological non-equilibrium systems.

In a study by Brangwynne *et al* [55], fluorescently labelled microtubuli were used to probe the active fluctuations in actin-myosin gels. The persistence lengths of microtubuli is on the order of millimeters [57], such that these filaments can be treated effectively as rigid on microscopic lengthscales under thermal conditions. By contrast, in actin-myosin gels, microtubuli exhibit significant fluctuations, caused by contractions of myosin, which deform the network in which the microtubules are embedded. A quantitative analysis of thermal bending mode fluctuations reveals a q^{-4}-decay in actin networks (without myosin). By contrast, adding myosin not only increases the amplitudes of fluctuations, but also results in a breakdown of the standard mode decay (see equation (47). The spatial extent of individual indentations in motor-agitated microtubuli can be used to extract forces induced by myosing. These force range between 0−30 pN, in accord with more recent studies in live cells [34, 45]. Importantly, the results also suggest a very narrow profile of the force exerted on the microtubules. Furthermore, in the cell cortex, microtubules often appear considerably more curved, despite their rigidity. Indeed, this curved microtubule structure is not due to

temporal bending fluctuations of the microtubule, but rather results from geometrical constraints that randomly deflect the microtubule tip during polymerization [158].

Motivated by these experimental observations, we can model the motor-induced force, exerted on the probe at the points where it is coupled elastically to the network, as a superposition of all active forces in the environment:

$$f_{\mathrm{M}}(s,t) = \sum_n f_n(s,t), \tag{49}$$

where each $f_n(s, t)$ denotes the force contribution from active motors, which affect the filament at the n_{th} entanglement point. Active forces have a characteristic spatial decay, since myosin motors exert forces in dipoles rather than in single directions [275]. The model in equation (49) does not account for such details; its main purpose is to provide a non-uniform force background $f(s)$ along the backbone s.

Measurements of myosin dynamics have revealed a Lorentzian power spectrum [111, 274]. A simple on-off telegraph process $\mathcal{T}(t)$ is in accord with these observations and appears to be adequate to model the stochastic force dynamics of individual motors. Taking furthermore into account the narrow profile of motor forces inferred from experiments [55], we arrive at a model for motor-induced forces, which reads $f_n(s,t) = f_n\delta(s-s_n)\mathcal{T}_n(t)$. Here $\mathcal{T}_n(t)$ is a telegraph process with exponential decorrelation $\langle \mathcal{T}(t)\mathcal{T}(t')\rangle = C_2\ \exp(-|t-t'|/\tau_M)$.

Using this simple description for the stochastic behavior of motor-generated forces together with equation (48), we compute the mode correlator, which decomposes into active and thermal contributions: $\langle a_q(t)a_w(t')\rangle = \langle a_q(t)a_w(t')\rangle^{\mathrm{Th}} + \langle a_q(t)a_w(t')\rangle^{\mathrm{M}}$, given by

$$\langle a_q(t)a_w(t')\rangle^{\mathrm{Th}} = \frac{k_{\mathrm{B}}T\tau_q}{L^2\gamma}\delta_{q,w}\mathrm{e}^{-\frac{|t-t'|}{\tau_q}} \tag{50}$$

$$\langle a_q(t)a_w(t')\rangle^{\mathrm{M}} = \frac{1}{L^2\gamma^2}\mathbf{F}_{q,w}C_2\mathcal{C}_{q,w}\,(t-t')\,. \tag{51}$$

$\mathbf{F}_{q,w}$ specifies the geometry of motor-induced forces in mode space and is defined by $\mathbf{F}_{q,w} = \sum_n f_n^2 y_q\,(s_n)\,y_w\,(s_n)$, where the sum runs over the filament-network contacts. The function $\mathcal{C}_{q,w}(\Delta t)$ denotes the temporal decorrelation of active mode fluctuations. In contrast to thermal equilibrium, active fluctuations decay as a double exponential

$$\mathcal{C}_{q,w}(t-t') = \tau_q\tau_w\left(\frac{\mathrm{e}^{-\frac{|t-t'|}{\tau_{\mathrm{M}}}}}{\left(1-\frac{\tau_q}{\tau_{\mathrm{M}}}\right)\left(1+\frac{\tau_w}{\tau_{\mathrm{M}}}\right)}\cdot\right.$$
$$\left.-2\frac{\tau_q}{\tau_{\mathrm{M}}}\frac{\mathrm{e}^{-\frac{|t'-t|}{\tau_q}}}{\left(1-\left(\frac{\tau_q}{\tau_{\mathrm{M}}}\right)^2\right)\left(1+\frac{\tau_w}{\tau_q}\right)}\right), \tag{52}$$

which indicates a competition between two decorrelating processes: mode relaxation and the internal decorrelation of the motor state. The correlator is not symmetric in the indices q and w as can be seen from equation (52), which results in a breaking of Onsager's time-reversal symmetry [60].

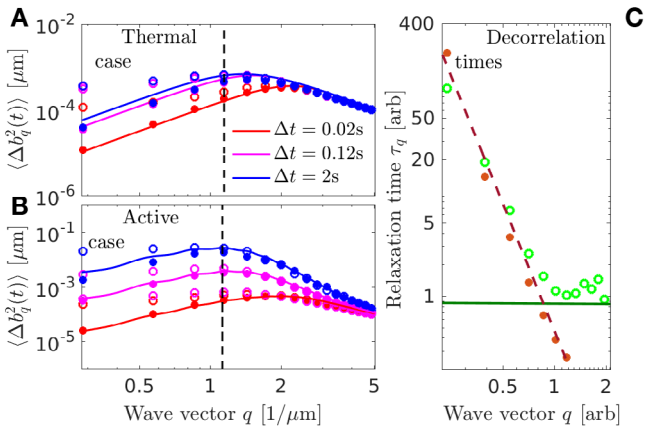

Figure 14. Mode fluctuations under (A) purely thermal agitated and (B) under additional influence of motor-induced forces. C) Convergence of mode decorrelation times onto the motor timescale. Different colors correspond to the different times Δt shown in the legend in panel (A). Adapted figure with permission from [55], Copyright (2008) by the American Physical Society.

This double exponential in equation (52) is the footprint of colour of the noise process, which we use to describe motor-induced forces. The q^{-4}-decay of mode amplitudes relaxation times, τ_q, levels off around τ_{M} as shown in figure 14(C). This saturation occurs because modes cannot decorrelate faster than the force that is driving them. Under coloured noise, the relaxation times cannot be directly inferred from decorrelation. This is indeed confirmed in Brownian dynamics simulations of filaments subject to active fluctuations [59]. To further illustrate these results, simulations of mode variances over mode vector in passive (figure 14(A)) and active (figure 14(B)) networks are shown together with theoretical predictions from equations (50) and (51). For comparison, experimentally obtained mode variances [55] are plotted over q in figure 15. As one would expect, in both cases mode variances are elevated in active environments.

In the long time regime $t \gg \tau_{\mathrm{M}}$, motor forces effectively appear as sources of white-noise. In this '*white-noise limit*', the motor correlator converges to a δ-function, $\langle \Delta\mathcal{T}(t)\Delta\mathcal{T}(t')\rangle \to C_2/2\tau_{\mathrm{M}}\delta(t-t')$ with a factor τ_{M}, which remains only as a scale of the variance of the motor process. The mode correlation function in the white-noise limit can be derived by a series expansion of $\mathcal{C}_{q,w}(t)$, which yields

$$\langle a_q(t)a_w(t')\rangle^{\mathrm{M}} = \frac{C_2\tau_M}{L^2\gamma^2}\mathbf{F}_{q,w}\frac{\tau_q\tau_w}{\tau_q+\tau_W}\delta(t-t'). \tag{53}$$

We can now contract the thermal and motor-white noise processes into a single process $\psi(t)$, with a correlator $\langle \psi_q(t)\psi_w(t')\rangle = (4k_{\mathrm{B}}T\gamma\delta_{q,w} + C_2\tau_{\mathrm{M}}\mathbf{F}_{q,w})\,\frac{\delta(t-t')}{2L^2}$.

It is useful at this stage to compare this scenario with that described in section 3.2: Here, mode variables are independent, but are subject to noise with a cross-mode correlations, such that different modes are simultanously excited by a motor event. By constrast, thermal noise is uniform in amplitude and uncorrelated throughout the system, giving rise to independent stochastic forces in mode-space. As we discussed in section 3.2, a correlation in the external noise in one coordinate system, may appear as a 'temperature'

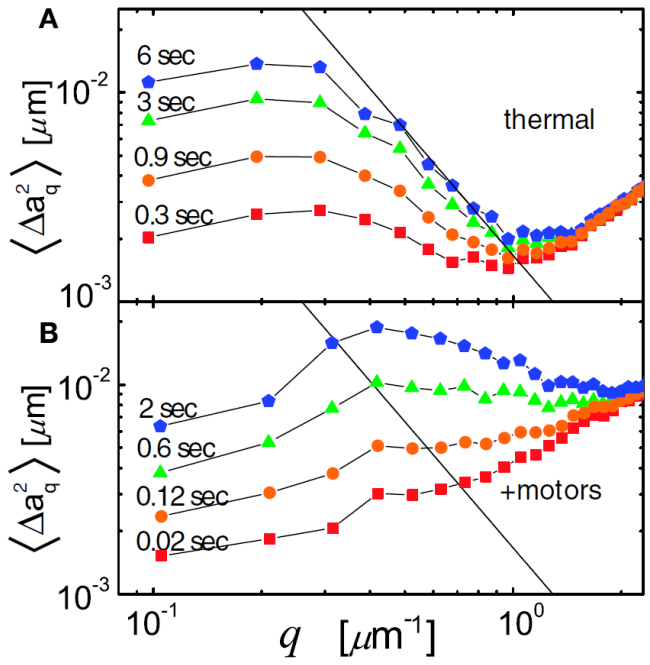

Figure 15. Mode amplitude variations in fluctuating microtubules embedded in actin-myosin gels over mode number q. (A) In ATP-depleted gels (purely thermal noise), mode variances follow a power law decay. (B) Active fluctuations result in enhanced mode variances in accord with the theory In figure 14. At high q-values measurement noise leads to an increase in mode variances. Adapted figure with permission from [59], Copyright (2016) by the American Physical Society.

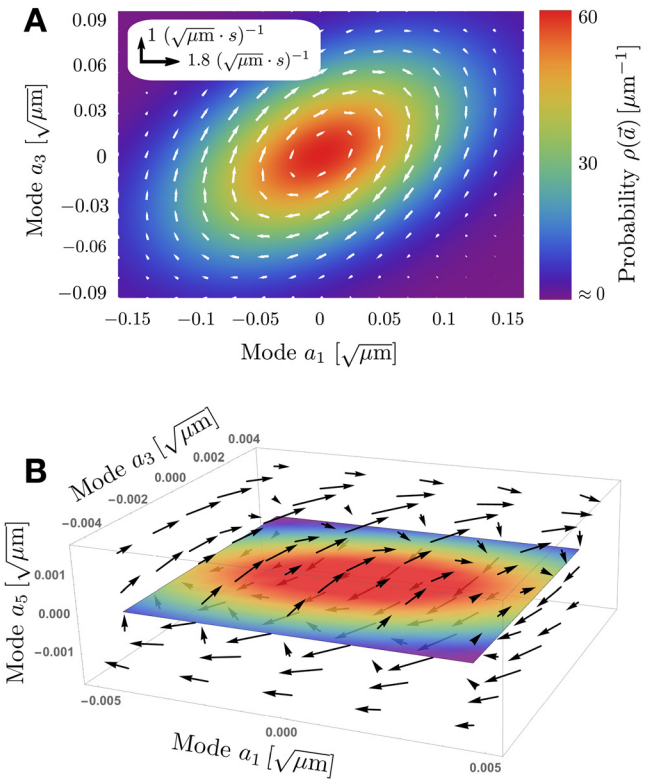

Figure 16. Steady-state probability currents in mode space. (A) Projection of the multidimensional current on the mode amplitude pair a_1 and a_3. (B) The same current in three dimensions a_1, a_3, and a_5. Due to the geometry of probe-network interactions in this example, only modes of similar number parity (e.g. odd–odd) couple. Adapted figure with permission from [59], Copyright (2016) by the American Physical Society.

gradient in different coordinates. It is this mechanism, which gives rise to a probability flux in mode space, which breaks detailed balance in the fluctuations of the probe filament. In other words, a motor-induced force background $\langle f_M(s,t)\rangle_{\text{temporal}} = \lim_{t_1\to\infty}\int_{t_0}^{t_1} \mathrm{d}t f_M(s,t)$ (see lower panel in figure 13), which varies along the filament, will lead to a breaking of detailed balance in a hyperplane spanned by the affected modes.

The magnitude and structure of this probability current, is given as a solution of the multivariate Fokker-Planck equation $\partial_t\rho(\vec{a},t) = -\vec{\nabla}\cdot\vec{j}(\vec{a},t)$ in mode space. The probability current, $\vec{j}(\vec{a})$, can be written in steady-state as

$$\vec{j}(\vec{a}) = (\mathbf{K} + \mathbf{D}\mathbf{C}^{-1})\vec{a}\rho(\vec{a}) \equiv \mathbf{\Omega}\vec{a}\rho(\vec{a}), \qquad (54)$$

where $\mathbf{K}_{q,w} = -1/\tau_q\delta_{q,w}$ is the deterministic matrix which defines the linear force field, and $\mathbf{D}$ and $\mathbf{C}$ represent respectively the diffusion and covariance matrices. Within this linear description, Ω is the matrix that captures the structure of the current [230, 276]. A rotational probability current in the Fokker-Planck picture is associated with a net rotation of variables in the Langevin description: On average, mode amplitudes cycle around the origin, when detailed balance is broken in steady-state, as illustrated in figure 16.

The circular character of the current is reflected mathematically by the skew-symmetry of $\mathbf{\Omega}^T = -\mathbf{\Omega}$ in the coordinate system where $\tilde{\mathbf{C}} = \mathbf{1}$ ('*correlation-identity coordinates*'). This can be seen from equation (41), which dictates that $\tilde{\mathbf{K}} + \tilde{\mathbf{K}}^T = -2\tilde{\mathbf{D}}$ in this system, such that $\tilde{\mathbf{\Omega}} = \frac{1}{2}\left(\tilde{\mathbf{K}} - \tilde{\mathbf{K}}^T\right)$.

The eigenvalues of any skew-symmetric matrix $\mathbf{R}$ are either zero or purely imaginary, with the latter leading to rotational currents in a hypothetical dynamical system described by $\dot{\vec{x}} = \mathbf{R}\vec{x}$. Moreover, since $\mathrm{Tr}\,(\mathbf{\Omega}) = 0$, in two dimensions, this implies that the eigenvalues can be rewritten as $\lambda_{1,2} = \pm i\omega$. In a steady-state, the probability current $\vec{j}$ (in any dimension) has to be orthogonal to the gradient of the density $\rho(\vec{a},t)$, since $\vec{\nabla}\cdot\vec{j}(\vec{a}) = \rho(\vec{a})\vec{\nabla}\cdot(\mathbf{\Omega}\vec{a}) + (\mathbf{\Omega}\vec{a})\cdot\vec{\nabla}\vec{\rho}(\vec{a}) = \partial_t\rho = 0$. The first term must be zero, since it is proportional to $\mathrm{Tr}\,(\mathbf{\Omega})\,\vec{a}$, so that the second term has to vanish as well. This, however, implies that $\vec{\nabla}\rho \perp \mathbf{\Omega}\vec{a}$: the gradient of the density must be perpendicular to the flow field. In a linear system, the probability density is always Gaussian $\rho \propto e^{-\frac{1}{2}\vec{a}^T\mathbf{C}^{-1}\vec{a}}$, such that the flow field must have an ellipsoidal structure [230]. In correlation-identity coordinates, where the density has a radial symmetry, the profile of $\tilde{\vec{j}}$ would thus be purely azimuthal, and its magnitude would represent an angular velocity. An average over the angular movements $\langle\dot{\varphi}\rangle$ of the mode vector $\vec{a}(t)$ in the plane will yield the cycling frequency. The imaginary part of the positive eigenvalue of $\mathbf{\Omega}$ must therefore represent the average cycling frequency of the mode vector in the plane.

In a reduced 2D system consisting only of $a_q(t)$ and $a_w(t)$, the cycling frequency can be calculated analytically and reads

$$\omega^{2D}_{q,w} = \frac{(\tau_q - \tau_w)\,\mathbf{F}_{q,w}}{\sqrt{\tau_q\tau_w\left((\tau_q+\tau_w)^2\,\beta - 4\tau_q\tau_w\mathbf{F}^2_{q,w}\right)}} \tag{55}$$

where $\beta = (\frac{2k_BT\gamma}{C_2\tau_M})^2 + \frac{2k_BT\gamma}{C_2\tau_M}(\mathbf{F}_{q,q} + \mathbf{F}_{w,w}) + \mathbf{F}_{w,w}\mathbf{F}_{q,q}$.

Interestingly, equation (55) shows that in the case of equal relaxation times $\tau_q = \tau_w$, the cycling frequency would be zero and thus, detailed balance would be restored, regardless of differences between the modes in motor-induced fluctuations. This hints at an important role of relaxation times in determining the shape of the current in multidimensional systems. Furthermore, the denominator of equation (55) shows how an increase in overall temperature T could mask broken detailed balance by reducing the cycling frequency.

In summary, filaments as multi-scale and multi-variable probes offer a novel perspective on non-equilibrium phenomena in active matter and could be used in the future as 'non-equilibrium antennae'. As we illustrated in this section, a heterogeneous force background $f_M(s,t)$ created by motor-induced fluctuations leads to a breaking of detailed balance in mode space of embedded filaments. The intricate structure of the probability current in steady-state may contain a wealth of information about the geometric and, perhaps, temporal structure of impinging active forces.

The theory laid out in this section can be generalized to other objects, such as membranes [35, 36, 167, 172]. In principle, the membrane mode decomposition described in section 2 could be used to detect a breaking of detailed balance, since active processes in the cortex of red blood cells might result in noise input that correlates over different membrane modes.

5. Outlook

The examples discussed in this review illustrate how experimental measurements of non-equilibrium activity and irreversibility can provide a deeper conceptual understanding of active biological assemblies and non-equilibrium processes in cells. In many cases, non-equilibrium fluctuations have successfully been identified and quantified using the combination of active and passive microrheology techniques to study the violation of the fluctuation-dissipation theorem, [36, 43]. Such studies can for instance reveal the force spectrum inside cells, [45]. However, these approaches require invasive micromechanical manipulation. Furthermore, a complete generalization of the fluctuation-dissipation theorem for non-equilibrium system is still lacking, such that the response of a non-equilibrium system can not be inferred from its spontaneous fluctuations. However, this does not mean that the fluctuations of a non-equilibrium steady state do not contain valuable information about the nature of the system. Indeed, non-invasive approaches to measure broken detailed balance from stochastic dynamics have now been establishes to reveal phase space currents in mesoscopic degrees of freedom of biological systems, [22]. It remains an open question what information can be inferred about the underlying system from such phase space currents, [59, 60]. However, recently derived theoretical relations for energy dissipation and entropy production to characterize non-equilibrium activity are finding traction in various biological systems such as molecular motors and chemical control systems [1, 2, 225, 247].

Taken together, the research discussed in this review illustrate that the gap between fundamental approaches in stochastic thermodynamics and its application to real biological system is slowly closing. Indeed, studies of biological active matter are not only yielding insights in non-equilibrium physics, they have also suggested conceptually novel mechanisms in cell biology. For instance, the collective effect of forces exerted by molecular motors has been implicated in intracellular transport and positioning of the nucleus [31, 32, 34, 45, 110]. This novel mode of transport, known as *active diffusion*, is thought to complement thermal diffusion and directed, motor-driven modes of transport in cells. Another intriguing example is the role of DNA-binding ATPases, which have been suggested to be capable of generating forces on the chromosomes through a DNA-relay mechanism [277] or loop extrusion [278, 279]. ATP- or GTPases can also interact with membranes or DNA to play a role in pattern forming systems [10–12], for instance in the Min system in *E. coli* and CDC42 in yeast. In these systems, certain proteins can switch irreversibly between different conformational states, affecting their affinity to be in the cytosol or the membrane. This, together with nonlinear interactions between these different proteins, can result in non-equilibrium dynamic pattern formation.

Another important example in this respect is how cells break symmetry to form a polarity axes. Intracellular myosin activity has been implicated in establishing a sense of direction ('polarity') in cells. In order to divide, cells must 'decide' on the axis of the mytotic spindle, which is a crucial part of the cell division apparatus [280–283]. Cortical flows resulting from asymmetries in myosin activity have been shown to effectively polarize *C. elegans* cells and break the initial cellular symmetry [284].

Non-equilibrium phenomena also emerge at the multicellular scale: Groups of motile cells exhibit collective active dynamics, such as flocking, swarming, non-equilibrium phase transitions or the coordinated movements of cells during embryonic developments [285, 286]. More broadly, non-equilibrium physics is emerging as a guiding framework to understand phenomena related to self-replication and adaptation [226–228], the origin of life (see for example [287, 288]), as well as synthetic life-like systems (See [289] and references therein).

Acknowledgments

This work was supported by the German Excellence Initiative via the program NanoSystems Initiative Munich (NIM) and by the German Research Council (DFG) within the framework of the Transregio 174 'Spatiotemporal dynamics of bacterial cells'. FM is supported by a DFG Fellowship through the Graduate School of Quantitative Biosciences Munich (QBM). This project has received funding from the European Union's Horizon 2020 research and innovation

programme under European Training Network (ETN) grant 674979-NANOTRANS (JG) and was performed in part at the Aspen Center for Physics (CPB), which is supported by National Science Foundation grant PHY-1607611. We thank T Betz, G Berman, W Bialek, D Braun, D Brückner, C Brangwynne, G Crooks, N Fakhri, B Fabry, E Frey, N Gov, M Guo, G Gradziuk, R Granek, L Jawerth, F Jülicher, G Koenderink, K Kroy, M Lenz, T Liverpool, T Lubensky, B Machta, F MacKintosh, J Messelink, K Miermans, J Rädler, P Ronceray, J Shaevitz, D Schwab, M Sheinman, Y Shokef, C Schmidt, C Storm, J Tailleur, M Tikhonov, D Weitz, M Wigbers, and N Wingreen, for many stimulating discussions.

ORCID iDs

C P Broedersz https://orcid.org/0000-0001-7283-3704

References

[1] Lan G, Sartori P, Neumann S, Sourjik V and Tu Y 2012 The energy speed accuracy trade-off in sensory adaptation *Nat. Phys.* **8** 422–8
[2] Mehta P and Schwab D J 2012 Energetic costs of cellular computation *Proc. Natl Acad. Sci. USA* **109** 17978–82
[3] Hopfield J J 1974 Kinetic proofreading: a new mechanism for reducing errors in biosynthetic processes requiring high specificity *Proc. Natl Acad. Sci. USA* **71** 4135–9
[4] Murugan A, Huse D A and Leibler S 2012 Speed, dissipation, and error in kinetic proofreading *Proc. Natl Acad. Sci. USA* **109** 12034–9
[5] Needleman D and Brugues J 2014 Determining physical principles of subcellular organization *Dev. Cell* **29** 135–8
[6] Fletcher D A and Mullins R D 2010 Cell mechanics and the cytoskeleton *Nature* **463** 485–92
[7] Brangwynne C P, Koenderink G H, MacKintosh F C and Weitz D A 2008 Cytoplasmic diffusion: molecular motors mix it up *J. Cell Biol.* **183** 583–7
[8] Juelicher F, Kruse K, Prost J and Joanny J-F 2007 Active behavior of the cytoskeleton *Phys. Rep.* **449** 3–28
[9] Cates M E 2012 Diffusive transport without detailed balance in motile bacteria: does microbiology need statistical physics? *Rep. Prog. Phys.* **75** 042601
[10] Huang K C, Meir Y and Wingreen N S 2003 Dynamic structures in *Escherichia Coli*: spontaneous formation of MinE rings and MinD polar zones *Proc. Natl Acad. Sci. USA* **100** 12724–8
[11] Frey E, Halatek J, Kretschmer S and Schwille P 2017 Protein pattern formation *Physical Biology Members* ed P Bassereau and P C A Sens (Heidelberg: Springer)
[12] Halatek J and Frey E 2012 Highly canalized MinD transfer and MinE sequestration explain the origin of robust MinCDE-protein dynamics *Cell Rep.* **1** 741–52
[13] Bialek W 2012 *Biophysics: Searching for Principles* (Princeton, NJ: Princeton University Press)
[14] Seifert U 2012 Stochastic thermodynamics, fluctuation theorems and molecular machines *Rep. Prog. Phys.* **75** 126001
[15] Ritort F 2007 Nonequilibrium fluctuations in small systems: from physics to biology *Advances in Chemical Physics* ed S A Rice, vol 137 (Hoboken, NJ: Wiley) (https://doi.org/10.1002/9780470238080.ch2)
[16] Van den Broeck C and Esposito M 2015 Ensemble and trajectory thermodynamics: a brief introduction *Physica* A **418** 6–16
[17] MacKintosh F C and Schmidt C F 2010 Active cellular materials *Curr. Opin. Cell Biol.* **22** 29–35
[18] Marchetti M C, Joanny J F, Ramaswamy S, Liverpool T B, Prost J, Rao M and Simha R A 2013 Hydrodynamics of soft active matter *Rev. Mod. Phys.* **85** 1143–89
[19] Ramaswamy S 2010 The mechanics and statistics of active matter *Annu. Rev. Condens. Matter Phys.* **1** 323–45
[20] Joanny J-F and Prost J 2009 Active gels as a description of the actin-myosin cytoskeleton *HFSP J.* **3** 94–104
[21] Prost J, Julicher F and Joanny J-F F 2015 Active gel physics *Nat. Phys.* **11** 111–7
[22] Battle C, Broedersz C P, Fakhri N, Geyer V F, Howard J, Schmidt C F and MacKintosh F C 2016 Broken detailed balance at mesoscopic scales in active biological systems *Science* **352** 604–7
[23] Zia R K P and Schmittmann B 2007 Probability currents as principal characteristics in the statistical mechanics of non-equilibrium steady states *J. Stat. Mech.* **2007** P07012
[24] Ajdari A, Prost J, Ju F and Jülicher F 1997 Modeling molecular motors *Rev. Mod. Phys.* **69** 1269–81
[25] Howard J 2001 Mechanics of motor proteins and the cytoskeleton *Sinauer* **7** 384
[26] Bausch A R and Kroy K 2006 A bottom-up approach to cell mechanics *Nat. Phys.* **2** 231–8
[27] Glaser J and Kroy K 2010 Fluctuations of stiff polymers and cell mechanics *Biopolymers* 509–34
[28] Egolf D A 2000 Equilibrium regained: from nonequilibrium chaos to statistical mechanics *Science* **287** 101–4
[29] Rupprecht J-F and Prost J 2016 A fresh eye on nonequilibrium systems *Science* **352** 514–5
[30] Weber S C, Spakowitz A J and Theriot J A 2012 Nonthermal ATP-dependent fluctuations contribute to the *in vivo* motion of chromosomal loci *Proc. Natl Acad. Sci. USA* **109** 7338–43
[31] Almonacid M, Ahmed W W, Bussonnier M, Mailly P, Betz T, Voituriez R, Gov N S and Verlhac M-H 2015 Active diffusion positions the nucleus in mouse oocytes *Nat. Cell Biol.* **17** 470–9
[32] Brangwynne C P, Koenderink G H, MacKintosh F C and Weitz D A 2009 Intracellular transport by active diffusion *Trends Cell Biol.* **19** 423–7
[33] Brangwynne C P, Mitchison T J and Hyman A A 2011 Active liquid-like behavior of nucleoli determines their size and shape in Xenopus laevis oocytes *Proc. Natl Acad. Sci. USA* **108** 4334–9
[34] Fakhri N, Wessel A D, Willms C, Pasquali M, Klopfenstein D R, MacKintosh F C and Schmidt C F 2014 High-resolution mapping of intracellular fluctuations using carbon nanotubes *Science* **344** 1031–5
[35] Betz T, Lenz M, Joanny J-F and Sykes C 2009 ATP-dependent mechanics of red blood cells *Proc. Natl Acad. Sci. USA* **106** 15320–5
[36] Turlier H, Fedosov D A, Audoly B, Auth T, Gov N S, Sylkes C, Joanny J-F, Gompper G and Betz T 2016 Equilibrium physics breakdown reveals the active nature of red blood cell flickering *Nat. Phys.* **12** 513–9
[37] Ben-Isaac E, Park Y, Popescu G, Brown F L H, Gov N S and Shokef Y 2011 Effective temperature of red-blood-cell membrane fluctuations *Phys. Rev. Lett.* **106** 238103
[38] Tuvia S, Almagor A, Bitler A, Levin S, Korenstein R and Yedgar S 1997 Cell membrane fluctuations are regulated by medium macroviscosity: evidence for a metabolic driving force *Proc. Natl Acad. Sci.* **94** 5045–9
[39] Monzel C, Schmidt D, Kleusch C, Kirchenbüchler D, Seifert U, Smith A-S, Sengupta K and Merkel R 2015 Measuring fast stochastic displacements of bio-membranes with dynamic optical displacement spectroscopy *Nat. Commun.* **6** 8162

[40] Battle C, Ott C M, Burnette D T, Lippincott-Schwartz J and Schmidt C F 2015 Intracellular and extracellular forces drive primary cilia movement *Proc. Natl Acad. Sci. USA* **112** 1410–5

[41] Fodor É, Mehandia V, Comelles J, Thiagarajan R, Gov N S, Visco P, van Wijland F and Riveline D 2015 From motorinduced fluctuations to mesoscopic dynamics in epithelial tissues **1** 1–5 (arXiv:1512.01476)

[42] Lau A W C, Hoffman B D, Davies A, Crocker J C and Lubensky T C 2003 Microrheology, stress fluctuations, and active behavior of living cells *Phys. Rev. Lett.* **91** 198101

[43] Mizuno D, Tardin C, Schmidt C F and MacKintosh F C 2007 Nonequilibrium mechanics of active cytoskeletal networks *Science* **315** 370–3

[44] Mizuno D, Head D A, MacKintosh F C and Schmidt C F 2008 Active and passive microrheology in equilibrium and nonequilibrium systems *Macromolecules* **41** 7194–202

[45] Guo M, Ehrlicher A J, Jensen M H, Renz M, Moore J R, Goldman R D, Lippincott-Schwartz J, Mackintosh F C and Weitz D A 2014 Probing the stochastic, motor-driven properties of the cytoplasm using force spectrum microscopy *Cell* **158** 822–32

[46] Schaller V, Weber C, Semmrich C, Frey E and Bausch A R 2010 Polar patterns of driven filaments *Nature* **467** 73–7

[47] Schaller V, Weber C A, Hammerich B, Frey E and Bausch A R 2011 Frozen steady states in active systems *Proc. Natl Acad. Sci. USA* **108** 19183–8

[48] Soares e Silva M *et al* 2011 Active multistage coarsening of actin networks driven by myosin motors *Proc. Natl Acad. Sci. USA* **108** 9408–13

[49] Murrell M P and Gardel M L 2012 F-actin buckling coordinates contractility and severing in a biomimetic actomyosin cortex *Proc. Natl Acad. Sci. USA* **109** 20820–5

[50] Alvarado J, Sheinman M, Sharma A, MacKintosh F C and Koenderink G H 2013 Molecular motors robustly drive active gels to a critically connected state *Nat. Phys.* **9** 591–7

[51] Lenz M 2014 Geometrical origins of contractility in disordered actomyosin networks *Phys. Rev.* X **4** 041002

[52] Koenderink G H, Dogic Z, Nakamura F, Bendix P M, MacKintosh F C, Hartwig J H, Stossel T P and Weitz D A 2009 An active biopolymer network controlled by molecular motors *Proc. Natl Acad. Sci. USA* **106** 15192–7

[53] Sheinman M, Broedersz C P and MacKintosh F C 2012 Actively stressed marginal networks *Phys. Rev. Lett.* **109** 238101

[54] Broedersz C P and MacKintosh F C 2011 Molecular motors stiffen non-affine semiflexible polymer networks *Soft Matter* **7** 3186–91

[55] Brangwynne C P, Koenderink G H, MacKintosh F C and Weitz D A 2008 Nonequilibrium microtubule fluctuations in a model cytoskeleton *Phys. Rev. Lett.* **100** 118104

[56] Aragon S R and Pecora R 1985 Dynamics of wormlike chains *Macromolecules* **18** 1868–75

[57] Gittes F, Mickey B, Nettleton J and Howard J 1993 Flexural rigidity of microtubules and actin filaments measured from thermal fluctuations in shape *J. Cell Biol.* **120** 923–34

[58] Brangwynne C P, Koenderink G H, Barry E, Dogic Z, MacKintosh F C and Weitz D A 2007 Bending dynamics of fluctuating biopolymers probed by automated high-resolution filament tracking *Biophys. J.* **93** 346–59

[59] Gladrow J, Fakhri N, MacKintosh F C, Schmidt C F and Broedersz C P 2016 Broken detailed balance of filament dynamics in active networks *Phys. Rev. Lett.* **116** 248301

[60] Gladrow J, Broedersz C P and Schmidt C F 2017 Nonequilibrium dynamics of probe filaments in actin-myosin networks *Phys. Rev.* E **96** 022408

[61] Cicuta P and Donald A M 2007 Microrheology: a review of the method and applications *Soft Matter* **3** 1449–55

[62] Mason T G, Ganesan K, van Zanten J H, Wirtz D and Kuo S C 1997 Particle tracking microrheology of complex fluids *Phys. Rev. Lett.* **79** 3282–5

[63] MacKintosh F and Schmidt C 1999 Microrheology *Curr. Opin. Colloid Interface Sci.* **4** 300–7

[64] Waigh T A 2005 Microrheology of complex fluids *Rep. Prog. Phys.* **68** 685

[65] Levine A J and Lubensky T C 2000 One- and two-particle microrheology *Phys. Rev. Lett.* **85** 1774–7

[66] Jensen M H, Morris E J and Weitz D A 2015 Mechanics and dynamics of reconstituted cytoskeletal systems *Biochim. Biophys. Acta* **1853** 3038–42

[67] Lieleg O, Claessens M M A E, Heussinger C, Frey E and Bausch A R 2007 Mechanics of bundled semiflexible polymer networks *Phys. Rev. Lett.* **99** 88102

[68] Lieleg O, Claessens M M A E and Bausch A R 2010 Structure and dynamics of cross-linked actin networks *Soft Matter* **6** 218–25

[69] Mahaffy R E, Shih C K, MacKintosh F C and Käs J 2000 Scanning probe-based frequency-dependent microrheology of polymer gels and biological cells *Phys. Rev. Lett.* **85** 880–3

[70] Gardel M L, Valentine M T, Crocker J C, Bausch A R and Weitz D A 2003 Microrheology of entangled F-actin solutions *Phys. Rev. Lett.* **91** 158302

[71] Tseng Y, Kole T P and Wirtz D 2002 Micromechanical mapping of live cells by multiple-particle-tracking microrheology *Biophys. J.* **83** 3162–76

[72] Keller M, Tharmann R, Dichtl M A, Bausch A R and Sackmann E 2003 Slow filament dynamics and viscoelasticity in entangled and active actin networks *Phil. Trans. R. Soc.* **361** 699–712

[73] Uhde J, Keller M, Sackmann E, Parmeggiani A and Frey E 2004 Internal motility in stiffening actin-myosin networks *Phys. Rev. Lett.* **93** 268101

[74] Wilhelm C 2008 Out-of-equilibrium microrheology inside living cells *Phys. Rev. Lett.* **101** 28101

[75] Fabry B, Maksym G N, Butler J P, Glogauer M, Navajas D and Fredberg J J 2001 Scaling the microrheology of living cells *Phys. Rev. Lett.* **87** 148102

[76] Bausch A R, Möller W and Sackmann E 1999 Measurement of local viscoelasticity and forces in living cells by magnetic tweezers *Biophys. J.* **76** 573–9

[77] Ma R, Klindt G S, Riedel-Kruse I H, Jülicher F and Friedrich B M 2014 Active phase and amplitude fluctuations of flagellar beating *Phys. Rev. Lett.* **113** 048101

[78] Callen H B and Welton T A 1951 Irreversibility and generalized noise *Phys. Rev.* **83** 34–40

[79] Kubo R 1966 The fluctuation-dissipation theorem *Rep. Prog. Phys.* **29** 255

[80] Martin P, Hudspeth A J and Jülicher F 2001 Comparison of a hair bundle's spontaneous oscillations with its response to mechanical stimulation reveals the underlying active process *Proc. Natl Acad. Sci. USA* **98** 14380–5

[81] Van Dijk P, Mason M J, Schoffelen R L, Narins P M and Meenderink S W 2011 Mechanics of the frog ear *Hear. Res.* **273** 46–58

[82] Cugliandolo L F, Kurchan J and Peliti L 1997 Energy flow, partial equilibration, and effective temperatures in systems with slow dynamics *Phys. Rev.* E **55** 3898–914

[83] Loi D, Mossa S and Cugliandolo L F 2008 Effective temperature of active matter *Phys. Rev.* E **77** 51111

[84] Bursac P, Lenormand G, Fabry B, Oliver M, Weitz D A, Viasnoff V, Butler J P and Fredberg J J 2005 Cytoskeletal remodelling and slow dynamics in the living cell *Nat. Mater.* **4** 557–61

[85] Prost J, Joanny J-F and Parrondo J M R 2009 Generalized fluctuation-dissipation theorem for steady-state systems *Phys. Rev. Lett.* **103** 090601

[86] Cugliandolo L F 2011 *J. Phys. A Math. Theor.* **44** 483001
[87] Fodor É, Nardini C, Cates M E, Tailleur J, Visco P and van Wijland F 2016 How far from equilibrium is active matter? *Phys. Rev. Lett.* **117** 038103
[88] Fodor É, Guo M, Gov N S, Visco P, Weitz D A and van Wijland F 2015 Activity-driven fluctuations in living cells *Europhys. Lett.* **110** 48005
[89] Dieterich E, Seifert U, Ritort F, Camunas-Soler J, Ribezzi-Crivellari M, Seifert U and Ritort F 2015 Single-molecule measurement of the effective temperature in non-equilibrium steady states *Nat. Phys.* **11** 1–8
[90] Chaikin P M and Lubensky T C 1995 *Principles of Condensed Matter Physics* (Cambridge: Cambridge University Press)
[91] Yamada S, Wirtz D and Kuo S C 2000 Mechanics of living cells measured by laser tracking microrheology *Biophys. J.* **78** 1736–47
[92] Mason T G and Weitz D A 1995 Optical measurements of frequency-dependent linear viscoelastic moduli of complex fluids *Phys. Rev. Lett.* **74** 1250–3
[93] Ziemann F, Rädler J and Sackmann E 1994 Local measurements of viscoelastic moduli of entangled actin networks using an oscillating magnetic bead micro-rheometer *Biophys. J.* **66** 2210–6
[94] Amblard F, Maggs A C, Yurke B, Pargellis A N and Leibler S 1996 Subdiffusion and anomalous local viscoelasticity in actin networks *Phys. Rev. Lett.* **77** 4470–3
[95] Schmidt F G, Ziemann F and Sackmann E 1996 Shear field mapping in actin networks by using magnetic tweezers *Eur. Biophys. J.* **24** 348–53
[96] Beroz F, Jawerth L M, Münster S, Weitz D A, Broedersz C P and Wingreen N S 2017 Physical limits to biomechanical sensing in disordered fibre networks *Nat. Commun.* **8** 16096
[97] Jones C A R, Cibula M, Feng J, Krnacik E A, McIntyre D H, Levine H and Sun B 2015 Micromechanics of cellularized biopolymer networks *Proc. Natl Acad. Sci. USA* **112** E5117–22
[98] Crocker J C, Valentine M T, Weeks E R, Gisler T, Kaplan P D, Yodh A G and Weitz D A 2000 Two-point microrheology of inhomogeneous soft materials *Phys. Rev. Lett.* **85** 888–91
[99] Schnurr B, Gittes F, MacKintosh F C and Schmidt C F 1997 Determining microscopic viscoelasticity in flexible and semiflexible polymer networks from thermal fluctuations *Macromolecules* **30** 7781–92
[100] Addas K M, Schmidt C F and Tang J X 2004 Microrheology of solutions of semiflexible biopolymer filaments using laser tweezers interferometry *Phys. Rev.* E **70** 021503
[101] Gittes F and MacKintosh F C 1998 Dynamic shear modulus of a semiflexible polymer network *Phys. Rev.* E **58** R1241–4
[102] Gittes F, Schnurr B, Olmsted P D, MacKintosh F C and Schmidt C F 1997 Microscopic viscoelasticity: shear moduli of soft materials determined from thermal fluctuations *Phys. Rev. Lett.* **79** 3286–9
[103] Chen D T, Weeks E R, Crocker J C, Islam M F, Verma R, Gruber J, Levine A J, Lubensky T C and Yodh A G 2003 Rheological microscopy: local mechanical properties from microrheology *Phys. Rev. Lett.* **90** 108301
[104] Mason T G 2000 Estimating the viscoelastic moduli of complex fluids using the generalized Stokes–Einstein equation *Rheol. Acta* **39** 371–8
[105] Helfer E, Harlepp S, Bourdieu L, Robert J, MacKintosh F C and Chatenay D 2000 Microrheology of biopolymer-membrane complexes *Phys. Rev. Lett.* **85** 457
[106] Fedosov D A, Caswell B and Karniadakis G E 2010 A multiscale red blood cell model with accurate mechanics, rheology, and dynamics *Biophys. J.* **98** 2215–25
[107] Lee M H, Reich D H, Stebe K J and Leheny R L 2010 Combined passive and active microrheology study of protein-layer formation at an AirWater interface *Langmuir* **26** 2650–8
[108] Prasad V, Koehler S A and Weeks E R 2006 Two-particle microrheology of quasi-2D viscous systems *Phys. Rev. Lett.* **97** 176001
[109] Ortega F, Ritacco H and Rubio R G 2010 Interfacial microrheology: particle tracking and related techniques *Curr. Opin. Colloid Interface Sci.* **15** 237–45
[110] Caspi A, Granek R and Elbaum M 2000 Enhanced diffusion in active intracellular transport *Phys. Rev. Lett.* **85** 5655
[111] MacKintosh F C and Levine A J 2008 Nonequilibrium mechanics and dynamics of motor-activated gels *Phys. Rev. Lett.* **100** 18104
[112] Vella F 1994 Molecular biology of the cell (third edition): By B Alberts, D Bray, J Lewis, M Raff, K Roberts and J D Watson. pp 1361. Garland Publishing, New York and London. 1994 *Biochem. Educ.* **22** 164
[113] Kasza K E, Rowat A C, Liu J, Angelini T E, Brangwynne C P, Koenderink G H and Weitz D A 2007 The cell as a material *Curr. Opin. Cell Biol.* 19 101–7
[114] Köhler S and Bausch A R 2012 Contraction mechanisms in composite active actin networks *PLoS One* **7** e39869
[115] Stricker J, Falzone T and Gardel M L 2010 Mechanics of the F-actin cytoskeleton *J. Biomech.* **43** 9–14
[116] Lin Y-C, Koenderink G H, MacKintosh F C and Weitz D A 2007 Viscoelastic properties of microtubule networks *Macromolecules* **40** 7714–20
[117] Kasza K E, Broedersz C P, Koenderink G H, Lin Y C, Messner W, Millman E A, Nakamura F, Stossel T P, MacKintosh F C and Weitz D A 2010 Actin filament length tunes elasticity of flexibly cross-linked actin networks *Biophys. J.* **99** 1091–100
[118] Gardel M L, Kasza K E, Brangwynne C P, Liu J and Weitz D A 2008 Mechanical response of cytoskeletal networks *Methods Cell Biol.* **89** 487–519
[119] Pelletier V, Gal N, Fournier P and Kilfoil M L 2009 Microrheology of microtubule solutions and actin-microtubule composite networks *Phys. Rev. Lett.* **102** 188303
[120] Murrell M, Oakes P W, Lenz M and Gardel M L 2015 Forcing cells into shape: the mechanics of actomyosin contractility *Nat. Rev. Mol. Cell Biol.* **16** 486–98
[121] Schaller V, Weber C, Frey E and Bausch A R 2011 Polar pattern formation: hydrodynamic coupling of driven filaments *Soft Matter* **7** 3213–8
[122] Bendix P M, Koenderink G H, Cuvelier D, Dogic Z, Koeleman B N, Brieher W M, Field C M, Mahadevan L and Weitz D A 2008 A quantitative analysis of contractility in active cytoskeletal protein networks *Biophys. J.* **94** 3126–36
[123] Ronceray P, Broedersz C P and Lenz M 2016 Fiber networks amplify active stress *Proc. Natl Acad. Sci. USA* **113** 2827–32
[124] Lenz M, Thoresen T, Gardel M L and Dinner A R 2012 Contractile units in disordered actomyosin bundles arise from F-actin buckling *Phys. Rev. Lett.* **108** 238107
[125] Wang S and Wolynes P G 2012 Active contractility in actomyosin networks *Proc. Natl Acad. Sci. USA* **109** 6446–51
[126] Howard J 2002 Mechanics of motor proteins *Physics of Bio-Molecules and Cells Physics des Biomolfégcules des Cellules* (New York: Springer) pp 69–94
[127] Levine A J and MacKintosh F C 2009 The mechanics and fluctuation spectrum of active gels *J. Phys. Chem.* B **113** 3820–30
[128] Storm C, Pastore J J, MacKintosh F C, Lubensky T C and Janmey P A 2005 Nonlinear elasticity in biological gels *Nature* **435** 191–4
[129] Gardel M L 2004 Elastic behavior of cross-linked and bundled actin networks *Science* **304** 1301–5

[130] Kasza K E, Koenderink G H, Lin Y C, Broedersz C P, Messner W, Nakamura F, Stossel T P, Mac Kintosh F C and Weitz D A 2009 Nonlinear elasticity of stiff biopolymers connected by flexible linkers *Phys. Rev.* E **79** 41928

[131] Lin Y-C, Yao N Y, Broedersz C P, Herrmann H, MacKintosh F C and Weitz D A 2010 Origins of elasticity in intermediate filament networks *Phys. Rev. Lett.* **104** 58101

[132] Shokef Y and Safran S A 2012 Scaling laws for the response of nonlinear elastic media with implications for cell mechanics *Phys. Rev. Lett.* **108** 178103

[133] Ronceray P and Lenz M 2015 Connecting local active forces to macroscopic stress in elastic media *Soft Matter* **11** 1597–605

[134] Hawkins R J and Liverpool T B 2014 Stress reorganization and response in active solids *Phys. Rev. Lett.* **113** 28102

[135] Xu X and Safran S A 2015 Nonlinearities of biopolymer gels increase the range of force transmission *Phys. Rev.* E **92** 032728

[136] Chen P and Shenoy V B 2011 Strain stiffening induced by molecular motors in active crosslinked biopolymer networks *Soft Matter* **7** 355–8

[137] Tee S-Y, Bausch A R and Janmey P A 2009 The mechanical cell *Curr. Biol.* **19** R745–8

[138] Lam W A, Chaudhuri O, Crow A, Webster K D, Li T-D, Kita A, Huang J and Fletcher D A 2011 Mechanics and contraction dynamics of single platelets and implications for clot stiffening *Nat. Mater.* **10** 61

[139] Jansen K A, Bacabac R G, Piechocka I K and Koenderink G H 2013 Cells actively Stiffen Fibrin networks by generating contractile stress *Biophys. J.* **105** 2240–51

[140] Toyota T, Head D A, Schmidt C F and Mizuno D 2011 Non-Gaussian athermal fluctuations in active gels *Soft Matter* **7** 3234–9

[141] Stuhrmann B, Soares e Silva M, Depken M, MacKintosh F C and Koenderink G H 2012 Nonequilibrium fluctuations of a remodeling *in vitro* cytoskeleton *Phys. Rev.* E **86** 20901

[142] Bertrand O J N, Fygenson D K and Saleh O A 2012 Active, motor-driven mechanics in a DNA gel *Proc. Natl Acad. Sci. USA* **109** 17342–7

[143] Deng L, Trepat X, Butler J P, Millet E, Morgan K G, Weitz D A and Fredberg J J 2006 Fast and slow dynamics of the cytoskeleton *Nat. Mater.* **5** 636–40

[144] Ahmed W W and Betz T 2015 Dynamic cross-links tune the solid–fluid behavior of living cells *Proc. Natl Acad. Sci. USA* **112** 6527–8

[145] Ehrlicher A J, Krishnan R, Guo M, Bidan C M, Weitz D A and Pollak M R 2015 Alpha-actinin binding kinetics modulate cellular dynamics and force generation *Proc. Natl Acad. Sci. USA* **112** 6619–24

[146] Yao N Y, Broedersz C P, Depken M, Becker D J, Pollak M R, MacKintosh F C and Weitz D A 2013 Stress-enhanced gelation: a dynamic nonlinearity of elasticity *Phys. Rev. Lett.* **110** 18103

[147] Humphrey D, Duggan C, Saha D, Smith D and Kas J 2002 Active fluidization of polymer networks through molecular motors *Nature* **416** 413–6

[148] Fernández P and Ott A 2008 Single cell mechanics: stress stiffening and kinematic hardening *Phys. Rev. Lett.* **100** 238102

[149] Wolff L, Fernández P and Kroy K 2012 Resolving the stiffening-softening paradox in cell mechanics *PLoS One* **7** 1–7

[150] Krishnan R *et al* 2009 Reinforcement versus fluidization in cytoskeletal mechanoresponsiveness *PLoS One* **4** e5486

[151] Trepat X, Deng L, An S S, Navajas D, Tschumperlin D J, Gerthoffer W T, Butler J P and Fredberg J J 2007 Universal physical responses to stretch in the living cell *Nature* **447** 592–5

[152] Sollich P, Lequeux F, Hébraud P and Cates M E 1997 Rheology of soft glassy materials *Phys. Rev. Lett.* **78** 2020–3

[153] Semmrich C, Storz T, Glaser J, Merkel R, Bausch A R and Kroy K 2007 Glass transition and rheological redundancy in F-actin solutions *Proc. Natl Acad. Sci. USA* **104** 20199–203

[154] Hoffman B D and Crocker J C 2009 Cell mechanics: dissecting the physical responses of cells to force *Annu. Rev. Biomed. Eng.* **11** 259–88

[155] Balland M, Desprat N, Icard D, Féréol S, Asnacios A, Browaeys J, Hénon S and Gallet F 2006 Power laws in microrheology experiments on living cells: comparative analysis and modeling *Phys. Rev.* E **74** 21911

[156] Sakaue T and Saito T 2017 Active diffusion of model chromosomal loci driven by athermal noise *Soft Matter* **13** 81–7

[157] Alcaraz J, Buscemi L, Grabulosa M, Trepat X, Fabry B, Farré R and Navajas D 2003 Microrheology of human lung epithelial cells measured by atomic force microscopy *Biophys. J.* **84** 2071–9

[158] Brangwynne C P, MacKintosh F C and Weitz D A 2007 Force fluctuations and polymerization dynamics of intracellular microtubules *Proc. Natl Acad. Sci. USA* **104** 16128–33

[159] Razin N, Voituriez R, Elgeti J and Gov N S 2017 Generalized Archimedes' principle in active fluids *Phys. Rev.* E **96** 032606

[160] Razin N, Voituriez R, Elgeti J and Gov N S 2017 Forces in inhomogeneous open active-particle systems *Phys. Rev.* E **96** 052409

[161] Ahmed W W, Fodor E, Almonacid M, Bussonnier M, Verlhac M-H, Gov N S, Visco P, van Wijland F and Betz T 2015 Active mechanics reveal molecular-scale force kinetics in living oocytes (arXiv:1510.08299)

[162] Weber S C, Spakowitz A J and Theriot J A 2010 Bacterial chromosomal loci move subdiffusively through a viscoelastic cytoplasm *Phys. Rev. Lett.* **104** 238102

[163] Vandebroek H and Vanderzande C 2015 Dynamics of a polymer in an active and viscoelastic bath *Phys. Rev.* E **92** 060601

[164] MacKintosh F C 2012 Active diffusion: the erratic dance of chromosomal loci *Proc. Natl Acad. Sci. USA* **109** 7138–9

[165] Parry B R, Surovtsev I V, Cabeen M T, O'Hern C S, Dufresne E R and Jacobs-Wagner C 2014 The bacterial cytoplasm has glass-like properties and is fluidized by metabolic activity *Cell* **156** 183–94

[166] Evans E A 1983 Bending elastic modulus of red blood cell membrane derived from buckling instability in micropipet aspiration tests *Biophys. J.* **43** 27–30

[167] Granek R 1997 From semi-flexible polymers to membranes: anomalous diffusion and reptation *J. Phys.* II **7** 1761–88

[168] Granek R 2011 Membrane surrounded by viscoelastic continuous media: anomalous diffusion and linear response to force *Soft Matter* **7** 5281

[169] Lin L C, Gov N and Brown F L H 2006 Nonequilibrium membrane fluctuations driven by active proteins *J. Chem. Phys.* **124** 074903

[170] Milner S T and Safran S A 1987 Dynamical fluctuations of droplet microemulsions and vesicles *Phys. Rev.* A **36** 4371–9

[171] Brochard F and Lennon J 1975 Frequency spectrum of the flicker phenomenon in erythrocytes *J. Phys.* **36** 1035–47

[172] Strey H, Peterson M and Sackmann E 1995 Measurement of erythrocyte membrane elasticity by flicker eigenmode decomposition *Biophys. J.* **69** 478–88

[173] Gov N 2004 Membrane undulations driven by force fluctuations of active proteins *Phys. Rev. Lett.* **93** 268104

[174] Gov N and Safran S 2005 Red blood cell membrane fluctuations and shape controlled by ATP-induced cytoskeletal defects *Biophys. J.* **88** 1859–74

[175] Park Y, Best C A, Auth T, Gov N S, Safran S A, Popescu G, Suresh S and Feld M S 2010 Metabolic remodeling of the human red blood cell membrane *Proc. Natl Acad. Sci. USA* **107** 1289–94

[176] Yoon Y Z, Kotar J, Brown A T and Cicuta P 2011 Red blood cell dynamics: from spontaneous fluctuations to non-linear response *Soft Matter* **7** 2042–51

[177] Rodríguez-García R, López-Montero I, Mell M, Egea G, Gov N S and Monroy F 2016 Direct cytoskeleton forces cause membrane softening in red blood cells *Biophys. J.* **111** 1101

[178] Helfrich W 1973 Elastic properties of lipid bilayers: theory and possible experiments *Z. Nat.forsch.* C **28** 693–703

[179] Fenz S F, Bihr T, Schmidt D, Merkel R, Seifert U, Sengupta K and Smith A-S 2017 Membrane fluctuations mediate lateral interaction between cadherin bonds *Nat. Phys. Nat. Phys.* **13** 906

[180] Gallet F, Arcizet D, Bohec P and Richert A 2009 Power spectrum of out-of-equilibrium forces in living cells: amplitude and frequency dependence *Soft Matter* **5** 2947

[181] Osmanović D and Rabin Y 2017 Dynamics of active Rouse chains *Soft Matter* **13** 963–8

[182] Samanta N and Chakrabarti R 2016 Chain reconfiguration in active noise *J. Phys. A: Math. Theor.* **49** 195601

[183] Romanczuk P, Bär M, Ebeling W, Lindner B and Schimansky-Geier L 2012 Active Brownian particles *Eur. Phys. J. Spec. Top.* **202** 1–162

[184] Gardel M L, Valentine M T and Weitz D A 2005 Microrheology *Microscale Diagnostic Technology* (New York: Springer) pp 1–49

[185] Ben-Isaac E, Fodor É, Visco P, van Wijland F and Gov N S 2015 Modeling the dynamics of a tracer particle in an elastic active gel *Phys. Rev.* E **92** 12716

[186] Doi M 2013 *Soft Matter Physics* (Oxford: Oxford University Press)

[187] Gardiner C 1985 *Stochastic Methods* (*Springer Series in Synergetics*) (Berlin: Springer)

[188] Jarzynski C 2017 Stochastic and macroscopic thermodynamics of strongly coupled systems *Phys. Rev.* X **7** 011008

[189] Gallavotti G and Cohen E G D 1995 Dynamical ensembles in nonequilibrium statistical mechanics *Phys. Rev. Lett.* **74** 2694–7

[190] Jarzynski C 1996 A nonequilibrium equality for free energy differences *Phys. Rev. Lett.* **78** 2690–3

[191] Crooks G E 1999 Entropy production fluctuation theorem and the nonequilibrium work relation for free energy differences *Phys. Rev.* E **60** 2721–6

[192] Kurchan J 1998 Fluctuation theorem for stochastic dynamics *J. Phys. A: Math. Gen.* **31** 3719

[193] Sekimoto K 1997 Kinetic characterization of heat bath and the energetics of thermal ratchet models *J. Phys. Soc. Japan* **66** 1234–7

[194] Sekimoto K 1998 Langevin equation and thermodynamics *Prog. Theor. Phys. Suppl.* **130** 17–27

[195] Seifert U 2005 Entropy production along a stochastic trajectory and an integral fluctuaction theorem *Phys. Rev. Lett.* **95** 14380–5

[196] Lebowitz J L and Spohn H 1999 A Gallavotti–Cohen-type symmetry in the large deviation functional for stochastic dynamics *J. Stat. Phys.* **95** 333–65

[197] Speck T, Blickle V, Bechinger C and Seifert U 2007 Distribution of entropy production for a colloidal particle in a nonequilibrium steady state *Europhys. Lett.* **79** 30002

[198] Schmiedl T and Seifert U 2007 Optimal finite-time processes in stochastic thermodynamics *Phys. Rev. Lett.* **98** 108301

[199] Machta B B 2015 Dissipation bound for thermodynamic control *Phys. Rev. Lett.* **115** 1–5

[200] Sivak D A and Crooks G E 2012 Thermodynamic metrics and optimal paths *Phys. Rev. Lett.* **108** 1–5

[201] Harada T and Sasa S-I 2006 Energy dissipation and violation of the fluctuation-response relation in nonequilibrium Langevin systems *Phys. Rev.* E **73** 026131

[202] Toyabe S, Okamoto T, Watanabe-Nakayama T, Taketani H, Kudo S and Muneyuki E 2010 Nonequilibrium energetics of a single F-ATPase molecule *Phys. Rev. Lett.* **104** 198103

[203] Ariga T, Tomishige M and Mizuno D 2017 Nonequilibrium energetics of molecular motor, kinesin-1 *Biophys. J.* **114** 509a

[204] Esposito M 2012 Stochastic thermodynamics under coarse graining *Phys. Rev.* E **85** 41125

[205] Wang S-W, Kawaguchi K, Sasa S-I and Tang L-H 2016 Entropy production of nanosystems with time scale separation *Phys. Rev. Lett.* **117** 70601

[206] Polettini M and Esposito M 2017 Effective thermodynamics for a marginal observer *Phys. Rev. Lett.* **119** 240601

[207] Shiraishi N and Sagawa T 2015 Fluctuation theorem for partially masked nonequilibrium dynamics *Phys. Rev.* E **91** 012130

[208] Bisker G, Polettini M, Gingrich T R and Horowitz J M 2017 Hierarchical bounds on entropy production inferred from partial information *J. Stat. Mech.* **2017** 093210

[209] Roldán É, Neri I, Dörpinghaus M, Meyr H and Jülicher F 2015 Decision making in the arrow of time *Phys. Rev. Lett.* **115** 250602

[210] Neri I, Roldán É and Jülicher F 2017 Statistics of infima and stopping times of entropy production and applications to active molecular processes *Phys. Rev.* X **7** 011019

[211] Berezhkovskii A, Hummer G and Bezrukov S 2006 Identity of distributions of direct uphill and downhill translocation times for particles traversing membrane channels *Phys. Rev. Lett.* **97** 020601

[212] Qian H and Sunney Xie X 2006 Generalized Haldane equation and fluctuation theorem in the steady-state cycle kinetics of single enzymes *Phys. Rev.* E **74** 010902

[213] Kolomeisky A B, Stukalin E B and Popov A A 2005 Understanding mechanochemical coupling in kinesins using first-passage-time processes *Phys. Rev.* E **71** 031902

[214] Stern F 1977 An independence in Brownian motion with constant drift *Ann. Probab.* **5** 571–2

[215] Pigolotti S, Neri I, Roldán É and Jülicher F 2017 Generic properties of stochastic entropy production *Phys. Rev. Lett.* **119** 140604

[216] Loutchko D, Eisbach M and Mikhailov A S 2017 Stochastic thermodynamics of a chemical nanomachine: the channeling enzyme tryptophan synthase *J. Chem. Phys.* **146** 025101

[217] Berg J 2008 Out-of-equilibrium dynamics of gene expression and the Jarzynski equality *Phys. Rev. Lett.* **100** 1–4

[218] Liphardt J 2002 Equilibrium information from nonequilibrium measurements in an experimental test of Jarzynski's equality *Science* **296** 1832–5

[219] Alemany A, Mossa A, Junier I and Ritort F 2012 Experimental free-energy measurements of kinetic molecular states using fluctuation theorems *Nat. Phys.* **8** 688–94

[220] Collin D, Ritort F, Jarzynski C, Smith S B, Tinoco I and Bustamante C 2005 Verification of the Crooks fluctuation theorem and recovery of RNA folding free energies *Nature* **437** 231–4

[221] Hayashi K, Ueno H, Iino R and Noji H 2010 Fluctuation theorem applied to F 1 -ATPase *Phys. Rev. Lett.* **104** 218103

[222] Ritort F 2006 Single-molecule experiments in biological physics: methods and applications *J. Phys.: Condens. Matter* **18** R531

[223] Schmiedl T and Seifert U 2007 Stochastic thermodynamics of chemical reaction networks *J. Chem. Phys.* **126** 044101

[224] Schmiedl T and Seifert U 2008 Efficiency of molecular motors at maximum power *Europhys. Lett.* **83** 30005

[225] Hartich D, Barato A C and Seifert U 2015 Nonequilibrium sensing and its analogy to kinetic proofreading *New J. Phys.* **17** 055026

[226] England J L 2013 Statistical physics of self-replication *J. Chem. Phys.* **139** 121923

[227] England J L 2015 Dissipative adaptation in driven self-assembly *Nat. Nanotechnol.* **10** 919–23

[228] Perunov N, Marsland R A and England J L 2016 Statistical physics of adaptation *Phys. Rev.* X **6** 021036

[229] Rouvas-Nicolis C and Nicolis G 2009 Butterfly effect *Scholarpedia* **4** 1720

[230] Weiss J B 2003 Coordinate invariance in stochastic dynamical systems *Tellus* A **55** 208–18

[231] Horowitz J M, Zhou K and England J L 2017 Minimum energetic cost to maintain a target nonequilibrium state *Phys. Rev.* E **95** 042102

[232] Barkai N and Leibler S 1997 Robustness in simple biochemical networks to transfer and process information *Nature* **387** 913–7

[233] Alon U, Surette M G, Barkai N and Leibler S 1999 Robustness in bacterial chemotaxis *Nature* **397** 168–71

[234] Qian H 2006 Reducing intrinsic biochemical noise in cells and its thermodynamic limit *J. Mol. Biol.* **362** 387–92

[235] Sartori P and Tu Y 2015 Free energy cost of reducing noise while maintaining a high sensitivity *Phys. Rev. Lett.* **115** 118102

[236] Lan G and Tu Y 2016 Information processing in bacteria: memory, computation, and statistical physics: a key issues review *Rep. Prog. Phys.* **79** 052601

[237] Ito S and Sagawa T 2013 Information thermodynamics on causal networks *Phys. Rev. Lett.* **111** 1–6

[238] Sartori P, Granger L, Lee C F and Horowitz J M 2014 Thermodynamic costs of information processing in sensory adaptation *PLoS Comput. Biol.* **10** e1003974

[239] Lang A H, Fisher C K, Mora T and Mehta P 2014 Thermodynamics of statistical inference by cells *Phys. Rev. Lett.* **113** 148103

[240] Cao Y, Wang H, Ouyang Q and Tu Y 2015 The free-energy cost of accurate biochemical oscillations *Nat. Phys.* **11** 772–8

[241] Tomé T and de Oliveira M J 2012 Entropy production in nonequilibrium systems at stationary states *Phys. Rev. Lett.* **108** 020601

[242] Stein W D and Litman T 2014 *Channels, Carriers and Pumps: an Introduction to Membrane Transport* (New York: Academic) pp 1–406

[243] Bezrukov S M, Berezhkovskii A M, Pustovoit M A and Szabo A 2000 Particle number fluctuations in a membrane channel *J. Chem. Phys.* **113** 8206–11

[244] Berezhkovskii A and Bezrukov S 2008 Counting translocations of strongly repelling particles through single channels: fluctuation theorem for membrane transport *Phys. Rev. Lett.* **100** 038104

[245] Grünwald D, Singer R H and Rout M 2011 Nuclear export dynamics of RNAprotein complexes *Nature* **475** 333–41

[246] Gingrich T R, Horowitz J M, Perunov N and England J L 2016 Dissipation bounds all steady-state current fluctuations *Phys. Rev. Lett.* **116** 120601

[247] Barato A C and Seifert U 2015 Thermodynamic uncertainty relation for biomolecular processes *Phys. Rev. Lett.* **114** 158101

[248] Pietzonka P, Barato A C and Seifert U 2016 Universal bound on the efficiency of molecular motors *J. Stat. Mech.* 124004

[249] Pietzonka P, Ritort F and Seifert U 2017 Finite-time generalization of the thermodynamic uncertainty relation *Phys. Rev.* E **96** 012101

[250] Horowitz J M and Gingrich T R 2017 Proof of the finite-time thermodynamic uncertainty relation for steady-state currents *Phys. Rev.* E **96** 020103

[251] Gingrich T R and Horowitz J M 2017 Fundamental bounds on first passage time fluctuations for currents *Phys. Rev. Lett.* **119** 170601

[252] Riedel I H, Hilfinger A, Howard J and Jülicher F 2007 How molecular motors shape the flagellar beat *HFSP J.* **1** 192–208

[253] Wan K Y and Goldstein R E 2014 Rhythmicity, recurrence, and recovery of flagellar beating *Phys. Rev. Lett.* **113** 238103

[254] Singla V 2006 The primary cilium as the cell's antenna: signaling at a sensory organelle *Science* **313** 629–33

[255] Barnes B G 1961 Ciliated secretory cells in the pars distalis of the mouse hypophysis *J. Ultrastruct. Res.* **5** 453–67

[256] Paijmans J, Lubensky D K and ten Wolde P R 2017 A thermodynamically consistent model of the post-translational Kai circadian clock *PLoS Comput. Biol.* **13** e1005415

[257] Kimmel J C, Chang A Y, Brack A S and Marshall W F 2018 Inferring cell state by quantitative motility analysis reveals a dynamic state system and broken detailed balance *PLoS Comput. Biol.* **14** e1005927

[258] Lander B, Mehl J, Blickle V, Bechinger C and Seifert U 2012 Noninvasive measurement of dissipation in colloidal systems *Phys. Rev.* E **86** 030401

[259] Shannon C E and Weaver W 1949 *The Mathematical Theory of Communication* (Urbana: University of Illinois Press) p 125

[260] Bérut A, Imparato A, Petrosyan A and Ciliberto S 2016 Theoretical description of effective heat transfer between two viscously coupled beads *Phys. Rev.* E **94** 052148

[261] Crisanti A, Puglisi A and Villamaina D 2012 Nonequilibrium and information: The role of cross correlations *Phys. Rev.* E **85** 061127

[262] Weber C A, Suzuki R, Schaller V, Aranson I S, Bausch A R and Frey E 2015 Random bursts determine dynamics of active filaments *Proc. Natl Acad. Sci. USA* **112** 10703–7

[263] Everaers R, Jülicher F, Ajdari A and Maggs A C 1999 Dynamic fluctuations of semiflexible filaments *Phys. Rev. Lett.* **82** 3717–20

[264] Liverpool T B 2003 Anomalous fluctuations of active polar filaments *Phys. Rev.* E **67** 031909

[265] Levine A J, Liverpool T B and MacKintosh F C 2004 Dynamics of rigid and flexible extended bodies in viscous films and membranes *Phys. Rev. Lett.* **93** 038102

[266] Kikuchi N, Ehrlicher A, Koch D, Kas J A, Ramaswamy S and Rao M 2009 Buckling, stiffening, and negative dissipation in the dynamics of a biopolymer in an active medium *Proc. Natl Acad. Sci. USA* **106** 19776–9

[267] Loi D, Mossa S and Cugliandolo L F 2011 Non-conservative forces and effective temperatures in active polymers *Soft Matter* **7** 10193

[268] Ghosh A and Gov N S 2014 Dynamics of active semiflexible polymers *Biophys. J.* **107** 1065–73

[269] Eisenstecken T, Gompper G and Winkler R G 2017 Internal dynamics of semiflexible polymers with active noise *J. Chem. Phys.* **146** 154903

[270] Kratky O and Porod G 1949 Röntgenuntersuchung gelöster fadenmoleküle *Recueil Travaux Chim. Pays-Bas* **68** 1106–22

[271] Goldstein R E and Langer S A 1995 Nonlinear dynamics of stiff polymers *Phys. Rev. Lett.* **75** 1094–7
[272] Hallatschek O, Frey E and Kroy K 2007 Tension dynamics in semiflexible polymers. I. Coarse-grained equations of motion *Phys. Rev.* E **75** 031905
[273] Koenderink G H, Atakhorrami M, MacKintosh F C and Schmidt C F 2006 High-frequency stress relaxation in semiflexible polymer solutions and networks *Phys. Rev. Lett.* **96** 138307
[274] Mizuno D, Bacabac R, Tardin C, Head D and Schmidt C F 2009 High-resolution probing of cellular force transmission *Phys. Rev. Lett.* **102** 168102
[275] Yuval J and Safran S A 2013 Dynamics of elastic interactions in soft and biological matter *Phys. Rev.* E **87** 042703
[276] Weiss J B 2007 Fluctuation properties of steady-state Langevin systems *Phys. Rev.* E **76** 061128
[277] Lim H C, Surovtsev I V, Beltran B G, Huang F, Bewersdorf J and Jacobs-Wagner C 2014 Evidence for a DNA-relay mechanism in ParABS-mediated chromosome segregation *Elife* **3** e02758
[278] Wang X, Llopis P M and Rudner D Z 2013 Organization and segregation of bacterial chromosomes *Nat. Rev. Genet.* **14** 191–203
[279] Wilhelm L, Bürmann F, Minnen A, Shin H C, Toseland C P, Oh B H and Gruber S 2015 SMC condensin entraps chromosomal DNA by an ATP hydrolysis dependent loading mechanism in Bacillus subtilis *Elife* **4** https://doi.org/10.7554/eLife.06659
[280] Grill S W, Gönczy P, Stelzer E H and Hyman A A 2001 Polarity controls forces governing asymmetric spindle positioning in the Caenorhabditis elegans embryo *Nature* **409** 630–3
[281] Grill S W 2003 The distribution of active force generators controls mitotic spindle position *Science* **301** 518–21
[282] Pecreaux J, Röper J C, Kruse K, Jülicher F, Hyman A A, Grill S W and Howard J 2006 Spindle oscillations during asymmetric cell division require a threshold number of active cortical force generators *Curr. Biol.* **16** 2111–22
[283] Ou G, Stuurman N, D'Ambrosio M and Vale R D 2010 Polarized myosin produces unequal-size daughters during asymmetric cell division *Science* **330** 677–80
[284] Mayer M, Depken M, Bois J S, Jülicher F and Grill S W 2010 Anisotropies in cortical tension reveal the physical basis of polarizing cortical flows *Nature* **467** 617–21
[285] Thutupalli S, Sun M, Bunyak F, Palaniappan K and Shaevitz J W 2015 Directional reversals enable Myxococcus xanthus cells to produce collective 1D streams during fruiting-body formation *J. R. Soc. Interface* **12** 20150049
[286] Peruani F, Starruß J, Jakovljevic V, Søgaard-Andersen L, Deutsch A and Bär M 2012 Collective motion and nonequilibrium cluster formation in colonies of gliding bacteria *Phys. Rev. Lett.* **108** 098102
[287] Frauenfelder H, Wolynes P G and Austin R H 1999 Biological physics *Rev. Mod. Phys.* **71** S419–30
[288] Agerschou E D, Mast C B and Braun D 2017 Emergence of life from trapped nucleotides? Non-equilibrium behavior of oligonucleotides in thermal gradients *Synlett* **28** 56–63
[289] Schwille P and Diez S 2009 Synthetic biology of minimal systems *Crit. Rev. Biochem. Mol. Biol.* **44** 223–42

Chapter 2

Non-equilibrium scaling behavior in driven biological assemblies

Chapter abstract As we discussed in the Introduction and Chapter 1, measuring and quantifying non-equilibrium dynamics in active biological systems is a major challenge in biophysics. The stochastic nature of the dynamics and the limited number of accessible variables in any experiment are the two main challenges to overcome. In this chapter, we investigate what information on the non-equilibrium dynamics can be extracted from non-invasive measurements, using a stochastic model of soft elastic networks. We describe the enzymatic force generation with a heterogeneous distribution of activities. Within this model, we investigate how the non-equilibrium activity, detected by tracking two probes in the network, scales as a function of the distance between the probes. We quantify the non-equilibrium dynamics through the cycling frequencies and the area enclosing rates, and show that these non-equilibrium measures exhibit a power law scaling behavior with the distance between the probes. In addition, we show that this scaling behavior governs also the amount of entropy production rate that can be recovered from the two traced probes. The results presented in this chapter provide insights into how internal enzymatic driving generates non-equilibrium dynamics on different scales in soft biological assemblies.

Research question: *How does non-equilibrium activity manifest itself at different length scales?*

Results: *We predict the average measured non-equilibrium activity to scale as a power law with the observed length scale. The characteristic exponent of this power law depends on the dimensionality of the system. The prefactor of the power law is dependent on the variance of the active noise in the system.*

2.1 Soft biological assemblies

In this section we briefly discuss what we refer to as driven biological assemblies, giving some examples of the systems that motivated our study, and briefly discussing the main models proposed in the literature to describe such systems.

Biological assemblies All living systems require structures that maintain their organization and also, at the same time, allow them to adapt their shape to different environments. A prominent example of these structures is the cellular cytoskeleton. The cytoskeleton is a meshwork that works as an intracellular scaffold providing mechanical resistance to the cell. In higher organisms, similar structures are present also outside the cells. One example is the extracellular matrix, a collagen network that guides the organization of cells in complex tissues. Most of the structural components in biological systems are made of flexible fibers which entangle, or bind together via specific cross-linking proteins, to form biopolymer assemblies [11].

Biopolymer assemblies present interesting mechanical properties that can be explained and described from a physical standpoint. A characteristic of these polymer structures is that they are semiflexible, meaning that their dynamics arise from the competition of entropic and bending contributions. The entropic tendency of the polymer to collapse into a random coil is balanced by its bending stiffness, so that semiflexible polymers exhibit stochastic fluctuations around a network-like structure (Fig.2.1). A general feature of such polymers is their nonlinear response to applied strain: for instance, they exhibit a rapid increase of the network stiffening as a response to strain. As a consequence of such nonlinear behavior, these materials are sensible to small deformations but resistant to large deformations. This behavior plays an important role as protection against tissue damage [11, 80].

Another peculiarity of these networks is the non-equilibrium state that characterizes both their surrounding and their constituents [24, 49, 53]. As an example, we can consider the continuous action of motors proteins, such as myosin, which can enhance the local fluctuations of the network by tugging the F-actin filaments which are part of the cytoskeletal structure. The action of motor proteins may also give rise to non-equilibrium fluctuations indirectly: molecular motors seem to play a key role in regulating cytoskeleton reorganization, controlling microtubules length, and continuously polymerizing and depolymerizing the actin filaments [57]. This internal activity and network reorganization result in fluctuations in the stress on the network itself, as well as on its surrounding [36]. However, motors proteins are not the only source of non-equilibrium fluctuations in living systems. Several experiments performed with different kinds of enzymes (catalase, urease, aldolase, etc.) revealed a substrate-dependent increase in enzyme diffusivity during catalysis [85]. Non-equilibrium fluctuations can also be found at the level of collagen networks and extracellular matrix. There, stochastic stresses are due to cellular traction, for instance during cancer development and progression [15, 64].

Theoretical models Because of their importance in living systems, biological assemblies have been the subject of many experimental and theoretical studies. Various ex-

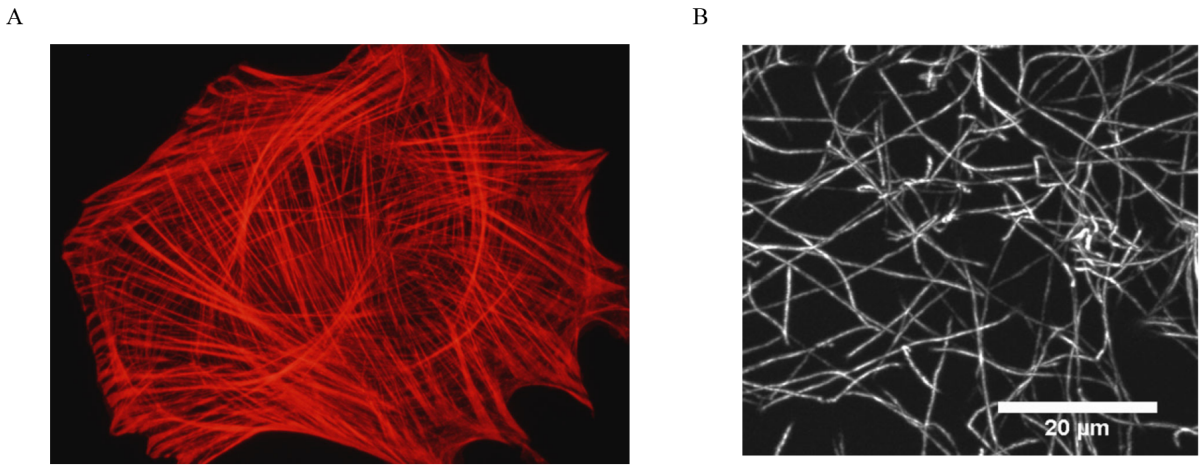

Figure 2.1: A) Confocal microscopy image of the actin cytoskeleton of an Indian Muntjac Cell. Reproduced from MicroscopyU (<http://www.microscopyu.com>). B) Confocal microscopy image of a fluorescently labeled collagen network. Reproduced from [11].

periments have been performed on reconstituted networks of biopolymers to investigate the remarkable mechanical and dynamical properties of these materials [11, 34]. At the same time, many theoretical models have been proposed to describe these experimental findings [11]. Since the features of these experimental systems are difficult to incorporate into a single theory, most of the proposed models focus on understanding what minimal features are sufficient to recreate some aspects of the experimental results.

For instance, models based on nematic and hydrodynamic theories have been proposed to describe the active nature of the cytoskeleton. These models have been very successful in predicting the emergence of large scale patterns, spontaneous oscillations, and traveling waves [4, 20, 29, 55, 67, 75]. Two further classes of models are the disordered lattice-based model and the Mikado network [11]. The former consists of identical stretchable and bendable fibers randomly arranged on a regular lattice. The latter is obtained by randomly depositing identical rod-like filaments (stretchable and bendable as well) in a two/three-dimensional system, and by adding freely hinging cross-links at the intersections between filaments. Interestingly, these models, even if composed of purely linear elastic elements interconnected together, show a global nonlinear elastic response at the network level [80]. Such minimal models allow to investigate how the complex viscosity of fibrous networks is related to processes at the molecular scale: the binding dynamics of the crosslinker and the active stresses induced by molecular motors [10].

However, disordered networks are not the only way to describe biological assemblies: for instance, a description based on regular elastic triangular networks has been used to study the non-equilibrium fluctuations of the red blood cell membrane [39, 79]. Furthermore, it is possible to apply an effective medium theory to map disordered lattice-based models to uniform networks, which are more suitable for analytical calculations [11, 12]. These effective theories allow to obtain insightful results on the viscoelastic response of such

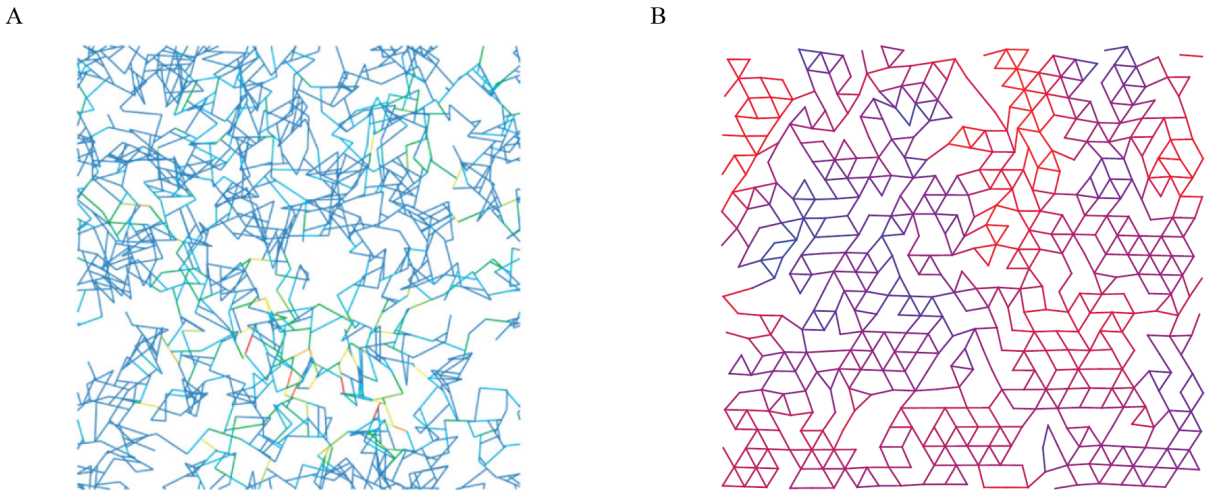

Figure 2.2: A) Example of a simulation of 2D Mikado network at low density. Reproduced from [11] B) Example of a simulated 2D disordered triangular lattice. Reproduced from [12]

complex networks.

2.2 Model

We introduce here a simplified yet general toy model to describe soft biological assemblies, which allows us to develop an analytical framework to study non-equilibrium propagation through different length scales. We will then discuss in Sec. 2.3 to what extent the results obtained within this model apply to some of the more complex descriptions of biological assemblies, mentioned in Sec.2.1.

We model soft subcellular or extracellular assemblies using d-dimensional overdamped networks of Nd coupled beads (see Fig. 2.3) [11, 54, 63, 84]. We impose fixed boundary conditions and consider the network suspended in a viscous fluid, assumed to be at thermal equilibrium, at temperature T. We indicate with γ the friction coefficient. The thermal fluctuations resulting from the fluid are modeled as Gaussian white noise processes acting independently on all the beads with the same amplitude $\frac{k_B T}{\gamma}$. Besides the thermal fluctuations, we want to describe the additional active fluctuations deriving from the incoherent non-equilibrium activity of enzymes and molecular motors. These active contributions may in principle be heterogeneously distributed along the network, depending on local features, such as the local activity and the local structures of the network. To take into account the possibility of spatial heterogeneity, we implement the active forces as independent Gaussian white noise processes with site-dependent amplitudes α_i. We extract the ensemble of independent active noise amplitudes α_i from a probability distribution p_α with average $\bar{\alpha}$ and variance σ_α^2. Here, the noise intensities at different locations are independent, but in Chapter 3, we will apply this theoretical framework to the case of

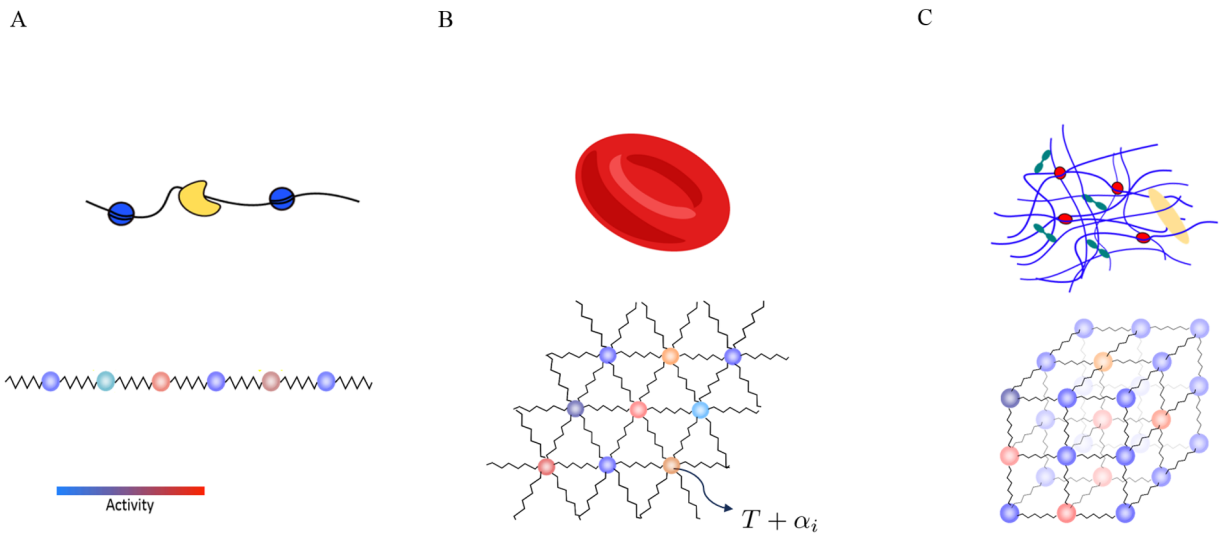

Figure 2.3: Schematic illustrating soft viscoelastic networks with heterogeneous driving for various types of cellular systems. A) chromatin B) red blood cell membrane C) cytoskeletal network; Below each figure the corresponding bead-spring model with heterogeneous active driving. The color of the bead indicates the intensity of activity, representing the variance (increasing from blue to red) of the associated active noise process.

spatially correlated activities.

By modeling the active forces as white noise, we substantially restrict our model to systems in which the correlation times of the active processes are shorter than the typical relaxation times of the network. Such an assumption makes our model mathematically equivalent to embedding the beads in local thermal baths at temperatures $T + \alpha_i$ [23].

We indicate with $\mathbf{x}$ the displacements of the beads relative to their equilibrium positions, and with $p(\mathbf{x}, t)$ the probability distribution of $\mathbf{x}$ at time t. We also assume that the elastic forces are linear in $\mathbf{x}$, i.e. $\mathbf{f}(\mathbf{x})/\gamma = \mathbf{A}\mathbf{x}$ via a symmetric matrix $\mathbf{A}$. This simplified description allows us to study the dynamics of the system using a Fokker-Planck equation

$$\partial_t p(\mathbf{x}, t) = -\nabla \cdot (\mathbf{A}\mathbf{x} - \mathbf{D}\nabla) p(\mathbf{x}, t) \coloneqq -\nabla \cdot \mathbf{j}(\mathbf{x}, t), \tag{2.1}$$

where $\mathbf{D} = (k_B/\gamma)\,\mathrm{diag}\{T + \alpha_1, \ldots, T + \alpha_N\}$ is the diffusion matrix. The right hand side of the Eq. (2.1) can be interpreted as the divergence of the probability current density $\mathbf{j}(\mathbf{x}, t) = (\mathbf{A}\mathbf{x} - \mathbf{D}\nabla) p(\mathbf{x}, t)$. The steady-state probability density $p(x)$ of this active network is described by

$$p(\mathbf{x}) = \frac{1}{\sqrt{(2\pi)^{Nd} \det \mathbf{C}}} e^{-\frac{1}{2}\mathbf{x}^T \mathbf{C}^{-1} \mathbf{x}}, \tag{2.2}$$

where $\mathbf{C} = \langle \mathbf{x} \otimes \mathbf{x} \rangle$ is the covariance matrix, which can be obtained by solving the Lyapunov equation [69]

$$\mathbf{A}\mathbf{C} + \mathbf{C}\mathbf{A}^{\mathrm{T}} = -2\mathbf{D}. \tag{2.3}$$

At steady-state, the non-vanishing dissipative probability currents constitute a measure of non-equilibrium dynamics in a system and thus play a key role in our approach.

2.2.1 Non-equilibrium in a reduced subspace

Description of a subset of degrees of freedom

If we were able to observe the stochastic motion of all beads in the network, we could directly measure the full probability current $\mathbf{j}(\mathbf{x})$ and extract information about the whole non-equilibrium dynamics of the system. However, in a typical experiment, only a small subset of the degrees of freedom can be tracked (Fig. 2.4A). The question we ask here is: Can we extract information about the non-equilibrium dynamics from these limited observations?

To address this question, we consider a scenario where only a few degrees of freedom are accessible. In our model, this corresponds to reducing our description to the marginal distribution, $p_{\mathrm{r}}(\mathbf{x}_{\mathrm{r}}) = \int dx_{k\notin[\mathrm{r}]} p(x_1, x_2, .., x_{dN})$, of a subset [r] of n tracked degrees of freedom $\mathbf{x}_{\mathrm{r}}$. By integrating out the subset [l] of m unobserved degrees of freedom $\mathbf{x}_{\mathrm{l}}$ on both sides of Eq. (2.1), and taking the steady-state limit it is possible to show that the marginal distribution satisfies the following equation

$$0 = -\nabla \cdot [\mathbf{A}_{\mathrm{eff}} \mathbf{x}_{\mathrm{r}} p_{\mathrm{r}}(\mathbf{x}_{\mathrm{r}})] + \nabla \cdot \mathbf{D}_{[\mathrm{r,r}]} \nabla p_{\mathrm{r}}(\mathbf{x}_{\mathrm{r}}), \tag{2.4}$$

where the sub-index [r, r] indicates the sub-matrix corresponding to the reduced set of observed variables. We indicate with $\mathbf{A}_{\mathrm{eff}}$ a matrix such that the average elastic force acting on the reduced degrees of freedom is $\langle \mathbf{f}_{\mathrm{r}}(\mathbf{x}) | \mathbf{x}_{\mathrm{r}} \rangle / \gamma = \mathbf{A}_{\mathrm{eff}} \mathbf{x}_{\mathrm{r}}$, where $\mathbf{f}_{\mathrm{r}}(\mathbf{x})$ is the vector of forces acting on the reduced set of coordinates . Thus, $\mathbf{A}_{\mathrm{eff}}$ is an effective force combining the forces acting on the considered observables directly and indirectly through interactions with the rest of the network (see Fig. 2.4B). It can be expressed as $\mathbf{A}_{\mathrm{eff}} = \mathbf{A}_{[\mathrm{r,r}]} + \mathbf{A}_{[\mathrm{r,l}]} \mathbf{C}_{[\mathrm{l,r}]} \mathbf{C}^{-1}_{[\mathrm{r,r}]}$. Here, $\mathbf{A}_{[\mathrm{r,l}]}$ and $\mathbf{C}_{[\mathrm{l,r}]}$ are rectangular matrices of sizes $[n \times m]$ and $[m \times n]$, given by the elements of indices [r, l] of $\mathbf{A}$ and [l, r] of $\mathbf{C}$, respectively.

We consider the simplest case of a reduced system where only two beads (i and j) can be probed, as illustrated in Fig. 2.4A. We then consider a two-dimensional subset of coordinates, for example x-coordinates or y-coordinates relative to these particles: $\mathbf{x}_{\mathrm{r}} = \{x_i, x_j\}$. In this reduced subspace, we can characterize the presence of non-equilibrium dynamics by using the non-equilibrium measures introduced in Sec. I.0.1.

Two point non-equilibrium measures

From equation Eq. (2.4) it is clear that traces of the non-equilibrium in the system may also appear in the reduced subspace. In fact there may be a non-vanishing current $\mathbf{j}_{\mathrm{r}} = \mathbf{A}_{\mathrm{eff}} \mathbf{x}_{\mathrm{r}} p_{\mathrm{r}}(\mathbf{x}_{\mathrm{r}}) + \mathbf{D}_{[\mathrm{r,r}]} \mathbf{C}^{-1}_{[\mathrm{r,r}]} \mathbf{x}_{\mathrm{r}} p_{\mathrm{r}}(\mathbf{x}_{\mathrm{r}}) = \mathbf{\Omega}_{\mathrm{r}} \mathbf{x}_{\mathrm{r}} p_{\mathrm{r}}(\mathbf{x}_{\mathrm{r}}) \neq 0$, which gives rise to an elliptical circulation (Fig. 2.4C-D), in analogy to what is discussed in Sec. I.0.1 for the two beads system.

As a first measure to quantify such circulation, we use the average area enclosing rates $\mathcal{A}_{ij}$ of the trajectory in the reduced subspace of the coordinates x_i and x_j. For an

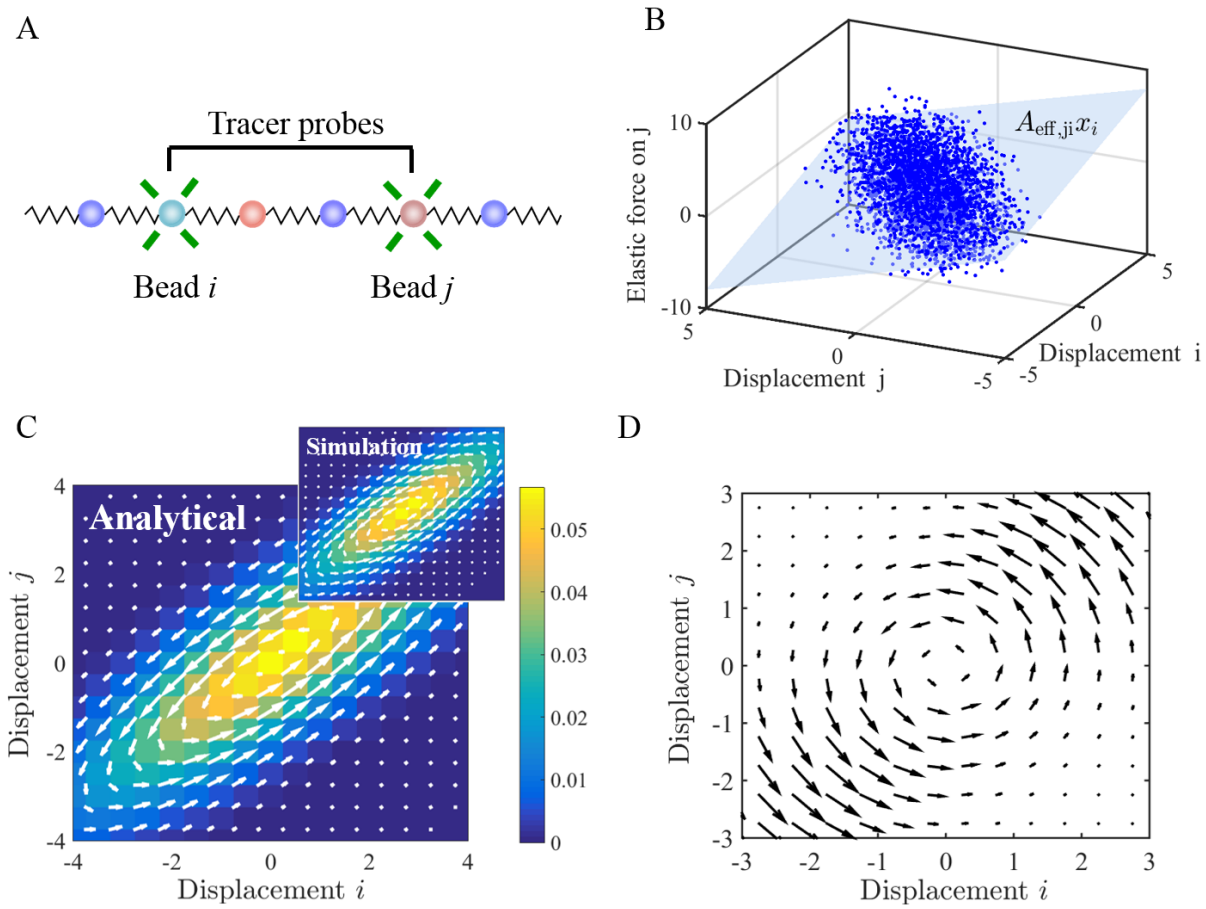

Figure 2.4: Reduced system of tracked probes. A) Schematic of two fluorescently labeled probe beads in a larger system. B) Elastic force acting on bead j obtained at different time steps of a simulation of the Langevin dynamics of the full system (blue points), and the effective linear force, $\mathbf{A}_{\mathrm{eff}}\mathbf{x}_{\mathrm{r}}$, from analytical calculations (light blue plane). C) Probability density (color map) and probability current (white arrows) calculated analytically from the effective 2D system, together with results from simulating the full system in the inset. D) The non-conservative part of the effective force field: $\frac{(\mathbf{A}_{\mathrm{eff}}-\mathbf{A}_{\mathrm{eff}}^{T})}{2}\mathbf{x}_{\mathrm{r}}$ (black arrows) can contribute to the rotation in phase space in non-equilibrium systems. Note, for $\alpha_i = \alpha \; \forall \, i$ (effective equilibrium scenario), $\mathbf{A}_{\mathrm{eff}}$ becomes symmetric.

overdamped system, in which the velocity is proportional to the force, this quantity can be expressed as

$$\mathcal{A}_{ij} = \frac{1}{2\gamma}\langle \mathbf{x}_\mathrm{r} \times \mathbf{f}_\mathrm{r}(\mathbf{x})\rangle, \tag{2.5}$$

where $\mathbf{f}_\mathrm{r}(\mathbf{x}) = \{f_i, f_j\}$ is the vector of forces acting on the coordinate i and j, respectively. By replacing $\gamma^{-1}\langle \mathbf{x}_\mathrm{r} \times \mathbf{f}_\mathrm{r}(\mathbf{x})\rangle = \gamma^{-1}\langle x_i f_j(\mathbf{x}) - x_j f_i(\mathbf{x})\rangle = (\mathbf{C}\mathbf{A}^\mathrm{T} - \mathbf{A}\mathbf{C})_{ij}$ we obtain [31, 38, 40]

$$\mathcal{A}_{ij} = \frac{1}{2}(\mathbf{C}\mathbf{A}^\mathrm{T} - \mathbf{A}\mathbf{C})_{ij}. \tag{2.6}$$

As we already know from the analysis of the simple case of two elastically coupled Brownian particles in Sec. I.0.1, this non-equilibrium measure is closely related to the cycling frequency, which is the rate at which the trajectory revolves in the coordinates space. By applying the expression for the cycling frequencies for a two-dimensional system (Eq. (I.14) of Sec. I.0.1) to the two-dimensional reduced system, we obtain

$$\begin{aligned}
\omega_{ij} &= \frac{1}{2}\frac{(\mathbf{C}_{[\mathrm{r,r}]}\mathbf{A}_{\mathrm{eff}}^\mathrm{T} - \mathbf{A}_{\mathrm{eff}}\mathbf{C}_{[\mathrm{r,r}]})_{ij}}{\sqrt{\det(\mathbf{C}_{[\mathrm{r,r}]})}} \\
&= \frac{1}{2}\frac{\left(\mathbf{C}_{[\mathrm{r,r}]}\mathbf{A}_{[\mathrm{r,r}]}^\mathrm{T} + \mathbf{C}_{[\mathrm{r,l}]}\mathbf{A}_{[\mathrm{l,r}]} - \mathbf{A}_{[\mathrm{r,r}]}\mathbf{C}_{[\mathrm{r,r}]} - \mathbf{A}_{[\mathrm{r,l}]}\mathbf{C}_{[\mathrm{l,r}]}\right)_{ij}}{\sqrt{\det(\mathbf{C}_{[\mathrm{r,r}]})}} \\
&= \frac{1}{2}\frac{\left(\mathbf{C}\mathbf{A}^\mathrm{T} - \mathbf{A}\mathbf{C}\right)_{ij}}{\sqrt{\det(\mathbf{C}_{[\mathrm{r,r}]})}},
\end{aligned} \tag{2.7}$$

where we recall that $\mathbf{C}_{[\mathrm{r,r}]}$ is a $[2 \times 2]$ matrix with entries $\mathbf{C}_{[\mathrm{r,r}]} = \{\{c_{ii}, c_{ij}\}, \{c_{ji}, c_{jj}\}\}$.

In Sec. 2.3 we will discuss how we can use these non-equilibrium measures to investigate how detailed balance breaks down at different length scales in the network.

2.3 Results

We are now ready to investigate how non-equilibrium manifests itself at different length scales in soft assemblies. To this end, we calculate the cycling frequencies and area enclosing rates between couples of beads at distance r in the network. We aim to compute how these measures depend on r after averaging over all activity configurations. Since ω and $\mathcal{A}$ are expected to be distributed symmetrically around 0, here we study the spatial scaling behaviors for $\langle \mathcal{A}^2(r)\rangle_\alpha$ and $\langle \omega^2(r)\rangle_\alpha$. We indicate with $\langle \ldots \rangle_\alpha$ the ensemble average over the activities which, for a large enough system, can be obtained as a spatial average over the network.

Intuitively, we expect the circulation, and consequently ω and $\mathcal{A}$ to decrease with the distance between probes, because the interaction between the beads also decreases with the distance. We can obtain an exact estimate of $\langle \mathcal{A}^2(r)\rangle_\alpha$ and $\langle \omega^2(r)\rangle_\alpha$ by numerically calculating Eq. (2.6) and Eq. (2.7), where the covariance matrix $\mathbf{C}$ comes from the numerical solution of the Lyapunov equation (Eq. (2.3)). Interestingly, we observe a power law scaling for the non-equilibrium measures, as shown in Fig. 2.5.

To get more insights on such a scaling behavior, we investigate whether it is affected by the type of noise that we set in the network and by the architecture of the network itself. The numerical results for the scaling behavior of one dimensional systems with different settings of the noise distribution are reported in Fig. 2.5B. The results for different network geometries, such as triangular and square lattices, and different dimensionalities are shown in Fig. 2.5C-D. The scaling behavior appears strongly dependent on the dimensionality of the system but not so much on the geometry of the lattice or on the distribution of the activities.

To gain a better understanding of the features of the system which underlie such power law behavior, we consider the simple case of a one dimensional system, for which we derive an analytical expression for the scaling of the non-equilibrium measures as a function of the distance r.

2.3.1 One dimensional chain

In this section, we will derive an analytical expression for the scaling behavior of $\langle \mathcal{A}^2(r) \rangle_\alpha$ in one-dimensional systems starting from equation Eq. (2.6). We will later relate the scaling of $\langle \mathcal{A}^2(r) \rangle_\alpha$ to the one of $\langle \omega^2(r) \rangle_\alpha$.

For a one-dimensional system the interaction matrix $\mathbf{A}$ has a simple form with entries: $a_{ij} = \frac{k}{\gamma}(-2\delta_{ij} + \delta_{i,i+1} + \delta_{i,i-1})$. By inserting this expression into Eq. (2.6), we can express the area enclosing rates between any two tracer particles i and j as

$$\mathcal{A}_{ij} = \frac{k}{\gamma} \widetilde{\partial}_x^2 c, \tag{2.8}$$

where we indicate the discrete second derivative along the rows of the covariance matrix with $\widetilde{\partial}_x^2 c = c_{i,j+1} - 2c_{i,j} + c_{i,j-1}$. Therefore, we reduced the problem of finding the scaling of the area enclosing rates with the distance r to find the scaling of $\widetilde{\partial}_x^2 c$ with r. As the following shows, this can be achieved by solving Eq. (2.3) via a continuous approximation.

The structure of $\mathbf{D}$ and the linearity of the Lyapunov equation suggest a natural decomposition of the covariance matrix $\mathbf{C}$ into equilibrium ($\overline{\mathbf{C}}$) and non-equilibrium ($\mathbf{C}^*$) contributions: $\mathbf{C} = (k_B T/k)\overline{\mathbf{C}} + (k_B \bar{\alpha}/k)\mathbf{C}^*$, such that $\overline{\mathbf{C}}$ and $\mathbf{C}^*$ are dimensionless. Both $\overline{\mathbf{C}}$ and $\mathbf{C}^*$ could be found by solving the Lyapunov equation (Eq. (2.3)). The principle of detailed balance imposes $\omega_{ij} = \mathcal{A}_{ij} = 0$ at thermal equilibrium, which together with Eq. (2.8) implies $\widetilde{\partial}_x^2 \bar{c}_{ij} = 0$ and $\widetilde{\partial}_x^2 c_{ij} = (k_B \bar{\alpha}/k)\widetilde{\partial}_x^2 c^*_{ij}$. So the only equation left to solve is the Lyapunov equation for the non-equilibrium contribution

$$\widetilde{\partial}_x^2 c^*_{ij} + \widetilde{\partial}_y^2 c^*_{ij} = -2\delta_{ij} \frac{\alpha_i}{\bar{\alpha}}, \tag{2.9}$$

where $\widetilde{\partial}_y^2$ indicates the discrete second derivative along columns. This equation represents a discrete stationary diffusion equation, with sources of divergence given by $\delta_{ij}(\alpha_i/\bar{\alpha})$.

Activity at a single site

Our goal is to calculate $\mathbf{C}^*$ for a given distribution of activities $\{\alpha_i\}$. However, due to the linearity of Eq. (2.9), $\mathbf{C}^*$ is a superposition of steady-state solutions to the single-source

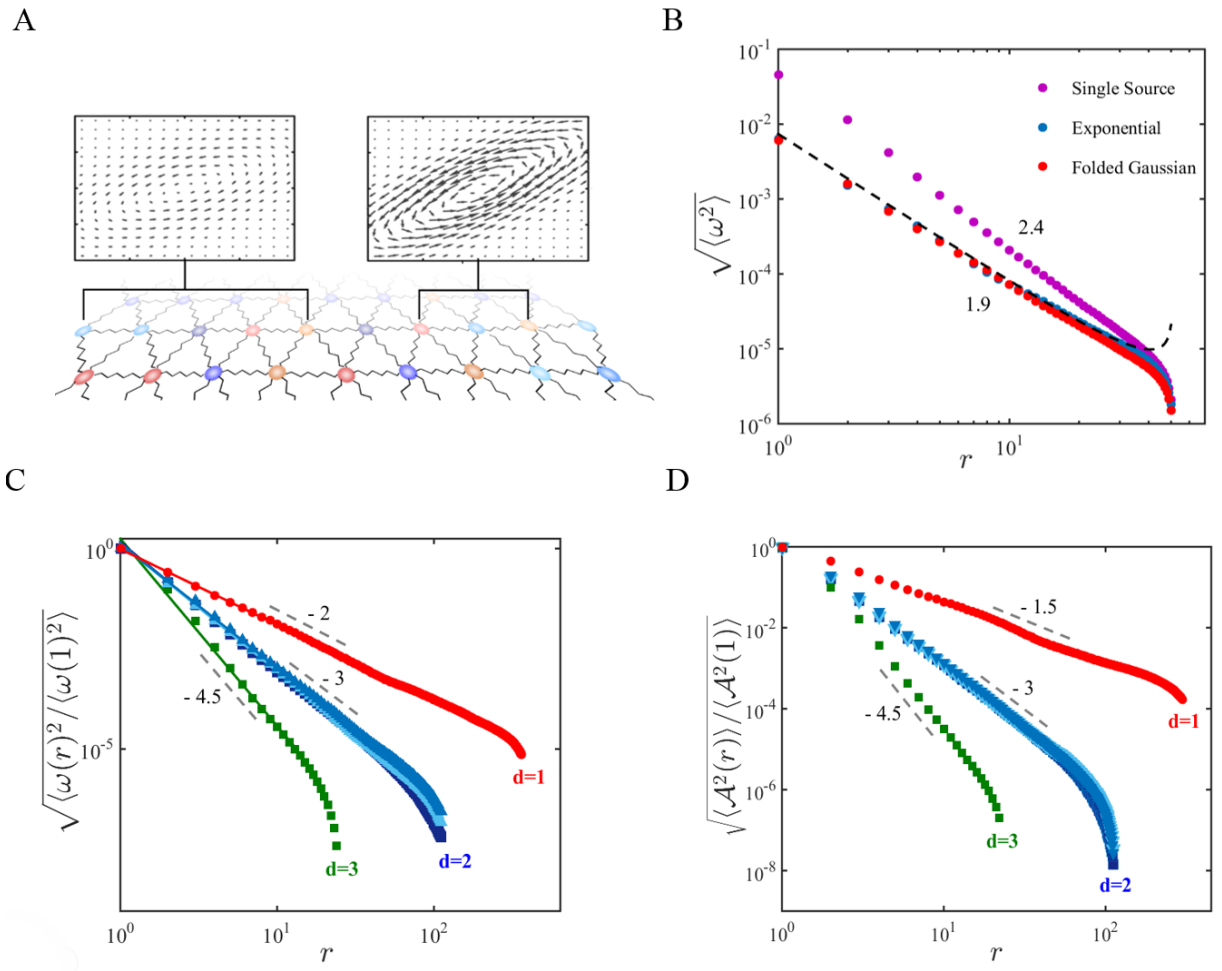

Figure 2.5: Spatial scaling behavior of cycling frequencies and area enclosing rates. A) Steady-state current cycles in phase space of the displacements (along the lattice direction) of two tracer beads for a nearby pair of probes (right) and distant pair of probes (left). B) Scaling behavior of the cycling frequencies, $\sqrt{\langle\omega^2(r)\rangle}$, of pairs of probes beads as a function of their spatial distances, obtained for a 1D chain and different activity distributions, as indicated in the legend. C) Scaling behavior of the cycling frequencies, $\sqrt{\langle\omega^2(r)\rangle/\langle\omega^2(1)\rangle}$, obtained for different lattices and a folded Gaussian activity distribution. Triangular and square markers represent triangular and square/cubic lattices, respectively. Light/dark blue triangles represent triangular networks with zero/finite rest length springs. D) The same results as in C), but obtained for the area enclosing rates $\sqrt{\langle\mathcal{A}^2(r)/\mathcal{A}^2(1)\rangle}$. In B), C) and D) we used $\bar{\alpha}/T = 0.15$

problem, i.e. a delta-distribution for which all but one of the activities would be set to zero, precisely: $\alpha_i = \alpha\delta_{i0}$ and $\bar{\alpha} = \alpha$. Therefore, we first proceed with calculating the solution for a single source problem. We denote by $\rho = \sqrt{i^2 + j^2}$ the distance from the center of $\mathbf{C}^*$, which is in (0,0). If we consider a continuous analog of our discrete problem and neglect the boundary conditions, we can assume a rotational symmetry of the solution $c^*(\rho)$. The corresponding continuous diffusion equation takes the form: $\frac{1}{\rho}\partial_\rho\rho\partial_\rho c^*(\rho) = 0$. Consequently, $\rho\partial_\rho c^*(\rho) = -a$ and $c^*(\rho) = -a\ln(\rho) + b$, where a and b are integration constants. Since at this point we are only interested in finding an expression for the second derivative of the covariance matrix, the constant b is not relevant for this purpose. The constant a can be set by demanding that the covariance flux through a circle of radius ϵ centered around the source is not dependent on ϵ and equals 2 (Eq. (2.9)). This allows to set $a = 1/\pi$. To find the scaling of the area enclosing rate measured between the active bead and a bead a distance r from it, we can evaluate Eq. (2.8) in $(i = 0, j = r)$. We can indeed write the scaling of the area enclosing rate for a single source as

$$\mathcal{A}_{\text{single}}(r) = \frac{\alpha k_B}{\pi\gamma}\frac{1}{r^2}. \tag{2.10}$$

Note that the distance r is dimensionless and measured in units of lattice spacing ℓ. The same procedure can be applied to Eq. (2.7) to obtain the cycling frequency scaling and lead to

$$\omega_{\text{single}}(r) = \frac{\alpha k_B}{\pi\gamma\sqrt{\det \mathbf{C}_{[\mathrm{r,r}]}}}\frac{1}{r^2}. \tag{2.11}$$

Note the presence of the term $\sqrt{\det \mathbf{C}_{[\mathrm{r,r}]}}$ in the denominator of Eq. (2.11). This term introduce a further contribution to the scaling of ω. We can calculate this contribution in the limit of small displacements, by Taylor expanding $\sqrt{\det \mathbf{C}_{[\mathrm{r,r}]}}$ in power of α/T, and we arrive at

$$\omega_{\text{single}}(r) = \frac{\alpha k}{T\pi\gamma\sqrt{\det \overline{\mathbf{C}}_{[\mathrm{r,r}]}}}\frac{1}{2r^2} + \mathcal{O}\left(\frac{\alpha^2}{T^2}\right) \sim r^{-\frac{5}{2}}, \tag{2.12}$$

where in the last step we used that $(\det \overline{\mathbf{C}}_{[\mathrm{r,r}]}(r))^{-\frac{1}{2}} = (\frac{1}{2}r(N-r))^{-\frac{1}{2}} \sim r^{-\frac{1}{2}}$ for $r \ll N$ [40]. The comparison with numerical results is shown in Fig. 2.5B.

Spatially varying activity

The results obtained for the single activity provides the basis for the solution of the more complicated problem of a distribution of spatially varying activities. Here, we consider a distribution of activities $\{\alpha_i\}$ with average $\bar{\alpha}$ and variance σ_α^2. We will exploit the linearity of the Lyapunov equation to find a solution for the covariance matrix in the case of a distribution of active sources, given by a superposition of single source solutions. In general, owing to the linearity of the Lyapunov equation (see Eq. (2.3)), the covariance matrix can be expressed as

$$\mathbf{C} = \frac{k_{\mathrm{B}}}{k}\left(T\overline{\mathbf{C}} + \sum_z \alpha_z \mathbf{C}_z^*\right), \tag{2.13}$$

where the index z runs along the chain positions. For simplicity, we index the beads so that the bead in the center of the system has index 0. We calculate the area enclosing rate in the coordinates space of two beads at distance $2r$. In particular, we want to find an expression for $\mathcal{A}(2r) = \mathcal{A}_{-r,r}$. Therefore, we need to determine $\widetilde{\partial}_x^2 c^*(2r) = \widetilde{\partial}_x^2 c^*_{-r,r}$. For beads far enough from the boundary we can use the results obtained for the case of activity at a single site, and approximate $c_z^*(2r)$ by a logarithmic decay centered at (z, z). We obtain

$$\begin{aligned}\widetilde{\partial}_x^2 c_z^*(2r) &= \frac{1}{\pi}\frac{(r+z)^2-(r-z)^2}{((r+z)^2+(r-z)^2)^2} \\ &= \frac{1}{\pi}\frac{rz}{(r^2+z^2)^2}. \end{aligned} \tag{2.14}$$

Equipped with Eqs. (2.13) and (2.14), we can now proceed to calculate the scaling expressions for the ensemble averages $\langle \mathcal{A}^2(2r)\rangle$ and $\langle \omega^2(2r)\rangle$. Specifically, we calculate $\langle(\sum_z \alpha_z \widetilde{\partial}_x^2 c_z^*(2r))^2\rangle$ which is the main factor in the expression for $\langle \mathcal{A}^2(2r)\rangle$ and $\langle \omega^2(2r)\rangle$:

$$\langle(\sum_z \alpha_z \widetilde{\partial}_x^2 c_z^*(2r))^2\rangle = \left\langle \left(\sum_z \frac{rz\alpha_z}{\pi(r^2+z^2)^2}\right)\left(\sum_{z'} \frac{rz'\alpha_{z'}}{\pi(r^2+z'^2)^2}\right)\right\rangle \tag{2.15}$$

$$\begin{aligned} &= \sum_z \frac{r^2z^2\langle\alpha_z^2\rangle}{\pi^2(r^2+z^2)^4} + \sum_z \frac{rz\,\langle\alpha_z\rangle}{\pi(r^2+z^2)^2}\sum_{z'\neq z}\frac{rz'\,\langle\alpha_{z'}\rangle}{\pi(r^2+z'^2)^2} \\ &= \sum_z \frac{r^2z^2(\langle\alpha_z^2\rangle - \langle\alpha_z\rangle^2)}{\pi^2(r^2+z^2)^4} \approx \frac{\sigma_\alpha^2}{\pi^2}\int_{-\infty}^{\infty}\frac{r^2z^2dz}{(r^2+z^2)^4} = \frac{\sigma_\alpha^2}{\pi^2 16 r^3}, \end{aligned} \tag{2.16}$$

where, in the second line, we used that $\sum_{z'\neq z}\frac{rz'}{(r^2+z'^2)^2} = -\frac{rz}{(r^2+z^2)^2}$ and approximated the sum by an integral. Rescaling $2r \to r$, we can use Eq. (2.8) to finally obtain

$$\langle \mathcal{A}^2(r)\rangle_\alpha = \left(\frac{k_B}{\gamma}\right)^2 \frac{\sigma_\alpha^2}{2\pi r^3}, \tag{2.17}$$

and for the cycling frequencies

$$\langle \omega^2(r)\rangle_\alpha = \frac{k^2}{\gamma^2}\frac{\sigma_\alpha^2}{T^2}\frac{1}{2\pi r^3}\frac{1}{\det \overline{\mathbf{C}}_{[\mathrm{r,r}]}(r)} \sim r^{-4}. \tag{2.18}$$

From Eq. (2.17) we can conclude that $\sqrt{\langle \mathcal{A}^2(r)\rangle} \sim r^{-1.5}$ (See Fig. 2.6), and from Eq. (2.18) that, in the limit of weak activity, $\sqrt{\langle \omega^2(r)\rangle} \sim r^{-2}$ (See Fig. 2.5B and Fig. 2.6A). Interestingly, our theoretical framework not only predicts the scaling behavior of the non-equilibrium measures, but also the prefactor, which is directly proportional to the variance of the active noise σ_α^2.

2.3.2 d-dimensional lattices

The calculation presented in Sec. 2.3 for a one dimensional chain can be generalized to the case of d-dimensional cubic lattices. Here we report the main results for the scaling behav-

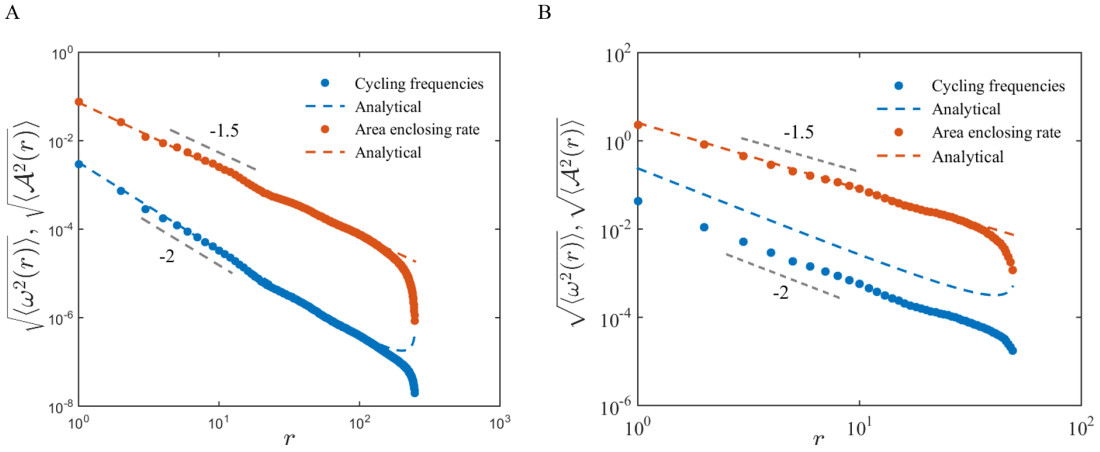

Figure 2.6: A) Comparison between the cycling frequencies (lower blue) and the area enclosing rates (upper orange) in the weak noise limit ($\bar{\alpha}/T = 0.2$). B) Comparison between the cycling frequencies (lower blue) and the area enclosing rates (upper orange) above the weak noise limit ($\bar{\alpha}/T = 4$). All data points correspond to results obtained by numerically solving Lyapunov equation (Eq. (2.3)).

ior of the area enclosing rates. A detailed derivation can be found in our manuscript [40], included at the end of this Chapter.

We denote the bead indices corresponding to d independent directions with $n_1, \ldots, n_d$. We indicate the elements of the covariance matrix $\mathbf{C}$ as $c_{n_1,\ldots,n_d;\bar{n}_1,\ldots,\bar{n}_d} \coloneqq c_{\mathbf{n},\bar{\mathbf{n}}}$. We assume zero rest length for the springs so that the degrees of freedom corresponding to different directions decouple. Therefore, by $\mathbf{C}$ we actually mean the covariance matrix of only the degrees of freedom that correspond to a single chosen direction, for instance, the one corresponding to the index n_1. From Eq. (2.6) we obtain for the area enclosing rate

$$\mathcal{A}_{\mathbf{n},\bar{\mathbf{n}}} \approx \frac{k}{\gamma} \sum_{i=1}^{d} \tilde{\partial}_{n_i}^2 c_{\mathbf{n},\bar{\mathbf{n}}}. \tag{2.19}$$

Furthermore, for this particular network, the Lyapunov equation is equivalent to

$$\left(\sum_{i=1}^{d} \tilde{\partial}_{n_i}^2 + \sum_{i=1}^{d} \tilde{\partial}_{\bar{n}_i}^2 \right) c_{\mathbf{n},\bar{\mathbf{n}}} = -2 d_{\mathbf{n},\bar{\mathbf{n}}}. \tag{2.20}$$

Similarly to the 1-dimensional case, here we recognize a discretized stationary diffusion equation in $2d$ dimensions, with the divergence of the sources given by the elements of $\mathbf{D}$. Following the same procedure as for the one dimensional case, we can solve Eq. (2.20) in the continuous limit, for the case of a single source in $(0, \ldots, 0)$. This gives

$$c^*_{\mathbf{n},\bar{\mathbf{n}}} = a_d \left(\sum_{i=1}^{d} n_i^2 + \sum_{i=1}^{d} \bar{n}_i^2 \right)^{-(d-1)} = a_d \left(\mathbf{n}^2 + \bar{\mathbf{n}}^2 \right)^{-(d-1)}, \tag{2.21}$$

where the constant $a_d = (d-2)!/(2\pi^d)$ can be obtained from the divergence theorem, as we did in the 1-dimensional case. By replacing Eq. (2.21) in Eq. (2.19), and performing

similar calculation to the one dimensional case, for $d = 2$ and $d = 3$ we obtain

$$\left\langle \mathcal{A}^2_{d=2}(r) \right\rangle_\alpha = \frac{k_B^2 \sigma_\alpha^2}{\gamma^2} \frac{8}{5\pi^3 r^6}, \tag{2.22}$$

$$\left\langle \mathcal{A}^2_{d=3}(r) \right\rangle_\alpha = \frac{k_B^2 \sigma_\alpha^2}{\gamma^2} \frac{27}{8\pi^4 r^9}. \tag{2.23}$$

As Fig. 2.5D demonstrates, these scaling exponents match their numerical counterparts.

2.3.3 Lower bound for the entropy production rate

Nonzero area enclosing rates and cycling frequencies are both measures that directly reflect broken detailed balance, suggesting a connection between these non-equilibrium measures and the rate of entropy production of the system. We have seen in Sec. I.0.1 that for a two bead system, the following relation between entropy production and cycling frequencies holds

$$\Pi = k_B \omega^2 \mathrm{Tr}(\mathbf{D}^{-1}\mathbf{C}). \tag{2.24}$$

Here we show that the same expression also applies to the case of a reduced system in the lattice and, in this case, it provides a lower bound to the total entropy production of the system Π_{tot}. Like for the two bead system case (see Sec. I.0.1), the entropy production in the reduced system can be derived from its integral definition [60]

$$\Pi^{(2)}_{\mathrm{r}} = k_B \int d\mathbf{x}_{\mathrm{r}} \frac{\mathbf{j}^T_{\mathrm{r}}(\mathbf{x}_{\mathrm{r}}) \mathbf{D}^{-1}_{[\mathrm{r,r}]} \mathbf{j}_{\mathrm{r}}(\mathbf{x}_{\mathrm{r}})}{p_{\mathrm{r}}(\mathbf{x}_{\mathrm{r}})} = k_B \omega^2 \mathrm{Tr}(\mathbf{C}_{[\mathrm{r,r}]} \mathbf{D}^{-1}_{[\mathrm{r,r}]}), \tag{2.25}$$

where $\mathbf{j}_{\mathrm{r}}$ is the probability current in the reduced subspace. This result provides an explicit relation between the partial entropy production rate and the cycling frequency ω. Note, all quantities in the expression for $\Pi^{(2)}_{\mathrm{r}}$ can be observed in an experiment, providing a direct way to non-invasively determine the reduced rate of entropy production for a set of traced degrees of freedom. To make a prediction on the scaling behavior of $\Pi^{(2)}_{\mathrm{r}}$ we can make the following observation: Since $\mathrm{Tr}(\mathbf{C}_{[\mathrm{r,r}]} \mathbf{D}^{-1}_{[\mathrm{r,r}]})$ depends only weakly on r, as long as $1 \ll r \ll N$, we expect a scaling behavior $\langle \Pi^{(2)}_{\mathrm{r}} \rangle \sim r^{-2\mu}$, where μ is the characteristic exponent of the cycling frequencies: $\sqrt{\omega^2} \sim r^{-\mu}$. Therefore, the spatial scaling behavior of the cycling frequencies directly determines the spatial scaling behavior of the entropy production rate (see Fig. 2.7).

Up to this point, we defined the partial entropy production rate, and related this quantity to the cycling frequencies (Eq. (2.25)). However, we still need to discuss how this partial entropy production rate can be informative on the total entropy production rate of the system Π_{tot}

$$\Pi_{\mathrm{tot}} = k_{\mathrm{B}} \int d\mathbf{x} \frac{\mathbf{j}^T(\mathbf{x}) \mathbf{D}^{-1} \mathbf{j}(\mathbf{x})}{p(\mathbf{x})}, \tag{2.26}$$

where we indicate with $\mathbf{j}(\mathbf{x})$ the probability current in the full coordinate space.

In the following part of this section we show that Eq. (2.25), can be experimentally useful to set a lower bound to Π_{tot}.

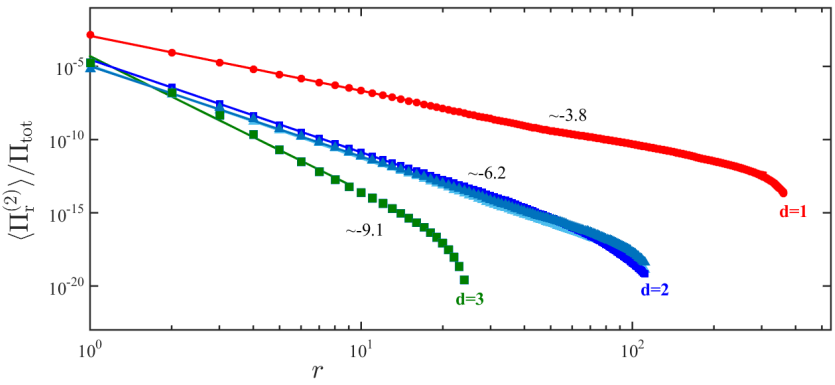

Figure 2.7: Spatial scaling behavior of the average entropy production rate, $\langle \Pi_r^{(2)} \rangle$, of a pair of probe beads as a function of their spatial distance r, obtained for different lattices and a folded Gaussian activity distribution with $\bar{\alpha}/T = 0.15$. Note, the entropy production rate of the reduced system is scaled by the total entropy production rate of the whole network, Π_{tot}. Triangular and square markers represent triangular and square/cubic lattices, respectively. Light/dark blue triangles represent triangular networks with zero/finite rest length springs.

As first step, we want to show with a direct calculation that $\frac{\Pi_{tot}-\Pi_r}{k_B} > 0$.

$$
\begin{aligned}
\frac{\Pi_{tot}-\Pi_r}{k_B} &= \int d\mathbf{x} \frac{\mathbf{j}^T(\mathbf{x})\mathbf{D}^{-1}\mathbf{j}(\mathbf{x})}{p(\mathbf{x})} - \int d\mathbf{x}_r \frac{\mathbf{j}_r^T(\mathbf{x}_r)\mathbf{D}_{[r,r]}^{-1}\mathbf{j}_r(\mathbf{x}_r)}{p(\mathbf{x}_r)} \\
&= \frac{\gamma}{k_B}\sum_{j\in[l]}\int d\mathbf{x}\frac{v_j^2(\mathbf{x})}{(T+\alpha_j)}p(\mathbf{x}) + \frac{\gamma}{k_B}\sum_{i\in[r]}\left[\left(\int d\mathbf{x}\frac{v_i^2(\mathbf{x})}{(T+\alpha_i)}p(\mathbf{x})\right) - \int d\mathbf{x}_r \frac{\langle v_i(\mathbf{x})|\mathbf{x}_r\rangle^2}{(T+\alpha_i)}p(\mathbf{x}_r)\right] \\
&= \frac{\gamma}{k_B}\left[\sum_{j\in[l]}\int d\mathbf{x}\frac{v_j^2(\mathbf{x})}{(T+\alpha_j)}p(\mathbf{x}) + \sum_{i\in[r]}\int d\mathbf{x}_r\left[\left(\int d\mathbf{x}_l \frac{v_i^2(\mathbf{x})}{(T+\alpha_i)}p(\mathbf{x}_l|\mathbf{x}_r)p(\mathbf{x}_r)\right) - \frac{\langle v_i(\mathbf{x})|\mathbf{x}_r\rangle^2}{(T+\alpha_i)}p(\mathbf{x}_r)\right]\right] \\
&= \frac{\gamma}{k_B}\left[\sum_{j\in[l]}\frac{\langle v_j^2(\mathbf{x})\rangle}{(T+\alpha_j)} + \sum_{i\in[r]}\int d\mathbf{x}_r \underbrace{\left(\langle v_i^2(\mathbf{x})|\mathbf{x}_r\rangle - \langle v_i(\mathbf{x})|\mathbf{x}_r\rangle^2\right)}_{\geq 0}\frac{p(\mathbf{x}_r)}{(T+\alpha_i)}\right] \geq 0,
\end{aligned}
\tag{2.27}
$$

where in the second line we use that $\mathbf{D}$ is diagonal, $\mathbf{v}(\mathbf{x}) = \mathbf{j}(\mathbf{x})/p(\mathbf{x})$, and $\mathbf{j}_r(\mathbf{x}_r) = p(\mathbf{x}_r)\int d\mathbf{x}_l\, \mathbf{v}_r(\mathbf{x})p(\mathbf{x}_l|\mathbf{x}_r) = p(\mathbf{x}_r)\langle \mathbf{v}_r(\mathbf{x})|\mathbf{x}_r\rangle$, which follows from the derivation of Eq. (2.4). It is worth noting, from the derivation in Eq. (2.27), that the lower bound holds more generally for a reduced system with even more than two traced degrees of freedom. Specifically, a numerical calculation suggests that the fraction of the entropy production that we can recover from a system where n degrees of freedom can be tracked, is proportional to n^2 (See Fig. 2.8). Furthermore, if we consider several disjoint subsystems $[r_1]\ldots[r_n]$ of the entire system, through the same derivation we can obtain even the stronger bound

$$\Pi_{r_1} + \ldots + \Pi_{r_n} \leq \Pi_{tot}. \tag{2.28}$$

Such a relation is interesting from an experimental point of view because it allows to strengthen the experimental bound for the entropy production by analyzing several

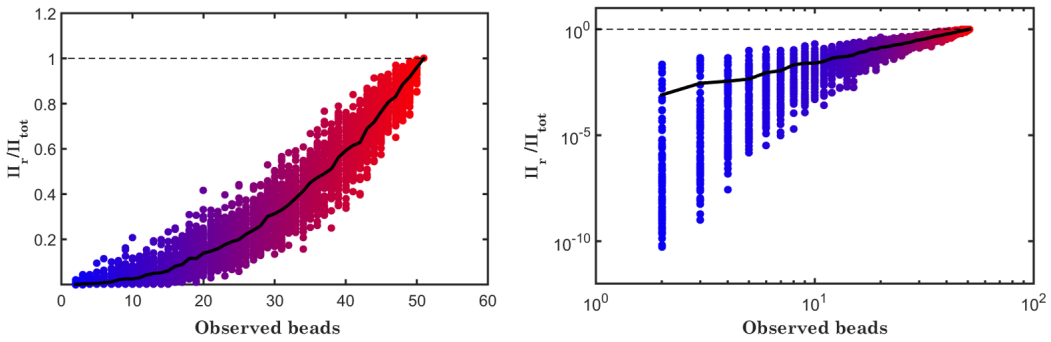

Figure 2.8: Entropy production rate as a function of the number of observed beads ($d = 1$). Different points, corresponding to a fixed number of observed beads, are obtained from the possible choices of the subsets of observed degrees of freedom. The same data are represented in linear scale on the left panel and in a log-log plot on the right panel. The black line represents the average recovered entropy production rate, and displays a power law dependency as a function of the number of observed beads, with a scaling exponent $\Pi_r/\Pi_{tot} \sim n^2$, where n is the number of observed degrees of freedom.

couples of beads in two-dimensional coordinates spaces, instead of analyzing trajectories in r-dimensional coordinates space.

2.3.4 Chapter summary

Our research predicts a power law behavior of mesoscopic non-equilibrium measures as a function of the distance between two probe particles.

While our analytical framework is derived for a simple case of cubic lattices of zero rest-length springs, it is possible to check numerically that our predictions also apply to more complex systems. For instance, the results for a triangular lattice with zero and finite rest length are shown in Fig. 2.5C,D, and we can see that they overlap with those obtained for a square lattice. This suggests the independence of our prediction from the lattice geometry. Such a claim is also reinforced by the observation of our predicted scaling exponent in diluted triangular networks, as we will see in Chapter 3 and as further investigated in [35].

The results presented in this chapter give insights into how non-equilibrium manifests at different length scales. Furthermore, our analytical framework suggests that the area enclosing rates and cycling frequencies are promising tools to study the features of stochastic driving in active elastic assemblies. By measuring the scaling behavior of these non-equilibrium measures would be possible to extract information on features of the active driving: For instance, we have seen that the ensemble average of the considered non-equilibrium measures is directly proportional to the variance of the active noise. Another interesting result is the connection between these measures and the entropy production rates. Our calculations show that these measures can be used to access the entropy production rate of reduced two dimensional subspaces of degrees of freedom, and the out-

comes can in turn be used to set a lower bound to the total entropy production of the system.

Our approach could be tested in reconstituted biological systems, for example *in vitro* actomyosin networks. But also in *in vivo* biological assemblies, for instance using colloidal particles embedded in the system or applying fluorescent tags to cellular organelles. Further details about possible experimental scenarios are discussed in Chapter 1 and in the Outlook. However, the results presented in this chapter are limited to the case of uncorrelated noise amplitudes. In Chapter 3 we will discuss more in detail how our results may change when this important assumption does not hold.

2.4 Publication reprint

Nonequilibrium Scaling Behavior in Driven Soft Biological Assemblies

by

F. Mura,*[1] G. Gradziuk,*[1] and C. P. Broedersz,[1]

* Contributed equally to this work
[1]Department of Physics, Arnold Sommerfeld Center for Theoretical Physics and Center for NanoScience, Ludwig-Maximilians-Universität München, Theresienstraße 37, 80333 München, Germany.

reprinted from

***Phys. Rev. Lett.* 121, 038002 (2018),**
doi:10.1103/PhysRevLett.121.038002.

Nonequilibrium Scaling Behavior in Driven Soft Biological Assemblies

Federica Mura, Grzegorz Gradziuk, and Chase P. Broedersz*
Arnold-Sommerfeld-Center for Theoretical Physics and Center for NanoScience, Ludwig-Maximilians-Universität München, D-80333 München, Germany

(Received 30 January 2018; revised manuscript received 13 April 2018; published 18 July 2018)

Measuring and quantifying nonequilibrium dynamics in active biological systems is a major challenge because of their intrinsic stochastic nature and the limited number of variables accessible in any real experiment. We investigate what nonequilibrium information can be extracted from noninvasive measurements using a stochastic model of soft elastic networks with a heterogeneous distribution of activities, representing enzymatic force generation. In particular, we use this model to study how the nonequilibrium activity, detected by tracking two probes in the network, scales as a function of the distance between the probes. We quantify the nonequilibrium dynamics through the cycling frequencies, a simple measure of circulating currents in the phase space of the probes. We find that these cycling frequencies exhibit power-law scaling behavior with the distance between probes. In addition, we show that this scaling behavior governs the entropy production rate that can be recovered from the two traced probes. Our results provide insight into how internal enzymatic driving generates nonequilibrium dynamics on different scales in soft biological assemblies.

DOI: 10.1103/PhysRevLett.121.038002

Cells and tissue constitute a class of nonequilibrium many-body systems [1–5]. Indeed, nonequilibrium activity has been observed in various biological systems, including membranes [6,7], chromosomes [8], and the cytoplasm [9–11]. A distinguishing physical feature of such biological assemblies is that they are driven out of equilibrium collectively by internal enzymatic processes that break the detailed balance at the molecular scale. The active nature of living matter on larger scales can be determined noninvasively by observing the steady-state stochastic dynamics of mesoscopic degrees of freedom using time-lapse microscopy experiments: the nonequilibrium dynamics of these systems can manifest as circulating probability currents in a phase space of mesoscopic coordinates [2,12–14]. However, it remains unclear how such nonequilibrium measures depend on the spatial scale on which the measurement is performed. A theoretical understanding of the spatial scaling behavior of broken detailed balance in internally driven biologically assemblies may reveal how to extract quantitative information from measurable phase space currents to characterize the active nature of the system.

Here we consider a simple, yet general model for an internally driven elastic assembly to study nonequilibrium scaling behavior. This assembly is driven out of equilibrium by heterogeneously distributed stochastic forces, representing internal enzymatic activity (Fig. 1). We quantify the nonequilibrium dynamics of such an assembly by the cycling frequencies associated with steady-state circulating currents in phase space [13,14]. To study how broken detailed balance manifests on different scales in a given system, we investigate how the cycling frequency of a pair of tracer probes depends on the spatial distance between these probes. Interestingly, the cycling frequencies in our model exhibit a power-law scaling with the distance between probes with an exponent that depends on the dimensionality of the system. To provide a conceptual understanding of this scaling behavior, we develop an analytical calculation of these exponents. Furthermore, we show that the exponent associated with the power law of the cycling frequencies also underlies the scaling behavior of the entropy production rate that can be recovered from measured trajectories. Therefore, we provide a framework to study the spatial scaling behavior of nonequilibrium measures in soft elastic assemblies.

Our model consists of a d-dimensional elastic network of N beads, immersed in a simple Newtonian liquid at temperature T [15–18]. We assume a lattice structure where each bead is connected to its nearest neighbours by springs of elastic constant k, as illustrated in Fig. 1. For simplicity, we model internal enzymatic activity by a Gaussian white noise with variance α_i at bead i. By assuming white noise, we effectively consider the dynamics of biological systems on timescales much longer than the characteristic timescales of the active processes [13,19,20]. Importantly, these activity amplitudes, $\alpha_i \geq 0$, are spatially heterogeneous, reflecting a spatial distribution of active processes in the system. These activity amplitudes are drawn independently from a distribution p_α with mean $\bar{\alpha} < \infty$ and standard deviation $\sigma_\alpha < \infty$ for each realization of the system. This description of a heterogeneously driven assembly is similar to bead-spring models in which the beads are coupled to distinct heat baths at different temperatures [21–23].

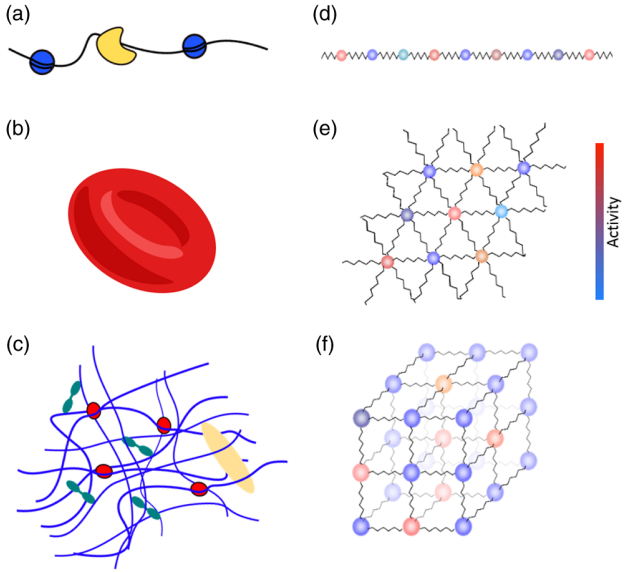

FIG. 1. Schematic illustrating soft viscoelastic networks with heterogeneous driving for various types of cellular systems. (a) Chromosome, (b) red blood cell membrane, (c) cytoskeletal network with (d)–(f) associated bead-spring models with heterogeneous active driving. The color of the bead indicates the intensity of activity, representing the variance (increasing from blue to red) of the associated active noise process.

The temporal evolution of the probability distribution $p(\mathbf{x},t)$ of the beads' displacements $\mathbf{x}$, relative to their rest positions, is governed by a Fokker-Planck equation

$$\frac{\partial p(\mathbf{x},t)}{\partial t} = -\boldsymbol{\nabla}\cdot[\mathbf{A}\mathbf{x}p(\mathbf{x},t)] + \boldsymbol{\nabla}\cdot\mathbf{D}\boldsymbol{\nabla}p(\mathbf{x},t), \\ = -\boldsymbol{\nabla}\cdot\mathbf{j}(\mathbf{x},t), \tag{1}$$

where $\mathbf{j}(\mathbf{x},t) = \mathbf{A}\mathbf{x}p(\mathbf{x},t) - \mathbf{D}\boldsymbol{\nabla}p(\mathbf{x},t)$ is the probability current. Here, $\mathbf{A}$ is the elastic interaction matrix, incorporating all nearest neighbor spring interactions between beads; the mobility matrix is assumed to be diagonal to exclude hydrodynamic interactions between the beads and is absorbed in $\mathbf{A}$. The diffusion matrix $\mathbf{D}$ is diagonal with elements $d_{ij} = \delta_{ij}[k_B(T+\alpha_i)/\gamma]$, where γ is the damping coefficient describing the viscous interaction between a bead and the immersing liquid. The steady-state dynamics of this active network is described by

$$p(\mathbf{x}) = \frac{1}{\sqrt{(2\pi)^{dN}\det\mathbf{C}}} e^{-\frac{1}{2}\mathbf{x}^T\mathbf{C}^{-1}\mathbf{x}}, \tag{2}$$

where $\mathbf{C} = \langle \mathbf{x}\otimes\mathbf{x}\rangle$ is the covariance matrix, which can be obtained by solving the Lyapunov equation $\mathbf{A}\mathbf{C} + \mathbf{C}\mathbf{A}^T = -2\mathbf{D}$ [24]. In the simplest limit, the activities are spatially homogeneous: $\alpha_i = \alpha\,\forall\, i$, resulting in effectively equilibrium dynamics, with $p(\mathbf{x})$ given by the Boltzmann distribution $[\mathbf{C}^{-1} = -\mathbf{A}/(T+\alpha)]$ and $\mathbf{j} = \mathbf{0}$. By contrast, in heterogeneously driven systems with nonidentical α_i's, we obtain nonequilibrium steady-state dynamics with $\mathbf{j} \neq \mathbf{0}$ [24].

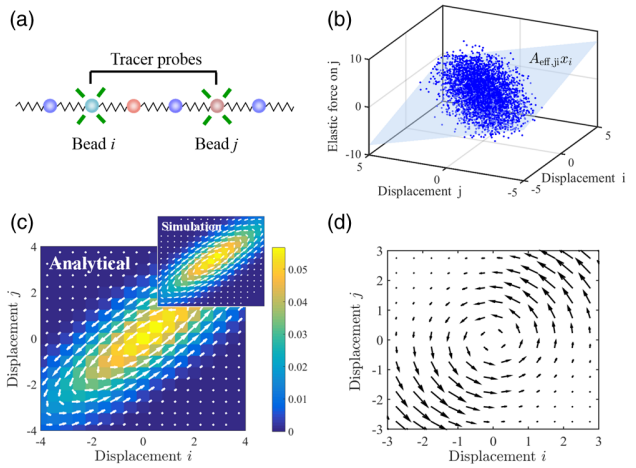

FIG. 2. Reduced system of tracked probed. (a) Schematic of two fluorescently labeled probe beads in a larger system. (b) Elastic force acting on bead j obtained at different time steps of a simulation of the Langevin dynamics of the full system (blue points) and the effective linear force $\mathbf{A}_{\text{eff}}\mathbf{x}_{\text{r}}$ from analytical calculations (light blue plane). (c) Probability density (color map) and probability current (white arrows) calculated analytically from the effective 2D system, together with results from simulating the full system in the inset. (d) The nonconservative part of the effective force field, $[(\mathbf{A}_{\text{eff}} - \mathbf{A}_{\text{eff}}^T)/2]\mathbf{x}_{\text{r}}$ (black arrows), can contribute to the rotation in phase space in nonequilibrium systems. Note, for $\alpha_i = \alpha\,\forall\, i$ (effective equilibrium scenario), $\mathbf{A}_{\text{eff}}$ becomes symmetric.

If we were able to observe the stochastic motion of all beads in the network, we could directly measure the full probability current $\mathbf{j}(\mathbf{x})$ and extract information about the complete nonequilibrium dynamics of the system. However, in an actual experiment, typically only a small subset of the degrees of freedom can be tracked [Fig. 2(a)]. What information on the nonequilibrium dynamics of the system can be extracted from such limited observations? To address this question, we investigate a scenario where only a few degrees of freedom are accessible.

We start by reducing our description to the marginal distribution, $p_{\text{r}}(\mathbf{x}_{\text{r}}) = \int dx_{k\notin[\text{r}]}\, p(x_1, x_2, \ldots, x_{dN})$, of a subset [r] of n tracked degrees of freedom $\mathbf{x}_{\text{r}}$. By integrating out the subset [l] of m unobserved degrees of freedom $\mathbf{x}_{\text{l}}$ on both sides of Eq. (1) and taking the steady-state limit, we obtain (see Supplemental Material [25])

$$0 = -\boldsymbol{\nabla}\cdot[\mathbf{A}_{\text{eff}}\mathbf{x}_{\text{r}}p_{\text{r}}(\mathbf{x}_{\text{r}})] + \boldsymbol{\nabla}\cdot\mathbf{D}_{[\text{r,r}]}\boldsymbol{\nabla}p_{\text{r}}(\mathbf{x}_{\text{r}}), \tag{3}$$

where the subindex [r, r] of a matrix indicates the submatrix corresponding to the reduced set of observed variables. In addition, we introduce the effective linear interaction [Fig. 2(b)], which can be written as $\mathbf{A}_{\text{eff}}\mathbf{x}_{\text{r}}$, with $\mathbf{A}_{\text{eff}} = \mathbf{A}_{[\text{r,r}]} + \mathbf{A}_{[\text{r,l}]}\mathbf{C}_{[\text{l,r}]}\mathbf{C}^{-1}_{[\text{r,r}]}$. Here, $\mathbf{A}_{[\text{r,l}]}$ and $\mathbf{C}_{[\text{l,r}]}$ are rectangular matrices of sizes $[n\times m]$ and $[m\times n]$, given by the

elements of indices [r, l] of $\mathbf{A}$ and [l, r] of $\mathbf{C}$, respectively. Thus, we obtain an effective stationary Fokker-Planck equation for the reduced system (3). From this, we obtain the exact steady-state reduced probability distribution $p_{\mathrm{r}}(\mathbf{x}_{\mathrm{r}})$ and probability current density:

$$\mathbf{j}_{\mathrm{r}}(\mathbf{x}_{\mathrm{r}}) = \mathbf{A}_{\mathrm{eff}}\mathbf{x}_{\mathrm{r}}p_{\mathrm{r}}(\mathbf{x}_{\mathrm{r}}) + \mathbf{D}_{[\mathrm{r,r}]}\mathbf{C}^{-1}_{[\mathrm{r,r}]}\mathbf{x}_{\mathrm{r}}p_{\mathrm{r}}(\mathbf{x}_{\mathrm{r}}), \qquad (4)$$

which can, in principle, be measured from the trajectories of the observed degrees of freedom [Fig. 2(c)].

We can use this reduced description to investigate how broken detailed balance manifests at different scales in the network. In particular, we consider the simplest case of a reduced system of only two tracked beads in a larger system, as illustrated in Fig. 2(a). It is convenient to quantify the probability currents in the 2D phase space of these two tracer beads by a pseudoscalar quantity: the average cycling frequency around the origin [13,14,26]. For linear systems, we can express the reduced probability current as $\mathbf{j}_{\mathrm{r}}(\mathbf{x}_{\mathrm{r}}) = \mathbf{\Omega}_{\mathrm{r}}\mathbf{x}_{\mathrm{r}}p_{\mathrm{r}}(\mathbf{x}_{\mathrm{r}})$, where $\mathbf{\Omega}_{\mathrm{r}}$ is a 2D matrix with purely imaginary eigenvalues $\lambda = \pm i\omega$, with ω representing the cycling frequency.

This cycling frequency can be measured experimentally for a pair of degrees of freedom; e.g. the displacements in a certain direction of two probe beads at a distance r. This frequency will depend on the specific configuration of all activity amplitudes α_i. We aim to compute how this cycling frequency depends on r after averaging over all activity configurations. Since ω is expected to be distributed symmetrically around zero, we calculate $\sqrt{\langle\omega^2(r)\rangle_\alpha}$ for pairs of beads separated by a distance r. Here, the average $\langle\cdots\rangle_\alpha$ is taken over an ensemble of activities $\{\alpha_i\}$ drawn from the distribution p_α. Intuitively, the magnitude of the circulation of currents in phase space typically decreases with the distance between the probes, as shown in Fig. 3(a). This reduction of the circulation is reflected by a decrease of the cycling frequency ω with distance. Remarkably, $\sqrt{\langle\omega^2(r)\rangle_\alpha}$ appears to depend on the distance between the tracer beads r as a power law, $\sqrt{\langle\omega^2(r)\rangle_\alpha} \propto r^{-\mu}$, with $\mu \approx 1.9$ for a 1D chain with a folded Gaussian or an exponential distribution of activities, as depicted in Fig. 3(b).

To investigate how the architecture of the system affects the scaling behavior of the cycling frequencies, we considered different network structures, including square, triangular, and cubic lattices. In particular, we determined the ensemble average $\langle\cdots\rangle_\alpha$ by performing a spatial average for computational convenience (see Supplemental Material [25]). Interestingly, we find that the characteristic exponent μ appears to depend strongly on the dimensionality of the lattice, but not on its geometry, as shown in Figs. 3(b) and 3(c). These results suggest that the distance dependence of the cycling frequency is determined in part by the long wavelength elastic properties of the system. Importantly, however, the scaling of cycling frequency is sensitive to the spatial structure of the

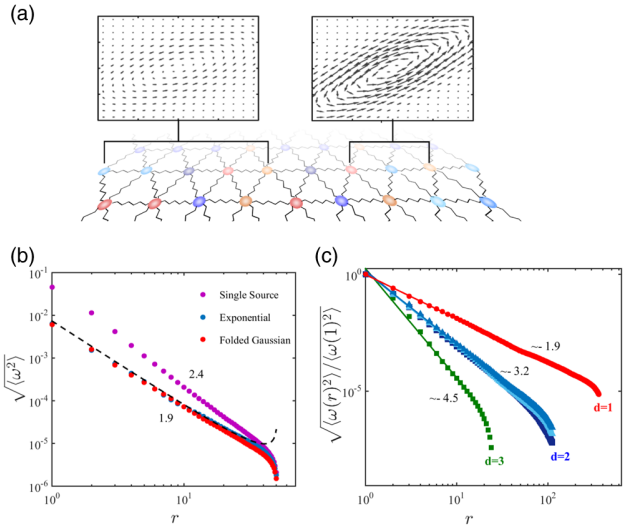

FIG. 3. Spatial scaling behavior of cycling frequencies. (a) Steady-state current cycles in phase space of the displacements (along the lattice direction) of two tracer beads for a nearby pair of probes (left) and distant pair of probes (right). (b) Scaling behavior of the cycling frequencies $\sqrt{\langle\omega^2(r)\rangle}$ of a pair of probes beads as a function of their spatial distances, obtained for a 1D chain and different activity distributions, as indicated in the legend. Black dashed line is obtained from Eq. (10). (c) Scaling behavior of the cycling frequencies $\sqrt{\langle\omega^2(r)\rangle/\langle\omega^2(1)\rangle}$, obtained for different lattices and a folded Gaussian activity distribution. Triangular and square markers represent triangular and square or cubic lattices, respectively. Light (dark) blue triangles represent triangular networks with zero (finite) rest length springs. In both (b) and (c), we used $\bar{\alpha}/T = 0.15$.

activities. For example, in the simple case of a δ-distributed (single-source) activity on a 1D chain, we find $\mu_{\mathrm{single}} \approx 2.4$ [Fig. 3(b)] in contrast to the value 1.9 obtained above for spatially distributed activities.

To obtain more insight into the scaling behavior of the cycling frequencies, we derive an analytical expression for the cycling frequency as a function of the distance between the observed beads $\omega(r)$. In general, it can be shown that, for a linear system described by a Fokker-Planck equation, the cycling frequencies are given by (see Supplemental Material [25])

$$\omega_{ij} = \frac{1}{2\gamma}\frac{\langle\tau_{ij}\rangle}{\sqrt{\det\mathbf{C}_{[\mathrm{r,r}]}}}, \qquad (5)$$

where $\tau_{ij} \coloneqq \mathbf{x}_{\mathrm{r}} \times \mathbf{f}_{\mathrm{r}}(\mathbf{x}) = x_i f_j(\mathbf{x}) - x_j f_i(\mathbf{x})$ is a generalized phase space torque in the x_i-x_j plane, with $f_i(\mathbf{x})$ denoting the deterministic force acting on the ith bead. This result is intuitive: for an overdamped system, the mean angular velocity is proportional to the mean torque and the factor $1/\sqrt{\det\mathbf{C}_{[\mathrm{r,r}]}}$ ensures coordinate invariance. For the 1D chain of beads [Fig. 1(d)], Eq. (5) reduces to

$$\omega_{ij} = \frac{k}{\gamma}\frac{\tilde{\partial}_2^2 c_{ij}}{\sqrt{\det \mathbf{C}_{[\mathrm{r,r}]}}}, \tag{6}$$

where c_{ij} is the ith, jth element of the covariance matrix $\mathbf{C}$, with the discrete second derivative across rows denoted as $\tilde{\partial}_2^2 c_{ij} = c_{i,j+1} - 2c_{i,j} + c_{i,j-1}$. Thereby, we have reduced the problem of calculating $\omega(r)$ to finding the covariance matrix of the system.

The structure of $\mathbf{D}$ suggests a natural decomposition of the covariance matrix $\mathbf{C}$ into equilibrium ($\bar{\mathbf{C}}$) and nonequilibrium ($\mathbf{C}^*$) contributions: $\mathbf{C} = (k_B T/k)\bar{\mathbf{C}} + (k_B\bar{\alpha}/k)\mathbf{C}^*$, such that $\bar{\mathbf{C}}$ and $\mathbf{C}^*$ are dimensionless. Both $\bar{\mathbf{C}}$ and $\mathbf{C}^*$ can be found by solving the Lyapunov equation, which for the 1D chain is given by

$$\tilde{\partial}_1^2 \bar{c}_{ij} + \tilde{\partial}_2^2 \bar{c}_{ij} = -2\delta_{ij}, \tag{7}$$

$$\tilde{\partial}_1^2 c^*_{ij} + \tilde{\partial}_2^2 c^*_{ij} = -2\delta_{ij}\frac{\alpha_i}{\bar{\alpha}}, \tag{8}$$

where $\tilde{\partial}_1^2$ indicates the discrete second derivative across columns. These equations represent discrete stationary diffusion equations, with sources of divergence given by δ_{ij} and $\delta_{ij}(\alpha_i/\bar{\alpha})$, respectively. This result prescribes how a spatial distribution of activities structures the covariance matrix.

We can make further progress by noting that the principle of detailed balance imposes $\omega_{ij} = 0$ at thermal equilibrium, which together with Eq. (6) implies $\tilde{\partial}_2^2 \bar{c}_{ij} = 0$. We can, therefore, substitute $\tilde{\partial}_2^2 c_{ij}$ in Eq. (6) by $\tilde{\partial}_2^2 c^*_{ij}$, and then expand this equation up to linear order in $\bar{\alpha}/T$ to obtain

$$\omega_{ij} = \frac{k}{\gamma}\frac{\bar{\alpha}}{T}\frac{\tilde{\partial}_2^2 c^*_{ij}}{\sqrt{\det \bar{\mathbf{C}}_{[\mathrm{r,r}]}}}. \tag{9}$$

We proceed by calculating $\mathbf{C}^*$ for a given distribution of activities $\{\alpha_i\}$. Because of the linearity of Eq. (8), $\mathbf{C}^*$ is a superposition of steady-state solutions to single-source problem, i.e., a δ-distribution for which all but one of the activities would be set to zero. Denoting the element of $\mathbf{C}^*$ at a distance r from the single activity source by $c^*(r)$, we obtain the "covariance current" $\partial_r c^*(r) \sim 1/r$. Here we employed a continuous approximation of the discrete diffusion problem in Eqs. (7) and (8). Thus, $c^*(r) = -a\ln(r) + b$ for a single-source problem, with integration constants a and b, representing the Green's function for our problem. Using this expression for $c^*(r)$ together with Eq. (9), we obtain for the single-source case $\omega^2_{\mathrm{single}}(r) = (k^2/\gamma^2)(\alpha^2/T^2)(a^2/r^4)\{1/\det \bar{\mathbf{C}}_{[\mathrm{r,r}]}(r)\}$, where α is the source's activity.

Next, we use a superposition of single-source solutions for $c^*(r)$ to obtain the nonequilibrium contribution of the covariance matrix $\mathbf{C}^*$ for a specific configuration of many activity sources $\{\alpha_i\}$. Using this result in conjunction with Eq. (9) and performing an ensemble average over the distribution of activity realizations, we arrive at the central result

$$\langle \omega^2(r)\rangle_\alpha = \frac{k^2}{\gamma^2}\frac{\sigma_\alpha^2}{T^2}\frac{\pi a^2}{2r^3}\frac{1}{\det \bar{\mathbf{C}}_{[\mathrm{r,r}]}(r)}. \tag{10}$$

Finally, we note that the elements of the equilibrium covariance matrix are given by $\bar{c}_{i,j} = \min(i,j) - ij/(N+1)$ and find that, for $r \ll N$, $\det \bar{\mathbf{C}}_{[\mathrm{r,r}]}(r)$ exhibits a power-law behavior $\det \bar{\mathbf{C}}_{[\mathrm{r,r}]}(r) \sim Nr$. Therefore, from this analysis, we find for a 1D chain with heterogenous activities $\mu = 2$, independent of the activity distribution p_α. Furthermore, we find $\mu_{\mathrm{single}} = 2.5$ for a single-source activity, in accord with our numerical result [see Fig. 3(b)]. This calculation provides insight into how a combination of features of the equilibrium and nonequilibrium contributions to the covariance matrix determine the spatial scaling behavior of cycling frequencies.

Nonzero cycling frequencies directly reflect broken detailed balance, suggesting a connection between ω and measures of the internal driving, including the rate of entropy production. For a Markovian system described by a Fokker-Planck equation, the total entropy production rate under steady-state conditions is given by [27]

$$\Pi_{\mathrm{tot}} = k_B \int d\mathbf{x}\, \frac{\mathbf{j}^T(\mathbf{x})\mathbf{D}^{-1}\mathbf{j}(\mathbf{x})}{p(\mathbf{x})}, \tag{11}$$

where k_B is Boltzmann's constant. The validity of this result relies on the equivalence between the Fokker-Planck and Langevin descriptions. However, the marginal probability density of the reduced system is described by a Fokker-Planck equation only at steady state [see Eq. (3) and Supplemental Material [25]], reflecting the loss of Markovianity after coarse graining. Even if the real dynamics of the reduced system are non-Markovian, we can define an effective Markovian dynamics through the Langevin equation

$$\frac{d\mathbf{x}_{\mathrm{r}}(t)}{dt} = \mathbf{A}_{\mathrm{eff}}\mathbf{x}_{\mathrm{r}}(t) + \sqrt{2\mathbf{D}_{[\mathrm{r,r}]}}\boldsymbol{\xi}_{\mathrm{r}}(t), \tag{12}$$

with Gaussian white noise $\boldsymbol{\xi}_{\mathrm{r}}(t)$. This equation of motion results in the exact steady-state probability and current densities, but with an approximate stochastic dynamics. In particular, the effective interaction matrix $\mathbf{A}_{\mathrm{eff}}$ [see Eq. (3)] captures only the average interaction between the traced variables, as illustrated in Fig. 2(b). Furthermore, in contrast to the full deterministic forces ($\mathbf{Ax}$), these effective interactions [Fig. 2(c)] need not derive from a potential and thus may contain a nonconservative component [Fig. 2(d)].

The entropy production rate associated with the effective Markovian dynamics in Eq. (12) is given by

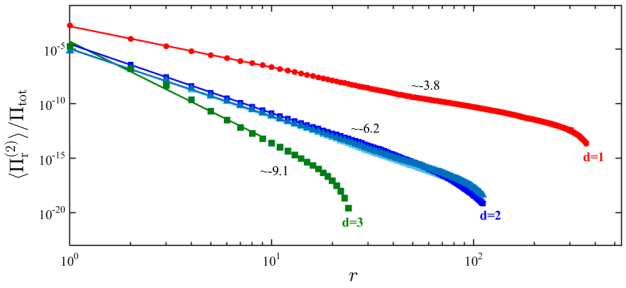

FIG. 4. Spatial scaling behavior of the average entropy production rate $\langle \Pi_r^{(2)} \rangle$ of a pair of probe beads as a function of their spatial distance r, obtained for different lattices, and a folded Gaussian activity distribution with $\bar{\alpha}/T = 0.15$. Note the entropy production rate of the reduced system is scaled by the total entropy production rate of the whole network Π_{tot}. Triangular and square markers represent triangular and square or cubic lattices, respectively. Light (dark) blue triangles represent triangular networks with zero (finite) rest length springs.

$$\Pi_r = k_B \int d\mathbf{x}_r \frac{\mathbf{j}_r^T(\mathbf{x}_r)\mathbf{D}_{[r,r]}^{-1}\mathbf{j}_r(\mathbf{x}_r)}{p_r(\mathbf{x}_r)} \leq \Pi_{tot}, \tag{13}$$

where $\mathbf{j}_r(\mathbf{x}_r)$ is defined in Eq. (4). Note, estimating Π_r by using the Markovian formalism allows us to set a lower bound for the total entropy production rate Π_{tot} (see Supplemental Material [25]), similar to what has already been shown for discrete systems [28]. In the $n = 2$ case with two traced degrees of freedom that we consider here, Eq. (13) reduces to (see Supplemental Material [25])

$$\Pi_r^{(2)} = k_B \omega^2 \mathrm{Tr}(\mathbf{C}_{[r,r]}\mathbf{D}_{[r,r]}^{-1}). \tag{14}$$

This result provides an explicit relation between the partial entropy production rate and the cycling frequency ω. Note, all quantities in the expression for $\Pi_r^{(2)}$ can be observed in an experiment, providing a direct way to noninvasively determine the reduced rate of entropy production for a set of traced degrees of freedom. Since $\mathrm{Tr}(\mathbf{C}_{[r,r]}\mathbf{D}_{[r,r]}^{-1})$ depends only weakly on r, as long as $1 \ll r \ll N$, we expect a scaling behavior $\langle \Pi_r^{(2)} \rangle \sim r^{-2\mu}$. This result shows that the spatial scaling behavior of the cycling frequencies directly determines the spatial scaling behavior of the entropy production rate [see Fig. 4].

In summary, we here demonstrate theoretically how experimental measures of nonequilibrium activity in internally driven linear networks are affected by the length scale at which the system is observed. Specifically, we developed a general framework to predict the scaling behavior of cycling frequencies and the entropy production rate that can be inferred by tracing pairs of degrees of freedom. We showed that the exponent μ that governs this behavior for a system with heterogeneous random activities is insensitive to the details of distribution of activities. However, this exponent depends sensitively on the dimensionality of the system. The predicted scaling behavior can be tested, for instance, by analyzing the fluctuations of pairs of tracer particles embedded in biological [9–11,29,30] and artificial [31–36] systems under nonequilibrium steady-state conditions.

We thank S. Ceolin, E. Frey, J. Gladrow, F. Gnesotto, P. Ronceray, and C. Schmidt for stimulating discussions. This work was supported by the German Excellence Initiative via the program NanoSystems Initiative Munich (NIM), by a DFG Fellowship through the Graduate School of Quantitative Biosciences Munich (QBM). Part of this work was performed at the Aspen Center for Physics supported by NSF Grant No. PHY-1607611.

F. M. and G. G. contributed equally to this work.

*C.broedersz@lmu.de

[1] E. Fodor and M. C. Marchetti, arXiv:1708.08652.
[2] F. Gnesotto, F. Mura, J. Gladrow, and C. P. Broedersz, Rep. Prog. Phys. **81**, 066601 (2018).
[3] F. Jülicher, K. Kruse, J. Prost, and J.-F. Joanny, Phys. Rep. **449**, 3 (2007).
[4] D. Needleman and Z. Dogic, Nat. Rev. Mater. **2**, 17048 (2017).
[5] C. F. Schmidt and F. C. MacKintosh, Curr. Opin. Cell Biol. **22**, 29 (2010).
[6] T. Betz, M. Lenz, J. F. Joanny, and C. Sykes, Proc. Natl. Acad. Sci. U.S.A. **106**, 15320 (2009).
[7] H. Turlier, D. A. Fedosov, B. Audoly, T. Auth, N. S. Gov, J.-F. Joanny, G. Gompper, and T. Betz, Nat. Phys. **12**, 513 (2016).
[8] S. C. Weber, A. J. Spakowitz, and J. A. Theriot, Proc. Natl. Acad. Sci. U.S.A. **109**, 7338 (2012).
[9] A. W. C. Lau, B. D. Hoffman, A. Davies, J. C. Crocker, and T. C. Lubensky, Phys. Rev. Lett. **91**, 198101 (2003).
[10] M. Guo, A. J. Ehrlicher, M. H. Jensen, M. Renz, J. R. Moore, R. D. Goldman, J. L. Schwartz, F. C. Mackintosh, and D. A. Weitz, Cell **158**, 822 (2014).
[11] N. Fakhri, A. D. Wessel, C. Willms, M. Pasquali, D. R. Klopfenstein, F. C. Mackintosh, and C. F. Schmidt, Science **344**, 1031 (2014).
[12] C. Battle, C. P. Broedersz, N. Fakhri, J. Howard, C. F. Schmidt, and F. C. MacKintosh, Science **352**, 604 (2016).
[13] J. Gladrow, N. Fakhri, F. C. MacKintosh, C. F. Schmidt, and C. P. Broedersz, Phys. Rev. Lett. **116**, 248301 (2016).
[14] J. Gladrow, C. P. Broedersz, and C. F. Schmidt, Phys. Rev. E **96**, 022408 (2017).
[15] M. G. Yucht, M. Sheinman, and C. P. Broedersz, Soft Matter **9**, 7000 (2013).
[16] C. P. Broedersz and F. C. MacKintosh, Rev. Mod. Phys. **86**, 995 (2014).
[17] D. Osmanovic and Y. Rabin, Soft Matter **13**, 963 (2017).
[18] X. Mao and T. C. Lubensky, Annu. Rev. Condens. Matter Phys. **9**, 413 (2018).

[19] F. C. MacKintosh and A. J. Levine, Phys. Rev. Lett. **100**, 018104 (2008).
[20] J. Ruostekoski and J. R. Anglin, Phys. Rev. Lett. **91**, 190402 (2003).
[21] Z. Rieder, J. L. Lebowitz, and E. Lieb, J. Math. Phys. (N.Y.) **8**, 1073 (1967).
[22] F. Bonetto, J. L. Lebowitz, and J. Lukkarinen, J. Stat. Phys. **116**, 783 (2004).
[23] G. Falasco, M. Baiesi, L. Molinaro, L. Conti, and F. Baldovin, Phys. Rev. E **92**, 022129 (2015).
[24] H. Risken, *The Fokker-Planck Equation* (Springer, Berlin, 1996).
[25] See Supplemental Material at http://link.aps.org/supplemental/10.1103/PhysRevLett.121.038002 for additional details on the derivations of the results in the main text.
[26] J. B. Weiss, Tellus A **55**, 208 (2003).
[27] U. Seifert, Rep. Prog. Phys. **75**, 126001 (2012).
[28] G. Bisker, M. Polettini, T. R. Gingrich, and J. M. Horowitz, J. Stat. Mech. (2017) 093210.
[29] D. Mizuno, C. Tardin, C. F. Schmidt, and F. C. MacKintosh, Science **315**, 370 (2007).
[30] A. D. Wessel, M. Gumalla, J. Grosshans, and C. F. Schmidt, Biophys. J. **108**, 1899 (2015).
[31] O. Lieleg, M. M. A. E. Claessens, and A. R. Bauch, Soft Matter **6**, 218 (2010).
[32] J. Palacci, S. Sacanna, A. P. Steinberg, D. J. Pine, and P. M. Chaikin, Science **339**, 936 (2013).
[33] I. Buttinoni, J. Bialké, F. Kümmel, H. Löwen, C. Bechinger, and T. Speck, Phys. Rev. Lett. **110**, 238301 (2013).
[34] G. H. Koenderink, Z. Dogic, F. Nakamura, P. M. Bendix, F. C. MacKintosh, J. H. Hartwig, T. P. Stossel, and D. A. Weitz, Proc. Natl. Acad. Sci. U.S.A. **106**, 15192 (2009).
[35] M. H. Jensen, E. J. Morris, and D. A. Weitz, Biochim. Biophys. Acta **1853**, 3038 (2015).
[36] V. Schaller, C. Weber, C. Semmrich, E. Frey, and A. R. Bausch, Nature (London) **467**, 73 (2010).
[37] Y. L. Tong, *Springer Series in Statistics* (Springer-Verlag, Berlin, 1990).

Supplement: Non-equilibrium scaling behaviour in driven soft biological assemblies

Federica Mura,[1,*] Grzegorz Gradziuk,[1,*] and Chase P. Broedersz[1,†]

[1] *Arnold-Sommerfeld-Center for Theoretical Physics and Center for NanoScience, Ludwig-Maximilians-Universität München, D-80333 München, Germany.*

(Dated: July 6, 2018)

DERIVATION OF EQ. (3)

Here, we derive Eq. (3), which describes the steady state distribution of traced variables. Integrating out the unobserved degrees of freedom on both sides of the Fokker-Plank equation (Eq. (1)), and using the Einstein notation for summing over repeated indexes, we obtain:

$$\overbrace{\int d\mathbf{x}_\mathrm{l}\partial_t p(\mathbf{x})}^{(I)} = -\overbrace{\int d\mathbf{x}_\mathrm{l}\partial_i[a_{ij}x_j p(\mathbf{x},t)]}^{(II)} + \overbrace{\int d\mathbf{x}_\mathrm{l} d_{ij}\partial_i\partial_j p(\mathbf{x},t)}^{(III)} \tag{S1}$$

where a_{ij} and d_{ij} are the elements of the interaction matrix $\mathbf{A}$ and the diffusion matrix $\mathbf{D}$, respectively. Rewriting the probability as $p(\mathbf{x},t) = p(\mathbf{x}_\mathrm{l}|\mathbf{x}_\mathrm{r},t)p_\mathrm{r}(\mathbf{x}_\mathrm{r},t)$, we can separately calculate each term in Eq.($S1$). The first term (I) gives:

$$\int d\mathbf{x}_\mathrm{l}\partial_t p_\mathrm{r}(\mathbf{x}_\mathrm{r},t)p(\mathbf{x}_\mathrm{l}|\mathbf{x}_\mathrm{r},t) = \partial_t p_\mathrm{r}(\mathbf{x}_\mathrm{r},t)\int d\mathbf{x}_\mathrm{l} p(\mathbf{x}_\mathrm{l}|\mathbf{x}_\mathrm{r},t) = \partial_t p_\mathrm{r}(\mathbf{x}_\mathrm{r},t) \tag{S2}$$

For the second term (II), we obtain

$$\begin{aligned}\int d\mathbf{x}_\mathrm{l}\partial_i[p_\mathrm{r}(\mathbf{x}_\mathrm{r},t)p(\mathbf{x}_\mathrm{l}|\mathbf{x}_\mathrm{r},t)a_{ij}x_j] &= \delta_{i,[\mathrm{r}]}\partial_i[p_\mathrm{r}(\mathbf{x}_\mathrm{r},t)\int d\mathbf{x}_\mathrm{l} p(\mathbf{x}_\mathrm{l}|\mathbf{x}_\mathrm{r},t)a_{ij}x_j] \\ &= \delta_{i,[\mathrm{r}]}\partial_i[p_\mathrm{r}(\mathbf{x}_\mathrm{r},t)a_{ij}\langle x_j|\mathbf{x}_\mathrm{r},t\rangle]\end{aligned} \tag{S3}$$

where $\delta_{i,[\mathrm{r}]} = 1$ if x_i is one of the observed coordinates and zero otherwise. In the first line we use that the probability density vanishes at infinity faster than $1/x$. Similarly, the third term (III) can be written as

$$\begin{aligned}\int d\mathbf{x}_\mathrm{l} d_{ij}\partial_i\partial_j[p_\mathrm{r}(\mathbf{x}_\mathrm{r},t)p(\mathbf{x}_\mathrm{l}|\mathbf{x}_\mathrm{r},t)] &= \delta_{i,[\mathrm{r}]}\delta_{j,[\mathrm{r}]}d_{ij}\partial_i\partial_j[p_\mathrm{r}(\mathbf{x}_\mathrm{r},t)\int d\mathbf{x}_\mathrm{l} p(\mathbf{x}_\mathrm{l}|\mathbf{x}_\mathrm{r},t)] \\ &= \delta_{i,[\mathrm{r}]}\delta_{j,[\mathrm{r}]}d_{ij}\partial_i\partial_j p_\mathrm{r}(\mathbf{x}_\mathrm{r},t)\end{aligned} \tag{S4}$$

We seek a description for the stochastic dynamics, which only depends on the observed degrees of freedom. This can be achieved by taking the steady-state limit. In this case, the conditional average appearing in Eq.(S3) yields $\langle\mathbf{x}_\mathrm{l}|\mathbf{x}_\mathrm{r}\rangle = \mathbf{C}_{[\mathrm{l,r}]}\mathbf{C}^{-1}_{[\mathrm{r,r}]}\mathbf{x}_\mathrm{r}$ [S1]. We substitute Eqs. (S2)-(S4) in Eq. (S1) to obtain Eq. (3), which therefore holds only at steady-state.

DERIVATION OF EQ. (5)

Here we derive the expression in Eq. (5) for the cycling frequencies. To this end, we first show that the right hand side of this equation is invariant under orientation preserving linear transformations restricted to the 2-dimensional reduced subspace. Let us consider such a transformation: $\mathbf{x}'_\mathrm{r} = \mathbf{B}\mathbf{x}_\mathrm{r}$, $\mathbf{f}'_\mathrm{r} = \mathbf{B}\mathbf{f}_\mathrm{r}$, and denote by $\mathbf{C}'_{[\mathrm{r,r}]}$ the reduced covariance matrix in the transformed coordinates.

$$\mathbf{B}\mathbf{C}_{[\mathrm{r,r}]}\mathbf{B}^T = \mathbf{C}'_{[\mathrm{r,r}]} \quad\Longrightarrow\quad \det\mathbf{B} = \sqrt{\frac{\det\mathbf{C}'_{[\mathrm{r,r}]}}{\det\mathbf{C}_{[\mathrm{r,r}]}}} \tag{S5}$$

Using this result together with the transformation properties of the vector product, we obtain

$$\frac{\langle\tau_{ij}\rangle}{\sqrt{\det\mathbf{C}_{[\mathrm{r,r}]}}} = \frac{\langle\mathbf{x}_\mathrm{r}\times\mathbf{f}_\mathrm{r}(\mathbf{x})\rangle}{\sqrt{\det\mathbf{C}_{[\mathrm{r,r}]}}} = \frac{\langle\mathbf{x}'_\mathrm{r}\times\mathbf{f}'_\mathrm{r}(\mathbf{x}')\rangle}{\sqrt{\det\mathbf{C}_{[\mathrm{r,r}]}}}\frac{1}{\det\mathbf{B}} = \frac{\langle\tau'_{ij}\rangle}{\sqrt{\det\mathbf{C}'_{[\mathrm{r,r}]}}}. \tag{S6}$$

The coordinate invariance of this term allows us to specifically consider the convenient coordinates in which $\mathbf{C}_{[\mathrm{r},\mathrm{r}]} = \mathbf{I}$:

$$\frac{1}{\gamma}\langle \tau_{ij}\rangle = \frac{1}{\gamma}\langle \mathbf{x}_\mathrm{r}\times\mathbf{f}_\mathrm{r}(\mathbf{x})\rangle = \frac{1}{\gamma}\int d\mathbf{x}_\mathrm{r}\,\langle \mathbf{x}_\mathrm{r}\times\mathbf{f}_\mathrm{r}(\mathbf{x})|\mathbf{x}_\mathrm{r}\rangle\, p_\mathrm{r}(\mathbf{x}_\mathrm{r}) = \frac{1}{\gamma}\int d\mathbf{x}_\mathrm{r}\;\mathbf{x}_\mathrm{r}\times\langle \mathbf{f}_\mathrm{r}(\mathbf{x})|\mathbf{x}_\mathrm{r}\rangle\, p_\mathrm{r}(\mathbf{x}_\mathrm{r}) \tag{S7}$$

We can further expand this expression by using $\mathbf{\Omega}_\mathrm{r} = \mathbf{A}_\mathrm{eff} + \mathbf{D}_{[\mathrm{r},\mathrm{r}]}\mathbf{C}^{-1}_{[\mathrm{r},\mathrm{r}]}$. (The expression for $\mathbf{\Omega}_\mathrm{r}$ follows immediately from Eq. (4), since we require $\mathbf{j}_\mathrm{r}(\mathbf{x}_\mathrm{r}) = \mathbf{\Omega}_\mathrm{r}\mathbf{x}_\mathrm{r}p_\mathrm{r}(\mathbf{x}_\mathrm{r})$.)

$$\frac{1}{\gamma}\langle \mathbf{f}_\mathrm{r}(\mathbf{x})|\mathbf{x}_\mathrm{r}\rangle = \mathbf{A}_\mathrm{eff}\mathbf{x}_\mathrm{r} = \mathbf{\Omega}_\mathrm{r}\mathbf{x}_\mathrm{r} - \mathbf{D}_{[\mathrm{r},\mathrm{r}]}\mathbf{C}^{-1}_{[\mathrm{r},\mathrm{r}]}\mathbf{x}_\mathrm{r}. \tag{S8}$$

Combining this result with Eq. (S7), we arrive at

$$\frac{1}{\gamma}\langle \tau_{ij}\rangle = \int d\mathbf{x}_\mathrm{r}\;\mathbf{x}_\mathrm{r}\times(\mathbf{\Omega}_\mathrm{r}\mathbf{x}_\mathrm{r})p_\mathrm{r}(\mathbf{x}_\mathrm{r}) - \int d\mathbf{x}_\mathrm{r}\;\mathbf{x}_\mathrm{r}\times(\mathbf{D}_{[\mathrm{r},\mathrm{r}]}\mathbf{C}^{-1}_{[\mathrm{r},\mathrm{r}]}\mathbf{x}_\mathrm{r})p_\mathrm{r}(\mathbf{x}_\mathrm{r}). \tag{S9}$$

Using the explicit form of $\mathbf{\Omega}_\mathrm{r}$ (see Eq. (S15)), we evaluate the first term in this expression,

$$\int d\mathbf{x}_\mathrm{r}\;\mathbf{x}_\mathrm{r}\times(\mathbf{\Omega}_\mathrm{r}\mathbf{x}_\mathrm{r})p_\mathrm{r}(\mathbf{x}_\mathrm{r}) = \int d\mathbf{x}_\mathrm{r}\;\omega_{ij}(x_i^2+x_j^2)p_\mathrm{r}(\mathbf{x}_\mathrm{r}) = \omega_{ij}(c_{ii}+c_{jj}) = 2\omega_{ij}. \tag{S10}$$

In addition, we confirm by direct calculation, that, as expected, the second term in Eq. (S9) vanishes:

$$\begin{aligned}
-\int d\mathbf{x}_\mathrm{r}\;\mathbf{x}_\mathrm{r}\times(\mathbf{D}_{[\mathrm{r},\mathrm{r}]}\mathbf{x}_\mathrm{r})p_\mathrm{r}(\mathbf{x}_\mathrm{r}) &= \int d\mathbf{x}_\mathrm{r}\;(-x_j,\;x_i)\begin{pmatrix} d_{ii} & d_{ij}\\ d_{ij} & d_{jj}\end{pmatrix}\begin{pmatrix}x_i\\ x_j\end{pmatrix}p_\mathrm{r}(\mathbf{x}_\mathrm{r})\\
&= \int d\mathbf{x}_\mathrm{r}\;[-d_{ii}x_ix_j - d_{ij}x_j^2 + d_{ij}x_i^2 + d_{jj}x_ix_j]p_\mathrm{r}(\mathbf{x}_\mathrm{r})\\
&= \underbrace{c_{ij}}_{0}(d_{jj}-d_{ii}) + d_{ij}\underbrace{(c_{ii}-c_{jj})}_{0} = 0
\end{aligned} \tag{S11}$$

Altogether, this gives us the desired result:

$$\frac{1}{2\gamma}\frac{\langle\tau_{ij}\rangle}{\sqrt{\det\mathbf{C}_{[\mathrm{r},\mathrm{r}]}}} = \omega_{ij} \tag{S12}$$

DERIVATION OF EQ. (13)

Here we show that $\Pi_\mathrm{tot} \geq \Pi_\mathrm{r}$.

$$\begin{aligned}
\frac{\Pi_\mathrm{tot}-\Pi_\mathrm{r}}{k_B} &= \int d\mathbf{x}\frac{\mathbf{j}^T(\mathbf{x})\mathbf{D}^{-1}\mathbf{j}(\mathbf{x})}{p(\mathbf{x})} - \int d\mathbf{x}_\mathrm{r}\frac{\mathbf{j}_\mathrm{r}^T(\mathbf{x}_\mathrm{r})\mathbf{D}^{-1}_{[\mathrm{r},\mathrm{r}]}\mathbf{j}_\mathrm{r}(\mathbf{x}_\mathrm{r})}{p(\mathbf{x}_\mathrm{r})}\\
&= \frac{\gamma}{k_B}\sum_{j\in[l]}\int d\mathbf{x}\frac{v_j^2(\mathbf{x})}{(T+\alpha_j)}p(\mathbf{x}) + \frac{\gamma}{k_\mathrm{B}}\sum_{i\in[r]}\left[\left(\int d\mathbf{x}\frac{v_i^2(\mathbf{x})}{(T+\alpha_i)}p(\mathbf{x})\right) - \int d\mathbf{x}_\mathrm{r}\frac{\langle v_i(\mathbf{x})|\mathbf{x}_\mathrm{r}\rangle^2}{(T+\alpha_i)}p(\mathbf{x}_\mathrm{r})\right]\\
&= \frac{\gamma}{k_B}\left\{\sum_{j\in[l]}\int d\mathbf{x}\frac{v_j^2(\mathbf{x})}{(T+\alpha_j)}p(\mathbf{x}) + \sum_{i\in[r]}\int d\mathbf{x}_\mathrm{r}\left[\left(\int d\mathbf{x}_\mathrm{l}\frac{v_i^2(\mathbf{x})}{(T+\alpha_i)}p(\mathbf{x}_\mathrm{l}|\mathbf{x}_\mathrm{r})p(\mathbf{x}_\mathrm{r})\right) - \frac{\langle v_i(\mathbf{x})|\mathbf{x}_\mathrm{r}\rangle^2}{(T+\alpha_i)}p(\mathbf{x}_\mathrm{r})\right]\right\}\\
&= \frac{\gamma}{k_B}\left(\sum_{j\in[l]}\frac{\langle v_j^2(\mathbf{x})\rangle}{(T+\alpha_j)} + \sum_{i\in[r]}\int d\mathbf{x}_\mathrm{r}\underbrace{\left(\langle v_i^2(\mathbf{x})|\mathbf{x}_\mathrm{r}\rangle - \langle v_i(\mathbf{x})|\mathbf{x}_\mathrm{r}\rangle^2\right)}_{\geq 0}\frac{p(\mathbf{x}_\mathrm{r})}{(T+\alpha_i)}\right) \geq 0
\end{aligned} \tag{S13}$$

where in the second line we use that $\mathbf{D}$ is diagonal, $\mathbf{v}(\mathbf{x}) = \mathbf{j}(\mathbf{x})/p(\mathbf{x})$, and $\mathbf{j}_\mathrm{r}(\mathbf{x}_\mathrm{r}) = p(\mathbf{x}_\mathrm{r})\int d\mathbf{x}_\mathrm{l}\;\mathbf{v}_\mathrm{r}(\mathbf{x})p(\mathbf{x}_\mathrm{l}|\mathbf{x}_\mathrm{r}) = p(\mathbf{x}_\mathrm{r})\,\langle\mathbf{v}_\mathrm{r}(\mathbf{x})|\mathbf{x}_\mathrm{r}\rangle$, which follows from the derivation of Eq. (3).

DERIVATION OF EQ. (14)

Here we derive the expression for the partial entropy production rate in terms of the cycling frequencies (see Eq. (14)). It is convenient to substitute the current field $\mathbf{j} = \mathbf{\Omega x} p(\mathbf{x})$ in Eq. (11), which gives

$$\begin{aligned} \Pi &= k_B \int d\mathbf{x} (\mathbf{\Omega x})^T \mathbf{D}^{-1} (\mathbf{\Omega x}) p(\mathbf{x}) = k_B \int d\mathbf{x}\, x_i \Omega_{ij}^T (\mathbf{D}^{-1})_{jl} \Omega_{lm} x_m p(\mathbf{x}) \\ &= k_B \Omega_{ij}^T (\mathbf{D}^{-1})_{jl} \Omega_{lm} c_{mi} = k_B \,\mathrm{Tr}\,(\mathbf{\Omega}^T \mathbf{D}^{-1} \mathbf{\Omega C}). \end{aligned} \tag{S14}$$

Since the entropy production is invariant under coordinate transformations, we can use a more suitable coordinate system. In particular, we choose a set of coordinates such that $\mathbf{C} = \mathbf{I}$. In this set of coordinates, the entries of the matrix Ω_{ij} correspond to the cycling frequencies in the coordinates space of the i^{th} and j^{th} coordinates [S2]. Thus, in the 2D case $\mathbf{\Omega}_\mathrm{r}$ is given by

$$\mathbf{\Omega}_\mathrm{r} = \begin{pmatrix} 0 & \omega \\ -\omega & 0 \end{pmatrix} \tag{S15}$$

Furthermore, in this coordinate system $\mathbf{C}_{[\mathrm{r,r}]}$ and $\mathbf{\Omega}_\mathrm{r}$ commute, yielding

$$\Pi_\mathrm{r}^{(2)} = k_B \omega^2 \,\mathrm{Tr}\,(\mathbf{C}_{[\mathrm{r,r}]} \mathbf{D}_{[\mathrm{r,r}]}^{-1}) \tag{S16}$$

Note, this expression is invariant under coordinate transformations.

SYSTEM SIZE AND SPATIAL AVERAGE

We determined the scaling of cycling frequencies for a range of system sizes (Fig. S1A). By properly rescaling both axes (see Eq.(10)), we can collapse all data on a mastercurve, which is consistent with a power-law over at least two decades (Fig. S1B). This analysis suggests a universal behavior, which is not dependent on the size of the system. These results provides additional numerical evidence for a power law scaling.

To determine ensemble averages of the cycling frequencies in Fig.(3) and Fig.(4) we employ spatial averages. For an infinite heterogeneous system, the ensemble average is equivalent to a spatial average. In a finite system, we need to be careful when using spatial averages because of edge effects. We investigated this aspect in a 1D chain, for which edge effects will be stronger than in higher dimensional systems. We performed a spatial average over all the different beads at distance r in the system, where we excluded data from beads at distances < 10 from the edge of system. Using this procedure, we find results that are consistent with those obtained with the ensemble average. (Fig. S2)

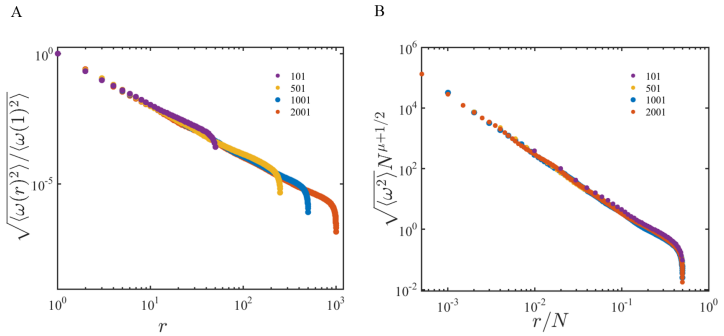

FIG. S1. Spatial scaling behavior of cycling frequencies. A) Scaling behavior of the frequency for different system sizes in the 1D chain (other parameters as in Fig. 3). B) Data collapse obtained by properly rescaling both axes.

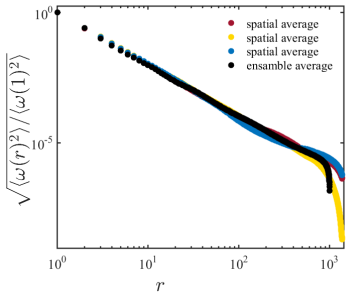

FIG. S2. Comparison between spatial and ensemble averages of the cycling frequencies for a 1D chain of size N=1501 (other parameters as in Fig. 3).

* These authors contributed equally
† C.broedersz@lmu.de

[S1] Y. L. Tong, *Springer Series in Statistics*, (Springer-Verlag, Berlin, 1990).
[S2] J. B. Weiss, Tellus A **3**, 55 (2003).

2.5 Publication reprint

Scaling behavior of non-equilibrium measures in internally driven elastic assemblies

by

G. Gradziuk,[1] F. Mura, [1] and C. P. Broedersz,[1]

[1]Department of Physics, Arnold Sommerfeld Center for Theoretical Physics and Center for NanoScience, Ludwig-Maximilians-Universität München, Theresienstraße 37, 80333 München, Germany.

reprinted from

***Phys. Rev. E.* 99, 052406 ,**
doi:10.1103/PhysRevE.99.052406.

Scaling behavior of nonequilibrium measures in internally driven elastic assemblies

Grzegorz Gradziuk, Federica Mura, and Chase P. Broedersz*

Arnold-Sommerfeld-Center for Theoretical Physics and Center for NanoScience, Ludwig-Maximilians-Universität München, D-80333 München, Germany

(Received 14 January 2019; published 15 May 2019)

Detecting and quantifying nonequilibrium activity is essential for studying internally driven assemblies, including synthetic active matter and complex living systems such as cells or tissue. We discuss a noninvasive approach of measuring nonequilibrium behavior based on the breaking of detailed balance. We focus on "cycling frequencies"—the average frequency with which the trajectories of pairs of degrees of freedom revolve in phase space—and explain their connection with other nonequilibrium measures, including the area enclosing rate and the entropy production rate. We test our approach on simple toy models composed of elastic networks immersed in a viscous fluid with site-dependent internal driving. We prove both numerically and analytically that the cycling frequencies obey a power law as a function of distance between the tracked degrees of freedom. Importantly, the behavior of the cycling frequencies contains information about the dimensionality of the system and the amplitude of active noise. The mapping we use in our analytical approach thus offers a convenient framework for predicting the behavior of two-point nonequilibrium measures for a given activity distribution in the network.

DOI: 10.1103/PhysRevE.99.052406

I. INTRODUCTION

The field of active matter has developed over recent decades to provide a physical description of classical many-body systems operating far from thermodynamic equilibrium [1–3]. A prominent class of such active matter are living systems: Schools of fish [4], flocks of birds [5], and colonies of bacteria [6,7] can all exhibit collective dynamics that are manifestly out of equilibrium. However, the non equilibrium activity of biological assemblies at smaller subcelluar scales is not always straightforward to discern [8,9]. Examples include the stochastic fluctuations of biological assemblies such as chromosomes [10], the cytoskeleton [2,11–14], and cellular membranes [15–17]. Indeed, while these fluctuations can at first sight appear indistinguishable from thermal Brownian motion, they are in many cases driven by energy-consuming processes at molecular scales [1,2,8,9,18,19]. This molecular-scale activity can propagate to mesoscopic scales, giving rise to nonequilibrium dynamics that breaks detailed balance [9,20–25] or that violates the fluctuation dissipation theorem [12,15,16,26–28]. Soft-driven assemblies can also be realized in synthetic systems, including chemical fueled synthetic fibers [29], crystals of active colloidal particles [30], and artificial lipid membranes [31,32]. Numerous experimental studies showed how molecular nonequilibrium processes affect the mesoscopic mechanical properties of *in vivo* biological assemblies [2,11–13], *in vitro* reconstituted cytoskeletal networks [33–35], and synthetic materials [36]. It still remains unclear, however, how to characterize the nonequilibrium fluctuations of soft-driven assemblies.

To make further progress on characterizing active systems, various candidates for a reliable and informative nonequilibrium measure have been proposed. A natural and commonly used measure of the time-irreversibility of a process is the entropy production rate. In some cases, this measure is related to the energy dissipation in a system [37]. Recent studies made significant progress in inferring the entropy production rate from the observed trajectories [25,38,39]. In general, for complex systems it is unclear how to interpret measures of the partial entropy production rate or how to relate the measured quantities to the real entropy production rate of the full system. It is possible, however, to set a lower bound to the total entropy production from the observation of a few mesoscopic degrees of freedom [23,40–43]. An alternative approach of using area enclosing rates (AER) of stochastic trajectories in phase space as a metric for the breaking of detailed balance was presented in Refs. [44] and [45]. A closely related concept—the cycling frequencies of the stochastic trajectory—was used to analyze the nonequilibrium behavior emerging in the mode-space trajectories of a probe filament in an active gel [21,22] or the dynamics of a driven disordered elastic network near its isostatic point [24].

Despite the multitude of available nonequilibrium measures, it is still unclear how to use them to extract useful information about the nature of active driving in a system. The cycling frequencies can be used to investigate the nonequilibrium dynamics emerging on different lengthscales in driven elastic networks [23]. In particular, the cycling frequencies measured from trajectories of two probe particles in an internally driven elastic network display a power-law behavior as function of the distance between the particles, with an exponent that depends on the dimensionality of the system; the prefactor of this scaling law depends on the statistical properties of the internal driving. Thus, these experimentally

*C.broedersz@lmu.de

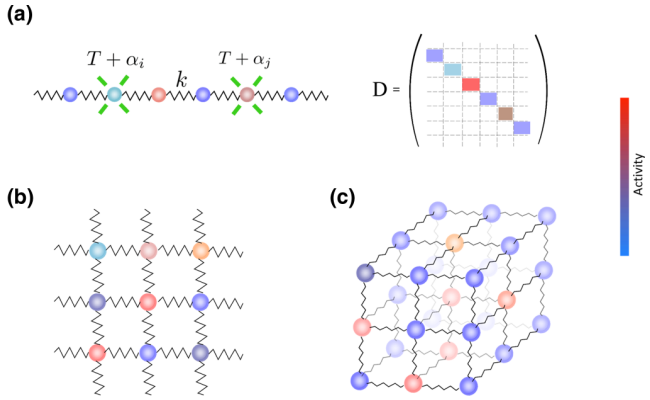

FIG. 1. (a) One-dimensional elastic chain of beads at temperature T with spatially varying white-noise driving intensity α_i, and the corresponding diffusion matrix D. The tracked pair of beads is indicated in green. (b) Two-dimensional and (c) three-dimensional elastic networks investigated in Sec. V A.

accessible cycling frequencies and their associated scaling behavior provide a promising candidate for a nonequilibrium measure that may provide access to properties of the internal driving.

In this work we present a detailed derivation of the scaling behavior of cycling frequencies for d-dimensional elastic networks with internal driving. Thus, we derive a theoretical framework that allows us to relate the cycling frequency to the lengthscale of the observation and to the properties of the network and of the active noise. Furthermore, we clarify the relation between the cycling frequencies and other nonequilibrium measures such as the area enclosing rate and the entropy production rate.

II. DRIVEN ELASTIC NETWORKS

We use overdamped networks of elastically coupled beads suspended in a viscous fluid (see Fig. 1) as a simple model for soft subcellular assemblies, such as a chromosome, a cell membrane, or the cytoskeleton [46–49]. For simplicity we choose units in which the elastic spring constant, the damping coefficient of the beads, and the Boltzmann constant k_B equal 1. The fluid is assumed to be at thermal equilibrium and the resulting thermal fluctuations in the system are thus modeled as Gaussian white noise processes acting independently on all the beads with the same amplitude T. Additional active force fluctuations, which in a biological system would be generated by enzymatic activity, drive the system out of thermal equilibrium. In real systems, the binding kinetics of enzymes such as molecular motors may depend on local structural properties of the network. Consequently, we expect the variance of the stochastic forces that these enzymes generate to depend on local features. We account for this possible spatial heterogeneity implicitly by implementing the active forces as independent Gaussian white noise processes with site-dependent amplitudes α_i. Here we shall only focus on the case of spatially uncorrelated intensities of the noise, but the theoretical framework we present in this paper can also be applied in other scenarios.

By modeling the active forces as "white," we essentially restrict our model to systems in which the correlation times of the active driving are shorter than the intrinsic relaxation times of the network. This model is mathematically equivalent to embedding the beads in local thermal baths at temperatures $T+\alpha_i$ [50].

This simplified description allows us to study the dynamics of the system using a Fokker-Planck equation:

$$\partial_t p(\mathbf{x},t) = -\nabla\cdot(\mathbf{A}\mathbf{x}-\mathbf{D}\nabla)p(\mathbf{x},t) := -\nabla\cdot\mathbf{j}(\mathbf{x},t), \quad (1)$$

where $\mathbf{x}$ represents the displacements of the beads relative to their equilibrium positions, and $p(\mathbf{x},t)$ is the probability distribution of $\mathbf{x}$ at time t. We also assume that the forces are linear in $\mathbf{x}$, i.e., $\mathbf{f}(\mathbf{x}) = \mathbf{A}\mathbf{x}$ with a symmetric matrix $\mathbf{A}$, and $\mathbf{D} = \mathrm{diag}\{T+\alpha_1,\ldots,T+\alpha_N\}$ is the diffusion matrix. The right-hand side of Eq. (1) can be interpreted as the divergence of the probability current density $\mathbf{j}(\mathbf{x},t) = (\mathbf{A}\mathbf{x}-\mathbf{D}\nabla)p(\mathbf{x},t)$. At steady state, the nonvanishing dissipative probability currents constitute a measure of nonequilibrium dynamics in a system and thus play the key role in our approach.

III. CYCLING FREQUENCIES AND PHASE SPACE TORQUE

The steady-state probability currents, $\mathbf{j}(\mathbf{x})$, are mathematical objects that capture the presence of nonequilibrium activity by revealing time-irreversibility of the dynamics at the level of the Fokker-Planck equation. This time-irreversibility manifests through the emergence of a mean velocity field $\mathbf{v}(\mathbf{x})$ in the coordinate space, which is related to the probability current through $\mathbf{j}(\mathbf{x}) = \mathbf{v}(\mathbf{x})p(\mathbf{x})$ [51]. Therefore, from an experimental perspective, an ideal way to quantify the nonequilibrium dynamics of a system would be to measure such a velocity field $\mathbf{v}(\mathbf{x})$. However, inferring the full $\mathbf{v}(\mathbf{x})$ field is a challenge on its own. The most straightforward approaches require a discretization of the phase space. Such a measurement would require tracking many degrees of freedom for long time periods, which is difficult in practice.

Instead of inferring $\mathbf{v}(\mathbf{x})$ in full detail, one can alternatively measure some coarse-grained quantities related to $\mathbf{v}(\mathbf{x})$, which still retain key information about the nonequilibrium dynamics of the system. For instance, we could track a pair of degrees of freedom $\mathbf{x}_r = \{x_i, x_j\}$ and measure the time average of the angular velocity $\langle\dot{\beta}_{ij}\rangle$, or equivalently, the rate at which the trajectory revolves around the origin in this reduced two-dimensional subspace (Fig. 2). This simple measurement does not require any discretization of phase space or inference of the force field. We shall refer to $\langle\dot{\beta}_{ij}\rangle$ as the *cycling frequency*.

In general, $\langle\dot{\beta}_{ij}\rangle$ may contain only limited information about $\mathbf{v}(\mathbf{x})$. For linear systems, however, the mean phase space velocity can be written as [52]

$$\mathbf{v}(\mathbf{x}) = \boldsymbol{\Omega}\mathbf{x}, \quad \boldsymbol{\Omega} = \mathbf{A} + \mathbf{D}\mathbf{C}^{-1}, \quad (2)$$

where $\mathbf{C} = \langle\mathbf{x}\otimes\mathbf{x}\rangle$ is the steady-state covariance matrix obeying the Lyapunov equation

$$\mathbf{A}\mathbf{C} + \mathbf{C}\mathbf{A}^T = -2\mathbf{D}. \quad (3)$$

Equation (2) sets strong constraints on the structure of $\mathbf{v}(\mathbf{x})$: for dynamics projected on any two-dimensional subspace $\{x_i, x_j\}$ the probability currents have an elliptical structure.

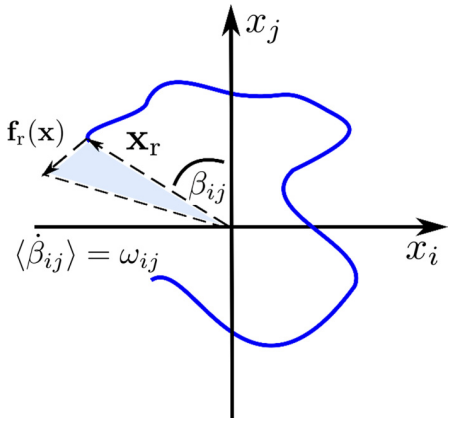

FIG. 2. Schematic trajectory in the coordinate space $[x_i, x_j]$ of two tracer beads. The light blue area enclosed in the triangle represents $\mathbf{x}_\mathrm{r} \times \mathbf{f}_\mathrm{r}(\mathbf{x})/2$ appearing in Eq. (6), which gives the area enclosing rate upon averaging over phase space.

The remaining information about the amplitude of the currents is set by the cycling frequencies $\langle\dot{\beta}_{ij}\rangle$.

To show this, we denote the velocity of the system in the reduced ij-subspace by $\mathbf{v}_\mathrm{r}(\mathbf{x}) = \{v_i(\mathbf{x}), v_j(\mathbf{x})\}$. Note, what we observe while looking at the $\mathbf{x}_r$-subspace only is a conditional mean $\langle\mathbf{v}_\mathrm{r}(\mathbf{x})|\mathbf{x}_r\rangle$. Similar to Eq. (2), we find that $\langle\mathbf{v}_\mathrm{r}(\mathbf{x})|\mathbf{x}_\mathrm{r}\rangle = \mathbf{\Omega}_\mathrm{r}\mathbf{x}_\mathrm{r}$, with $\mathbf{\Omega}_\mathrm{r} = \mathbf{A}_\mathrm{eff} + \mathbf{D}_{[\mathrm{r,r}]}\mathbf{C}^{-1}_{[\mathrm{r,r}]}$ [23]. Here $\mathbf{A}_\mathrm{eff}$ is a matrix such that $\langle\mathbf{f}_\mathrm{r}(\mathbf{x})|\mathbf{x}_\mathrm{r}\rangle = \langle\{f_i(\mathbf{x}), f_j(\mathbf{x})\}|\mathbf{x}_\mathrm{r}\rangle = \mathbf{A}_\mathrm{eff}\mathbf{x}_\mathrm{r}$; note, $\mathbf{C}_{[\mathrm{r,r}]}$ and $\mathbf{D}_{[\mathrm{r,r}]}$ are matrices of size $[2 \times 2]$, given by $\mathbf{C}_{[\mathrm{r,r}]} = \{\{c_{ii}, c_{ij}\}, \{c_{ji}, c_{jj}\}\}$ and $\mathbf{D}_{[\mathrm{r,r}]} = \{\{d_{ii}, d_{ij}\}, \{d_{ji}, d_{jj}\}\}$.

Next, we show that the eigenvalues of $\mathbf{\Omega}_\mathrm{r}$ coincide with the cycling frequencies $\langle\dot{\beta}_{ij}\rangle$. First, note that $\langle\dot{\beta}_{ij}\rangle$ is invariant under orientation preserving linear transformations of the reduced subspace. We can therefore work in *covariance identity coordinates*, $\mathbf{y}_\mathrm{r}$, such that $\mathbf{C}_{[\mathrm{r,r}]} = \mathbf{I}$. In this basis, $\mathbf{\Omega}_\mathrm{r}$ takes a particularly simple form [52]

$$\mathbf{\Omega}_\mathrm{r} = \begin{pmatrix} 0 & \omega_{ij} \\ -\omega_{ij} & 0 \end{pmatrix}, \tag{4}$$

with the imaginary parts of its eigenvalues on the antidiagonal. This form of $\mathbf{\Omega}_\mathrm{r}$ implies that for $\mathbf{C}_{[\mathrm{r,r}]} = \mathbf{I}$, the probability current field has a circular structure. Using Eq. (4), we find that

$$\begin{aligned}\langle\dot{\beta}_{ij}|\mathbf{y}_r\rangle &= \left\langle \frac{\mathbf{y}_\mathrm{r} \times \dot{\mathbf{y}}_\mathrm{r}}{|\mathbf{y}_\mathrm{r}|^2}\middle|\mathbf{y}_\mathrm{r}\right\rangle = \frac{y_2\langle\dot{y}_1|\mathbf{y}_r\rangle - y_1\langle\dot{y}_2|\mathbf{y}_r\rangle}{y_1^2 + y_2^2} \\ &= \frac{y_2\langle v_1(\mathbf{y})|\mathbf{y}_r\rangle - y_1\langle v_2(\mathbf{y})|\mathbf{y}_r\rangle}{y_1^2 + y_2^2} = \omega_{ij}.\end{aligned} \tag{5}$$

This means that the conditional average of the angular velocity $\langle\dot{\beta}_{ij}|\mathbf{y}_r\rangle$ is $\mathbf{y}_r$-independent and equals ω_{ij} at all points in the reduced phase space. Hence, averaging over $\mathbf{y}_\mathrm{r}$ leads to $\langle\dot{\beta}_{ij}\rangle = \omega_{ij}$, with $\omega_{ij}^2 = \det\mathbf{\Omega}_\mathrm{r}$.

Recently, new approaches have been developed to infer current fields in nonlinear systems by considering an expansion of the inferred force field [38]. Up to first order these methods reduce to calculating area enclosing rates, which are indeed closely related to the cycling frequencies, as we discuss further below.

One of our central objectives is to derive a relation between the observed currents and the properties of the system and the active driving. Given that the cycling frequencies are set by ω_{ij}—the imaginary parts of the eigenvalues of $\mathbf{\Omega}_\mathrm{r}$—we can make further progress by showing that for a general linear system [23]

$$\omega_{ij} = \frac{1}{2}\frac{\langle\mathbf{x}_\mathrm{r} \times \mathbf{f}_\mathrm{r}(\mathbf{x})\rangle}{\sqrt{\det\mathbf{C}_r}}, \tag{6}$$

where $\langle\mathbf{x}_\mathrm{r} \times \mathbf{f}_\mathrm{r}(\mathbf{x})\rangle = \langle x_i f_j(\mathbf{x}) - x_j f_i(\mathbf{x})\rangle = (\mathbf{C}\mathbf{A}^T - \mathbf{A}\mathbf{C})_{ij}$ is the mean phase space torque (Fig. 2). Intuitively, Eq. (6) implies that for an overdamped linear system the mean phase space angular velocity is proportional to the mean phase space torque. A detailed derivation is presented in Ref. [23]. Moreover, in covariance identity coordinates Eq. (6) reduces to $\omega_{ij} = \frac{1}{2}(A^T - A)_{ij} = \Omega_{ij}$, in accord with previous studies [21,22,52]. One can equivalently identify $(\mathbf{C}\mathbf{A}^T - \mathbf{A}\mathbf{C})_{ij}$ with mean area enclosing rates in the ij-subspace, as considered in [44]. Here, we focus on the cycling frequencies, since they are more directly related to the probability currents, which constitute the basis of our work. In some instances, however, the area enclosing rates turn out to be particularly advantageous to work with. In these cases we shall briefly discuss how switching to the area enclosing rates simplifies the analysis (see Sec. IV).

Since the cycling frequencies contain information about the amplitudes of the phase space probability currents, they can be related to the entropy production rate. For linear systems, in covariance identity coordinates, the full entropy production rate can be expressed as a weighted sum of the cycling frequencies squared: $\Pi = \sum_{i-\mathrm{odd}}^{n}\omega_{i,i+1}^2[(\mathbf{D}^{-1})_{i,i} + (\mathbf{D}^{-1})_{i+1,i+1}]$. However, in many experimental contexts it is typically impossible to track all the degrees of freedom or to resolve all steps of a process. This practical limitation motivated the introduction of various measures of reduced/apparent entropy production rate [23,40–43]. For the case of a two-point measurement, as the ones discussed in this paper, one can consider a reduced entropy production rate directly related to the cycling frequency: $\Pi_\mathrm{r}^{(2)} = \omega_{ij}^2\mathrm{Tr}(\mathbf{C}_{[\mathrm{r,r}]}\mathbf{D}^{-1}_{[\mathrm{r,r}]})$, which gives a lower bound on the full contribution to the total entropy production rate from the observed pair of degrees of freedom [23].

IV. ONE-DIMENSIONAL CHAIN AND DIFFUSION EQUATION

While Eq. (6) sets a relation between the cycling frequencies observable in an experiment and the properties of both the network and the active noise distribution, it is not straightforward to explicitly derive these properties from the cycling frequencies. In the following sections, we use Eq. (6) to build a framework for extracting specific information about the system from the behavior of the cycling frequencies ω_{ij}.

We first consider the simplest case of a one-dimensional chain of $2N - 1$ beads coupled by harmonic springs. This example will help us build intuition for more complex lattices. To obtain insight into how nonequilibrium behavior manifests at different length scales, we consider a two-point nonequilibrium measure. Specifically, we study how the cycling

frequency in the subspace of displacements of two chosen beads $\{x_i, x_{i+r}\}$ depends on the distance r between these beads. Note that the distance r is expressed in the units of the lattice constant. We study the behavior of the cycling frequencies for two scenarios:

(i) Active noise present only at single site,

(ii) Random spatial distribution of activities $\{\alpha_i\}$.

In case (i) we plot the cycling frequency, $\omega_{\text{single}}(r)$, between the active bead and another bead at distance r. In case (ii) we consider an ensemble of active noise distributions $\{\alpha_i\}$, in which the amplitude of the active noise at each site is drawn randomly from a probability distribution p_α, with mean $\bar{\alpha}$ and variance σ_α^2. The amplitudes α_i are spatially uncorrelated. We then calculate $\langle\omega^2(r)\rangle$—the squared cycling frequency between two beads at distance r averaged over the activity distributions α_i. The first observation is that in both scenarios the cycling frequencies follow a power law as a function of distance, as shown in Fig. 3. The exponent in the random distribution scenario is independent of the probability distribution p_α of the intensities, but different from the single activity case.

To understand the origin of the power-law behavior and to calculate the exponents, we use Eq. (6) to derive analytical expressions for $\omega_{\text{single}}(r)$ and $\langle\omega(r)^2\rangle$. In the case of a one-dimensional chain with spatially uncorrelated noise, the expression for the cycling frequency [Eq. (6)] reduces to

$$\omega_{ij} = \frac{\widetilde{\partial}_2^2 c_{ij}}{\sqrt{\det \mathbf{C}_{[\mathrm{r,r}]}}}, \tag{7}$$

where c_{ij} indicates the elements of the covariance matrix, and $\widetilde{\partial}_2^2 c_{ij}$ denotes the discrete second derivative across rows: $\widetilde{\partial}_2^2 c_{ij} = c_{i,j+1} - 2c_{i,j} + c_{i,j-1}$. Thus, this result reduces the problem of calculating ω_{ij} to finding the covariance matrix $\mathbf{C}$.

Motivated by the structure of $\mathbf{D}$, we decompose $\mathbf{C} = T\overline{\mathbf{C}} + \bar{\alpha}\mathbf{C}^*$ into equilibrium ($\overline{\mathbf{C}}$) and nonequilibrium ($\mathbf{C}^*$) parts [Fig. 4(a)]. For the one-dimensional chain, the Lyapunov equation [see Eq. (3)] is equivalent to

$$\widetilde{\partial}_1^2 \overline{c}_{ij} + \widetilde{\partial}_2^2 \overline{c}_{ij} = -2\delta_{ij}, \tag{8}$$

$$\widetilde{\partial}_1^2 c^*_{ij} + \widetilde{\partial}_2^2 c^*_{ij} = -2\delta_{ij}\frac{\alpha_i}{\bar{\alpha}}. \tag{9}$$

At equilibrium detailed balance is preserved, which implies $\widetilde{\partial}_2^2 \overline{c}_{ij} = 0\ \forall_{i\neq j}$ [see Eq. (7)]. We can therefore replace $\widetilde{\partial}_2^2 c_{ij}$ with $\widetilde{\partial}_2^2 c^*_{ij}$ in Eq. (7). Then, expanding the expression for the cycling frequency in powers of $(\bar{\alpha}/T)$, we get

$$\omega_{ij} = \frac{\bar{\alpha}}{T}\frac{\widetilde{\partial}_2^2 c^*_{ij}}{\sqrt{\det \overline{\mathbf{C}}_{[\mathrm{r,r}]}}} + \mathcal{O}\left(\frac{\bar{\alpha}^2}{T^2}\right). \tag{10}$$

Up to linear order in $(\bar{\alpha}/T)$ the contributions from $\overline{\mathbf{C}}$ and $\mathbf{C}^*$ separate; consequently, ω_{ij} becomes linear in $\{\alpha_i\}$. This linearity appearing in the limit of weak activity will later allow us to calculate cycling frequencies averaged over different realizations of the activity $\{\alpha_i\}$. Note, if instead of ω_{ij}, we consider the area enclosing rates (AER $= \bar{\alpha}\widetilde{\partial}_2^2 c^*_{ij}$), the factor $\sqrt{\det \mathbf{C}_{[\mathrm{r,r}]}}$ does not enter, implying that the expression for the area enclosing rates is linear in $\{\alpha_i\}$ irrespective of the magnitude of $\bar{\alpha}$.

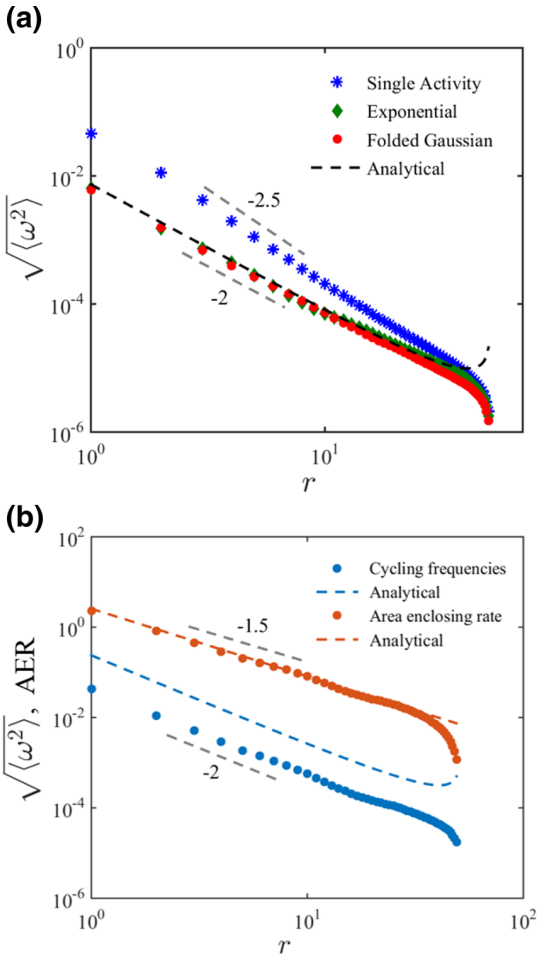

FIG. 3. (a) Scaling behavior of the cycling frequencies as a function of distance between the beads, obtained for a 1D chain with a single activity (blue stars) and with spatial distribution of activities with amplitudes drawn randomly from exponential (green diamonds) and folded Gaussian (red circles) distributions. (b) Comparison between the cycling frequencies (lower blue) and the Area Enclosing Rates (AER) (upper orange) above the weak noise limit ($\bar{\alpha}/T = 4$). All data points correspond to results obtained by numerically solving Lyapunov equation.

A. Activity at a single site

To obtain insight into what determines the cycling frequencies in a concrete example, we first find the solution to Eq. (9) for the case of activity appearing only at a single site in the center of the chain. Later, we will use this solution to construct $\mathbf{C}^*$ for a more general case. For now, let us assume that $\alpha_i = \alpha\delta_{iN}$ and $\bar{\alpha} = \alpha$.

We can think of Eq. (9) as a discretized stationary diffusion equation with a single source with a divergence of 2 in the middle of the $\mathbf{C}^*$ matrix, and with absorbing boundary conditions at the edges. The absorbing boundaries in the diffusion equation reflect the fixed boundary conditions for the elastic chain. We denote by $r = \sqrt{(i-N)^2 + (j-N)^2}$ the distance

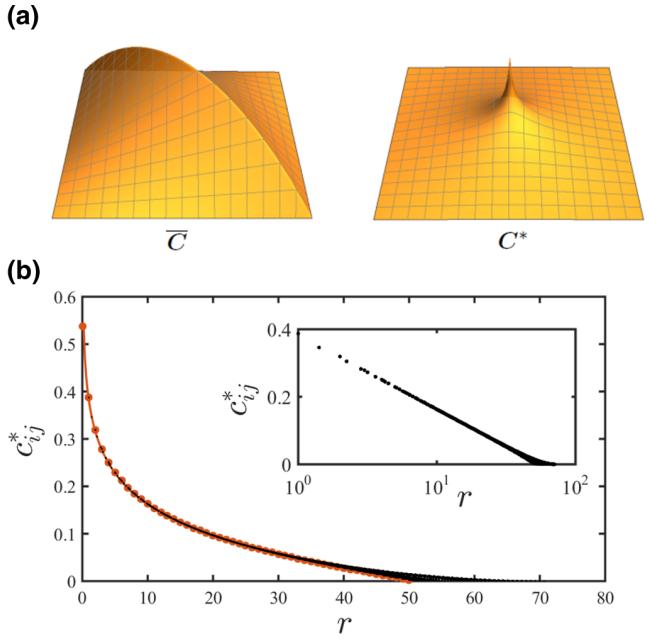

FIG. 4. (a) Profiles of the matrices $\overline{\mathbf{C}}$ and $\mathbf{C}^*$ in the single activity case. For visual purposes, the discrete data points have been interpolated to a 2D surface. $\overline{c}_{ij}$ is linear in both indices, resulting in $\omega_{ij} = 0$ for $\alpha_i = 0$. (b) Values of c^*_{ij} versus the distance from the center of the matrix $r = \sqrt{(i-N)^2 + (j-N)^2}$. Large orange points correspond to the entries at positions (i, N). The inset depicts the same plot in log-linear scale.

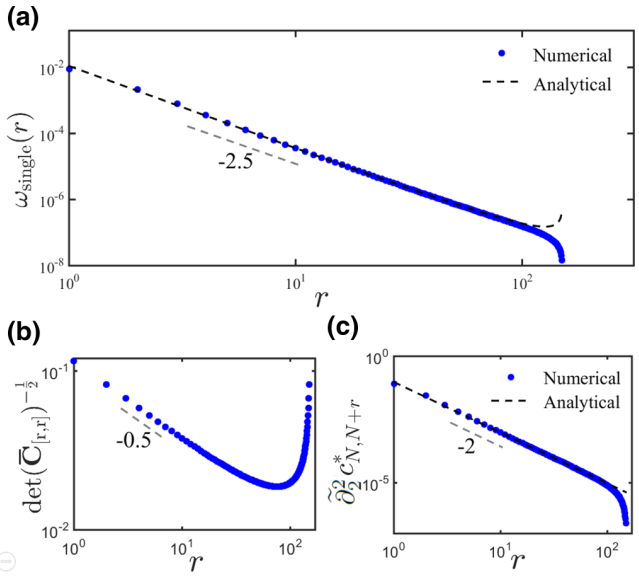

FIG. 5. (a) Scaling behavior of $\omega_{\text{single}}(r)$ as a function of the distance between the beads and comparison with the analytical prediction (dashed line) in Eq. (11). Below, the behavior of the (b) equilibrium and (c) nonequilibrium contributions to $\omega_{\text{single}}(r)$. The contribution presented in (c) coincides with the area enclosing rates. All data points correspond to results obtained by numerically solving Lyapunov equation.

from the center of $\mathbf{C}^*$. If we consider a continuous analog of our discrete problem and neglect the boundary conditions, then we can assume a rotational symmetry of the solution $c^*(r)$. The corresponding continuous diffusion equation takes the form: $\frac{1}{r}\partial_r r \partial_r c^*(r) = 0$. Consequently, $r\partial_r c^*(r) = -a$ and $c^*(r) = -a\ln(r) + b$.

One could also argue for $\partial_r c^*(r) \sim 1/r$ scaling of the "covariance current," by demanding that the total "covariance flux" through a circle of radius r, centered at 0 is independent of r and equals 2—the divergence of the source. This also allows us to identify $a = 1/\pi$. The integration constant b is system-size dependent and has to be set such that the covariance vanishes at the edge of the covariance matrix.

The functional form that we obtain from this approximate analysis accurately describes the actual numerically obtained values of c^*_{ij} far from the boundaries [see Fig. 4(b)]. Note, the deviations that appear close to the boundaries are due to neglecting the absorbing boundary conditions and not due to the discrete nature of the problem. We can also consider a continuous limit of the problem, in which the chain is replaced by a string, by taking the limit $N \to \infty$, $k \to \infty$, while keeping $k/N = \text{const}$. In this limit the discrete diffusion equation is replaced by a continuous one, but the boundary effects still play the same role. We shall return to the continuous limit in Sec. V B, where we discuss more complex networks.

We can use the approximate form of $c^*(r)$ together with Eq. (10) to calculate $\omega_{\text{single}}(r)$. For large N, we can replace $\widetilde{\partial}^2_2 c^*_{N,N+r}$ with $\partial^2_r c^*(r)$, to arrive at

$$\omega_{\text{single}}(r) = \frac{\alpha}{T}\frac{1}{\pi r^2}\frac{1}{\sqrt{\det \overline{\mathbf{C}}_{[\mathrm{r,r}]}(r)}} + \mathcal{O}\left(\frac{\alpha^2}{T^2}\right). \tag{11}$$

Interestingly, it turns out that b, which is in general unknown, does not enter the equation for $\omega(r)$.

To find the equilibrium part $\overline{\mathbf{C}}$, we make the following observation. At equilibrium all cycling frequencies ω_{ij} must vanish, which combined with Eq. (7) gives: $\widetilde{\partial}^2_2 \overline{c}_{ij} = 0\ \forall_{i\neq j}$. Using Eq. (8) at point (i, i) and the symmetry of $\overline{\mathbf{C}}$ we find $\widetilde{\partial}^2_2 \overline{c}_{ii} = -1$. In general, we can therefore write the equation for $\overline{\mathbf{C}}$ as $\widetilde{\partial}^2_2 \overline{c}_{ij} = -\delta_{ij}$. Note that this condition is equivalent to a discrete stationary diffusion equation in one dimension, with a single source at site i and with absorbing boundary conditions. This implies that $\overline{c}_{ij}$ is linear in both indices and one can easily verify that $\overline{c}_{ij} = \min(i, j) - ij/(2N)$ satisfies Eq. (8). Using this solution, we find that $[\det \overline{\mathbf{C}}_{[\mathrm{r,r}]}(r)]^{-\frac{1}{2}} = [\frac{1}{2}r(N-r)]^{-\frac{1}{2}} \sim r^{-\frac{1}{2}}$ for $r \ll N$. Therefore, $\omega_{\text{single}}(r) \sim r^{-\frac{5}{2}}$, as shown together with the numerical results in Fig. 5. The good agreement between the numerical and analytical results allows us to conclude that the scaling exponent is determined by the $\ln(r)$-like profile of $\mathbf{C}^*$, which in turn is set by the dimensionality of the system. One could in principle find an analytical solution for $c^*(r)$ that accounts for the boundary conditions, but the $\ln(r)$ scaling captures the essential features.

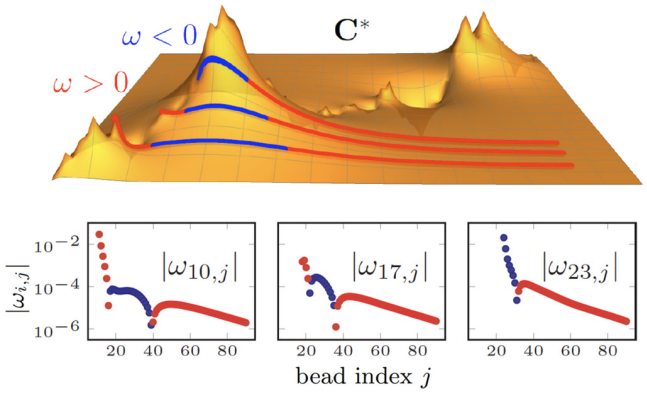

FIG. 6. Profile of $\mathbf{C}^*$ in the case of spatially correlated amplitudes of the active noise, together with the lines $\{(i, j, c^*_{ij})\}_{j=i,\ldots,2N-1}$ for $i = 10, 17, 23$. The color of a line indicates the sign of its curvature. The red (blue) points in the plots of $|\omega_{i,j}|$ correspond to positive (negative) cycling frequencies. Here, the profile of $\mathbf{C}^*$ is presented for activities $\{\alpha_i - \bar{\alpha}\}$. This transformation of activities is justified in Appendix A.

B. Spatially varying activity

Equipped with the results from the previous section, we now consider a system with spatially varying activity. First, we will further clarify the connection between calculating cycling frequencies and solving a discretized steady-state diffusion equation for the covariance function. To this end, we consider a generic activity distribution $\{\alpha_i\}$ and plot the corresponding active part of the covariance matrix $\mathbf{C}^*$ obtained by solving Eq. (9) (see Fig. 6). From the form of Eq. (7), we see that the cycling frequencies $\{\omega_{ij}\}_{j=1,\ldots,2N-1}$ are proportional to the curvature of the line $\{(i, j, c^*_{ij})\}_{j=1,\ldots,2N-1}$, as illustrated by the plots in Fig. 6. The connection with the steady-state diffusion equation [see Eq. (9)] allows us to understand how a given distribution of activities translates to a particular profile of the $\mathbf{C}^*$ matrix and how this in turn determines the behavior of the cycling frequencies.

In general, the amplitudes of the active noise may be spatially correlated. Here, however, we restrict ourselves exclusively to the case of spatially uncorrelated activities, which is valid in the limit of distances larger than the correlation length of the amplitudes. To the "ith" bead we assign a randomly sampled amplitude α_i. We assume all α_i to be pairwise independent and identically distributed with distribution $p(\alpha)$. For simplicity we index the beads so that the bead in the center of the system has index 0. To calculate $\omega(2r) = \omega_{-r,r}$, we need to determine $\widetilde{\partial}^2_2 c^*_{-r,r}$. For a given activity distribution $\{\alpha_i\}$ we can exploit the linearity of Eq. (9) to obtain the corresponding $\mathbf{C}^*(\{\alpha_i\})$ as a superposition of single-source solutions. Thus, we can write

$$\widetilde{\partial}^2_2 c^*_{-r,r}(\{\alpha_i\}) = \sum_z \widetilde{\partial}^2_2 c^*_{-r,r}(\{\alpha_i \delta_{iz}\}). \tag{12}$$

For beads far enough from the boundary, we approximate $\mathbf{C}^*(\{\alpha_i\delta_{ij}\})$ by a logarithmic decay centered at (j, j) to obtain

$$\begin{aligned}\widetilde{\partial}^2_2 c^*_{-r,r}(\{\alpha_i\delta_{iz}\}) &= \frac{1}{\pi}\frac{\alpha_z}{\bar{\alpha}}\frac{(r+z)^2-(r-z)^2}{[(r+z)^2+(r-z)^2]^2} \\ &= \frac{1}{\pi}\frac{\alpha_z}{\bar{\alpha}}\frac{rz}{(r^2+z^2)^2}.\end{aligned} \tag{13}$$

Combining Eqs. (12) and (13), we calculate $\langle[\widetilde{\partial}^2_2 c^*_{-r,r}(\{\alpha_i\})]^2\rangle$, which is the main factor in the expression for $\langle\omega^2(2r)\rangle$.

$$\begin{aligned}(\pi\bar{\alpha})^2\langle[\widetilde{\partial}^2_2 c^*_{-r,r}(\{\alpha_i\})]^2\rangle &= \left\langle\left[\sum_z \frac{rz\alpha_z}{(r^2+z^2)^2}\right]\left[\sum_{z'}\frac{rz'\alpha_{z'}}{(r^2+z'^2)^2}\right]\right\rangle = \sum_z \frac{r^2z^2\langle\alpha_z^2\rangle}{(r^2+z^2)^4} + \sum_z \frac{rz\langle\alpha_z\rangle}{(r^2+z^2)^2}\sum_{z'\neq z}\frac{rz'\langle\alpha_{z'}\rangle}{(r^2+z'^2)^2} \\ &= \sum_z \frac{r^2z^2\left(\langle\alpha_z^2\rangle - \langle\alpha_z\rangle^2\right)}{(r^2+z^2)^4} \approx \sigma_\alpha^2\int_{-\infty}^{\infty}\frac{r^2z^2dz}{(r^2+z^2)^4} = \frac{\pi\sigma_\alpha^2}{16r^3}.\end{aligned} \tag{14}$$

In the second line of this result, we used that $\sum_{z'\neq z}\frac{rz'}{(r^2+z'^2)^2} = -\frac{rz}{(r^2+z^2)^2}$ and approximated the sum by an integral. Evaluating the integral and rescaling $2r \to r$, we arrive at the final result:

$$\langle\omega^2(r)\rangle_\alpha = \frac{\sigma_\alpha^2}{T^2}\frac{1}{2\pi r^3}\frac{1}{\det\overline{\mathbf{C}}_{[\mathrm{r,r}]}(r)}. \tag{15}$$

Given the asymptotic behavior $1/\det\overline{\mathbf{C}}_{[\mathrm{r,r}]}(r) \sim r^{-1}$ for $r \ll N$ we conclude that in the limit of weak activity $\sqrt{\langle\omega^2(r)\rangle} \sim r^{-2}$ (see Fig. 3). Importantly, apart from reproducing the observed exponent of the power law, our result gives a correct prediction for the prefactor, which contains information about the variance of the active forces.

V. d-DIMENSIONAL LATTICES

A. Cubic lattice

To explain the origin of the scaling behavior of $\omega(r)$ for multidimensional networks we now focus on the simplest possible case of a d-dimensional cubic lattice. Importantly, the calculation presented for this case also provides us with intuition for more complex lattices. Let us denote the bead indices corresponding to d independent directions with $n_1, \ldots, n_d$. We will denote the elements of the covariance matrix $\mathbf{C}$ as $c_{n_1,\ldots,n_d;\bar{n}_1,\ldots,\bar{n}_d} := c_{\mathbf{n},\bar{\mathbf{n}}}$. We assume zero-restlength for the springs, so that the degrees of freedom corresponding to different directions decouple. Therefore, by $\mathbf{C}$ we actually mean the covariance matrix of only these degrees of freedom that correspond to a single chosen direction, for instance the one corresponding to the index n_1.

For this particular network, the Lyapunov equation is equivalent to

$$\left(\sum_{i=1}^{d}\tilde{\partial}_{n_i}^2+\sum_{i=1}^{d}\tilde{\partial}_{\bar{n}_i}^2\right)c_{\mathbf{n},\bar{\mathbf{n}}}=-2d_{\mathbf{n},\bar{\mathbf{n}}}. \tag{16}$$

Similar to the one-dimensional case, here we recognize a discretized stationary diffusion equation in $2d$ dimensions, with the divergence of the sources given by the elements of $\mathbf{D}$. For convenience we index the beads such that the one in the middle of the lattice is $(0,\ldots,0)$.

Our goal is to calculate the cycling frequency $\omega_{r,\ldots,r;-r,\ldots,-r}=\omega(2\sqrt{d}r)$. Here we consider a particular case of relative position of the beads with respect to the principal directions of the lattice. It turns out, however, that the final result depends only on the distance between the beads. From Eq. (6), we find that

$$\omega_{r,\ldots,r;-r,\ldots,-r}\approx\frac{(\bar{\alpha}/T)}{\sqrt{\det\overline{\mathbf{C}}_{[\mathrm{r,r}]}}}\sum_{i=1}^{d}\tilde{\partial}_{n_i}^2 c^*_{\mathbf{n},\bar{\mathbf{n}}}\big|_{r,\ldots,r;-r,\ldots,-r}. \tag{17}$$

Following the procedure used for the one-dimensional chain, we begin with finding the solution to a single source problem with one active bead at site $(0,\ldots,0)$. As before, we will then use this solution as a Green's function for our diffusion problem with a generic activity distribution.

Taking a continuous limit of the diffusion equation and neglecting the boundary conditions, we expect that $\partial_r c(r)\sim 1/r^{2d-1}$ and consequently $c(r)\sim 1/r^{2d-2}$, where r is the distance from the center of the $2d$-dimensional covariance matrix. Therefore, for a single active bead at site $(0,\ldots,0)$, we obtain

$$c^*_{\mathbf{n},\bar{\mathbf{n}}}=a_d\left(\sum_{i=1}^{d}n_i^2+\sum_{i=1}^{d}\bar{n}_i^2\right)^{-(d-1)}=a_d(\mathbf{n}^2+\bar{\mathbf{n}}^2)^{-(d-1)}. \tag{18}$$

The constant $a_d=(d-2)!/(2\pi^d)$ can be obtained from the divergence theorem, as we did in the one-dimensional case.

The contribution to $\omega_{\mathbf{n},\bar{\mathbf{n}}}$ from a single activity at site $(0,\ldots,0)$ is then given by (Appendix A)

$$\sum_{i=1}^{d}\partial_{n_i}^2 c^*_{\mathbf{n},\bar{\mathbf{n}}}=2d(d-1)a_d\frac{\mathbf{n}^2-\bar{\mathbf{n}}^2}{(\mathbf{n}^2+\bar{\mathbf{n}}^2)^{d+1}}. \tag{19}$$

Performing calculations analogous to those for the one-dimensional chain, we arrive at (Appendix A)

$$\left\langle\omega_{d=2}^2(r)\right\rangle_\alpha=\frac{\sigma_\alpha^2}{T^2}\frac{8}{5\pi^3 r^6}\frac{1}{\det\overline{\mathbf{C}}_{[\mathrm{r,r}]}}, \tag{20}$$

$$\left\langle\omega_{d=3}^2(r)\right\rangle_\alpha=\frac{\sigma_\alpha^2}{T^2}\frac{27}{8\pi^4 r^9}\frac{1}{\det\overline{\mathbf{C}}_{[\mathrm{r,r}]}}. \tag{21}$$

Importantly, we obtain exactly the same results when considering different directions across the lattice, such as $\omega_{(r,0,\ldots,0),(-r,0,\ldots,0)}$. In general, for a d-dimensional lattice we expect

$$\partial_r^2 c(r)\sim r^{-2d}, \tag{22}$$

$$\omega^2_{\mathrm{single},d}(r)\sim r^{-4d}/\det\overline{\mathbf{C}}_{[\mathrm{r,r}]}(r), \tag{23}$$

$$\langle\omega_d^2(r)\rangle_\alpha\sim r^{-3d}/\det\overline{\mathbf{C}}_{[\mathrm{r,r}]}(r). \tag{24}$$

For completeness we investigate the behavior of $\det\overline{\mathbf{C}}_{[\mathrm{r,r}]}(r)$ for different dimensions. At equilibrium all cycling frequencies vanish, leading to

$$\sum_{i=1}^{d}\tilde{\partial}_{n_i}^2\bar{c}_{\mathbf{n},\bar{\mathbf{n}}}=0\quad\forall_{\mathbf{n}\neq\bar{\mathbf{n}}}. \tag{25}$$

For all points on the diagonal of the covariance matrix $(\mathbf{n},\mathbf{n})=(n_1,\ldots,n_d;n_1,\ldots,n_d)$ the diffusion equation [see Eq. (16)] reads

$$\sum_{i=1}^{d}\tilde{\partial}_{n_i}^2\bar{c}_{\mathbf{n},\mathbf{n}}+\sum_{i=1}^{d}\tilde{\partial}_{\bar{n}_i}^2\bar{c}_{\mathbf{n},\mathbf{n}}=-2. \tag{26}$$

Using the symmetry of the system, we conclude that the two sums in Eq. (26) are equal, which together with Eq. (25) imply that

$$\left(\sum_{i=1}^{d}\tilde{\partial}_{n_i}^2\right)\bar{c}_{\mathbf{n},\bar{\mathbf{n}}}=-\delta_{\mathbf{n},\bar{\mathbf{n}}} \tag{27}$$

for all points $(\mathbf{n},\bar{\mathbf{n}})$. This result can be interpreted in the following way: for a given $(\bar{n}_1,\ldots,\bar{n}_d)$, $\bar{c}_{\mathbf{n},\bar{\mathbf{n}}}$ as a function of $(n_1,\ldots,n_d)$ is a solution to a d-dimensional discretized stationary diffusion equation with a single source at position $(\bar{n}_1,\ldots,\bar{n}_d)$, and with absorbing boundary conditions. Note, there is an interesting symmetry of the diffusion equation implied by the symmetry $\bar{c}_{\mathbf{n},\bar{\mathbf{n}}}=\bar{c}_{\bar{\mathbf{n}},\mathbf{n}}$: the solution at point $\mathbf{n}$ from a source at point $\bar{\mathbf{n}}$ is equal to the solution at point $\bar{\mathbf{n}}$ from a source at point $\mathbf{n}$. While this property of the diffusion equation would be obvious in an infinite space, it surprisingly holds also in the presence of absorbing boundaries.

It can further be shown that

$$\bar{c}_{\mathbf{n},\bar{\mathbf{n}}}\sim\ln[(n_1-\bar{n}_1)^2+(n_2-\bar{n}_2)^2]\quad\text{for } d=2,$$
$$\bar{c}_{\mathbf{n},\bar{\mathbf{n}}}\sim\left[\sum_{i=1}^{d}(n_i-\bar{n}_i)^2\right]^{-\left(\frac{d-2}{2}\right)}\quad\text{for } d>2. \tag{28}$$

This result can also be understood using a simple dimensionality argument: A diffusion problem in d dimensions with a source forming a d_s-dimensional plane can be mapped to a $(d-d_s)$-dimensional diffusion problem with a point source. In our case we are dealing with a diffusion problem in a $2d$-dimensional space, with a d-dimensional source. Reducing the $2d$-dimensional problem to a point source problem in d dimensions, we arrive exactly at Eq. (28). From this equation we conclude that for dimensions $d\geqslant 2$, the diagonal terms of $\overline{\mathbf{C}}_{[\mathrm{r,r}]}(r)$ strongly dominate over the off-diagonal ones. In fact one can verify that for dimensions $d\geqslant 2$ and for systems large enough $\det\overline{\mathbf{C}}_{[\mathrm{r,r}]}(r)$ depends on r only weakly and does not influence the scaling behavior of $\omega^2(r)$ anymore (see Fig. 7). This is a consequence of the shorter range of elastic interactions in higher dimensions.

It is important to note here that, as discussed after introducing Eq. (10), the area enclosing rates do not depend on $\det\mathbf{C}_{[\mathrm{r,r}]}$. This allows us to perform calculations analogous to the ones presented in this section, without assuming the limit of weak activities. As a result we predict a scaling $\sigma_\alpha r^{-3d/2}$

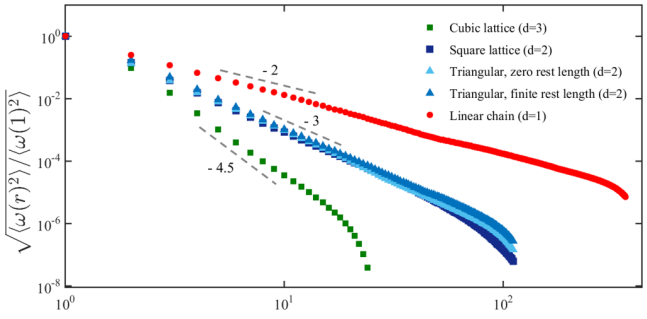

FIG. 7. Scaling behavior of the cycling frequencies as function of the distance between the beads. The results are obtained for different lattices and a folded Gaussian activity distribution [23]. Triangles, big squares, and small squares represent triangular, square, and cubic lattices, respectively. Light (dark) blue triangles represent triangular networks with zero (finite) rest length springs. In all cases we used $\frac{\bar{\alpha}}{T} = 0.15$. For computational convenience we determined the ensemble average by performing a spatial average. All data points correspond to results obtained by numerically solving Lyapunov equation.

for the area enclosing rates even for high amplitudes of the active noise.

B. Generic lattices

In Sec. V A we investigated the simplest possible case of a d-dimensional zero-rest length cubic lattice $\mathcal{L}^d$. For such systems the Lyapunov equation for the covariance matrix could be viewed as a discretized steady-state diffusion equation defined on a space $\mathcal{L}^d \times \mathcal{L}^d \sim \mathcal{L}^{2d}$. For instance, for a two-dimensional square lattice we had to solve a diffusion equation in a four-dimensional cube. A natural question is how general the connection is between the Lyapunov equation and diffusion equations. It turns out that for many zero-rest length lattices there is simple procedure for translating a particular lattice structure to a corresponding diffusion equation for the covariance. The condition which allows us to identify the terms appearing in the Lyapunov equation with second derivatives, as in Eq. (9), is that at all sites of the lattice a spring pointing in one direction is accompanied by a spring pointing in the opposite direction. If this is the case, then we can directly read out the diffusion equation from the structure of the lattice, as illustrated in Fig. 8. Each such pair of springs gives rise to diffusive terms in the corresponding directions, with diffusion constant proportional to the spring constant.

In the case of finite rest length elastic networks with linearized forces, the same condition allows us to write the Lyapunov equation as a discretized second order partial differential equation for the covariance. Importantly, the displacements in x and y directions are no longer decoupled and one has to solve a differential equation for three different covariances: c^{xx}, c^{xy}, c^{yy}. An example of such an equation for a two-dimensional triangular lattice is included in Appendix B. Importantly, the structure of the network determines not only the equation for the covariance matrix but also the cycling frequencies according to Eq. (6).

For a wide range of networks, including randomly diluted networks [24], the condition given above is not satisfied and

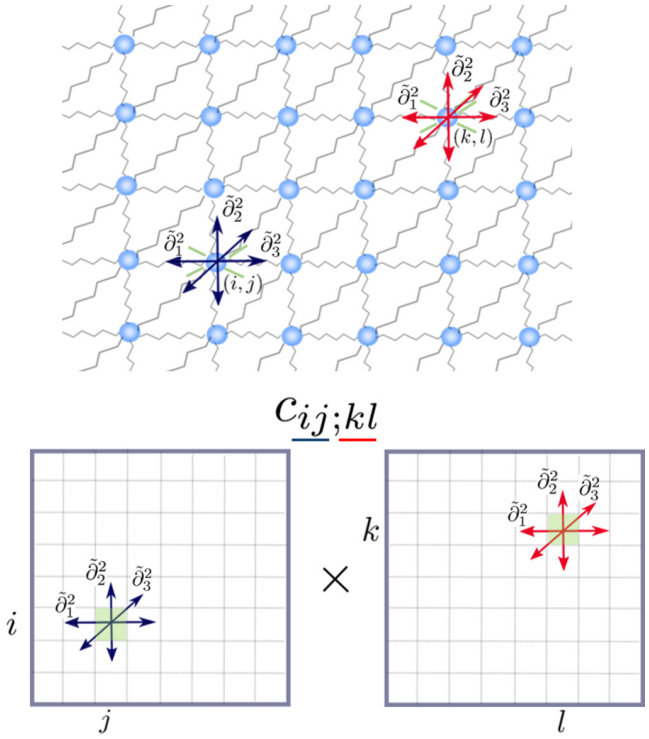

FIG. 8. An exemplary lattice for which the Lyapunov equation can be interpreted as a diffusion equation with nonisotropic diffusion. The presented lattice is equivalent to the triangular lattice, if we consider them in the zero-rest length case.

there is no straightforward way of translating the Lyapunov equation to a continuous diffusionlike equation for the covariance. Nevertheless, for a given network $\mathcal{G}$, which can be thought of as a graph, we can still interpret the Lyapunov equation as a Poisson equation on a graph $\mathcal{G} \times \mathcal{G}$ and relate the cycling frequency between a pair of degrees of freedom to the covariance flux through a corresponding vertex of $\mathcal{G} \times \mathcal{G}$. The theory of graph Laplacians, introduced by Kirchhoff in his study of the properties of resistor networks, has found applications in elasticity theory, graph theory, and computer science [53–56].

Our numerical calculations reveal that the exponents of the power laws for the cycling frequencies observed for various lattices are set by the dimensionality of the system and are independent of the detailed structure of the lattice [23]. Heuristically, this can be understood as follows: any d-dimensional rigid network, with a given average coordination number can be seen as an approximation to a continuous d-dimensional elastic medium. For such an elastic medium, a continuous diffusion equation, as the one we used to study d-dimensional cubic lattices, would be an exact equation for the covariance field, and we conjecture that the cycling frequencies for a continuous medium can be obtained by taking appropriate limits of our results for a discrete system. Note that a study of the cycling frequencies directly at the level of a continuous system would require introducing the Fokker-Planck equation for fields and make the analysis considerably more difficult. Since our results presented for the d-dimensional cubic lattice should coincide with the results for a d-dimensional

continuous medium, we argue that our analytical calculation captures the essential origins of the power-law phenomenon for all lattices that approximate a continuous medium well.

VI. CONCLUSIONS

Here we considered a simple model of an internally driven elastic assembly. Using this model, we investigated the properties of cycling frequencies—a two-point measure of nonequilibrium dynamics, which can be used in experimental and theoretical studies of active systems. We discussed how to relate the cycling frequencies to other commonly used nonequilibrium measures, such as the area enclosing rates or the reduced entropy production rate. Furthermore, based on our analytical approach, reinforced with numerical results, we predict that the cycling frequencies follow a power law as a function of distance between the two probes in an elastic network. The exponent of the power law depends on the dimensionality of the system, but not on the detailed structure of the network. In the case of a random spatial distribution of activities, we showed that the mean cycling frequencies $\sqrt{\langle\omega^2(r)\rangle}$ are proportional to the standard deviation of the intensities of the active noise σ_α. Interestingly, the case of a single-site activity gives a different exponent than the one with randomly distributed activities.

For more complex activity distributions, the connection between the Lyapunov equation and a diffusion equation, that we presented in Secs. IV and V B, provides some intuition for how the cycling frequencies in a system depend on the structure of the active noise. Since the diffusive terms in the Lyapunov equation originate solely from the structure of the lattice, we expect that a similar framework can be used to study the behavior of the cycling frequencies for more complex distributions of the active noise, which include spatial correlations [57].

The analytical approach we developed aims at finding a mapping between the properties of the active noise and two-point nonequilibrium measures. Based on the results we obtained and their robustness to the detailed structure of a network, we argue that the cycling frequencies and the area enclosing rates are promising tools for studying the nature of the stochastic driving in an active elastic assembly. Examples of numerical studies of actively driven elastic assemblies in which the nonequilibrium measures presented in our work could be applied include [58–61]. Experimentally our approach can be tested on reconstituted actomyosin networks [33–35] and other noise-driven biological [10,15,16] or synthetic systems [29–32,36], which can be well approximated by an elastic assembly at steady state. Such experiments could be performed in chromosomes, membranes, or tissues, using embedded colloidal particles or fluorescently tagged cellular organelles.

ACKNOWLEDGMENTS

We thank F. Gnesotto, B. Remlein, and P. Ronceray for many stimulating discussions. This work was supported by the German Excellence Initiative via the program NanoSystems Initiative Munich (NIM), the Graduate School of Quantitative Biosciences Munich (QBM), and was funded by the Deutsche Forschungsgemeinshaft (DFG, German Research Foundation), Grant No. 418389167.

APPENDIX A: CALCULATION FOR A D-DIMENSIONAL ZERO-RESTLENGTH CUBIC LATTICE

First we find the profile of the $\mathbf{C}^*$ matrix for the case of a single activity at site $(0,\ldots,0)$. Neglecting the boundary conditions and assuming a rotational symmetry of the solution we find

$$c^*_{\mathbf{n},\bar{\mathbf{n}}} = a_d\left(\sum_{i=1}^{d} n_i^2 + \sum_{i=1}^{d}\bar{n}_i^2\right)^{-(d-1)}, \quad \text{with} \quad a_d = \frac{(d-2)!}{2\pi^d}, \tag{A1}$$

$$\partial_{n_i} c^*_{\mathbf{n},\bar{\mathbf{n}}} = -(d-1)a_d\frac{2n_i}{\left(n_1^2+\ldots+\bar{n}_d^2\right)^d}, \tag{A2}$$

$$\partial^2_{n_i} c^*_{\mathbf{n},\bar{\mathbf{n}}} = d(d-1)a_d\frac{4n_i^2}{\left(n_1^2+\ldots+\bar{n}_d^2\right)^{d+1}} - (d-1)a_d\frac{2}{\left(n_1^2+\ldots+\bar{n}_d^2\right)^d} \tag{A3}$$

$$= \frac{2(d-1)a_d}{\left(n_1^2+\ldots+\bar{n}_d^2\right)^{d+1}}\left[2dn_i^2 - \left(n_1^2+\ldots+\bar{n}_d^2\right)\right]. \tag{A4}$$

Adding contributions from the all the second derivatives appearing in Eq. (17) we get

$$\sum_{i=1}^{d}\partial^2_{n_i} c^*_{\mathbf{n},\bar{\mathbf{n}}} = 2d(d-1)a_d\frac{\left[\left(n_1^2+\ldots+n_d^2\right)-\left(\bar{n}_1^2+\ldots+\bar{n}_d^2\right)\right]}{\left(n_1^2+\ldots+\bar{n}_d^2\right)^{d+1}} = 2d(d-1)a_d\frac{\mathbf{n}^2-\bar{\mathbf{n}}^2}{(\mathbf{n}^2+\bar{\mathbf{n}}^2)^{d+1}}. \tag{A5}$$

To get an expression for $\sum_{i=1}^{d}\partial^2_{x_i} c$ in the case of one active bead at site $(z_1,\ldots,z_d)$, one simply has to substitute $n_i \to (n_i - z_i)$, $\bar{n}_i \to (\bar{n}_i - z_i)$ in Eq. (A5). Therefore, the contribution to ω from an activity $\alpha_{z_1,\ldots,z_d}$ at site $(z_1,\ldots,z_d)$ reads

$$\sum_{i=1}^{d}\partial^2_{n_i} c_{r,\ldots,r;-r,\ldots,-r} = 2d(d-1)a_d\frac{\sum_{i=1}^{d}(r-z_i)^2 - \sum_{i=1}^{d}(-r-z_i)^2}{\left(\sum_{i=1}^{d}(r-z_i)^2 + \sum_{i=1}^{d}(-r-z_i)^2\right)^{d+1}}\alpha_{z_1,\ldots,z_d} \tag{A6}$$

$$= 2d(d-1)a_d \frac{\sum_{i=1}^{d}(-4rz_i)}{\left(2r^2d + 2\sum_{i=1}^{d} z_i^2\right)^{d+1}} \alpha_{z_1,\ldots,z_d} \tag{A7}$$

$$= -\frac{d(d-1)a_d}{2^{d-2}} \frac{\sum_{i=1}^{d} rz_i}{\left(r^2d + \sum_{i=1}^{d} z_i^2\right)^{d+1}} \alpha_{z_1,\ldots,z_d}. \tag{A8}$$

Finally, we can proceed to calculating $\langle \omega^2(2\sqrt{d}\, r)\rangle$:

$$\left\langle \left(\sum_{z_1,\ldots,z_d} \frac{\left(\sum_{i=1}^{d} rz_i\right)\alpha_{z_1,\ldots,z_d}}{\left(r^2d + \sum_{i=1}^{d} z_i^2\right)^{d+1}} \right) \left(\sum_{\tilde{z}_1,\ldots,\tilde{z}_d} \frac{\left(\sum_{i=1}^{d} r\tilde{z}_i\right)\alpha_{\tilde{z}_1,\ldots,\tilde{z}_d}}{\left(r^2d + \sum_{i=1}^{d} \tilde{z}_i^2\right)^{d+1}} \right) \right\rangle \tag{A9}$$

$$\overset{(1)}{=} \sum_{z_1,\ldots,z_d} \frac{\left(\sum_{i=1}^{d} rz_i\right)^2 \sigma_\alpha^2}{\left(r^2d + \sum_{i=1}^{d} z_i^2\right)^{2d+2}} \overset{(2)}{=} \sum_{z_1,\ldots,z_d} \frac{\sum_{i=1}^{d} r^2 z_i^2 \sigma_\alpha^2}{\left(r^2d + \sum_{i=1}^{d} z_i^2\right)^{2d+2}} \tag{A10}$$

$$\overset{\text{cont.}}{\approx} \int_{z_1,\ldots,z_d} \frac{\sum_{i=1}^{d} r^2 z_i^2 \sigma_\alpha^2}{\left(r^2d + \sum_{i=1}^{d} z_i^2\right)^{2d+2}}. \tag{A11}$$

Step (1) follows from $\langle \alpha_{z_1,\ldots,z_d} \alpha_{\tilde{z}_1,\ldots,\tilde{z}_d}\rangle = \sigma_\alpha^2 \delta_{z_1,\tilde{z}_1} \cdots \delta_{z_d,\tilde{z}_d}$. Thereby we have assumed that $\bar{\alpha} = 0$. This can be achieved by replacing the noise amplitudes α_i with $\alpha_i - \bar{\alpha}$. This transformation is justified, because any shift of the active noise amplitudes by a constant value does not affect $\widetilde{\partial}^2 c_{ij}^*$ (compare with $\widetilde{\partial}^2 \bar{c}_{ij} = 0\ \forall_{i\neq j}$). Note that $\alpha_i - \bar{\alpha}$ are introduced just for convenience and one should not think of them as of any noise amplitudes. Step (2) results from the fact that the terms odd in z_i sum up to 0. In the last step we approximated the sum by an integral.

APPENDIX B: CALCULATION FOR FINITE RESTLENGTH TRIANGULAR LATTICE

Here we derive equation for the covariance matrix for the case of a finite restlength triangular lattice. We index the beads in the lattice as shown in Fig. 9. Let us denote by f_{ij}^x and f_{ij}^y the x and y components of the force acting on bead (i, j), and by x_{ij}, y_{ij} the x and y displacements of bead (i, j). Expanding the force up to linear order in displacements we find

$$\begin{aligned} f_{ij}^x &= \alpha(x_{i-1,j-1} + x_{i+1,j+1} - 2x_{i,j} + x_{i-1,j} + x_{i+1,j} - 2x_{i,j}) + (x_{i,j-1} + x_{i,j+1} - 2x_{i,j}) \\ &\quad - \beta(y_{i-1,j-1} + y_{i+1,j+1} - 2y_{i,j}) + \beta(y_{i-1,j} + y_{i+1,j} - 2y_{i,j}), \\ f_{ij}^y &= \gamma(y_{i-1,j-1} + y_{i+1,j+1} - 2y_{i,j} + y_{i-1,j} + y_{i+1,j} - 2y_{i,j}) \\ &\quad - \delta(x_{i-1,j-1} + x_{i+1,j+1} - 2x_{i,j}) + \delta(x_{i-1,j} + x_{i+1,j} - 2x_{i,j}), \end{aligned}$$

with $\alpha = 1/4$, $\beta = \sqrt{3}/4$, $\gamma = 3/4$, $\delta = \sqrt{3}/4$. It is convenient to rewrite the Lyapunov equation in the following way:

$$-2\mathbf{D} = \mathbf{AC} + \mathbf{CA} = \langle \mathbf{A}\mathbf{x}\mathbf{x}^T + \mathbf{x}(\mathbf{A}\mathbf{x})^T\rangle = \langle \mathbf{f}\mathbf{x}^T + \mathbf{x}\mathbf{f}^T\rangle. \tag{B1}$$

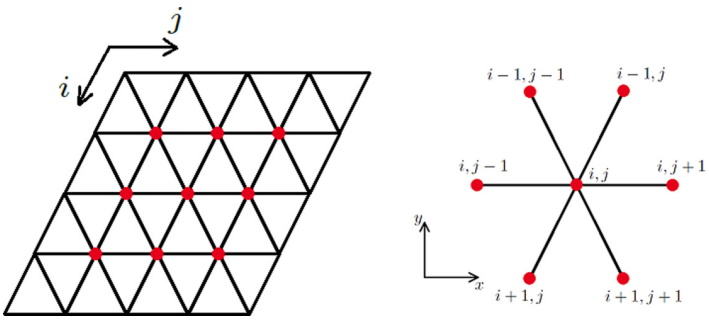

FIG. 9. Triangular lattice and indexing of beads.

Let us denote the elements of the covariance matrix by: $\langle x_{ij}x_{kl}\rangle = c^{xx}_{ij;kl}$, $\langle x_{ij}y_{kl}\rangle = c^{xy}_{ij;kl}$, $\langle y_{ij}y_{kl}\rangle = c^{yy}_{ij;kl}$ and introduce the discrete derivative operators:

$$\tilde{\partial}_1^2 c_{ij;kl} = c_{i-1,j;k,l} - 2c_{i,j;k,l} + c_{i+1,j;k,l}, \qquad \tilde{\partial}_{\bar{1}}^2 c_{ij;kl} = c_{i,j;k-1,l} - 2c_{i,j;k,l} + c_{i,j;k+1,l},$$
$$\tilde{\partial}_2^2 c_{ij;kl} = c_{i,j-1;k,l} - 2c_{i,j;k,l} + c_{i,j+1;k,l}, \qquad \tilde{\partial}_{\bar{2}}^2 c_{ij;kl} = c_{i,j;k,l-1} - 2c_{i,j;k,l} + c_{i,j;k,l+1},$$
$$\tilde{\partial}_3^2 c_{ij;kl} = c_{i-1,j-1;k,l} - 2c_{i,j;k,l} + c_{i+1,j+1;k,l}, \qquad \tilde{\partial}_{\bar{3}}^2 c_{ij;kl} = c_{i,j;k-1,l-1} - 2c_{i,j;k,l} + c_{i,j;k+1,l+1}.$$

Then, the Lyapunov equation translates to

$$\left\langle f^x_{ij}x_{kl} + x_{ij}f^x_{kl}\right\rangle = \left[\alpha\left(\tilde{\partial}_3^2 + \tilde{\partial}_1^2\right) + \tilde{\partial}_2^2\right]c^{xx}_{ij;kl} - \beta\left(\tilde{\partial}_3^2 - \tilde{\partial}_1^2\right)c^{yx}_{ij;kl} + \left[\alpha\left(\tilde{\partial}_{\bar{3}}^2 + \tilde{\partial}_{\bar{1}}^2\right) + \tilde{\partial}_{\bar{2}}^2\right]c^{xx}_{ij;kl} - \beta\left(\tilde{\partial}_{\bar{3}}^2 - \tilde{\partial}_{\bar{1}}^2\right)c^{xy}_{ij;kl} = -2\delta_{(ij),(kl)}d_{ij}, \tag{B2}$$

$$\left\langle f^x_{ij}y_{kl} + x_{ij}f^y_{kl}\right\rangle = \left[\alpha\left(\tilde{\partial}_3^2 + \tilde{\partial}_1^2\right) + \tilde{\partial}_2^2\right]c^{xy}_{ij;kl} - \beta\left(\tilde{\partial}_3^2 - \tilde{\partial}_1^2\right)c^{yy}_{ij;kl} + \gamma\left(\tilde{\partial}_{\bar{3}}^2 + \tilde{\partial}_{\bar{1}}^2\right)c^{xy}_{ij;kl} - \delta\left(\tilde{\partial}_{\bar{3}}^2 - \tilde{\partial}_{\bar{1}}^2\right)c^{xx}_{ij;kl} = 0, \tag{B3}$$

$$\left\langle f^x_{ij}y_{kl} + x_{ij}f^y_{kl}\right\rangle = \left[\alpha\left(\tilde{\partial}_3^2 + \tilde{\partial}_1^2\right) + \tilde{\partial}_2^2\right]c^{yx}_{ij;kl} - \beta\left(\tilde{\partial}_3^2 - \tilde{\partial}_1^2\right)c^{yy}_{ij;kl} + \gamma\left(\tilde{\partial}_3^2 + \tilde{\partial}_1^2\right)c^{yx}_{ij;kl} - \delta\left(\tilde{\partial}_3^2 - \tilde{\partial}_1^2\right)c^{xx}_{ij;kl} = 0, \tag{B4}$$

$$\left\langle f^y_{ij}y_{kl} + y_{ij}f^y_{kl}\right\rangle = \gamma\left(\tilde{\partial}_3^2 + \tilde{\partial}_1^2\right)c^{yy}_{ij;kl} - \delta\left(\tilde{\partial}_3^2 - \tilde{\partial}_1^2\right)c^{xy}_{ij;kl} + \gamma\left(\tilde{\partial}_{\bar{3}}^2 + \tilde{\partial}_{\bar{1}}^2\right)c^{yy}_{ij;kl} - \delta\left(\tilde{\partial}_{\bar{3}}^2 - \tilde{\partial}_{\bar{1}}^2\right)c^{yx}_{ij;kl} = -2\delta_{(ij),(kl)}d_{ij}. \tag{B5}$$

If we want to move to a continuous picture, then we replace $\tilde{\partial}_1^2 \to \partial_1^2$, $\tilde{\partial}_2^2 \to \partial_2^2$, $\tilde{\partial}_3^2 \to (\partial_1+\partial_2)^2$. In this picture c^{xx}, c^{xy}, c^{yx}, c^{yy} should be seen as functions on a four-dimensional cube.

One can also write down equations for the cycling frequencies using

$$\omega_{x_{ij},y_{kl}} = \frac{\left\langle f^x_{ij}y_{kl} - x_{ij}f^y_{kl}\right\rangle}{2\sqrt{\det \mathbf{C}_{[\mathrm{r,r}]}}} \overset{\mathbf{D}-\mathrm{diag.}}{=} \frac{\left\langle f^x_{ij}y_{kl}\right\rangle}{\sqrt{\det \mathbf{C}_{[\mathrm{r,r}]}}}. \tag{B6}$$

In the last step we used the Lyapunov equation together with the fact that $\mathbf{D}$ is a diagonal matrix.

[1] É. Fodor and M. Cristina Marchetti, Phys. A Stat. Mech. Appl. **504**, 106 (2018).
[2] F. Jülicher, K. Kruse, J. Prost, and J. F. Joanny, Phys. Rep. **449**, 3 (2007).
[3] M. C. Marchetti, J. F. Joanny, S. Ramaswamy, T. B. Liverpool, J. Prost, M. Rao, and R. A. Simha, Rev. Mod. Phys. **85**, 1143 (2013).
[4] A. Filella, F. Nadal, C. Sire, E. Kanso, and C. Eloy, Phys. Rev. Lett. **120**, 198101 (2018).
[5] M. Ballerini, N. Cabibbo, R. Candelier, A. Cavagna, E. Cisbani, I. Giardina, V. Lecomte, A. Orlandi, G. Parisi, A. Procaccini, M. Viale, and V. Zdravkovic, Proc. Natl. Acad. Sci. USA **105**, 1232 (2008).
[6] N. C. Damton, L. Turner, S. Rojevsky, and H. C. Berg, Biophys. J. **98**, 2082 (2010).
[7] S. Thutupalli, M. Sun, F. Bunyak, K. Palaniappan, and J. W. Shaevitz, J. R. Soc. Interface **12**, 20150049 (2015); arXiv:1410.7230.
[8] F. C. MacKintosh and C. F. Schmidt, Curr. Opin. Cell Biol. **22**, 29 (2010).
[9] F. S. Gnesotto, F. Mura, J. Gladrow, and C. P. Broedersz, Rep. Prog. Phys. **81**, 066601 (2018).
[10] S. C. Weber, A. J. Spakowitz, and J. A. Theriot, Proc. Natl. Acad. Sci. USA **109**, 7338 (2012).
[11] A. W. C. Lau, B. D. Hoffmann, A. Davies, J. C. Crocker, and T. C. Lubensky, Phys. Rev. Lett. **91**, 198101 (2003).
[12] M. Guo, A. J. Ehrlicher, M. H. Jensen, M. Renz, J. R. Moore, R. D. Goldman, J. Lippincott-Schwartz, F. C. Mackintosh, and D. A. Weitz, Cell **158**, 822 (2014).
[13] N. Fakhri, A. D. Wessel, C. Willms, M. Pasquali, D. R. Klopfenstein, F. C. MacKintosh, and C. F. Schmidt, Science. **344**, 1031 (2014).
[14] C. P. Brangwynne, G. H. Koenderink, F. C. MacKintosh, and D. A. Weitz, J. Cell Biol. **183**, 583 (2008).
[15] T. Betz, M. Lenz, J.-F. Joanny, and C. Sykes, Proc. Natl. Acad. Sci. USA **106**, 15320 (2009).
[16] H. Turlier, D. A. Fedosov, B. Audoly, T. Auth, N. S. Gov, C. Sylkes, J.-F. Joanny, G. Gompper, and T. Betz, Nat. Phys. **12**, 513 (2016).
[17] E. Ben-Isaac, Y. K. Park, G. Popescu, F. L. H. Brown, N. S. Gov, and Y. Shokef, Phys. Rev. Lett. **106**, 238103 (2011).
[18] D. Needleman and Z. Dogic, Nat. Rev. Mater. **2** 17048 (2017).
[19] R. Suzuki, C. A. Weber, E. Frey, and A. R. Bausch, Nat. Phys. **11**, 839 (2015).
[20] C. Battle, C. P. Broedersz, N. Fakhri, V. F. Geyer, J. Howard, C. F. Schmidt, and F. C. MacKintosh, Science **352**, 604 (2016).
[21] J. Gladrow, N. Fakhri, F. C. MacKintosh, C. F. Schmidt, and C. P. Broedersz, Phys. Rev. Lett. **116**, 248301 (2016).
[22] J. Gladrow, C. P. Broedersz, and C. F. Schmidt, Phys. Rev. E **96**, 022408 (2017).
[23] F. Mura, G. Gradziuk, and C. P. Broedersz, Phys. Rev. Lett. **121**, 038002 (2018).
[24] F. S. Gnesotto, B. M. Remlein, and C. P. Broedersz, arXiv:1809.04639v1 (2018).
[25] J. Li, J. M. Horowitz, T. R. Gingrich, and N. Fakhri, Nat. Commun. **10**, 1666 (2019).
[26] D. Mizuno, C. Tardin, C. F. Schmidt, and F. C. MacKintosh, Science **315**, 370 (2007).

[27] P. Martin, A. J. Hudspeth, and F. Jülicher, Proc. Natl. Acad. Sci. USA **98**, 14380 (2001).
[28] É. Fodor, M. Guo, N. S. Gov, P. Visco, D. A. Weitz, and F. van Wijland, Europhys. Lett. **110**, 48005 (2015).
[29] J. H. v. E. Job Boekhoven, Wouter E. Hendriksen, Ger J. M. Koper, Rienk Eelkema, Science **349**, 1075 (2015).
[30] J. Palacci, S. Sacanna, A. P. Steinberg, D. J. Pine, and P. M. Chaikin, Science **339**, 936 (2013).
[31] J.-B. Manneville, P. Bassereau, D. Lévy, and J. Prost, Phys. Rev. Lett. **82**, 4356 (1999).
[32] J.-B. Manneville, P. Bassereau, S. Ramaswamy, and J. Prost, Phys. Rev. E **64**, 021908 (2001).
[33] J. Liu, M. L. Gardel, K. Kroy, E. Frey, B. D. Hoffman, J. C. Crocker, A. R. Bausch, and D. A. Weitz, Phys. Rev. Lett. **96**, 118104 (2006).
[34] G. H. Koenderink, Z. Dogic, F. Nakamura, P. M. Bendix, F. C. MacKintosh, J. H. Hartwig, T. P. Stossel, and D. A. Weitz, Proc. Natl. Acad. Sci. USA **106**, 15192 (2009).
[35] J. Alvarado, M. Sheinman, A. Sharma, F. C. MacKintosh, and G. H. Koenderink, Soft Matter **13**, 5624 (2017).
[36] O. J. N. Bertrand, D. K. Fygenson, and O. A. Saleh, Proc. Natl. Acad. Sci. USA **109**, 17342 (2012).
[37] U. Seifert, Rep. Prog. Phys. **75**, 126001 (2012).
[38] A. Frishman and P. Ronceray, arXiv:1809.09650 (2018).
[39] D. S. Seara, V. Yadav, I. Linsmeier, A. P. Tabatabai, P. W. Oakes, S. M. A. Tabei, S. Banerjee, and M. P. Murrell, Nat. Commun. **9**, 4948 (2018).
[40] É. Roldán, J. Barral, P. Martin, J. M. R. Parrondo, and F. Jülicher, arXiv:1803.04743v3.
[41] G. Bisker, M. Polettini, T. R. Gingrich, and J. M. Horowitz, J. Stat. Mech. Theory Exp. (2017) 093210.
[42] M. Esposito, Phys. Rev. E **85**, 041125 (2012).
[43] M. Polettini and M. Esposito, Phys. Rev. Lett. **119**, 240601 (2017).
[44] A. Ghanta, J. C. Neu, and S. Teitsworth, Phys. Rev. E **95**, 032128 (2017).
[45] J. P. Gonzalez, J. C. Neu, and S. W. Teitsworth, Phys. Rev. E **99**, 022143 (2019).
[46] M. G. Yucht, M. Sheinman, and C. P. Broedersz, Soft Matter **9**, 7000 (2013).
[47] C. P. Broedersz and F. C. MacKintosh, Rev. Mod. Phys. **86**, 995 (2014).
[48] D. Osmanović and Y. Rabin, Soft Matter **13**, 963 (2017).
[49] X. Mao and T. C. Lubensky, Annu. Rev. Condens. Matter Phys. **9**, 413 (2018).
[50] G. Falasco, M. Baiesi, L. Molinaro, L. Conti, and F. Baldovin, Phys. Rev. E **92**, 022129 (2015).
[51] H. Risken, *The Fokker-Planck Equation* (Springer, Berlin, 1996).
[52] J. B. Weiss, Tellus A **55**, 208 (2003).
[53] B. Mohar, in *Graph Theory, Combinatorics and Applications*, edited by Y. Alavi, G. Chartrand, O. R. Ollermann, and A. J. Schwenk (Wiley, New York, 1991), pp. 871–898.
[54] S. E. Schaeffer, Comput. Sci. Rev. **1**, 27 (2007).
[55] M. E. Fisher, J. Comb. theory **1**, 105 (1966).
[56] G. Kirchhoff, Ann. Phys. **148**, 497 (1847).
[57] F. Mura, G. Gradziuk, and C. P. Broedersz (unpublished).
[58] J. Harder, C. Valeriani, and A. Cacciuto, Phys. Rev. E **90**, 062312 (2014).
[59] S. A. Mallory, C. Valeriani, and A. Cacciuto, Phys. Rev. E **92**, 012314 (2015).
[60] Y. Li and P. R. ten Wolde, arXiv:1902.02684 (2019).
[61] A. Kaiser, S. Babel, B. Ten Hagen, C. Von Ferber, and H. Löwen, J. Chem. Phys. **142**, 124905 (2015).

Chapter 3

Non-equilibrium measures reveal intrinsic features of the active driving

Chapter abstract Up to this point, we discussed several approaches to detect non-equilibrium fluctuations in biological systems, and we developed a theoretical framework to study non-equilibrium in biological assemblies. We have seen that two points non-equilibrium measures, such as cycling frequencies, area enclosing rates, and partial entropy production rates scale as power laws as a function of the observed length scale. However, it is still unclear what kind of information about the system we can acquire by measuring these quantities. Inspired by the method of two-point microrheology, in which the equilibrium fluctuations of a pair of probe particles reveal the viscoelastic response of an equilibrium system, in this chapter we investigate whether we can extend such an approach to non-equilibrium assemblies: can one extract information on the nature of the active driving of a system from the analysis of a two-point non-equilibrium measure? The work presented in this chapter is devoted to answering this question theoretically, by extending the framework presented in Chapter 2. Athermal fluctuations in biological and synthetic systems can present various spatial features. We investigate how such features of the active noise may be reflected in the long-range scaling behavior of the two-point non-equilibrium measures.

Research question: *What information about the active driving in the system can we learn by detecting non-equilibrium dynamics?*

Results: *A direct observation of the scaling behavior of two point non-equilibrium measures may provide a way to infer qualitative information on the nature of the active forces in the system, and quantitative information on their densities, intensities, or their correlation length.*

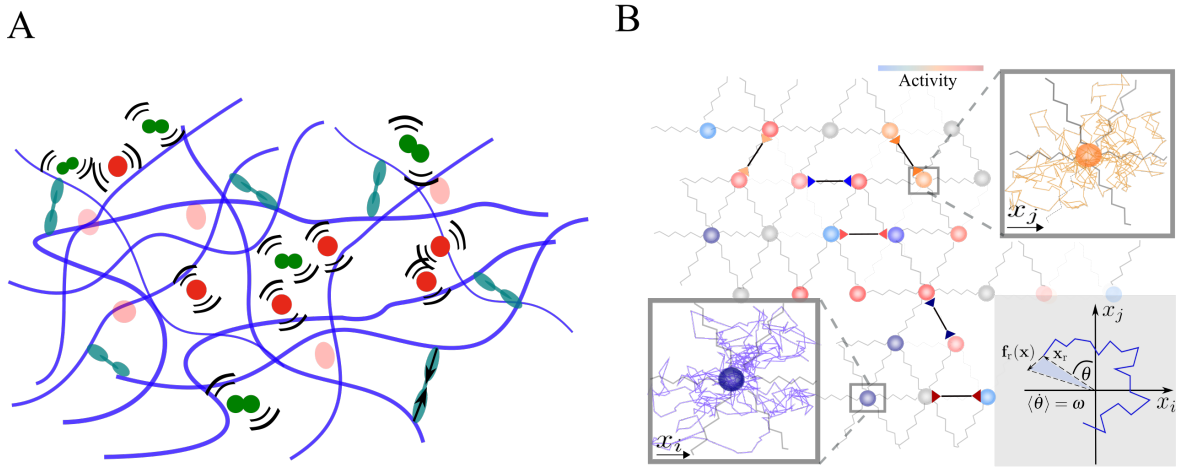

Figure 3.1: A) Cartoon of the cytoskeletal network. Molecular motors (light green) apply force dipoles directly on the network, while other active processes in the surroundings (red and dark green) can act on the network indirectly through hydrodynamic interactions. B) Schematic of the elastic network with monopole and dipole forces. The colors of the beads indicate the intensities of the monopole-like activity, the colors of the arrows indicate the intensity of the dipole-like activity. Inset on the lower right: schematic of a trajectory in the x_i and x_j coordinate space. The indicated non-equilibrium measures are: cycling frequency ω, and area enclosing rate (light blue area).

3.1 Different scenarios for the non-equilibrium driving

In this chapter we want to extend our model, by describing the non-equilibrium processes influencing the dynamics of biological assemblies with a greater level of detail. We will extend the model introduced in Chapter 2, including in the description several spatial features of the active driving. We will then investigate the effect of these features on the scaling behavior of the non-equilibrium measures.

Within the cellular environment, we can find several sources of athermal fluctuations, driven by a variety of biochemical processes. Such fluctuations also affect the motion of biological assemblies, i.e. the scaffold in which, or around which, these non-equilibrium processes take place. To describe the fluctuations of the assembly, we can divide these sources of non-equilibrium activity into two main groups, considering whether they act directly on the network or not. For instance, several experiments have shown that the active motion of molecular motors, enzymes, or pumps may indirectly influence the dynamics of other passive elements in their surroundings, through hydrodynamics interactions [41, 58]. From this perspective, we can think of parts of the network as passive objects, embedded in an active environment. We can indeed assume that the collection of the incoherent active processes in the network's surroundings can be effectively described as a collection of zero-average randomly fluctuating monopole-forces acting on the network's elements. The action of these forces results in a spatially heterogeneous enhanced diffusion of the network's elements.

However, certain classes of processes may also directly influence the network as, for instance, the active sliding of molecular motors along the network filaments, which gives rise to pairs of equal and opposite forces in the network [11, 46, 67, 70]. These direct contributions may also arise from intrinsic components of the network itself as, for instance, the forces generated by polymerization and depolymerization of microtubules [36]. Another example, at larger length scales, is given by cells exerting stresses on the extracellular matrix [43, 70, 72]. In all these cases, the direct action of a non-equilibrium source on the network is usually modeled, due to momentum conservation, as a force-dipole.

In addition to this first classification, other features of the non-equilibrium processes that could significantly affect the network dynamics are spatial and temporal correlations. For instance, the intracellular organization of enzymes and the clustering of molecular motors may results in long-range spatial correlation in the distribution of active processes inside cells [42, 71, 78]. Moreover, molecular motors have a typical processivity time, that introduces a temporal correlation of the forces that they generate [2]. While, as we will see in the next sections, we can easily take into account the spatial correlation of the active noise in our model, it is not straightforward to also include the temporal correlation. In fact, systems with time correlations are not Markovian and can not be described by a Fokker-Planck Equation. These systems would require a completely different theoretical framework, and are therefore not covered in this thesis.

3.2 Model

To describe a general scenario where both direct and indirect active processes are taken into account, we generate the active driving in our network as Gaussian white noise of either a monopole or a dipole nature, with respective densities ρ^{M} and ρ^{D} (Fig. 3.1). We recall that by modeling the active forces as a white noise process, we assume the dynamics of the microscopic active forces to take place on timescales shorter than the relaxation times of the system.

We denote the displacements of the beads relative to their rest positions by the vector $\mathbf{x} = \{x_1, \ldots, x_{Nd}\}$. The overdamped equation of motion for the displacement of the i_{th} degree of freedom in the lattice reads

$$\frac{dx_i(t)}{dt} = a_{ij}x_j(t) + \eta_i^T(t) + b_i^{\mathrm{M}}\eta_i^{\mathrm{M}}(t) + \sum_{k\in \mathrm{nn}} b_{ik}^{\mathrm{D}}\eta_{ik}^{\mathrm{D}}(t), \tag{3.1}$$

where a_{ij} are the entries of the elastic interaction matrix $\mathbf{A}$, divided by the friction coefficient γ. The thermal noise is described by the standard fluctuation-dissipation relation

$$\langle \eta_i^T(t)\eta_j^T(t')\rangle = \frac{2k_{\mathrm{B}}T}{\gamma}\delta_{i,j}\delta(t-t'). \tag{3.2}$$

The coefficients b_i^{M} and b_{ik}^{D} are introduced to describe the presence of monopole and dipole active noise; they are time-independent random variables such that $b_{i/ik}^{\mathrm{M/D}} \in \{0,1\}$, $b_{ik}^{\mathrm{D}} = b_{ki}^{\mathrm{D}}$, with probability distribution $P\left(b_{i/ik}^{\mathrm{M/D}} = 1\right) = \rho^{\mathrm{M/D}}$. The sum $\sum_{k\in \mathrm{nn}}$ runs only over

nearest-neighbor beads. Finally, the stochastic variables for monopole forces $\eta^{\mathrm{M}}(t)$ and dipole forces $\eta^{\mathrm{D}}(t)$ are characterized by

$$\begin{aligned}\langle \eta_i^{\mathrm{M}}(t)\eta_j^{\mathrm{M}}(t')\rangle &= \frac{k_{\mathrm{B}}}{\gamma}\delta_{i,j}\alpha_i^{\mathrm{M}}\delta(t-t') \\ \langle \eta_{ij}^{\mathrm{D}}(t)\eta_{kl}^{D}(t')\rangle &= \frac{k_{\mathrm{B}}}{\gamma}\left(\delta_{ij,kl}-\delta_{ij,lk}\right)\alpha_{ij}^{\mathrm{D}}\delta(t-t').\end{aligned} \tag{3.3}$$

Here we indicate with α_i^{M} and α_{ij}^{D} the respective amplitudes of the monopole force acting on the i_{th} coordinate and of the dipole force acting between the i_{th} and j_{th} coordinates.

This simple model still admits a Fokker-Planck description for the evolution of the probability distribution $p(\mathbf{x},t)$ of $\mathbf{x}$ at time t

$$\partial_t p(\mathbf{x},t) = -\nabla\cdot(\mathbf{A}\mathbf{x}-\mathbf{D}\nabla)p(\mathbf{x},t) \coloneqq -\nabla\cdot\mathbf{j}(\mathbf{x},t), \tag{3.4}$$

where $\mathbf{j}(\mathbf{x},t)$ is the probability current density, and $\mathbf{D}$ is the diffusion matrix. The steady-state solution of Eq. (3.4) is a Gaussian distribution with covariance matrix $\mathbf{C}$, satisfying the Lyapunov equation:

$$\mathbf{A}\mathbf{C}+\mathbf{C}\mathbf{A}^{\mathrm{T}} = -2\mathbf{D}. \tag{3.5}$$

The diffusion matrix can be expressed as $\mathbf{D} = \bar{\mathbf{D}}+\mathbf{D}^*$, where $\bar{\mathbf{D}}$ is a diagonal matrix with entries $\bar{d}_{ij} = \delta_{ij}k_{\mathrm{B}}T/\gamma$, representing the thermal noise contributions, and $\mathbf{D}^*$ is the non-equilibrium part of the diffusion matrix which contains information on the activities. While in Chapter 2 we considered a diagonal diffusion matrix, here the presence of dipole forces gives rise to anticorrelations between neighboring beads and therefore to non-zero off-diagonals terms in $\mathbf{D}^*$, as will be discussed in Sec. (3.3.1). As we will see, these correlations in the diffusion matrix have a strong impact on the spatial scaling of mesoscopic non-equilibrium measures of the system.

3.3 Results

To investigate the impact of the features of the active driving on the system dynamics, we still employ the cycling frequencies and area enclosing rates as measures of non-equilibrium in the reduced subspaces of two degrees of freedom (see Eq. (2.6) and Eq. (2.7)). Following similar steps as those presented in Chapter 2, we investigate analytically and numerically how these measures scale with the distance between a couple of observed degrees of freedom. In particular, since both cycling frequencies and area enclosing rates have zero average, we focus on the spatial scaling behaviors for $\langle\mathcal{A}^2(r)\rangle_\alpha$ and $\langle\omega^2(r)\rangle_\alpha$, the squared area enclosing rate and cycling frequency between two tracer beads at distance r, averaged over the distribution of activities $\alpha_{i/ij}^{M/D}$. Maintaining the same notation as in Chapter 2, we indicate with $\langle\ldots\rangle_\alpha$ the ensemble average over the activities which, for a large enough system, can be obtained as a spatial average over the network [60].

Also in this more complex model we will be able to derive closed form expressions for the scaling of $\langle\mathcal{A}^2(r)\rangle_\alpha$ and $\langle\omega^2(r)\rangle_\alpha$, which provide us with a direct connection between these non-equilibrium measures and the properties of the active noise, such as the densities

and activity intensities of monopoles and dipoles forces. The validity of the analytical results obtained in the following sections will be tested by making a direct comparison with numerical solutions of Eq. (2.6) and Eq. (2.7).

In Sec. (3.3.1), we first focus on a one-dimensional chain subject to monopole and dipole active forces, and later we discuss the extension to a two-dimensional network. Finally, in Sec. (3.3.2) we discuss how the scaling law is affected by the presence of finite spatial correlation of the intensities of the active noise.

The results presented in the following sections are in many aspects built on the framework already presented in Chapter 2. To lighten the reading, we will omit the technical aspects, only presenting the final results and the most important steps in their derivations. More detailed calculations are reported in the manuscript [61], reprinted at the end of this chapter.

3.3.1 Monopole and dipole activity

One dimensional chain

It is instructive to start analyzing the simple case of a one-dimensional system. In the following, by using a continuous approximation of the Lyapunov equation, we find a solution of Eq. (3.5) for the covariance matrix, and derive the scaling laws for the non-equilibrium measures $\langle \mathcal{A}^2 \rangle_\alpha$ and $\langle \omega^2 \rangle_\alpha$ as function of the distance r between the tracer particles.

As a first step, we set the form of the non-equilibrium part of the diffusion matrix $\mathbf{D}$ appearing in Eq. (3.5). In the simple case of a one-dimensional chain we can replace the double index of the dipoles amplitudes $\{\alpha^{\mathrm{D}}_{12}, \alpha^{\mathrm{D}}_{23}, \dots, \alpha^{\mathrm{D}}_{i,i+1}, \dots, \alpha^{\mathrm{D}}_{N-1,N}\}$ with a single index running over the pairs of nearest-neighbor beads $\{\alpha^{\mathrm{D}}_1, \alpha^{\mathrm{D}}_2, \dots, \alpha^{\mathrm{D}}_i, \dots, \alpha^{\mathrm{D}}_{N-1}\}$. The activities amplitudes $\{\alpha^{\mathrm{M/D}}_i\}$ are sampled independently from a distribution $p^{M/D}_\alpha$ with mean $0 < \bar{\alpha}^{\mathrm{M/D}} < \infty$ and variance $\sigma^2_{\alpha^{\mathrm{M/D}}}$.

A monopole-like active noise at site z along the chain, contributes with an entry on the diagonal of the diffusion matrix $d_{z,z}$. By contrast, a dipole-like noise acts with completely anti-correlated forces on the beads at positions z and $z+1$, contributing with four entries in the diffusion matrix: $\left[d_{z,z} = d_{z+1,z+1} = (k_{\mathrm{B}}/\gamma)\alpha^D_z\right]$ and $\left[d_{z+1,z} = d_{z,z+1} = -(k_{\mathrm{B}}/\gamma)\alpha^D_z\right]$. Therefore, the non-equilibrium part of the diffusion matrix will be a sum over monopole and dipole contributions of the form

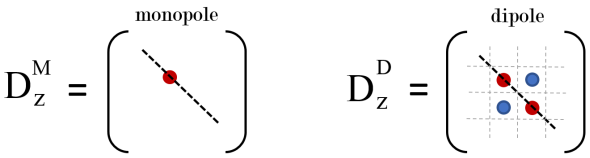

Considering the linearity of the Lyapunov equation (see Eq. (3.5)), the covariance matrix can be expressed as

$$\mathbf{C} = \frac{k_{\mathrm{B}}}{k}(T\overline{\mathbf{C}} + \sum_z \alpha^{\mathrm{M}}_z \mathbf{C}^{\mathrm{M}}_z + \alpha^{\mathrm{D}}_z \mathbf{C}^{\mathrm{D}}_z), \tag{3.6}$$

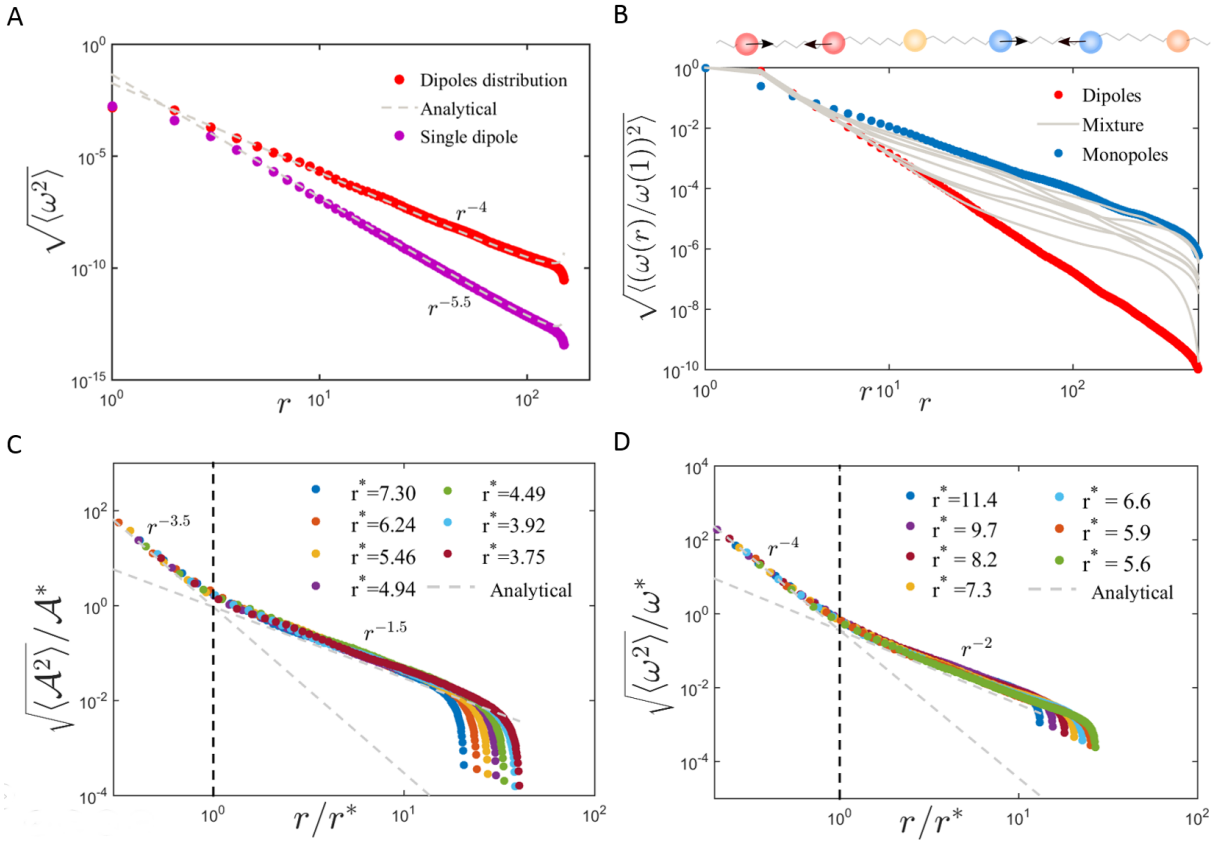

Figure 3.2: A) Above: scaling behavior of the average cycling frequency with the distance r for a system with only dipoles as active noise. Numeric results in red and analytic predictions in gray. Below: numeric results for a single dipole activity (purple) and its analytical prediction (gray). B) Scaling behavior of the cycling frequency with r for a system with activity given by: only dipoles (red), only monopoles (blue), mixture of dipoles and monopoles (gray) C) Rescaling of $\mathcal{A}$ for a range of r^* and $\mathcal{A}^*$ (crossover distance and area enclosing rate defined in Eq. (3.13) and Eq. (3.14)), and analytic prediction of the two scaling regimes in gray. D) Rescaling of ω for a range of r^* and ω^*, and analytic prediction of the two scaling regimes in gray.

such that $\overline{\mathbf{C}}$, $\mathbf{C}_z^{\mathrm{M}}$ and $\mathbf{C}_z^{\mathrm{D}}$ are dimensionless. Here $\overline{\mathbf{C}}$ is the equilibrium solution of Eq. (3.5) obtained for $\{\alpha_i^{\mathrm{M/D}}\} = 0$, and $\mathbf{C}_z^{\mathrm{M/D}}$ are solutions of Eq. (3.5) for single monopole/dipole noise source at position z along the chain. By inserting this expression for $\mathbf{A}$ together with Eq. (3.6) into Eq. (2.6), we get an expression for the area enclosing rate between any two tracer particles i and j that are not directly connected by a dipole activity ($d_{ij} = 0$), as

$$\mathcal{A}_{ij} = \frac{k_{\mathrm{B}}}{\gamma} \sum_z (\xi_z^{\mathrm{M}} \widetilde{\partial}_x^2 c_z^{\mathrm{M}} + \xi_z^{\mathrm{D}} \widetilde{\partial}_x^2 c_z^{\mathrm{D}}), \tag{3.7}$$

where $\xi_z^{\mathrm{M/D}} = b_z^{\mathrm{M/D}} \alpha^{\mathrm{M/D}}$, and we use $\widetilde{\partial}_x^2 c = c_{i,j+1} - 2c_{i,j} + c_{i,j-1}$ to indicate the discrete second derivative along rows. As we expected from the results in Chapter 2, also in this case the scaling behaviors of $\mathcal{A}_{ij}$, and therefore ω_{ij}, are determined by the curvature of the covariance matrix. To find an expression for the curvature, we can calculate the explicit form of $C_z^{\mathrm{M/D}}$, as a solution of the equation

$$\frac{k_{\mathrm{B}} \alpha_z^{\mathrm{M/D}}}{\gamma} \left(\widetilde{\partial}_y^2 c_z^{\mathrm{M/D}} + \widetilde{\partial}_x^2 c_z^{\mathrm{M/D}} \right) = -2 d_z^{\mathrm{M/D}}, \tag{3.8}$$

which is obtained from Eq. (3.5) by considering a single monopole/dipole contribution at position z along the chain. Eq. (3.8) can be viewed as a discretized Poisson equation with sources set by the elements of $\mathbf{D}$. The solution for a generic diffusion matrix will be obtained as a superposition of single-contribution solutions. We have seen in Chapter 2 that, in the continuous limit and considering a single entry in the diffusion matrix $d_{z,\tilde{z}}$, the single-source solution of Eq. (3.8) gives $c^{\mathrm{M}}(i,j) = -\frac{1}{\pi} \ln(\varrho) + b$. Here, $\varrho = \sqrt{(i-z)^2 + (j-\tilde{z})^2}$ indicates the distance from the source at $(z, \tilde{z})$ in the covariance matrix, and b is an integration constant. However, the profile of C_z is different in the case of a dipole single source, and exhibits a power-law scaling $c^{\mathrm{D}} \propto \varrho^{-3}$. These distinct scaling laws of the covariance will turn out to underlie the different scaling laws for the non-equilibrium measures.

To determine the area enclosing rate for a pair of beads at distance r we need to compute contributions of the form $\widetilde{\partial}_x^2 c_{z;-r/2,r/2}^{\mathrm{M/D}} := \widetilde{\partial}_x^2 c_z^{\mathrm{M/D}}(r)$. In the following we approximate the discrete derivatives applied to the matrix elements $\widetilde{\partial}_x^2 c_z^{\mathrm{M/D}}(r)$ with regular derivatives applied to the solutions of the Poisson equation $\partial_x^2 c_z^{\mathrm{M/D}}(r)$.

A single monopole activity at site z contributes a diagonal entry in the diffusion matrix $d_{z,z}$. This appears as a monopole source at position (z,z) in the Poisson equation. Using the continuous solution derived above, we obtain

$$\partial_x^2 c_z^{\mathrm{M}}(r) = \frac{8rz}{\pi(r^2 + 4z^2)^2}. \tag{3.9}$$

A single dipole activity between sites z and $z+1$ contributes four entries in the diffusion matrix: $[d_{z,z} = -d_{z+1,z} = -d_{z,z+1} = d_{z+1,z+1}]$. These enter the Poisson equation as a

quadrupole source. By summing these four contributions we obtain

$$\begin{aligned}\partial_x^2 c_z^{\mathrm{D}}(r) =& \frac{8rz}{\pi(r^2+4z^2)^2} \\ &- \frac{4(-1+r)(1+2z)}{\pi(2+(-2+r)r+4z(1+z))^2} \\ &- \frac{4(1+r)(1+2z)}{\pi(2+(2+r)r+4z(1+z))^2} \\ &+ \frac{8r(1+z)}{\pi(r^2+4(1+z)^2)^2}.\end{aligned} \tag{3.10}$$

We are now ready to obtain the first central results of this chapter, the scaling behaviors of $\langle \mathcal{A}^2(r)\rangle_\alpha$ and $\langle \omega^2(r)\rangle_\alpha$, when both monopoles and dipoles are present in the system. Inserting Eq. (3.9) and Eq. (3.10) into Eq. (3.7), and averaging over configurations of the activity intensities, we obtain in the limit $r \gg 1$ (Sec. (1) supplementary in [61]):

$$\langle \mathcal{A}^2(r)\rangle_\alpha = \frac{1}{\pi}\left(\frac{k_{\mathrm{B}}}{\gamma}\right)^2 \left(\rho^{\mathrm{M}}\sigma^2_{\alpha^{\mathrm{M}}}\frac{1}{2r^3} + \rho^{\mathrm{D}}\sigma^2_{\alpha^{\mathrm{D}}}\frac{45}{r^7}\right). \tag{3.11}$$

Thus, we observe two different regimes: a monopole-controlled regime $\langle \mathcal{A}^2(r)\rangle_\alpha \propto 1/r^3$ for long distances and a dipole-controlled regime $\langle \mathcal{A}^2(r)\rangle_\alpha \propto 1/r^7$ for short distances, as shown in Fig. 3.2C.

A similar scaling behavior can be obtained also for the cycling frequencies ω by applying a similar approach to Eq. (2.7): Decomposing $\mathbf{C} = \frac{k_B}{k}\left(T\overline{\mathbf{C}} + \bar{\alpha}^{\mathrm{M}}\mathbf{C}^{\mathrm{M}} + \bar{\alpha}^{\mathrm{D}}\mathbf{C}^{\mathrm{D}}\right)$ and expanding the factor $1/(\det\mathbf{C})$ up to linear order in $\frac{\bar{\alpha}^{\mathrm{M/D}}}{T}$, we obtain

$$\langle \omega^2(r)\rangle_\alpha = \frac{(k/\gamma)^2}{\pi T^2 \det\overline{\mathbf{C}}_{[\mathrm{r,r}]}}\left(\rho^{\mathrm{M}}\sigma^2_{\alpha^{\mathrm{M}}}\frac{1}{2r^3} + \rho^{\mathrm{D}}\sigma^2_{\alpha^{\mathrm{D}}}\frac{45}{r^7}\right). \tag{3.12}$$

Considering that for $r \ll N$, $\det\overline{\mathbf{C}}_{[\mathrm{r,r}]} \propto Nr$ [40], we obtain two different regimes also for the scaling of the cycling frequency: $\langle \omega^2(r)\rangle_\alpha \propto 1/r^4$ at short distances and $\langle \omega^2(r)\rangle_\alpha \propto 1/r^8$ at long distances (Fig. 3.2B,D). Interestingly, in analogy to the case of single monopole activity discussed in Chapter 2, also in the presence of a distribution of only dipoles in the systems ($\rho^{\mathrm{M}} = 0$), the scaling exponent for the average cycling frequency ($\sqrt{\langle\omega^2\rangle_\alpha} \sim r^{-4}$) differs from the exponent obtained with a single dipole activity at site $z = i = -r/2$ ($\sqrt{\omega^2} \sim r^{-5.5}$) (Fig. 3.2A).

We can also investigate what are the parameters of our model that determine the crossover distance r^* between the two scaling regimes. A direct calculation of r^* and the mean cycling frequency at the crossover distance $\langle\omega^2(r^*)\rangle$ leads to

$$r^* = \left(\frac{90\rho^{\mathrm{D}}\sigma^2_{\alpha^{\mathrm{D}}}}{\rho^{\mathrm{M}}\sigma^2_{\alpha^{\mathrm{M}}}}\right)^{1/4} \qquad \langle \omega^2(r^*)\rangle_\alpha = \frac{2k^2}{\pi T^2\gamma^2 45N}\frac{{\rho^{\mathrm{M}}}^2\sigma^4_{\alpha^{\mathrm{M}}}}{\rho^{\mathrm{D}}\sigma^2_{\alpha^{\mathrm{D}}}}. \tag{3.13}$$

For the the area enclosing rate at the crossover point, we find

$$\langle \mathcal{A}^2(r^*)\rangle_\alpha = \frac{k_{\mathrm{B}}^2}{\pi\gamma^2 90}\frac{{\rho^{\mathrm{M}}}^2\sigma^4_{\alpha^{\mathrm{M}}}}{\rho^{\mathrm{D}}\sigma^2_{\alpha^{\mathrm{D}}}}r^*, \tag{3.14}$$

as shown in Fig. 3.2C,D, where we obtain a collapse of data by rescaling the x-axes by r^* and the y-axes by $\mathcal{A}^*$ and ω^*.

Our results are informative on what kind of measurements could be performed to gain information on the non-equilibrium driving in an elastic system. For instance, we have learned that the experimental observation of one of the scaling behaviors discussed here, would allow one to discriminate the monopole or dipole nature of the active driving. In the more general case of a mixture of monopoles and dipoles, a direct measure of the transition points between two different scaling regimes would help to gain quantitative information on the quantities $\rho^{\mathrm{D}}\sigma^2_{\alpha^{\mathrm{D}}}$ and $\rho^{\mathrm{M}}\sigma^2_{\alpha^{\mathrm{M}}}$.

Two dimensional networks

By following similar steps as in the one dimensional case, we can extend our results to higher-dimensional networks (d>1). For simplicity, we consider a two-dimensional square network for the analytical derivation, but we make a direct check on how the results obtained for this simple case also apply to more complex geometries. We consider the dipole forces acting always along the principal axes of the network, which corresponds to the limit of small displacements in the systems. Under these assumptions, it is possible to perform calculations similar to those presented in Sec. 3.3.1. We recall that a detailed derivation of these calculations can be found in our manuscript [61], included at the end of this chapter. The square area enclosing rate as function of the distance r between the observed degrees of freedom turns out to be:

$$\langle \mathcal{A}^2(r)\rangle_\alpha \simeq \left(\frac{2k_{\mathrm{B}}}{\pi^2\gamma}\right)^2 \left[\rho^{\mathrm{M}}\sigma^2_{\alpha^{\mathrm{M}}}\frac{2\pi}{5r^6} + \rho^{\mathrm{D}}\sigma^2_{\alpha^{\mathrm{D}}}\frac{529}{r^{10}}\right]. \tag{3.15}$$

Similarly to the one-dimensional case (see Eq. (3.11)), we recognize the presence of two different regimes at short and long distances. The crossover distance $r^*{}_{2D}$ between the monopole and dipole dominated regimes and the corresponding $\langle \mathcal{A}^2(r^*_{2D})\rangle$ read:

$$\begin{aligned} r^*_{2D} &\simeq 4.5\left(\frac{\rho^{\mathrm{D}}\sigma^2_{\alpha^{\mathrm{D}}}}{\rho^{\mathrm{M}}\sigma^2_{\alpha^{\mathrm{M}}}}\right)^{1/4}, \\ \langle \mathcal{A}^2(r^*_{2D})\rangle_\alpha &\simeq \frac{k_{\mathrm{B}}^2 12\cdot 10^{-6}}{\gamma^2}\frac{\left(\rho^{\mathrm{M}}\sigma^2_{\alpha^{\mathrm{M}}}\right)^{5/2}}{(\rho^{\mathrm{D}}\sigma^2_{\alpha^{\mathrm{D}}})^{3/2}}. \end{aligned} \tag{3.16}$$

These analytical results are confirmed by the numerical data in Fig. 3.3A, B, where we obtain a collapse by properly rescaling the x-axis by r^* and the y-axis by $\mathcal{A}^2(r_{2D}{}^*)$.

To investigate the sensitivity of these results to the specific underlying lattice structure, we studied triangular and bond-diluted triangular networks. We find numerically that such lattice geometries are also well described by Eqs. (3.15) and (3.16). In fact, the curves numerically obtained for the scaling behavior of $\langle \mathcal{A}^2\rangle_\alpha$ in a triangular network and diluted triangular network, overlap with the curves corresponding to the square lattice, as shown in Fig. 3.3 B.

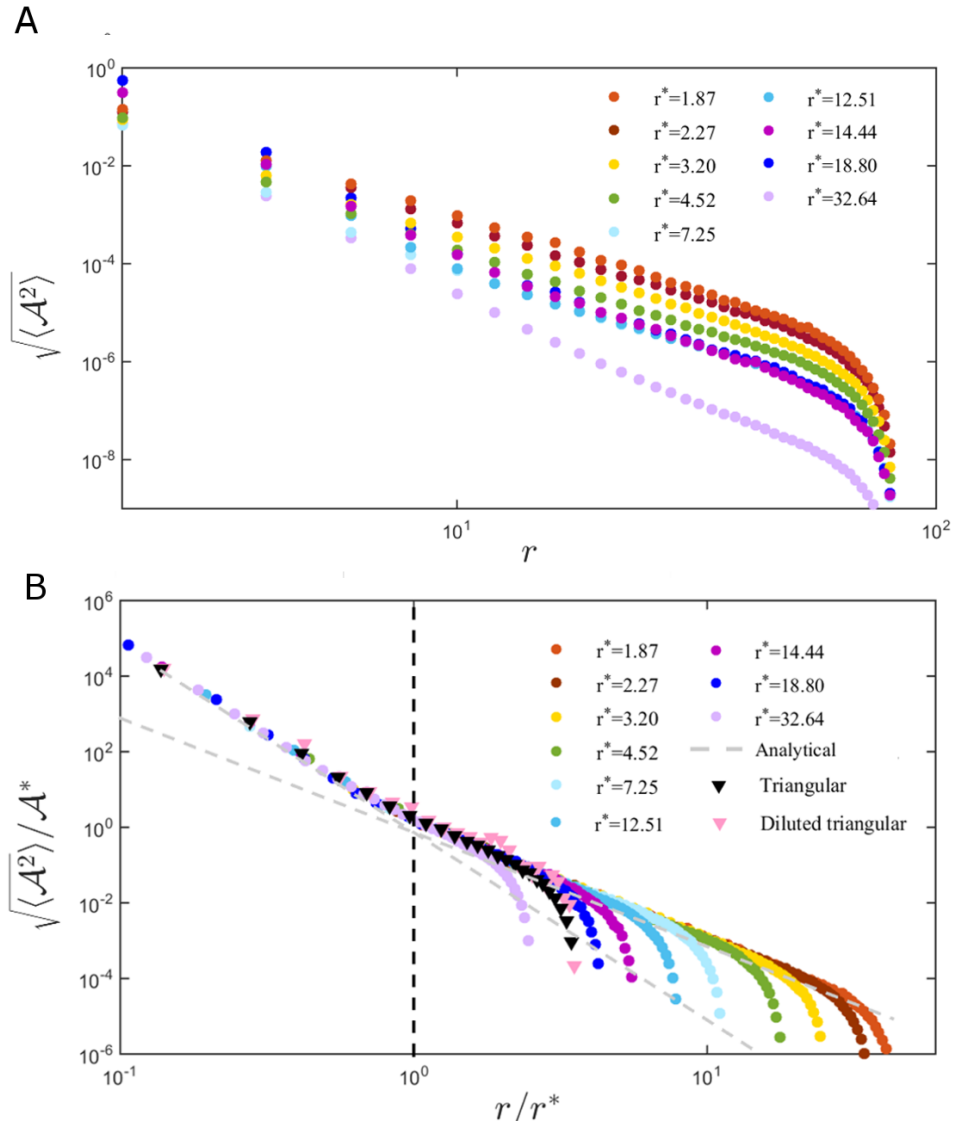

Figure 3.3: A) Scaling behavior of $\sqrt{\langle \mathcal{A}^2 \rangle}$ as function of the distance for two-dimensional lattices obtained for a square lattice and different values of r^*. B) Data-collapse of the results in A, obtained by rescaling the x and y axes respectively by r^*_{2d} and $\sqrt{\mathcal{A}^2(r_{2d^*})}$. The triangular markers correspond respectively to the data for a full triangular lattice (in black) and a randomly diluted triangular lattice (in pink) with dilution probability $p_d = 0.8$

3.3.2 Correlated activities

Up to this point, we considered two kinds of noise sources: dipoles and monopoles, randomly distributed in space. Now we want to determine how the spatial distribution of activities influences the scaling behavior of non-equilibrium measures. Therefore, we consider a system where the intensities of the active noise are spatially correlated.

As an illustrative example, we consider a one-dimensional chain with only monopole activities ($\rho^{\mathrm{D}} = 0$ and $\rho^{\mathrm{M}} = 1$). Thus, the diffusion matrix $\mathbf{D}$ is diagonal, with entries $d_{i,j} = (k_{\mathrm{B}}/\gamma)(T + \alpha_i)\delta_{i,j}$. We draw the amplitudes $\{\alpha_i\}$ randomly from a probability distribution with covariance: $\langle \alpha_i \alpha_j \rangle - \langle \alpha_i \rangle \langle \alpha_j \rangle = \sigma_\alpha^2 e^{-\frac{|i-j|}{\lambda}}$, exhibiting a characteristic correlation length $\lambda > 0$ (see Fig. 3.4A). Also in this case, even though the diffusion matrix is diagonal, the presence of correlations between its diagonal entries will have a marked effect on the scaling behavior of the non-equilibrium measures. By setting $c_z^{\mathrm{D}} = 0 \ \forall z$ in Eq. (3.7), and considering the monopole contributions as in Eq. (3.9), we obtain for the area enclosing rate:

$$\begin{aligned}
\langle \mathcal{A}^2(r) \rangle_\alpha &= \left(\frac{k_{\mathrm{B}}}{\pi\gamma}\right)^2 \sum_{z,z'} \langle \alpha_z \alpha_{z'} \rangle \frac{8rz}{(r^2+4z^2)^2} \frac{8rz'}{(r^2+4z'^2)^2} \\
&= \left(\frac{k_{\mathrm{B}}}{\pi\gamma}\right)^2 \sum_{z,z'} \sigma_\alpha^2 e^{-\frac{|z-z'|}{\lambda}} \frac{8rz}{(r^2+4z^2)^2} \frac{8rz'}{(r^2+4z'^2)^2} \\
&\simeq \left(\frac{k_{\mathrm{B}}}{\pi\gamma}\right)^2 \sum_{z,z'=z-\lambda}^{z'=z+\lambda} (1 - \frac{|z-z'|}{\lambda}) \frac{\sigma_\alpha^2 8rz}{(r^2+4z^2)^2} \frac{8rz'}{(r^2+4z'^2)^2},
\end{aligned} \tag{3.17}$$

where in the last step we approximated the exponential with a first order Taylor expansion inside the interval $[z-\lambda, z+\lambda]$, and zero outside the interval. Approximating the sum with an integral, we arrive at:

$$\langle \mathcal{A}^2(r) \rangle_\alpha \simeq \left(\frac{k_{\mathrm{B}}}{\gamma}\right)^2 \frac{\sigma_\alpha^2}{\pi} \left(\frac{\lambda}{2r^3 + 2r\lambda^2}\right). \tag{3.18}$$

We identify two different regimes:

$$\langle \mathcal{A}^2(r) \rangle_\alpha \sim \begin{cases} \frac{k_{\mathrm{B}}^2 \sigma_\alpha^2}{2\gamma^2\pi} \frac{\lambda}{r^3} & \text{if } r \gg \lambda \\ \frac{k_{\mathrm{B}}^2 \sigma_\alpha^2}{2\gamma^2\pi} \frac{1}{\lambda r} & \text{if } r \ll \lambda \end{cases}$$

A comparison between our analytical prediction (Eq. (3.18)) and numerical results is shown in Fig. 3.4A. The numerical results for correlated dipoles are shown in Fig. 3.4B.

We can notice that the behavior observed in the case of correlated activities is substantially different from what we observed for mixtures of uncorrelated dipoles and monopoles. In particular, the scaling exponent of the short distance regime is now smaller than the one of the long distances regime. Moreover, as one would expect, the exponent in the long-distance regime ($r \gg \lambda$) is the same as for the case of uncorrelated activities. Such a substantial difference in the observed scaling exponents would allow one to discern the cases of spatially correlated activities from that of a mixture of dipoles and monopoles. At last, we could also notice that a quantitative measure of the two scaling regimes would allow one to estimate the correlation length λ or the intensities of the activities σ_α^2.

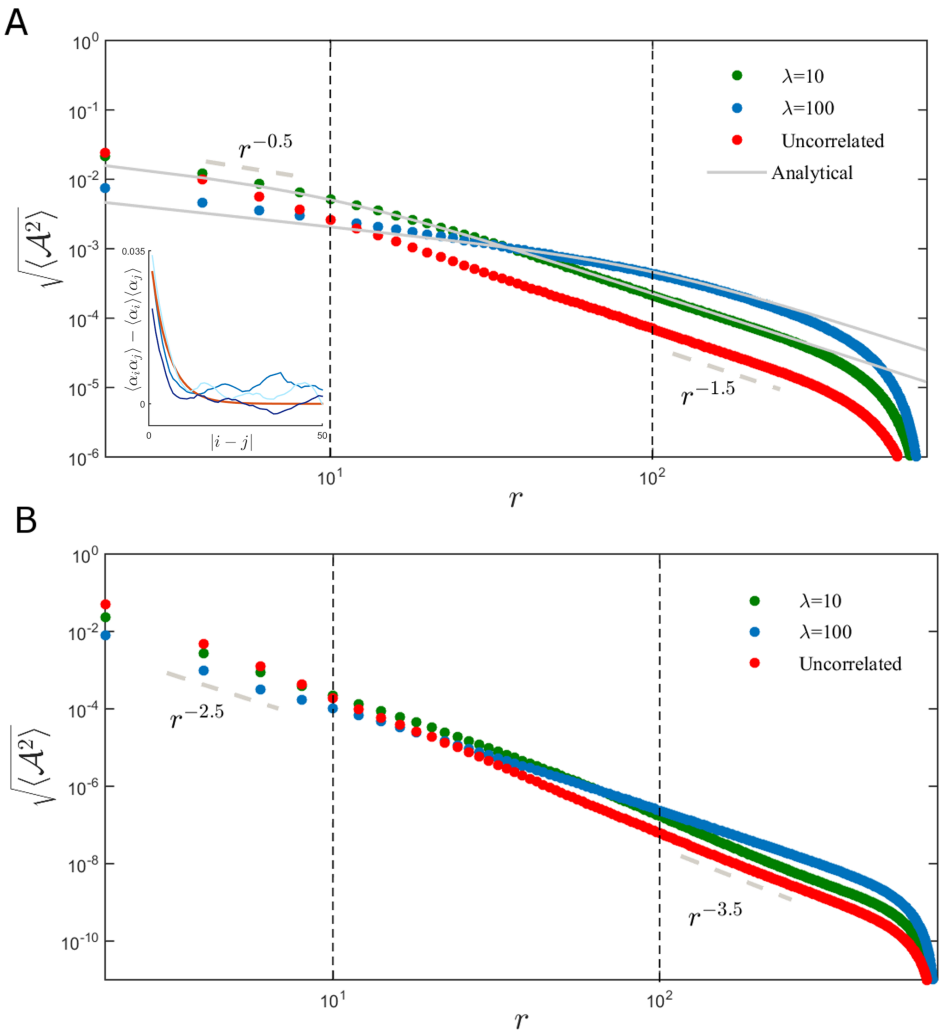

Figure 3.4: A) Scaling behavior of the area enclosing rate for a system with correlated monopole-activities with correlation length $\lambda = 10$ (green), $\lambda = 100$ (blue) and uncorrelated activities (red). In gray the comparison with the analytical prediction. In the inset: spatial correlation function of the activity amplitudes. In blue the correlation functions calculated for 3 different realizations of activities with correlation length $\lambda = 10$, and in red the theoretical prediction $\sigma_\alpha^2 e^{-\frac{|i-j|}{\lambda}}$. B) Scaling behavior of the area enclosing rate for a system with dipole-activities with $\lambda = 10$ (green), $\lambda = 100$ (blue) and uncorrelated activities (red).

3.3.3 Chapter summary

In this Chapter we discussed how non-equilibrium measures such as cycling frequencies and area enclosing rates may be used to learn information on the nature of the non-equilibrium driving in the system. The scaling behavior of these measures exhibits different scaling exponents for dipole-/monopole-like activity. In the presence of both monopole and dipole activity we observe the presence of two regimes: a dipole dominated regime and a monopole dominated regime. The prefactors of the two scaling functions as well as the crossover distance between the two regimes are set by the parameters characterizing the stochastic forces: densities of monopoles ρ^{M} and dipoles ρ^{D}, and the variance of the activities amplitudes $\sigma_{\alpha^{\mathrm{M/D}}}$. Even though our analytical framework is derived in the simple case of cubic lattices, we expect our predictions to hold also for more complex networks, as suggested from our findings for triangular and diluted triangular networks. Furthermore, we also showed that our framework can be used in the case of correlated intensities of the active noise.

Altogether our results provide a new perspective on how to interpret experimentally accessible two-point non-equilibrium measures: A direct observation of the scaling behavior of such non-equilibrium measures may provide a way to infer qualitative information on the nature of the active forces in the system, and quantitative information on their densities, intensities, or their correlation length. In the next chapter we will discuss which experimental settings would be good candidates to test the predictions of our framework.

3.4 Publication preprint

Mesoscopic non-equilibrium measures can reveal intrinsic features of the active driving

by

F. Mura,[1] G. Gradziuk, [1] and C. P. Broedersz,[1]

[1]Department of Physics, Arnold Sommerfeld Center for Theoretical Physics and Center for NanoScience, Ludwig-Maximilians-Universität München, Theresienstraße 37, 80333 München, Germany

Mesoscopic non-equilibrium measures can reveal intrinsic features of the active driving

Federica Mura, Grzegorz Gradziuk, and Chase P. Broedersz*
Arnold-Sommerfeld-Center for Theoretical Physics and Center for NanoScience, Ludwig-Maximilians-Universität München, D-80333 München, Germany.
(Dated: August 20, 2019)

Biological assemblies such as chromosomes, membranes, and the cytoskeleton are driven out of equilibrium at the nanoscale by enzymatic activity and molecular motors. Similar non-equilibrium dynamics can be realized in synthetic systems, such as chemically fueled colloidal particles. Characterizing the stochastic non-equilibrium dynamics of such active soft assemblies still remains a challenge. Recently, new non-invasive approaches have been proposed to determine non-equilibrium behavior, which are based on detecting broken detailed balance in the stochastic trajectories of several coordinates of the system. Inspired by the method of two-point microrheology, in which the equilibrium fluctuations of a pair of probe particles reveal the viscoelastic response of an equilibrium system, here we investigate whether we can extend such an approach to non-equilibrium assemblies: can one extract information on the nature of the active driving in a system from the analysis of a two-point non-equilibrium measure? We address this question theoretically in the context of a class of elastic systems, driven out of equilibrium by a spatially heterogeneous stochastic internal driving. We consider several scenarios for the spatial features of the internal driving that may be relevant in biological and synthetic systems, and investigate how such features of the active noise may be reflected in the long-range scaling behavior of two-point non-equilibrium measures.

I. INTRODUCTION

Active matter theories aim to provide a physical description for systems intrinsically out of thermal equilibrium. A prominent collection of such systems is classified as soft biological materials, with typical examples as tissue, membranes and cytoskeletal structures [1–5]. These soft materials can be easily deformed by thermally driven stresses. However, temperature is not the only source of fluctuations in these systems: additional athermal fluctuations are generated at the molecular scale by enzymes that drive the system out of thermal equilibrium. Examples of soft non-equilibrium materials are also found in artificial and biomimetic systems, such as chemically fueled synthetic fibers and crystals of active colloidal particles [6–8]. In all these systems, traces of non-equilibrium may propagate from molecular to larger scales, with striking examples in biology, such as the mitotic spindle and protein pattern formation [9–11]. However, non-equilibrium may also manifests as random fluctuations, seemingly indistinguishable from simple thermal motion. For instance, active dynamics were observed in the fluctuations of biological assemblies, such as chromosomes [12], tissue[13], membranes [14–16] and cytoplasm [17–20]. This active dynamics can affect the macroscopic mechanical properties of soft materials and a systematic non-equilibrium characterization could help guide the development of engineered biomaterials [2, 21–23]. While we have a comprehensive toolset to measure the equilibrium response of thermal soft materials, it still remains an outstanding challenge to characterize the stochastic non-equilibrium dynamics of active soft assemblies.

A well-established approach to quantify non-equilibrium is based on the violation of the fluctuation-dissipation theorem (FDT). The idea of this approach is to compare the fluctuation spectrum of a probe particle with the associated response function to investigate if these two quantities obey the FDT. This method has been used both in *in vivo* biological assemblies and *in vitro* reconstituted networks [15, 17, 19, 20, 24]. However, such an approach requires a measurement of the system's response function, which may be technically difficult especially in living systems. Recently, new non-invasive approaches have been proposed, based on the detection of the irreversibility of stochastic trajectories. Such irreversibility can be expressed, for instance, in the form of broken detailed balance [25–29] or in terms of the entropy production rate [28, 30–34]. Broken detailed balance can be determined from circulating currents in the coordinates space of pairs of mesoscopic degrees of freedom. Frequently used measures to quantify circulating currents in phase space are the area enclosing rate and the cycling frequency of the stochastic trajectories [26, 35, 36]. These measures are closely related to the entropy production rate [28, 29].

The interpretation of the results of various non-equilibrium measurements can be aided by considering concrete models for active systems. Recently, we considered a simple model of driven elastic assemblies consisting of a bead-spring network [28, 29] where the beads can experience both thermal and active fluctuations. Using this model, we estimated the area enclosing rate and the cycling frequency from the trajectories of two probe particles. On average such non-equilibrium measures exhibit a power law behavior as a function of the distance between the probe particles. Inspired by the approach of two-point microrheology, in which the fluctuations of a pair of probe particles reveal the viscoelastic response of

* C.broedersz@lmu.de

an equilibrium system [37], here we investigate whether we can extend such an approach to non-equilibrium assemblies: can one extract information on the nature of the active driving in an elastic assembly, simply from the analysis of a two-point non-equilibrium measure?

We consider this question in the context of a class of elastic systems with stochastic internal driving. This internal driving can be described as a stochastic process with specific statistical properties that characterize their spatial and temporal features. Here we focus on the spatial properties of the stochastic internal driving and investigate several scenarios that may be relevant in biological systems. For instance, the internal driving can be implemented as a heterogeneous distribution of spatially and temporally uncorrelated stochastic forces. This description may be adequate to represent the enhanced diffusion experienced within certain regions of a cellular environment due to catalytic enzymes [38–40]. However, the sources of activity in a biological environment can take a variety of forms, including contributions from chemophoresis [41] or molecular motors. For instance, force-generation by molecular motors such as myosin can be introduced as force dipoles randomly distributed over the network [21, 42–44]. Furthermore, the intracellular organization of enzymes and molecular motors may also result in long-range correlation of the activities [45–47].

In this work we investigate how such intrinsic spatial features of the active noise may be reflected in the long-range scaling behavior of two-point non-equilibrium measures. We employ a model of internally driven elastic networks to describe biological assemblies. To consider a general scenario, we describe internal activity with stochastic forces acting either as monopoles or as dipoles. Within this framework we show analytically and numerically how the scaling behavior of the cycling frequencies and area enclosing rates depends on the parameters that characterize the active noise, i.e intensity and density of the monopole- and dipole-like activities. Finally, we show how our framework can be extended to account for spatial correlations in the intensities of the noise. Our results give insights into possible methods of quantifying non-equilibrium in biological assemblies and, more specifically, into how an experimental observation of a particular scaling behavior of non-equilibrium measures can give access to the properties of the active driving.

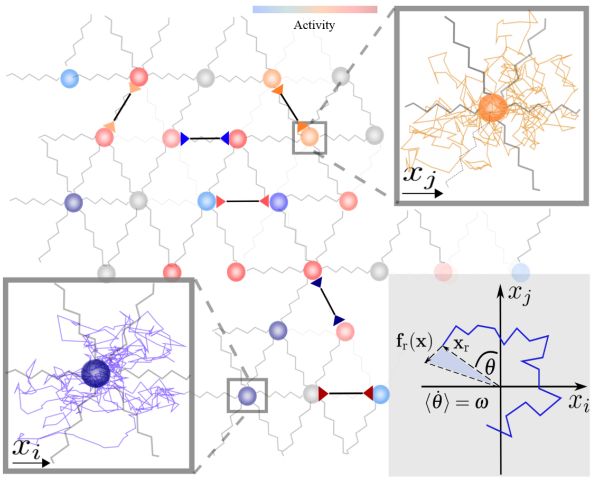

FIG. 1. A) Schematic of the elastic network with monopole and dipole forces. The colors of the beads indicate the intensities of the monopole-like activity, the colors of the arrows indicate the intensity of the dipole-like activity. Inset on the lower right: schematic of a trajectory in the x_i and x_j coordinate space. The indicated non-equilibrium measures are: cycling frequency ω, and area enclosing rate obtained upon averaging $(\mathbf{f}_r \times \mathbf{x}_r)/2\gamma$ (light blue area) in phase space.

II. MODEL

To establish a relation between mesoscopic non-equilibrium measures and the internal activity, we consider a model for an elastic assembly driven by stochastic activity [28, 48–50]. Our model consists of a network of N beads connected by springs of elastic constant k. The network is immersed in a thermal bath at temperature T, and we indicate with γ the friction coefficient.

Within the cellular environment there may be several sources of athermal fluctuations. Part of the active fluctuations of the assembly comes from the active agents exerting forces directly on the network. Examples are molecular motors sliding along the filaments, or the continuous (dis)assembly of biopolymers. Such contributions are often modelled as force-dipoles with zero net force [21, 42–44, 51–55]. In other cases, non-equilibrium fluctuations may also be generated indirectly, e.g. through hydrodynamic interactions between the active agents in the surrounding environment. Examples include enzymes, ion pumps and motors that generate hydrodynamic flows in the cytoplasm and indirectly influence the dynamics of the network. Such effects could lead to active contributions in the form of randomly fluctuating monopole-forces acting on the elements of the network [19, 56–58]. Here, we focus on the general effects of certain classes of active processes on the dynamics of the cellular environment, without specifying the underlying molecular mechanism. In our description, each class of active forces is distinguished by the moment of the forces.

To describe a general scenario, we generate the active driving in our network as Gaussian white noise of either a monopole or a dipole nature, with respective densities ρ^{M} and ρ^{D} (Fig. 1). By modeling the active forces as a white noise process, we assume a time scale separation between the dynamics of the microscopic active forces and the relaxation times of the system. We therefore expect our results to hold in the regime of large distances, at which the relaxation times of the network become larger than the correlation times of the active processes.

We denote the displacements of the beads relative to their rest positions by the vector $\mathbf{x} = \{x_1, \ldots, x_{Nd}\}$, where d indicates the dimensionality of the system. The overdamped equation of motion for the displacement of the $i_{\rm th}$ degree of freedom in the lattice reads

$$\frac{dx_i(t)}{dt} = a_{ij}x_j(t) + \eta_i^T(t) + b_i^{\rm M}\eta_i^{\rm M}(t) + \sum_{k\in {\rm nn}} b_{ik}^{\rm D}\eta_{ik}^{\rm D}(t), \quad (1)$$

where a_{ij} are the entries of the elastic interaction matrix $\mathbf{A}$, divided by the friction coefficient γ. The thermal noise is described by the standard fluctuation-dissipation relation

$$\langle \eta_i^T(t)\eta_j^T(t')\rangle = \frac{2k_{\rm B}T}{\gamma}\delta_{i,j}\delta(t-t'), \quad (2)$$

where $k_{\rm B}$ indicates the Boltzmann constant. The coefficients $b_i^{\rm M}$ and $b_{ik}^{\rm D}$ are introduced to describe the presence of monopole and dipole active noise; they are time-independent random variables such that $b_{i/ik}^{\rm M/D} \in \{0,1\}$, $b_{ik}^{\rm D} = b_{ki}^{\rm D}$, with probability distribution $P\left(b_{i/ik}^{\rm M/D} = 1\right) = \rho^{\rm M/D}$. The sum $\sum_{k\in {\rm nn}}$ runs only over nearest-neighbor beads. Finally, the stochastic variables for monopole forces $\eta^{\rm M}(t)$ and dipole forces $\eta^{\rm D}(t)$ are characterized by

$$\begin{aligned}\langle \eta_i^{\rm M}(t)\eta_j^{\rm M}(t')\rangle &= \frac{k_{\rm B}}{\gamma}\delta_{i,j}\alpha_i^{\rm M}\delta(t-t') \\ \langle \eta_{ij}^{\rm D}(t)\eta_{kl}^{D}(t')\rangle &= \frac{k_{\rm B}}{\gamma}\left(\delta_{ij,kl} - \delta_{ij,lk}\right)\alpha_{ij}^{\rm D}\delta(t-t').\end{aligned} \quad (3)$$

Here we indicate with $\alpha_i^{\rm M}$ and $\alpha_{ij}^{\rm D}$ the respective amplitudes of the monopole force acting on the $i_{\rm th}$ coordinate and of the dipole force acting between the $i_{\rm th}$ and $j_{\rm th}$ coordinates. We factored out the term $(k_{\rm B}/\gamma)$ for notational convenience.

This simple model admits a Fokker Planck description for the evolution of the probability distribution $p(\mathbf{x},t)$ of $\mathbf{x}$ at time t

$$\partial_t p(\mathbf{x},t) = -\nabla\cdot(\mathbf{A}\mathbf{x} - \mathbf{D}\nabla)p(\mathbf{x},t) \coloneqq -\nabla\cdot\mathbf{j}(\mathbf{x},t), \quad (4)$$

where $\mathbf{j}(\mathbf{x},t)$ is the probability current density, and $\mathbf{D}$ is the diffusion matrix. The steady-state solution of Eq. (4) is a Gaussian distribution $p(\mathbf{x}) \sim \exp[-\frac{1}{2}\mathbf{x}^T\mathbf{C}^{-1}\mathbf{x}]$, with covariance matrix $\mathbf{C}$, satisfying the Lyapunov equation [59]:

$$\mathbf{A}\mathbf{C} + \mathbf{C}\mathbf{A}^{\rm T} = -2\mathbf{D}. \quad (5)$$

The diffusion matrix can be expressed as $\mathbf{D} = \bar{\mathbf{D}} + \mathbf{D}^*$, where $\bar{\mathbf{D}}$ is a diagonal matrix with entries $\bar{d}_{ij} = \delta_{ij}k_{\rm B}T/\gamma$, representing the thermal noise contributions, and $\mathbf{D}^*$ is the non-equilibrium part of the diffusion matrix which contains information on the activities. The presence of dipole forces gives rise to anticorrelations between neighboring beads and therefore to non-zero off-diagonals terms in $\mathbf{D}^*$, as will be discussed in Sec. (III).

A. Two-point non-equilibrium measures

Our main goal is to connect a direct measure of non-equilibrium to the properties of the active driving. With this in mind, the first step is to define a two-point non-equilibrium measure which can be estimated from the trajectories of pairs of probe particles in the system.

Under steady-state conditions Eq. (4) reduces to $\nabla\cdot\mathbf{j}(\mathbf{x},t) = 0$. When $\mathbf{j}\neq 0$ the system is out of equilibrium, and exhibits on average a circulation in phase space. Such circulation may emerge also in the reduced subspace of a pair of degrees of freedom $\mathbf{x}_{\rm r} = \{x_i, x_j\}$. These reduced subspaces are more easily accessible experimentally as compared to the full set of degrees of freedom. For this reason we restrict our non-equilibrium measures to these two-dimensional subspaces.

As a first measure of circulation, we use the average area enclosing rates $\mathcal{A}_{ij}$ of the trajectory in the reduced subspace of the coordinates x_i and x_j, as illustrated in Fig. 1. For an overdamped system, for which the velocity is proportional to the force, this quantity can be expressed as [29]:

$$\mathcal{A}_{ij} = \frac{1}{2\gamma}\langle \mathbf{x}_{\rm r}\times\mathbf{f}_{\rm r}(\mathbf{x})\rangle \quad (6)$$

where $\mathbf{f}_{\rm r}(\mathbf{x}) = \{f_i, f_j\}$ is the vector of forces acting respectively on the coordinate i and j. By replacing $\gamma^{-1}\langle \mathbf{x}_{\rm r}\times\mathbf{f}_{\rm r}(\mathbf{x})\rangle = \gamma^{-1}\langle x_i f_j(\mathbf{x}) - x_j f_i(\mathbf{x})\rangle = (\mathbf{C}\mathbf{A}^{\rm T} - \mathbf{A}\mathbf{C})_{ij}$ we obtain [29, 35, 36].

$$\mathcal{A}_{ij} = \frac{1}{2}(\mathbf{C}\mathbf{A}^{\rm T} - \mathbf{A}\mathbf{C})_{ij}, \quad (7)$$

This non-equilibrium measure turns out to be closely related to the cycling frequency– the rate at which the trajectory revolves in the coordinates space:

$$\omega_{ij} = \frac{1}{2}\frac{(\mathbf{C}\mathbf{A}^{\rm T} - \mathbf{A}\mathbf{C})_{ij}}{\sqrt{\det(\mathbf{C}_{[{\rm r},{\rm r}]})}}, \quad (8)$$

where $\mathbf{C}_{[{\rm r},{\rm r}]}$ is a $[2\times 2]$ matrix with entries $\mathbf{C}_{[{\rm r},{\rm r}]} = \{\{c_{ii}, c_{ij}\}, \{c_{ji}, c_{jj}\}\}$. Unlike the area enclosing rate, the cycling frequency is invariant under an orientation preserving change of basis. This invariance is ensured by the factor $\sqrt{\det(\mathbf{C}_{[{\rm r},{\rm r}]})}$ in Eq. (8). Furthermore, the cycling frequency is informative of the partial rate of entropy produced in the reduced subspace of the pair of observed degrees of freedom, through the expression $\Pi^{(2)} = k_B\omega_{ij}^2\,{\rm Tr}(\mathbf{C}_{[{\rm r},{\rm r}]}\mathbf{D}_{[{\rm r},{\rm r}]}^{-1})$ [28].

Both these non-equilibrium measures display on average a power law behavior as function of the distance r between the tracked particles [28, 29]. However, different properties of the active noise in the system may give rise to different functional forms of the scaling behavior. In Sec. (III) we investigate this matter, and in particular we aim to connect the scaling of these experimentally accessible non-equilibrium measures to the intrinsic properties of the internal driving.

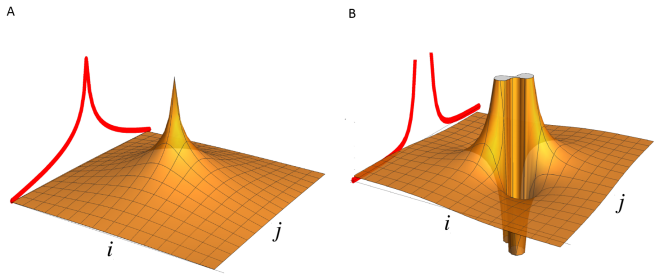

FIG. 2. A) Covariance matrix of single monopole source and its projection on the jz plane B) Covariance matrix of single dipole source and its projection on the jz plane.

III. RESULTS

In this section we analytically and numerically study the spatial scaling behaviors for $\langle \mathcal{A}^2(r)\rangle_\alpha$ and $\langle \omega^2(r)\rangle_\alpha$, the squared area enclosing rate and cycling frequency between two tracer beads at distance r, averaged over the distribution of activities $\alpha_{i/ij}^{M/D}$. Here we indicate with $\langle \ldots \rangle_\alpha$ the ensemble average over the activities, which for a large enough system can be obtained as a spatial average over the network [28]. Note, here we focus on the second moment of the non-equilibrium measures, because these measures are distributed symmetrically around zero with a vanishing first moment. Our analytical expressions for the scaling laws of $\langle \mathcal{A}^2(r)\rangle_\alpha$ and $\langle \omega^2(r)\rangle_\alpha$ provide a direct connection between these non-equilibrium measures and the properties of the active noise, such as the densities and activity intensities of monopoles and dipoles forces. The validity of our analytical results obtained in this section will be tested by making a direct comparison with numerical solutions of Eq. (7) and Eq. (8). In Sec. (III A) we focus for simplicity on a one-dimensional chain, and in Sec. (III B) we show an extension to a two-dimensional network. Finally, in Sec. (III C) we discuss how the scaling law is affected by the presence of finite spatial correlation of the intensities of the active noise.

A. One-dimensional chain

We consider here the simple yet instructive case of a one-dimensional chain. Using a continuous approximation, we find a solution of Eq. (5) for the covariance matrix and derive the scaling laws for the non-equilibrium measures $\langle \mathcal{A}^2\rangle_\alpha$ and $\langle \omega^2\rangle_\alpha$ as function of the distance r between the tracer particles.

As a first step, we determine the form of the non-equilibrium part of the diffusion matrix $\mathbf{D}$ appearing in Eq. (5). The simple configuration of a one-dimensional case allows us to replace the double index of the dipoles amplitudes $\{\alpha_{12}^{\mathrm{D}}, \alpha_{23}^{\mathrm{D}}, \ldots, \alpha_{i,i+1}^{\mathrm{D}}, \ldots, \alpha_{N-1,N}^{\mathrm{D}}\}$ with a single index running over the pairs of nearest-neighbor beads $\{\alpha_1^{\mathrm{D}}, \alpha_2^{\mathrm{D}}, \ldots, \alpha_i^{\mathrm{D}}, \ldots, \alpha_{N-1}^{\mathrm{D}}\}$. The activities amplitudes $\{\alpha_i^{\mathrm{M/D}}\}$ are sampled independently from a distribution $p_\alpha^{M/D}$ with mean $0 < \bar{\alpha}^{\mathrm{M/D}} < \infty$ and variance $\sigma^2_{\alpha^{\mathrm{M/D}}}$.

A monopole-like active noise at site z along the chain, contributes with an entry on the diagonal of the diffusion matrix $d_{z,z}$. By contrast, a dipole-like noise acts with completely anti-correlated forces on the beads at positions z and $z+1$, contributing with four entries in the diffusion matrix: $\left[d_{z,z} = d_{z+1,z+1} = (k_{\mathrm{B}}/\gamma)\alpha_z^D\right]$ and $\left[d_{z+1,z} = d_{z,z+1} = -(k_{\mathrm{B}}/\gamma)\alpha_z^D\right]$. Therefore, the non-equilibrium part of the diffusion matrix will be a sum over monopole and dipole contributions of the form

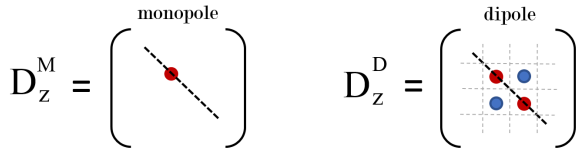

In general, owing to the linearity of the Lyapunov equation (see Eq. (5)), the covariance matrix can be expressed as

$$\mathbf{C} = \frac{k_{\mathrm{B}}}{k}(T\overline{\mathbf{C}} + \sum_z \alpha_z^{\mathrm{M}}\mathbf{C}_z^{\mathrm{M}} + \alpha_z^{\mathrm{D}}\mathbf{C}_z^{\mathrm{D}}), \tag{9}$$

such that $\overline{\mathbf{C}}$, $\mathbf{C}_z^{\mathrm{M}}$ and $\mathbf{C}_z^{\mathrm{D}}$ are dimensionless. Here $\overline{\mathbf{C}}$ is the equilibrium solution of Eq. (5) obtained for $\{\alpha_i^{\mathrm{M/D}}\} = 0$, and $\mathbf{C}_z^{\mathrm{M/D}}$ are solutions of Eq. (5) for single monopole/dipole noise of intensity $\alpha_z^{\mathrm{M/D}}$ at position z along the chain. For a one-dimensional system the interaction matrix $\mathbf{A}$ has a simple form with entries: $a_{ij} = \frac{k}{\gamma}(-2\delta_{ij} + \delta_{i,i+1} + \delta_{i,i-1})$. By inserting this expression for a_{ij} together with Eq. (9) into Eq. (7), we can express the area enclosing rate between any two tracer particles i and j that are not connected by a dipole activity ($d_{ij} = 0$), as [29]

$$\mathcal{A}_{ij} = \frac{k_{\mathrm{B}}}{\gamma}\sum_z (\xi_z^{\mathrm{M}}\widetilde{\partial}_2^2 c_z^{\mathrm{M}} + \xi_z^{\mathrm{D}}\widetilde{\partial}_2^2 c_z^{\mathrm{D}}), \tag{10}$$

where $\xi^{\mathrm{M/D}} = b^{\mathrm{M/D}}\alpha^{\mathrm{M/D}}$ and we replaced the double indices in the coefficients $\{b_{12}^{\mathrm{D}}, b_{23}^{\mathrm{D}}, \ldots, b_{i,i+1}^{\mathrm{D}}, \ldots, b_{N-1,N}^{\mathrm{D}}\}$ with single index $\{b_1^{\mathrm{D}}, b_2^{\mathrm{D}}, \ldots, b_i^{\mathrm{D}}, \ldots, b_{N-1}^{\mathrm{D}}\}$. For notational simplicity we omit the subscripts i, j on the right hand side, and we use $\widetilde{\partial}_2^2 c = c_{i,j+1} - 2c_{i,j} + c_{i,j-1}$ to indicate the discrete second derivative across rows. As can be seen from Eq. (10), the scaling behaviors of $\mathcal{A}_{ij}$, and therefore ω_{ij}, are determined by the curvature of the covariance matrix. To find an expression for the curvature, we can calculate the explicit form of $C_z^{\mathrm{M/D}}$, as a solution of the equation

$$\frac{k_{\mathrm{B}}\alpha_z^{\mathrm{M/D}}}{\gamma}\left(\widetilde{\partial}_1^2 c_z^{\mathrm{M/D}} + \widetilde{\partial}_2^2 c_z^{\mathrm{M/D}}\right) = -2d_z^{\mathrm{M/D}}, \tag{11}$$

which is obtained from Eq. (5) by considering a single monopole/dipole contribution at position z along the

chain. Eq. (11) can be viewed as a discretized Poisson equation with sources set by the elements of $\mathbf{D}$. The solution for a generic diffusion matrix will be obtained as a superposition of single-contribution solutions. In the continuous limit, for a single entry in the diffusion matrix $d_{z,\tilde{z}}$, the single-source solution of Eq. (11) gives $c(i,j) = -\frac{1}{\pi}\ln(\varrho) + b$, where $\varrho = \sqrt{(i-z)^2 + (j-\tilde{z})^2}$ indicates the distance from the source in the matrix and b is an integration constant. Here we assumed radial symmetry of the solution around the source. The profile of $C_z^{\mathrm{M/D}}$ is different for the monopole and dipole cases and exhibits respectively a logarithmic profile $c^{\mathrm{M}} \propto \ln(\varrho)$ and a power-law scaling $c^{\mathrm{D}} \propto \varrho^{-3}$, as illustrated in Fig. 2. These distinct scaling laws will later turn out to underlie the different scaling laws for the non-equilibrium measures.

To determine the area enclosing rate for a pair of beads at distance r we need to compute contributions of the form $\widetilde{\partial}_2^2 c^{\mathrm{M/D}}_{z;-r/2,r/2} := \widetilde{\partial}_2^2 c_z^{\mathrm{M/D}}(r)$. Here for concreteness we have chosen beads with indices $i = -r/2$, $j = r/2$, where the index 0 corresponds to the central bead. Note that the distance r is dimensionless and measured in units of lattice spacing ℓ. In the following we approximate the discrete derivatives applied to the matrix elements $\widetilde{\partial}_2^2 c_z^{\mathrm{M/D}}(r)$ with regular derivatives applied to the solutions of the Poisson equation $\partial_2^2 c_z^{\mathrm{M/D}}(r)$.

A single monopole activity at site z contributes a diagonal entry in the diffusion matrix $d_{z,z}$. This appears as a monopole source at position (z,z) in the Poisson equation. Using the continuous solution derived above we find [29]

$$\partial_2^2 c_z^{\mathrm{M}}(r) = \frac{8rz}{\pi(r^2+4z^2)^2}, \tag{12}$$

A single dipole activity between sites z and $z+1$ contributes four entries in the diffusion matrix: $[d_{z,z} = -d_{z+1,z} = -d_{z,z+1} = d_{z+1,z+1}]$. These enter the Poisson equation as a quadrupole source. By summing these four contributions we obtain

$$\begin{aligned}\partial_2^2 c_z^{\mathrm{D}}(r) =& \frac{8rz}{\pi(r^2+4z^2)^2} \\ &- \frac{4(-1+r)(1+2z)}{\pi(2+(-2+r)r+4z(1+z))^2} \\ &- \frac{4(1+r)(1+2z)}{\pi(2+(2+r)r+4z(1+z))^2} \\ &+ \frac{8r(1+z)}{\pi(r^2+4(1+z)^2)^2}.\end{aligned} \tag{13}$$

From Eq. (12) and Eq. (13), it follows that when the only activity in the chain appears at one of the observed beads, for instance $z = i = -r/2$, then $\mathcal{A}_{ij} \sim r^{-2}$ for a monopole activity and $\mathcal{A}_{ij} \sim r^{-5}$ for a dipole activity, in the limit $r \gg 1$. As we will see below, the scaling of the curvature of the covariance (Eq. (12) and Eq. (13) underlies also the scaling behavior of the average quantities $\langle\omega^2(r)\rangle$ and $\langle\mathcal{A}^2(r)\rangle$ with distance.

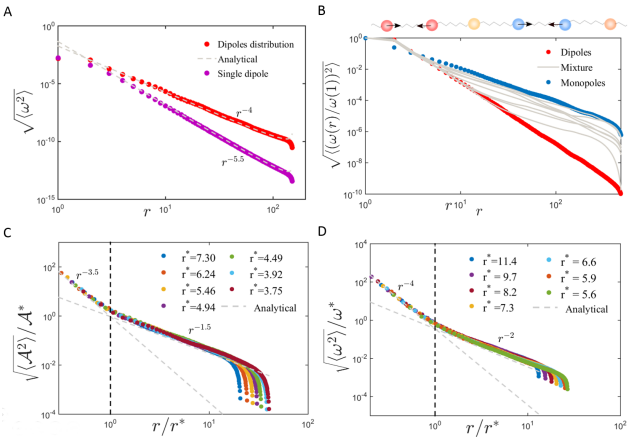

FIG. 3. A) Scaling behavior of the cycling frequency with r for a system with only dipoles as active noise. Numerical results in red and purple, and analytical predictions in gray. B) Scaling behavior of the cycling frequency with r for a system with activity given by: only dipoles (red), only monopoles (blue), mixture of dipoles and monopoles (gray) C) Rescaling of $\mathcal{A}$ for a range of r^* and $\mathcal{A}^*$, and analytical prediction of the two scaling regimes in gray. D) Rescaling of ω for a range of r^* and ω^*, and analytical prediction of the two scaling regimes in gray.

After this preparatory work, we are ready to obtain the first central results of this paper: Inserting Eq. (12) and Eq. (13) into Eq. (10), and averaging over configurations of the activity intensities, we obtain in the limit $r \gg 1$ (Sec. (1) supplementary):

$$\langle\mathcal{A}^2(r)\rangle_\alpha = \frac{1}{\pi}\left(\frac{k_{\mathrm{B}}}{\gamma}\right)^2\left(\rho^{\mathrm{M}}\sigma^2_{\alpha^{\mathrm{M}}}\frac{1}{2r^3} + \rho^{\mathrm{D}}\sigma^2_{\alpha^{\mathrm{D}}}\frac{45}{r^7}\right). \tag{14}$$

Thus, we observe two different regimes: a monopole-controlled regime $\langle\mathcal{A}^2(r)\rangle_\alpha \propto 1/r^3$ for long distances and a dipole-controlled regime $\langle\mathcal{A}^2(r)\rangle_\alpha \propto 1/r^7$ for short distances, as shown in Fig. 3C. Recall that r is measured in units of the lattice spacing ℓ. To rewrite Eq. 14 in terms of the actual distance, $r\ell$, between the particles would require introducing a dependence on ℓ in both terms. Furthermore, we notice that in our model the dipole size equals ℓ, and a generalization of the model to describe dipoles of arbitrary size would introduce a dependence on the dipole's size in the second term of Eq. 14

A similar scaling behavior can be obtained also for the cycling frequencies ω by applying a similar approach to Eq. (8): Decomposing $\mathbf{C} = \frac{k_B}{k}\left(T\overline{\mathbf{C}} + \bar{\alpha}^{\mathrm{M}}\mathbf{C}^{\mathrm{M}} + \bar{\alpha}^{\mathrm{D}}\mathbf{C}^{\mathrm{D}}\right)$ and expanding the factor $1/(\det\mathbf{C})$ up to linear order in $\frac{\bar{\alpha}^{\mathrm{M/D}}}{T}$, we obtain

$$\langle\omega^2(r)\rangle_\alpha = \frac{(k/\gamma)^2}{\pi T^2 \det\overline{\mathbf{C}}_{[\mathrm{r,r}]}}\left(\rho^{\mathrm{M}}\sigma^2_{\alpha^{\mathrm{M}}}\frac{1}{2r^3} + \rho^{\mathrm{D}}\sigma^2_{\alpha^{\mathrm{D}}}\frac{45}{r^7}\right). \tag{15}$$

Considering that [29] for $r \ll N$, $\det\overline{\mathbf{C}}_{[\mathrm{r,r}]} \propto Nr$, we obtain two different regimes also for the scaling of the cy-

cling frequency: $\langle\omega^2(r)\rangle_\alpha \propto 1/r^4$ at short distances and $\langle\omega^2(r)\rangle_\alpha \propto 1/r^8$ at long distances (Fig. 3B,D). Interestingly, in the presence of a distribution of only dipoles in the systems ($\rho^{\mathrm{M}} = 0$), the scaling exponent for the average cycling frequency ($\sqrt{\langle\omega^2\rangle_\alpha} \sim r^{-4}$) differs from the exponent obtained with a single dipole activity at site $z = i = -r/2$ ($\sqrt{\omega^2} \sim r^{-5.5}$) (Fig. 3A). The same holds for a distribution of only monopoles ($\rho^{\mathrm{D}} = 0$), for which the scaling exponent $\sqrt{\langle\omega^2\rangle_\alpha} \sim r^{-2}$ differs from the single monopole scaling ($\sqrt{\omega^2} \sim r^{-2.5}$) [29].

Which parameters of our model determine the crossover distance r^* between the two scaling regimes? A direct calculation of r^* and the mean cycling frequency at the crossover distance $\langle\omega^2(r^*)\rangle$ leads to

$$r^* = \left(\frac{90\rho^{\mathrm{D}}\sigma^2_{\alpha^{\mathrm{D}}}}{\rho^{\mathrm{M}}\sigma^2_{\alpha^{\mathrm{M}}}}\right)^{1/4} \qquad \langle\omega^2(r^*)\rangle_\alpha = \frac{2k^2}{\pi T^2\gamma^2 45N}\frac{{\rho^{\mathrm{M}}}^2\sigma^4_{\alpha^{\mathrm{M}}}}{\rho^{\mathrm{D}}\sigma^2_{\alpha^{\mathrm{D}}}}. \tag{16}$$

Note that $\langle\omega^2\rangle$ decreases as $1/N$, due to dependence of the determinant (see Eq. (15)) on system size: $\det \overline{\mathbf{C}}_{[\mathrm{r,r}]} \sim N$. However, such a scaling with system size is a property of one-dimensional systems, and will not appear in $d = 2$ and $d = 3$, where we expect respectively $\det \overline{\mathbf{C}}_{[\mathrm{r,r}]} \sim \ln(N)$ and $\det \overline{\mathbf{C}}_{[\mathrm{r,r}]} \sim$ constant [29].

For the the area enclosing rate at the crossover point, we find

$$\langle\mathcal{A}^2(r^*)\rangle_\alpha = \frac{k_{\mathrm{B}}^2}{\pi\gamma^2 90}\frac{{\rho^{\mathrm{M}}}^2\sigma^4_{\alpha^{\mathrm{M}}}}{\rho^{\mathrm{D}}\sigma^2_{\alpha^{\mathrm{D}}}}r^*, \tag{17}$$

as shown in Fig. 3C,D, where we obtain a collapse of data by rescaling the x-axes by r^* and the y-axes by $\mathcal{A}^*$ and ω^*.

Our results provide an indication of what kind of measurements could be performed to gain information on the non-equilibrium driving in an elastic system. For instance, the experimental observation of one of the scaling behaviors discussed here, e.g. for the cycling frequencies or area enclosing rates, would allow one to discriminate the monopole or dipole nature of the active driving. In the more general case of a mixture of monopoles and dipoles, a direct measure of the transition points between two different scaling regimes would help to gain quantitative information on the quantities $\rho^{\mathrm{D}}\sigma^2_{\alpha^{\mathrm{D}}}$ and $\rho^{\mathrm{M}}\sigma^2_{\alpha^{\mathrm{M}}}$.

Up to this point, we discussed the scaling behavior of both non-equilibrium measures: cycling frequencies and area enclosing rates. However, from the results presented so far, it is clear that these two quantities are closely related. Depending on the context, one measure might be preferable to the other. For instance, the cycling frequencies are more directly related to the probability currents and the entropy production rate [28]. However, the cycling frequencies may be more sensitive to experimental errors: for parts of trajectories that come close to the origin of phase space, a small error in the position measurement can lead to an error of order π for the angular displacement. By contrast, a measurement of the area

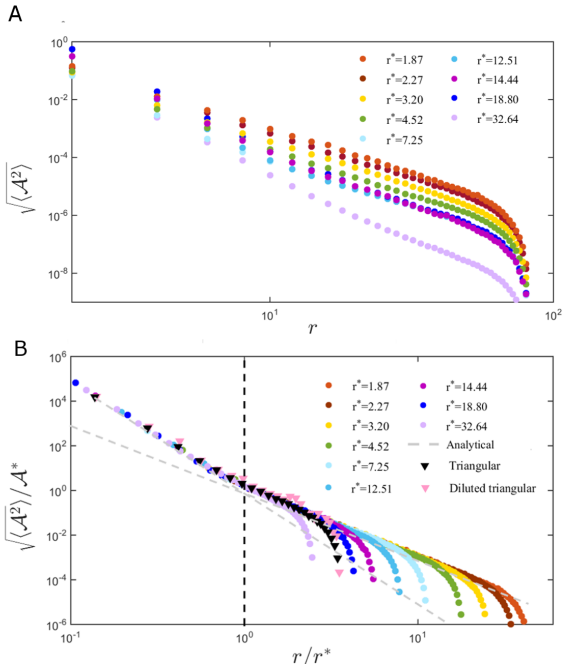

FIG. 4. A)Scaling behavior of $\langle\mathcal{A}^2\rangle$ as function of the distance for two-dimensional lattices obtained for a square lattice and different values of r^*. B) Data-collapse of the results in A, obtained by rescaling the x and y axes respectively by r^*_{2d} and $\mathcal{A}({r_{2d}}^*)^2$. The triangular markers correspond respectively to the data for a full triangular lattice (in black) and a randomly diluted triangular lattice (in pink) with dilution probability $p_d = 0.8$

enclosing rate does not require specifying the position of the origin. Furthermore, the derivation of the scaling law for the area enclosing rate does not require any approximation, and holds irrespectively of the magnitudes of the amplitudes of the active forces. In the limit of weak activity, one can always easily obtain the scaling behavior of the cycling frequencies using the approximate expressions for $\det \overline{\mathbf{C}}_{[\mathrm{r,r}]}$ introduced above. Keeping these considerations in mind, from now on we will only focus on the scaling behavior of the area enclosing rates.

B. Two-dimensional network

In this section we discuss how the results from Sec. (III A) can be extended to the case $d > 1$. For simplicity, we focus on a two-dimensional square network, but we will discuss how the results obtained for this simple case also apply to more complex geometries. In addition, we consider the dipole forces acting always along the principal axes of the network, which corresponds to the limit of small displacements in the systems (Sec. (2) supplementary).

We denote the elements of the covariance matrix, corresponding to beads at sites $\mathbf{i} = (i_x, i_y)$ and $\mathbf{j} = (j_x, j_y)$ in the lattice, as $c_{i_x,i_y;j_x,j_y}$. We consider zero rest length

springs in such a way that the x and y coordinates decouple. Therefore, by $\mathbf{C}$ we mean the covariance matrix of only the degrees of freedom that correspond to a single chosen direction, and we can restrict the dipoles forces to always act along such direction, for instance the y-direction. This allows us to employ a one to one correspondence between dipoles and sites of the network. From Eq. (7), we find [29]

$$\mathcal{A}_{i_x,i_y;j_x,j_y} = \frac{k}{\gamma}\sum_{l=1}^{2}\tilde{\partial}_l^2 c_{i_x,i_y;j_x,j_y}, \tag{18}$$

for beads not connected by a dipole activity ($d_{i_x,i_y;j_x,j_y} = 0$). Here, the index l runs over the directions i_x and i_y. As in the one-dimensional case, we have a direct relation between $\mathcal{A}$ and the second derivatives of the covariance matrix. Therefore, to find the scaling of $\mathcal{A}$ with the distance between two beads r, we need to find an expression for $\tilde{\partial}_l^2 c_{i_x,i_y;j_x,j_y}(r)$.

As in Sec. (III A), we can rewrite the covariance matrix as: $\mathbf{C} = \frac{k_\mathrm{B}}{k}\left(T\overline{\mathbf{C}} + \sum_{\mathbf{z}}\xi_{\mathbf{z}}^{\mathrm{M}}\mathbf{C}_{\mathbf{z}}^{\mathrm{M}} + \xi_{\mathbf{z}}^{\mathrm{D}}\mathbf{C}_{\mathbf{z}}^{\mathrm{D}}\right)$, where we summed over contributions from all the monopole and dipole activities at sites $\mathbf{z} = (z_x, z_y)$ in the lattice. The continuous limit of the Lyapunov equation (Eq. (5)) gives a Poisson equation in a four-dimensional space [29]. In the case of a single non-zero entry in the diffusion matrix, $d_{z_x,z_y;\tilde{z}_x,\tilde{z}_y}$, solving the Poisson equation gives $c(\mathbf{i},\mathbf{j}) \sim \varrho^{-2}$, where $\varrho = \sqrt{(\mathbf{i}-\mathbf{z})^2 + (\mathbf{j}-\tilde{\mathbf{z}})^2}$ is the distance from the source. Using this continuous solution and replacing the discretized derivatives with standard ones we find

$$\partial^2 c(\mathbf{i},\mathbf{j}) = \frac{2}{\pi^2}\frac{(\mathbf{i}-\mathbf{z})^2 - (\mathbf{j}-\tilde{\mathbf{z}})^2}{((\mathbf{i}-\mathbf{z})^2 + (\mathbf{j}-\tilde{\mathbf{z}})^2)^3}, \tag{19}$$

where we redefined $\partial^2 = \sum_{l=1}^{2}\partial_l^2$.

A monopole activity at site $\mathbf{z} = (z_x, z_y)$ contributes a diagonal entry in the diffusion matrix: $d_{z_x,z_y;z_x,z_y}$. As two beads at distance r we can take, for instance, $(i_x, i_y) = (0, r/2)$ and $(j_x, j_y) = (0, -r/2)$, where for convenience we index the beads with the network center at $(0, 0)$. Then, for the case of a single monopole activity at the site (z_x, z_y) we obtain

$$\partial^2 c_{\mathbf{z}}^{\mathrm{M}}(r) = \frac{2}{\pi^2}\frac{16 r z_y}{(r^2 + 4(z_x^2 + z_y^2))^3}. \tag{20}$$

If we now consider a dipole random force of intensity α_i between two neighboring beads at position (z_x, z_y) and $(z_x, z_y{+}1)$, this would correspond to four non-zero entries in the diffusion matrix: $[d_{z_x,z_y;z_x,z_y} = d_{z_x,z_y+1;z_x,z_y+1} = -d_{z_x,z_y;z_x,z_y+1} = -d_{z_x,z_y+1;z_x,z_y}]$. Therefore a single dipole activity enters the Poisson equation as a quadrupole source. Summing over all four contributions, we obtain for the second derivative of the covariance matrix for a single dipole activity

$$\begin{aligned}\partial^2 c_{\mathbf{z}}^{\mathrm{D}}(r) =& \frac{2}{\pi^2}\frac{8(1-r)(1+2z_y)}{(2+(-2+r)r+4z_x^2+4z_y(1+z_y))^3} \\ &- \frac{2}{\pi^2}\frac{8(1+r)(1+2z_y)}{(2+(2+r)r+4z_x^2+4z_y(1+z_y))^3} \\ &+ \frac{2}{\pi^2}\frac{16 r z_y}{(r^2+4(z_x^2+z_y^2))^3} \\ &+ \frac{2}{\pi^2}\frac{16 r(1+z_y)}{(r^2+4(z_x^2+(z_y+1)^2))^3},\end{aligned} \tag{21}$$

With similar steps as in the one-dimensional case, we find for the area enclosing rate:

$$\langle \mathcal{A}^2(r)\rangle_\alpha \simeq \left(\frac{2k_\mathrm{B}}{\pi^2\gamma}\right)^2\left[\rho^{\mathrm{M}}\sigma_{\alpha^{\mathrm{M}}}^2\frac{2\pi}{5r^6} + \rho^{\mathrm{D}}\sigma_{\alpha^{\mathrm{D}}}^2\frac{529}{r^{10}}\right]. \tag{22}$$

where to obtain the numerical prefactor and the scaling exponent in the second term we used a linear interpolation (Sec. (1) supplementary). Similarly to the one-dimensional case (see Eq. (14)), we recognize the presence of two different regimes at short and long distances. The crossover distance ${r^*}_{2D}$ between the monopole and dipole dominated regimes and the corresponding $\langle \mathcal{A}^2(r_{2D}^*)\rangle$ read:

$$\begin{aligned} r_{2D}^* &\simeq 4.5\left(\frac{\rho^{\mathrm{D}}\sigma_{\alpha^{\mathrm{D}}}^2}{\rho^{\mathrm{M}}\sigma_{\alpha^{\mathrm{M}}}^2}\right)^{1/4}, \\ \langle \mathcal{A}^2(r_{2D}^*)\rangle_\alpha &\simeq \frac{k_\mathrm{B}^2 12\cdot 10^{-6}}{\gamma^2}\frac{\left(\rho^{\mathrm{M}}\sigma_{\alpha^{\mathrm{M}}}^2\right)^{5/2}}{(\rho^{\mathrm{D}}\sigma_{\alpha^{\mathrm{D}}}^2)^{3/2}}. \end{aligned} \tag{23}$$

These analytical results are confirmed by the numerical data in Fig. 4A, B, where we obtain a collapse by properly rescaling the x-axis by r^* and the y-axis by $\mathcal{A}^2({r_{2D}}^*)$.

To investigate the sensitivity of these results to the specific underlying lattice structure, we studied triangular and bond-diluted triangular networks. We find numerically that such lattice geometries are also well described by Eqs. (22) and (23). In fact, the curves numerically obtained for the scaling behavior of $\langle \mathcal{A}^2\rangle_\alpha$ in a triangular network and diluted triangular network, overlap with the curves corresponding to the square lattice, as shown in Fig. 4 B.

C. Spatially correlated activities

Up to this point, we considered two kinds of noise sources: dipoles and monopoles, randomly distributed in space. However, in biological systems the intensities of active processes may exhibit spatial correlation, for example due to the spatial organization of enzymes and molecular motors [45–47]. Therefore, it is crucial to determine how the spatial distribution of activities influences the scaling behavior of non-equilibrium measures.

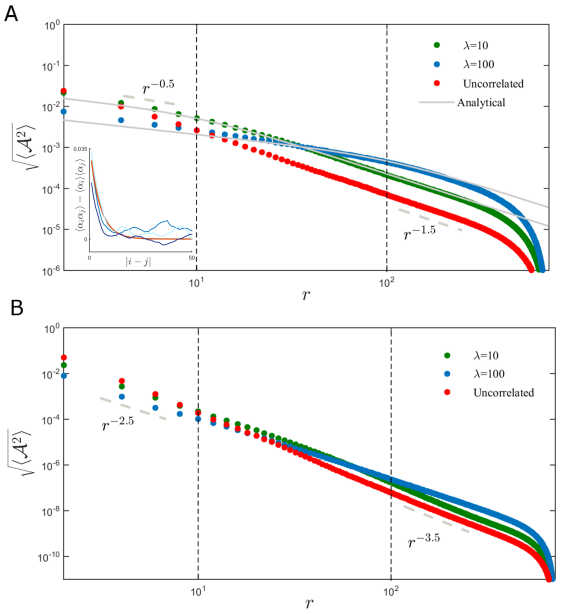

FIG. 5. A) Scaling behavior of the area enclosing rate for a system with correlated monopole-activities with correlation length $\lambda = 10$ (green), $\lambda = 100$ (blue) and uncorrelated activities (red). In gray the comparison with the analytical prediction. In the inset: spatial correlation function of the activity amplitudes. In blue the correlation functions calculated for 3 different realizations of activities with correlation length $\lambda = 10$, and in red the theoretical prediction $\sigma_\alpha^2 e^{-\frac{|i-j|}{\lambda}}$. B) Scaling behavior of the area enclosing rate for a system with dipole-activities with $\lambda = 10$ (green), $\lambda = 100$ (blue) and uncorrelated activities (red).

In this section, we consider a system where the intensities of the active noise are spatially correlated.

As an illustrative example we consider a one-dimensional chain with only monopole activities ($\rho^{\mathrm{D}} = 0$ and $\rho^{\mathrm{M}} = 1$) and thus the diffusion matrix $\mathbf{D}$ is diagonal, with entries $d_{i,j} = (k_{\mathrm{B}}/\gamma)(T + \alpha_i)\delta_{i,j}$. We draw the amplitudes $\{\alpha_i\}$ randomly from a probability distribution with covariance: $\langle \alpha_i \alpha_j \rangle - \langle \alpha_i \rangle \langle \alpha_j \rangle = \sigma_\alpha^2 e^{-\frac{|i-j|}{\lambda}}$, exhibiting a characteristic correlation length $\lambda > 0$ (see Fig. 5A). By setting $c^{\mathrm{D}} = 0$ in Eq. (10), and considering the monopole contributions as in Eq. (12), we obtain for the area enclosing rate:

$$\begin{aligned}\langle \mathcal{A}^2(r) \rangle_\alpha &= \left(\frac{k_{\mathrm{B}}}{\pi\gamma}\right)^2 \sum_{z,z'} \langle \alpha_z \alpha_{z'} \rangle \frac{8rz}{(r^2+4z^2)^2} \frac{8rz'}{(r^2+4z'^2)^2} \\ &= \left(\frac{k_{\mathrm{B}}}{\pi\gamma}\right)^2 \sum_{z,z'} \sigma_\alpha^2 e^{-\frac{|z-z'|}{\lambda}} \frac{8rz}{(r^2+4z^2)^2} \frac{8rz'}{(r^2+4z'^2)^2} \\ &\simeq \left(\frac{k_{\mathrm{B}}}{\pi\gamma}\right)^2 \sum_{z,z'=z-\lambda}^{z'=z+\lambda} (1 - \frac{|z-z'|}{\lambda}) \frac{\sigma_\alpha^2 8rz}{(r^2+4z^2)^2} \frac{8rz'}{(r^2+4z'^2)^2}, \end{aligned} \tag{24}$$

where in the last step we approximated the exponential

	single	$r < \lambda$	$r > \lambda$
	2 (2.5)	0.5 (1)	1.5 (2)
	5 (5.5)	2.5 (3)	3.5 (4)

TABLE I. Summary of the scaling exponents of area enclosing rate $\sqrt{\langle \mathcal{A}^2(r) \rangle_\alpha}$, and cycling frequency $\sqrt{\langle \omega(r)^2 \rangle_\alpha}$ (in brackets) obtained in $d = 1$ for different cases: in the first column the result for the case of a single monopole and dipole source, in the second and third columns the results for the monopoles and dipoles distributions, obtained for distances smaller and bigger then the correlation length λ.

with a first order Taylor expansion inside the interval $[z - \lambda, z + \lambda]$, and zero outside the interval. Approximating the sum with an integral, we arrive at:

$$\langle \mathcal{A}^2(r) \rangle_\alpha \simeq \left(\frac{k_{\mathrm{B}}}{\gamma}\right)^2 \frac{\sigma_\alpha^2}{\pi} \left(\frac{\lambda}{2r^3 + 2r\lambda^2}\right). \tag{25}$$

We identify two different regimes:

$$\langle \mathcal{A}^2(r) \rangle_\alpha \sim \begin{cases} \frac{k_{\mathrm{B}}^2 \sigma_\alpha^2}{2\gamma^2 \pi} \frac{\lambda}{r^3} & \text{if } r \gg \lambda \\ \frac{k_{\mathrm{B}}^2 \sigma_\alpha^2}{2\gamma^2 \pi} \frac{1}{\lambda r} & \text{if } r \ll \lambda \end{cases}$$

A comparison between our analytical prediction (Eq. (25)) and numerical results is shown in Fig. 5A, and the numerical results for correlated dipoles are shown in Fig. 5B.

We can notice how the case of correlated intensities exhibits a behavior that is quantitatively different from the previous case of dipoles and monopole mixtures. In contrast to the previous case, the scaling exponent of the short distance regime is weaker than the one of the long distances regime. The exponent for the long distances ($r \gg \lambda$) is the same as for the case of uncorrelated activities.

We summarized the scaling exponents obtained in $d = 1$ for the area enclosing rate and cycling frequencies in Tab. (I). The differences in the observed scaling exponents would allow one to discern the cases of spatially correlated activities and of mixture of dipoles and monopoles. Furthermore, a quantitative measure of the two scaling regimes, would allow one to estimate the correlation length λ or the intensities of the activities σ_α^2.

IV. CONCLUSIONS

In this work we asked how the scaling behavior of two-point non-equilibrium measures can be used to reveal properties of the internal driving in an active elastic assembly. To this end, we considered a lattice model of a driven elastic assembly. Using this model, we investigated how intrinsic features of the active noise influence the scaling behavior of non-equilibrium measures, such as cycling frequencies ω and area enclosing rates $\mathcal{A}$. These

measures are directly accessible from the stochastic trajectories of pairs of tracer particles in the network.

Using our theoretical framework, we considered several settings of the active noise. We started by focusing in Sec. (III A) on a one-dimensional system driven out of equilibrium by a mixture of stochastic monopole and dipole forces. We performed an analytical calculation to find an expression for the scaling law of $\sqrt{\langle \mathcal{A}^2 \rangle_\alpha}$ and $\sqrt{\langle \omega^2 \rangle_\alpha}$ as a function of the distance between the observed particles, which we confirmed by numerics. We predict two scaling regimes: a dipole-dominated regime at short distances and a monopole-dominated regime at long distances. The crossover length between these two regimes is set by the parameters characterizing the stochastic forces: the densities of dipoles ρ^{D} and monopoles ρ^{M}, and the variance of their intensities $\sigma^2_{\alpha^{\mathrm{M/D}}}$. We extended these results in Sec. (III B), where we performed analogous calculations for a two-dimensional network, and observed qualitatively the same behavior as for the one-dimensional system, but with different exponents. Importantly, we demonstrated numerically that our predictions, obtained for a square lattice, also apply to more complex networks such as triangular and diluted triangular networks, more commonly employed to describe soft biological materials [14, 21, 60, 61]. Since in real systems active noise amplitudes may be spatially correlated, in Sec. (III C) we considered an illustrative example of a system driven out of equilibrium by stochastic forces with intensities correlated exponentially in space. Interestingly, we find that these correlations are reflected as a weaker decay in the scaling behavior of our non-equilibrium measures on lengthscales below the correlation length (see Tab. (I)).

Altogether our results provide a new perspective to interpret experimentally accessible two-point non-equilibrium measures: A direct observation of the scaling behavior of such non-equilibrium measures may provide a way to infer qualitative information on the nature of the active forces in the system, and quantitative information on their densities, intensities, or their correlation length. A typical setting where our approach could be applied is time-lapse microscopy experiments in which several probe particles are tracked in active assemblies of soft materials [62, 63]. Promising examples would be *in vitro* or *in vivo* biological actomyosin networks, cellular membranes, DNA polymers, but also synthetic and biomimetic systems [2, 3, 7, 8, 64, 65]. Our approach could help connect mesoscale non-equilibrium dynamics to the microscopic properties of the internal driving in such systems.

ACKNOWLEDGEMENTS

We thank F. Gnesotto, S. Ceolin, B. Remlein, and G. Torregrosa Cortes for many stimulating discussions. This work was supported by the German Excellence Initiative via the program NanoSystems Initiative Munich (NIM), the Graduate School of Quantitative Biosciences Munich (QBM), and was funded by the Deutsche Forschungsgemeinshaft (DFG, German Research Foundation) - 418389167.

[1] É. Fodor and M. Cristina Marchetti, Phys. A Stat. Mech. its Appl. **504**, 106 (2018), arXiv:1708.08652.
[2] D. Needleman and Z. Dogic, Nat. Rev. Mater. **2**, 2 (2017).
[3] F. S. Gnesotto, F. Mura, J. Gladrow, and C. P. Broedersz, Reports Prog. Phys. **81**, 066601 (2018), arXiv:1710.03456.
[4] F. C. MacKintosh and C. F. Schmidt, Curr. Opin. Cell Biol. **22**, 29 (2010).
[5] C. P. Brangwynne, F. C. MacKintosh, and D. A. Weitz, Proceedings of the National Academy of Sciences **104**, 16128 (2007), https://www.pnas.org/content/104/41/16128.full.pdf.
[6] R. K. Grötsch, A. Angı, Y. G. Mideksa, C. Wanzke, M. Tena-Solsona, M. J. Feige, B. Rieger, and J. Boekhoven, Angew. Chemie - Int. Ed. **57**, 14608 (2018).
[7] J. Palacci, S. Sacanna, A. P. Steinberg, D. J. Pine, and P. M. Chaikin, Science. **339**, 936 (2013).
[8] O. J. N. Bertrand, D. K. Fygenson, and O. A. Saleh, Proc. Natl. Acad. Sci. U.S.A. **109**, 17342 (2012).
[9] E. Frey, J. Halatek, S. Kretschmer, and P. Schwille, in Phys. Biol. Membr., edited by P. Bassereau and P. C. A. Sens (Springer-Verlag GmbH, Heidelberg, 2017).
[10] J. Brugués and D. Needleman, Proc. Natl. Acad. Sci. U.S.A. **111**, 18496 (2014).
[11] S. Gadde and R. Heald, Curr. Biol. **14**, 797 (2004).
[12] S. C. Weber, A. J. Spakowitz, and J. A. Theriot, Proc. Natl. Acad. Sci. U.S.A. **109**, 7338 (2012).
[13] É. Fodor, V. Mehandia, J. Comelles, R. Thiagarajan, N. S. Gov, P. Visco, F. van Wijland, and D. Riveline, Biophys. J. **114**, 939 (2018), arXiv:1512.01476.
[14] H. Turlier, D. A. Fedosov, B. Audoly, T. Auth, N. S. Gov, C. Sylkes, J.-F. Joanny, G. Gompper, and T. Betz, Nat. Phys. **12**, 513 (2016).
[15] T. Betz, M. Lenz, J.-F. Joanny, and C. Sykes, Proc. Natl. Acad. Sci. U.S.A. **106**, 15320 (2009).
[16] E. Ben-Isaac, Y. Park, G. Popescu, F. L. Brown, N. S. Gov, and Y. Shokef, Phys. Rev. Lett. **106**, 1 (2011), arXiv:1102.4508.
[17] D. Mizuno, C. Tardin, C. F. Schmidt, and F. C. MacKintosh, Science. **315**, 370 (2007).
[18] C. P. Brangwynne, G. H. Koenderink, F. C. MacKintosh, and D. A. Weitz, J. Cell Biol. **183**, 583 (2008).
[19] M. Guo, A. J. Ehrlicher, M. H. Jensen, M. Renz, J. R. Moore, R. D. Goldman, J. Lippincott-Schwartz, F. C. Mackintosh, and D. A. Weitz, Cell **158**, 822 (2014).
[20] Fodor, M. Guo, N. S. Gov, P. Visco, D. A. Weitz, and F. Van Wijland, Epl **110**, 1 (2015).

[21] C. P. Broedersz and F. C. MacKintosh, Soft Matter **7**, 3186 (2011), arXiv:1009.3848v1.
[22] A. Agarwal and H. Hess, J. Nanotechnol. Eng. Med. **1**, 011005 (2009).
[23] G. H. Koenderink, Z. Dogic, F. Nakamura, P. M. Bendix, F. C. MacKintosh, J. H. Hartwig, T. P. Stossel, and D. A. Weitz, Proc. Natl. Acad. Sci. U.S.A. **106**, 15192 (2009).
[24] F. Jülicher, K. Kruse, J. Prost, and J. F. Joanny, Phys. Rep. **449**, 3 (2007).
[25] C. Battle, C. P. Broedersz, N. Fakhri, V. F. Geyer, J. Howard, C. F. Schmidt, and F. C. MacKintosh, Science. **352**, 604 (2016).
[26] J. Gladrow, N. Fakhri, F. C. MacKintosh, C. F. Schmidt, and C. P. Broedersz, Phys. Rev. Lett. **116**, 248301 (2016).
[27] J. Gladrow, C. P. Broedersz, and C. F. Schmidt, Phys. Rev. E **96**, 022408 (2017), arXiv:1704.06243.
[28] F. Mura, G. Gradziuk, and C. P. Broedersz, Phys. Rev. Lett. **121**, 38002 (2018), arXiv:1803.02797.
[29] G. Gradziuk, F. Mura, and C. P. Broedersz, Phys. Rev. E **99**, 052406 (2019).
[30] A. Frishman and P. Ronceray, Arxiv:1809.09650 (2018).
[31] J. Li, J. M. Horowitz, T. R. Gingrich, and N. Fakhri, Nat. Commun. **10** (2019), 10.1038/s41467-019-09631-x.
[32] D. S. Seara, V. Yadav, I. Linsmeier, A. P. Tabatabai, P. W. Oakes, S. M. A. Tabei, S. Banerjee, and M. P. Murrell, Nat. Commun. **9**, 4948 (2018), arXiv:1804.04232.
[33] A. I. Martínez, G. Bisker, M. J. Horowitz, and M. J. Parrondo, Arxiv:1809.02084 (2018).
[34] U. Seifert, Reports Prog. Phys. **75**, 126001 (2012).
[35] A. Ghanta, J. C. Neu, and S. Teitsworth, Phys. Rev. E **95**, 1 (2017).
[36] J. P. Gonzalez, J. C. Neu, and S. W. Teitsworth, Phys. Rev. E **99**, 022143 (2019).
[37] A. J. Levine and T. C. Lubensky, Phys. Rev. Lett. **85**, 1774 (2000), arXiv:0004103v1 [arXiv:cond-mat].
[38] A.-Y. Jee, Y.-K. Cho, S. Granick, and T. Tlusty, Proc. Natl. Acad. Sci. U.S.A. **115**, E10812 (2018).
[39] R. Golestanian, Phys. Rev. Lett. **115**, 1 (2015).
[40] C. Riedel, R. Gabizon, C. A. Wilson, K. Hamadani, K. Tsekouras, S. Marqusee, S. Pressé, and C. Bustamante, Nature **517**, 227 (2015), arXiv:NIHMS150003.
[41] T. Sugawara and K. Kaneko, Biophysics (Oxf). **7**, 77 (2011).
[42] P. Chen and V. B. Shenoy, Soft Matter **7**, 355 (2011).
[43] K. W. Möller, A. M. Birzle, and W. A. Wall, Proc. R. Soc. A Math. Phys. Eng. Sci. **472**, 2 (2016).
[44] J. F. Joanny and J. Prost, HFSP J. **3**, 94 (2009).
[45] H. Sutherland and W. A. Bickmore, Nat. Rev. Genet. **10**, 457 (2009).
[46] O. Hachet, M. Berthelot-Grosjean, K. Kokkoris, V. Vincenzetti, J. Moosbrugger, and S. G. Martin, Cell **145**, 1116 (2011).
[47] D. L. Schmitt and S. An, Biochemistry **56**, 3184 (2017).
[48] J. Harder, C. Valeriani, and A. Cacciuto, Phys. Rev. E **90**, 1 (2014).
[49] S. A. Mallory, C. Valeriani, and A. Cacciuto, Phys. Rev. E **92**, 1 (2015).
[50] A. Kaiser, S. Babel, B. Ten Hagen, C. Von Ferber, and H. Löwen, J. Chem. Phys. **142**, 1 (2015), arXiv:1501.07832v2.
[51] M. Lenz, Phys. Rev. X **4**, 041002 (2014).
[52] F. C. MacKintosh and A. J. Levine, Phys. Rev. Lett. **100**, 18104 (2008), arXiv:0704.3794.
[53] P. Ronceray, C. P. Broedersz, and M. Lenz, Proceedings of the National Academy of Sciences **113**, 2827 (2016), https://www.pnas.org/content/113/11/2827.full.pdf.
[54] U. S. Schwarz and S. A. Safran, Rev. Mod. Phys. **85**, 1327 (2013).
[55] D. Goldstein, S. Ramaswamy, and B. Chakraborty, Soft Matter **15**, 3520 (2019), arXiv:1901.08119.
[56] A. S. Mikhailov and R. Kapral, Proceedings of the National Academy of Sciences **112**, E3639 (2015), https://www.pnas.org/content/112/28/E3639.full.pdf.
[57] X. Zhao, K. K. Dey, S. Jeganathan, P. J. Butler, U. M. Córdova-Figueroa, and A. Sen, Nano Letters **17**, 4807 (2017), pMID: 28726415, https://doi.org/10.1021/acs.nanolett.7b01618.
[58] M. Dennison, R. Kapral, and H. Stark, Soft matter **13**, 3741 (2017).
[59] H. Risken, The Fokker-Planck equation, edited by S. (2nd ed.) (Berlin, 1996) pp. 153–154.
[60] F. S. Gnesotto, B. M. Remlein, and C. P. Broedersz, Phys. Rev. E **100**, 013002 (2019).
[61] M. Vahabi, A. Sharma, A. J. Licup, A. S. Van Oosten, P. A. Galie, P. A. Janmey, and F. C. Mackintosh, Soft Matter **12**, 5050 (2016).
[62] M. Balland, N. Desprat, D. Icard, S. Féréol, A. Asnacios, J. Browaeys, S. Hénon, and F. Gallet, Phys. Rev. E **74**, 21911 (2006).
[63] A. W. C. Lau, B. D. Hoffman, A. Davies, J. C. Crocker, and T. C. Lubensky, Phys. Rev. Lett. **91**, 198101 (2003).
[64] J. B. Manneville, P. Bassereau, S. Ramaswamy, and J. Prost, Phys. Rev. E **64**, 10 (2001).
[65] J.-B. Manneville, P. Bassereau, D. Lévy, and J. Prost, Phys. Rev. Lett. **82**, 4356 (1999).

SUPPLEMENTARY NOTES

Derivation of $\langle \mathcal{A}^2(r) \rangle_\alpha$ in $d = 1$ and $d = 2$

In this section we derive an expression for the average area enclosing rate $\langle \mathcal{A}^2 \rangle$ as function of the distance r between two observed probes. For a one-dimensional system the area enclosing rate can be expressed in terms of the elements of the covariance matrix as:

$$\mathcal{A}_{ij} = \frac{k_B}{\gamma} \sum_z \left(\xi_z^{\mathrm{M}} \widetilde{\partial}_2^2 c_z^{\mathrm{M}} + \xi_z^{D} \widetilde{\partial}_2^2 c_z^{\mathrm{D}} \right), \tag{S1}$$

where i and j are the bead indices such, that $d_{ij} = 0$, $\widetilde{\partial}_2^2 c = c_{i,j+1} - 2c_{i,j} + c_{i,j-1}$ indicates the discrete second derivative across rows, and $\xi^{\mathrm{M/D}} = b^{\mathrm{M/D}}\alpha^{\mathrm{M/D}}$. To find how $\langle \mathcal{A}^2(r)\rangle_\alpha$ depends on the distance r between the observed probes, we use the explicit expressions for $\partial^2 c_z^{\mathrm{M}}(r)$ and $\partial^2 c_z^{\mathrm{D}}(r)$, evaluated for $i = -r/2$ and $j = r/2$, appearing in Eq. (12) and Eq. (13) in the main text.

For notational simplicity we rename: $\partial^2 c_z^{\mathrm{M}}(r) = f^{\mathrm{M}}(z,r)$ and $\partial^2 c_z^{\mathrm{D}}(r) = f^{\mathrm{D}}(z,r)$. The functions $f^{\mathrm{M}}(z,r)$ and $f^{\mathrm{D}}(z,r)$ are informative of the contribution of a monopole or dipole activity, at position z, to $\mathcal{A}^2(r)$ measured between two tracers at $i = r/2$ and $j = -r/2$. Such contributions come primarily from activities in between the two beads, as shown in Fig. S1.

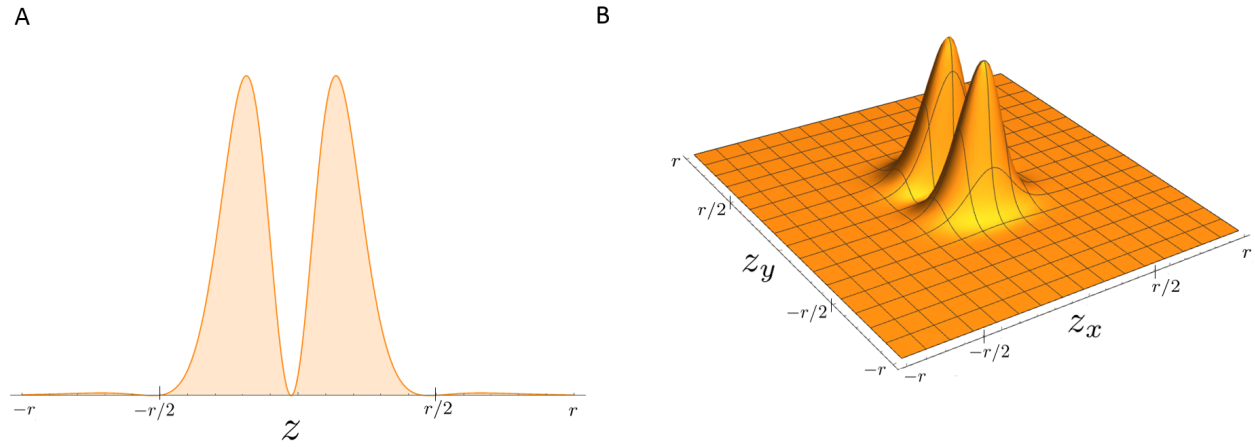

FIG. S1. A) Plot of $f^{\mathrm{D}^2}(z)$ in $d = 1$. The value of this function represents the contribution of a dipole, at position z, to the area enclosing rate measured between two tracers beads at $i = r/2$ and $j = -r/2$ B) Plot of $f^{\mathrm{D}^2}(z_x, z_y)$ in $d = 2$. The value of this function represents the contribution of a dipole activity, acting between the beads at $\{z_x, z_y\}$ and $\{z_x, z_y + 1\}$, to the area enclosing rate measured from the y-displacements of two beads at $\{0, r/2\}$ and $\{0, -r/2\}$.

By taking the square of Eq. (S1) and the ensemble average over the activities we obtain:

$$\begin{aligned}\langle \mathcal{A}^2(r)\rangle_\alpha &= \frac{k_B^2}{\gamma^2}\left\langle\left[\sum_z \xi_z^{\mathrm{M}} f^{\mathrm{M}}(z,r) + \xi_z^{\mathrm{D}} f^{\mathrm{D}}(z,r)\right]^2\right\rangle \\ &= \frac{k_B^2}{\gamma^2}\sum_z\left[\langle \xi_z^{\mathrm{M}^2}\rangle f^{\mathrm{M}^2}(z,r) + \langle \xi_z^{\mathrm{D}^2}\rangle f^{\mathrm{D}^2}(z,r)\right] + \frac{k_B^2}{\gamma^2}\langle \xi^{\mathrm{M}}\rangle^2 \sum_{z,z'\neq z} f^{\mathrm{M}}(z,r) f^{\mathrm{M}}(z',r) \\ &+ \frac{k_B^2}{\gamma^2}\langle \xi^{\mathrm{D}}\rangle^2 \sum_{z,z'\neq z} f^{\mathrm{D}}(z,r) f^{\mathrm{D}}(z',r) + \frac{k_B^2}{\gamma^2} 2\langle \xi^{\mathrm{M}}\rangle\langle \xi^{\mathrm{D}}\rangle \sum_z f^{\mathrm{M}}(z,r)\sum_{z'} f^{\mathrm{D}}(z',r).\end{aligned} \tag{S2}$$

where we assumed that the noise amplitudes ξ_z^{M} and $\xi_{z'}^{\mathrm{D}}$ are spatially uncorrelated and that their average does not depend on z. By rewriting $\sum_{z,z'\neq z} = \sum_{z,z'} - \sum_{z,z'=z}$ we obtain:

$$\begin{aligned}\langle \mathcal{A}^2(r)\rangle_\alpha &= \frac{k_B^2}{\gamma^2}\sum_z\left[\langle \xi_z^{\mathrm{M}^2}\rangle f^{\mathrm{M}^2}(z,r) + \langle \xi_z^{\mathrm{D}^2}\rangle f^{\mathrm{D}^2}(z,r)\right] + \frac{k_B^2}{\gamma^2}\langle \xi^{\mathrm{M}}\rangle^2\left[\sum_{z,z'} f^{\mathrm{M}}(z,r) f^{\mathrm{M}}(z',r) - \sum_z f^{\mathrm{M}^2}(z,r)\right] \\ &+ \frac{k_B^2}{\gamma^2}\langle \xi^{\mathrm{D}}\rangle^2\left[\sum_{z,z'} f^{\mathrm{D}}(z,r) f^{\mathrm{D}}(z',r) - \sum_z f^{\mathrm{D}^2}(z,r)\right] + \frac{k_B^2}{\gamma^2} 2\langle \xi^{\mathrm{M}}\rangle\langle \xi^{\mathrm{D}}\rangle \sum_z f^{\mathrm{M}}(z,r)\sum_{z'} f^{\mathrm{D}}(z',r).\end{aligned} \tag{S3}$$

and approximating the sum by an integral yields

$$\begin{aligned}\langle \mathcal{A}^2(r)\rangle_\alpha &= \frac{k_B^2}{\gamma^2}\int dz\left[\langle \xi_z^{\mathrm{M}^2}\rangle f^{\mathrm{M}^2}(z,r) + \langle \xi_z^{\mathrm{D}^2}\rangle f^{\mathrm{D}^2}(z,r)\right] + \frac{k_B^2}{\gamma^2}\langle \xi^{\mathrm{M}}\rangle^2\left[\int dz dz' f^{\mathrm{M}}(z,r) f^{\mathrm{M}}(z',r) - \int dz f^{\mathrm{M}^2}(z,r)\right] \\ &+ \frac{k_B^2}{\gamma^2}\langle \xi^{\mathrm{D}}\rangle^2\left[\int dz dz' f^{\mathrm{D}}(z,r) f^{\mathrm{D}}(z',r) - \int dz f^{\mathrm{D}}(z,r)^2\right] + \frac{k_B^2}{\gamma^2} 2\langle \xi^{\mathrm{M}}\rangle\langle \xi^{\mathrm{D}}\rangle \int dz f^{\mathrm{M}}(z,r)\int dz' f^{\mathrm{D}}(z',r).\end{aligned} \tag{S4}$$

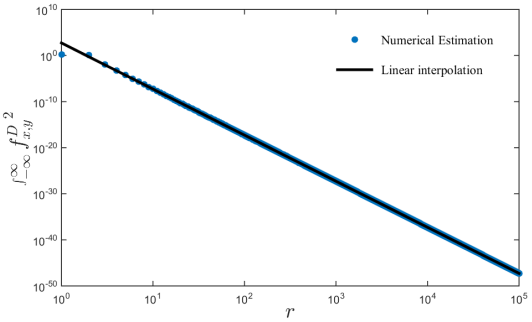

FIG. S2. Numerical estimation of the second integral in Eq. (S7) as function of the distance (blue), and result of the linear interpolation $f(x) = 6,27 - 9.99\ln(r)$ (black).

Considering that $\int f^{\mathrm{M/D}}(z,r)dz = 0$:

$$\langle \mathcal{A}^2(r)\rangle_\alpha = \left(\frac{k_B}{\gamma}\right)^2 \left(\sigma^2_{\xi^{\mathrm{M}}} \int dz f^{\mathrm{M}\,2}(z,r) + \sigma^2_{\xi^{\mathrm{D}}} \int dz f^{\mathrm{D}\,2}(z,r)\right). \tag{S5}$$

Since $\sigma^2_{\xi^{\mathrm{M/D}}}$ is the variance of a stochastic variable $\xi^{\mathrm{M/D}} = b^{\mathrm{M/D}}\alpha^{\mathrm{M/D}}$, where $b \in \{0,1\}$ with $\langle b\rangle = \rho^{\mathrm{M/D}}$ and $\langle b^2\rangle = \rho^{\mathrm{M/D}}$, we have $\sigma^2_{\xi^{\mathrm{M/D}}} = \rho^{\mathrm{M/D}}\sigma^2_{\alpha^{\mathrm{M/D}}}$. By solving the integral, and keeping only the leading terms in the limit $r \gg 1$, we obtain

$$\langle \mathcal{A}^2(r)\rangle_\alpha = \frac{1}{\pi}\left(\frac{k_B}{\gamma}\right)^2 \left(\rho^{\mathrm{M}}\sigma^2_{\alpha^{\mathrm{M}}}\frac{1}{2r^3} + \rho^{D}\sigma^2_{\alpha^{D}}\frac{45}{r^7}\right). \tag{S6}$$

Similar calculations can be performed in d=2, and lead to the integral form of the area enclosing rate:

$$\langle \mathcal{A}^2(r)\rangle_\alpha = \frac{k_B^2}{\gamma^2}\left[\rho^{\mathrm{M}}\sigma^2_{\alpha^{\mathrm{M}}}\int_{-\infty}^{\infty} dz_x dz_y f^{\mathrm{M}\,2}(z_x,z_y,r) + \rho^{\mathrm{D}}\sigma^2_{\alpha^{D}}\int_{-\infty}^{\infty} dz_x dz_y f^{D\,2}(z_x,z_y,r)\right]. \tag{S7}$$

where $f^{\mathrm{M}}(z_x,z_y,r)$ and $f^{\mathrm{D}}(z_x,z_y,r)$ are defined in Eq. (20) and Eq. (21) in the main text. The second integral in Eq. (S7) is arduous to calculate analytically. Therefore, we estimate the integral numerically for different values of the distance r. The result is reported in Fig. S2, together with the result of a linear interpolation of such numerical data $\int_{-\infty}^{\infty} dz_x dz_y f^{\mathrm{D}\,2}(z_x,z_y,r) \simeq \frac{4}{\pi^4} a r^{-b}$ with $a \simeq 529$ and $b \simeq 10$. Finally, for $d = 2$ we obtain :

$$\langle \mathcal{A}^2(r)\rangle_\alpha \simeq \left(\frac{2k_{\mathrm{B}}}{\pi^2\gamma}\right)^2 \left[\rho^{\mathrm{M}}\sigma^2_{\alpha^{\mathrm{M}}}\frac{2\pi}{5r^6} + \rho^{\mathrm{D}}\sigma^2_{\alpha^{\mathrm{D}}}\frac{529}{r^{10}}\right]. \tag{S8}$$

Small displacement approximation in $d = 2$

In a two-dimensional network, we assume that the dipole forces act along the directions of the springs at each point in time. Here we show that in the limit of small displacements we can consider the action of the dipole forces to be directed along the principal axes of the network at rest, as done in the main text. For simplicity, let's consider a square lattice of size $N = n \times n$, with zero-rest length springs. We index the coordinates as $\mathbf{x} = \{x_1,\ldots,x_N,y_1,\ldots,y_N\}$, and we assume the presence of only two dipole activities: one of intensity $\eta_{i,i+n}$ acting vertically between the beads of index i and $i+n$, and the other one of intensity $\eta_{i,i+1}$ acting horizontally between the beads of index i and $i+1$. The Langevin equations for the y-displacements of the i_{th} bead reads:

$$\frac{dy_i}{dt} = \frac{k}{\gamma}a_{i,l}y_l + \eta_i^T + \eta^{\mathrm{D}}_{i,i+n}\cos\left(\frac{\Delta x_{i,i+n}}{\ell}\right) + \eta^{\mathrm{D}}_{i,i+1}\sin\left(\frac{\Delta y_{i,i+1}}{\ell}\right) \tag{S9}$$

where we defined $\Delta x_{i,i+n} = x_i - x_{i+n}$, $\Delta y_{i,i+1} = y_i - y_{i+1}$ and ℓ is the lattice spacing. In the limit $\frac{\Delta x_{i,i+n}}{\ell} \ll 1$ and $\frac{\Delta y_{i,i+1}}{\ell} \ll 1$, the last term is negligible and the second last is $\simeq \eta^{\mathrm{D}}_{i,i+n}$. Therefore in the limit of small displacements we can consider the action of the dipole forces to be directed along the principal axes of the network.

To check the validity of this approximation for the non-equilibrium measure, we explicitly simulated the dynamics of the network. We employed the Euler-Maruyama method to numerically integrate the Langevin equation of a square lattice where both vertical and horizontal dipoles are distributed randomly along the network and act along the spring direction. When the standard deviation of displacements is small compared to the rest length of the springs ($\sigma_x/\ell < 1$), our theoretical prediction is in good agreement with the simulation, as shown in Fig. S3. However, also in the case of $\sigma_x/\ell > 1$, the simulation results are slightly shifted respect to our prediction, but the scaling exponent remains the same.

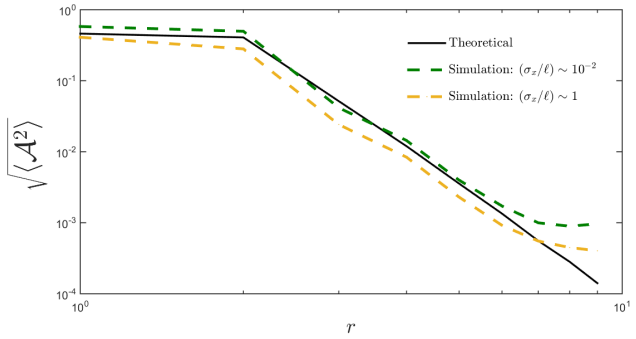

FIG. S3. Theoretical prediction (black) of the average area enclosing rate (obtained from Eq. 7 in the main text by numerically solving the Lyapunov equation), compared with simulation results for different values of the ratio σ_x/ℓ (green and yellow). For computational convenience the ensemble average over the activity distributions has been evaluated by performing a spatial average over the lattice.

Outlook

After having discussed our theoretical framework in detail, we want now touch upon some recent experimental findings that can be related to our results, and briefly outline some possible future directions of this research.
The work presented in this thesis is inspired in part by an experimental technique: Two-point microrheology [17]. This technique is commonly used to investigate the mechanical properties of biological systems, by embedding two tracer microparticles in an environment, for instance, a cellular cytoskeleton (Fig. O.1A). The coupling between the probe and the medium in which the particles are immersed generates long range interparticle coupling. Two-point microrheology takes advantage of such coupling to extract information on the mechanical properties of the material in between the particles. In a typical experiment, the bead positions are recorded and used to calculate the displacement correlation function [17]:

$$D_{\alpha,\beta}(r,\tau) = \langle \Delta r^i_\alpha(t,\tau) \Delta r^j_\beta(t,\tau) \delta[r - R_{ij}] \rangle, \tag{O.1}$$

where the displacement of a single particle is $\Delta r^i_\alpha(t,\tau) = r_\alpha(t+\tau) - r_\alpha(t)$, with t the absolute time and τ the lag time, and R_{ij} is the distance between the particles. At equilibrium and large distances r, the two point correlation function in Eq. O.1 is related to the shear modulus through [17]

$$\tilde{D}_\parallel(r,s) = \frac{k_B T}{2\pi r s \tilde{G}(s)}, \tag{O.2}$$

where $\tilde{D}_\parallel(r,s)$ is the Laplace transform of $D_\parallel(r,t)$, and $\parallel$ indicates the longitudinal component along the line connecting the two particles. We indicated with $\tilde{G}(s)$ the Laplace transform of the shear modulus, which describes the viscoelastic properties of the material.

The two-point correlation $D_\parallel(r,t)$ can be related to the scaling of the covariance matrix that we studied in the previous chapters and that shapes the scaling of our non-equilibrium measures (ω and $\mathcal{A}$). In fact, under steady-state conditions, and in the limit $\tau \to \infty$ we have $D_\parallel(r,t) \sim \langle r_{\parallel i}(t) r_{\parallel j}(t) \rangle = C(r)$, where $C(r)$ is the covariance between the longitudinal components of couples of particles i and j at distance r. As we can see from Eq. O.2, $D_\parallel(r,t) \sim 1/r$, and therefore also $C(r) \sim 1/r$. The scaling behavior of $D_\parallel(r,t)$ has been tested experimentally both in passive actin networks and in reconstituted active actomyosin networks (Fig. O.1C-D) [76, 77] . In both cases, a scaling regime $\sim 1/r$ has been observed for large interparticle distances. These findings are in agreement with our predictions of a scaling $\bar{C}(r) \sim 1/r$ for an equilibrium system [40].

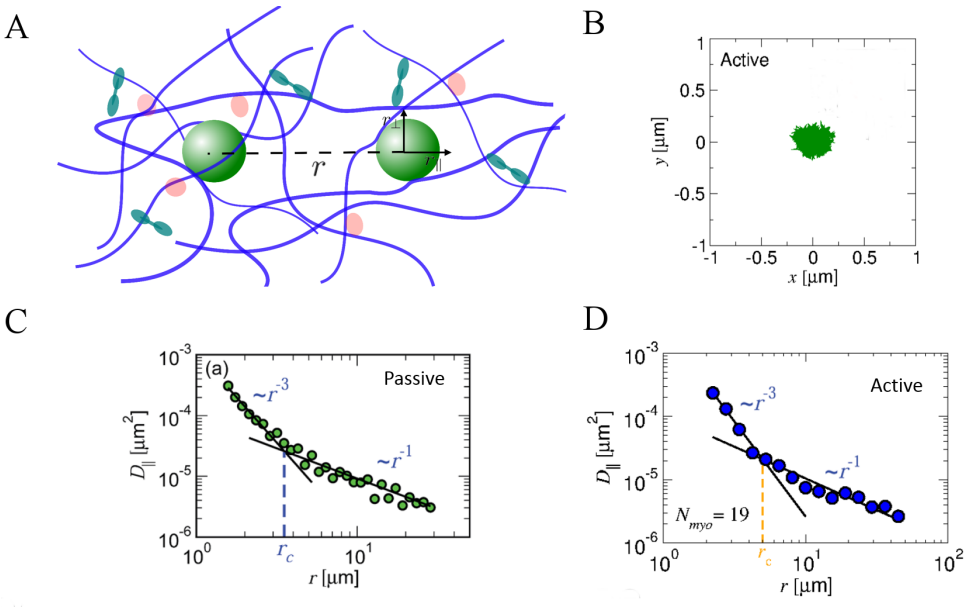

Figure O.1: A) Sketch of a two point microrheology experiment, with two probes at distance r embedded in an actomyosin network. B) Trajectory of a particle in an active actomyosin network. C) Scaling behavior of the displacements correlation function in Eq. O.1, measured in an *in vitro* actin network. At large distances, where the particle motion is governed by the network, a scaling behavior $\sim 1/r$ is observed. D) Scaling behavior of the displacements correlation function in Eq. O.1, measured in an *in vitro* actomyosin network. The scaling behavior is the same as the one observed in the passive case. B) and D) are adapted from [77]. C) is adapted from [76].

Since the scaling behaviors in the active and passive networks are the same, the measurement of the correlation function does not allow to easily quantify the contributions of equilibrium and non-equilibrium processes to the system's dynamics. The theoretical work presented in this thesis suggests that calculating the cycling frequencies and area enclosing rates would be a way to extract information on the non-equilibrium nature of the system.

Even though our model is a very simplified description of real soft materials, we can still use it to estimate the order of magnitude of our non-equilibrium measures in an experiment. To this end, we use some experimental results reported in the literature for actomyosin networks. To calculate the viscous friction acting on a node of the network, to a first approximation we can neglect the cylindrical shape of the actin filaments, and consider only the drag on an effective sphere of the same volume of the filament bond. In particular, we assume the viscosity $\eta \sim 10^{-3}$ Pa $\cdot$ s and the viscous friction of the network $\gamma = 6\pi\eta R_{eff}$, where $R_{eff} \sim 10^{-8}$ m corresponds to the radius of a sphere of volume $V = (d/2)^2 \cdot \ell\pi$. Here $\ell \simeq 10^{-7}$ m and $d \simeq 7 \cdot 10^{-9}$ m are respectively the mesh size of the actin network and the diameter of the actin filament [44, 56, 77, 83]. Based on the results reported in [77], we roughly estimate $\sqrt{\det \mathbf{C}} \simeq 0.04$ μm^2 (Fig. O.1B), and we assume σ_α to be comparable to room temperature, $\sigma_\alpha \simeq 300K$. We consider a

	1 μm	5 μm	10 μm	Units
$\sqrt{\langle \mathcal{A}^2 \rangle}$ $(d=2)$	0.03	$2.4 \cdot 10^{-4}$	$3 \cdot 10^{-5}$	$\mu m^2/s$
$\sqrt{\langle \mathcal{A}^2 \rangle}$ $(d=3)$	0.01	10^{-6}	$3 \cdot 10^{-7}$	$\mu m^2/s$
$\sqrt{\langle \omega^2 \rangle}$ $(d=2)$	0.7	$6 \cdot 10^{-3}$	$7 \cdot 10^{-4}$	Hz
$\sqrt{\langle \omega^2 \rangle}$ $(d=3)$	0.2	$2 \cdot 10^{-4}$	$6 \cdot 10^{-6}$	Hz

Table O.1: Estimation of the order of magnitude of the area enclosing rate and cycling frequencies for different distances between the observed particles, in $d = 2$ and $d = 3$. The results in this table are obtained from Eq. 2.22 and Eq. 2.23.

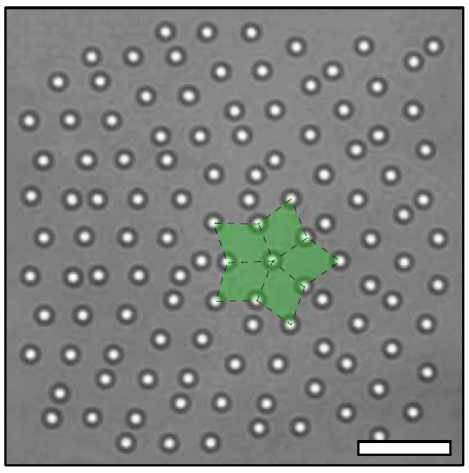

Figure O.2: Example of a bright-field image of colloidal silica spheres dispersed in water and organized in an optical trap array (green). The scale bar indicates 10 μm. Adapted from [66]

range of intracellular distances [77], $r \in [1 - 10]\mu$m. Under these assumptions, and using Eq. 2.22 and Eq. 2.23 we obtain the results presented in Tab. O.1. Overall, the results obtained in two-point microrheology experiments, together with our rough estimation of the non-equilibrium measures are encouraging regarding the possibility of experimentally testing the predictions of our analytical framework in real biological systems. The first goal of an experimental study would be to investigate what are the minimal features of the system that govern the scaling behavior of our non-equilibrium measures. However, even experiments in *in vitro* reconstituted systems may be challenging for an initial investigation. Ideally, for a first proof of principle, we would need to maintain full control over the system's parameters, and this may be difficult in such systems. A more artificial but more controllable approach may be to create an array of silica beads, trapped in a potential landscape obtained with holographic tweezers [66] (Fig. O.2). The non-equilibrium fluctuations of different beads can be tuned by controlling the positioning of the optical trap and randomly shaking the potential landscape. Such a setting would be ideal not only to control the spatial structure of the 'activity' in the system, but also to monitor

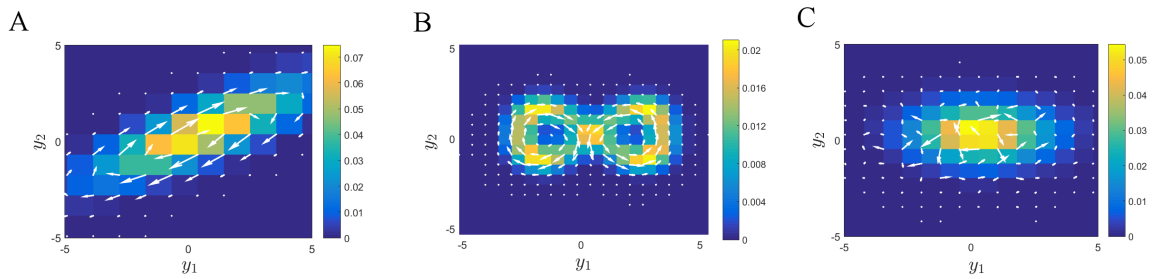

Figure O.3: A) Typical elliptical probability current obtained in our linear framework. B) Example of a probability current field obtained from a trajectory that exhibits an average ∞-shape circulation. C) Vanishing probability current field obtained for an equilibrium system.

the distance between the particles easily, and to record more statistics for large distances at which the measurement of cycling frequencies may be challenging.

From a theoretical standpoint, it would be interesting to try to go beyond the approximation of linear systems with stochastic driving made in our work. In the linear systems considered here, the probability currents exhibit an elliptical circulation in the phase space, with a cycling frequency at steady state that is different from zero (Fig. O.3A). In general, the velocity field may exhibit more complex structures, sometimes with a vanishing cycling frequency, even if the system is out of equilibrium. As an example, we can consider a trajectory that performs an average $\infty-$like shape circulation (Fig. O.3B). In this case, we would measure a vanishing cycling frequency, which would not allow us to distinguish this motion from that of an equilibrium system (Fig. O.3C). This observation suggests the need to look for non-equilibrium dynamics not only through the lens of the cycling frequencies and area enclosing rates, but looking at the entire shape of the probability current field. Promising attempts in this direction have been reported in the recent literature [28, 52]. These new approaches, based on modes expansion of the force field, allow us to infer the currents field in non-linear systems without performing any phase-space discretization. In analogy to the work presented in this thesis, it would be interesting to investigate whether also in these new frameworks some features of the active driving could be inferred from the full analysis of the current field. These general approaches could be applied to specific non-linear models of soft materials, and used to investigate the connections between the probability currents and the non-equilibrium driving. One more question to ask is whether it would still be possible to find some global property of the current fields that would serve as non-equilibrium measures for studying such complex non-linear systems.

Altogether, these potential future directions provide promising perspectives for an ever more extensive application of theoretical tools of non-equilibrium physics to the study of living systems.

Conclusions

This thesis aimed at investigating non-equilibrium detection and characterization in biological systems. We proposed a method to detect non-equilibrium dynamics in biological assemblies, based on the measurement of the cycling frequency and area enclosing rate of a stochastic trajectory in the coordinate space of two degrees of freedom.

In Chapter 1 we discussed the state-of-the-art approaches to detect non-equilibrium activity, also in systems where the presence of non-equilibrium dynamics is not always evident at first glance. In particular, in this chapter we reviewed a non-invasive method to detect non-equilibrium dynamics, based on the detection of broken detailed balance from mesoscale stochastic trajectories of pairs of degrees of freedom. This method was introduced for the first time in [5] and tested to detect the non-equilibrium fluctuations of primary cilia of canine kidney cells. However, the potential of such approach needed further investigation, leading us to develop the work presented in the following chapters of this thesis.

In Chapter 2, we proposed two measures to quantify broken detailed balance in systems out of equilibrium: the cycling frequency and the area enclosing rate of the stochastic trajectories. While the broken detailed balance detection introduced in [5] was based on the phase space discretization to measure the phase space currents, the two non-equilibrium measures proposed here do not require any phase space discretization and are therefore more easily accessible. We used a simple yet general model of driven elastic networks to build an analytical framework and investigate the properties of these non-equilibrium measures. In particular, we considered the cycling frequencies ω_{ij} and area enclosing rates $\mathcal{A}_{ij}$ of the trajectories of couples of beads, i and j, at distance r. To gain insights into how non-equilibrium manifests at different length scales, we investigated how these measures scale with the distance between the observed particles. We discovered that these non-equilibrium measures display an average power-law behavior as function of the distance, with an exponent that depends on the dimensionality of the system. Additionally, we found that the prefactor of this scaling law depends on the variance of the activity in the system. Thus, these experimentally accessible non-equilibrium measures and their associated scaling behaviors are promising candidates for a non-equilibrium measure that may give access to properties of the internal driving. This fact led us to develop the work presented in the third chapter of this thesis.

In Chapter 3, we investigated how the scaling behavior of the cycling frequencies and area enclosing rates can reveal the properties of the active driving in the system. To this end, we considered in our model of driven elastic networks several scenarios that may be relevant in biological systems, such as the presence of dipole active forces and spatial cor-

relation of the activities. Within this model we showed analytically and numerically that the scaling behavior of the cycling frequencies and area enclosing rates depends on the parameters that characterize the active noise, i.e intensity and density of the monopole- and dipole-like activities, and correlation length of the activities distribution. The results presented in this chapter confirm that an experimental observation of a particular scaling behavior of non-equilibrium measures may provide a way to infer qualitative and quantitative information on the non-equilibrium activity in the system.

In a broader context this work represents a small step toward the development of a theory for the description of biological assemblies. Several theories share this goal, each of them focusing on different aspects. For instance, hydrodynamics theories are promising in describing collective phenomena and traveling waves inside cells [55], while theories based on lattice models have been successful to capture the viscoelastic properties of such active assemblies [11]. Other 'two-fluid models' try to combine the hydrodynamics and viscoelastic interactions to describe the motion of elastic flexible polymers in solvents or colloidal particles in viscoelastic environments [18, 83]. An interesting challenge would be to extend the definition of the non-equilibrium measures defined in our simple model to other more complex theories and investigate their potential in providing information on different aspects of non-equilibrium activity in biological systems.

Bibliography

[1] A. Agarwal and H. Hess. Molecular Motors as Components of Future Medical Devices and Engineered Materials. J. Nanotechnol. Eng. Med., 1(1):011005, 2009.

[2] A. Ajdari, J. Prost, and F. Ju. RMP Colloquia Modeling molecular motors. October, 69(4):1269–1281, 1997.

[3] B. Alberts, A. Johnson, J. Lewis, M. Raff, R. Keith, and P. Walter. Molecular Biology of the Cell. New York, 4 edition, 2002.

[4] A. Basu, J. F. Joanny, F. Jülicher, and J. Prost. Thermal and non-thermal fluctuations in active polar gels. Eur. Phys. J. E, 27(2):149–160, 2008.

[5] C. Battle, C. P. Broedersz, N. Fakhri, V. F. Geyer, J. Howard, C. F. Schmidt, and F. C. MacKintosh. Broken detailed balance at mesoscopic scales in active biological systems. Science., 352(6285):604–607, 2016.

[6] E. Ben-Isaac, Y. Park, G. Popescu, F. L. Brown, N. S. Gov, and Y. Shokef. Effective temperature of red-blood-cell membrane fluctuations. Phys. Rev. Lett., 106(23):1–4, 2011.

[7] T. Betz, M. Lenz, J.-F. Joanny, and C. Sykes. ATP-dependent mechanics of red blood cells. Proc. Natl. Acad. Sci. U.S.A., 106(36):15320–15325, sep 2009.

[8] G. Bisker, M. Polettini, T. R. Gingrich, and J. M. Horowitz. Hierarchical bounds on entropy production inferred from partial information. J. Stat. Mech. Theory Exp., 2017(9):–, 2017.

[9] C. P. Brangwynne, G. H. Koenderink, F. C. MacKintosh, and D. A. Weitz. Nonequilibrium microtubule fluctuations in a model cytoskeleton. Phys. Rev. Lett., 100(11):118104, mar 2008.

[10] C. P. Broedersz and F. C. MacKintosh. Molecular motors stiffen non-affine semiflexible polymer networks. Soft Matter, 7(7):3186–3191, 2011.

[11] C. P. Broedersz and F. C. Mackintosh. Modeling semiflexible polymer networks. Rev. Mod. Phys., 86(3):995–1036, 2014.

[12] C. P. Broedersz, X. Mao, T. C. Lubensky, and F. C. Mackintosh. Criticality and isostaticity in fibre networks. Nat. Phys., 7(12):983–988, 2011.

[13] D. B. Brückner, A. Fink, C. Schreiber, P. J. Röttgermann, J. O. Rädler, and C. P. Broedersz. Stochastic nonlinear dynamics of confined cell migration in two-state systems. Nat. Phys., pages –, 2019.

[14] H. B. Callen and T. A. Welton. Irreversibility and Generalized Noise. Phys. Rev., 83(1):34–40, jul 1951.

[15] O. Chepizhko, C. Giampietro, E. Mastrapasqua, M. Nourazar, M. Ascagni, M. Sugni, U. Fascio, L. Leggio, C. Malinverno, G. Scita, S. Santucci, M. J. Alava, S. Zapperi, and C. A. M. La Porta. Bursts of activity in collective cell migration. Proc. Natl. Acad. Sci. U.S.A., 113(41):11408–11413, 2016.

[16] A. Crisanti, A. Puglisi, and D. Villamaina. Nonequilibrium and information: The role of cross correlations. Phys. Rev. E - Stat. Nonlinear, Soft Matter Phys., 85(6):–, 2012.

[17] J. C. Crocker, M. T. Valentine, E. R. Weeks, T. Gisler, P. D. Kaplan, A. G. Yodh, and D. A. Weitz. Two-Point Microrheology of Inhomogeneous Soft Materials. Phys. Rev. Lett., 85(4):888–891, jul 2000.

[18] P. G. De Gennes. Dynamics of Entangled Polymer Solutions. II. Inclusion of Hydrodynamic Interactions. Macromolecules, 9(4):594–598, 1976.

[19] K. K. Dey, X. Zhao, B. M. Tansi, W. J. Méndez-Ortiz, U. M. Córdova-Figueroa, R. Golestanian, and A. Sen. Micromotors Powered by Enzyme Catalysis. Nano Lett., 15(12):8311–8315, 2015.

[20] A. Doostmohammadi, J. Ignés-Mullol, J. M. Yeomans, and F. Sagués. Active nematics. Nat. Commun., 9(1):–, 2018.

[21] M. Esposito. Stochastic thermodynamics under coarse graining. Phys. Rev. E, 85:41125, 2012.

[22] N. Fakhri, A. D. Wessel, C. Willms, M. Pasquali, D. R. Klopfenstein, F. C. MacKintosh, and C. F. Schmidt. High-resolution mapping of intracellular fluctuations using carbon nanotubes. Science., 344(6187):1031–1035, 2014.

[23] G. Falasco, M. Baiesi, L. Molinaro, L. Conti, and F. Baldovin. Energy repartition for a harmonic chain with local reservoirs. Phys. Rev. E - Stat. Nonlinear, Soft Matter Phys., 92(2):1–7, 2015.

[24] D. a. Fletcher and R. D. Mullins. Cell mechanisms and cytoskeleton. Nature, 463(7280):485–492, 2010.

[25] É. Fodor, M. Guo, N. S. Gov, P. Visco, D. A. Weitz, and F. van Wijland. Activity-driven fluctuations in living cells. EPL (Europhysics Lett., 110(4):48005, 2015.

[26] É. Fodor and M. Cristina Marchetti. The statistical physics of active matter: From self-catalytic colloids to living cells. Phys. A Stat. Mech. its Appl., 504(ii):106–120, 2018.

[27] E. Frey, J. Halatek, S. Kretschmer, , and P. Schwille. Protein Pattern Formation. In P. Bassereau and P. C. A. Sens, editors, Phys. Biol. Membr. Springer-Verlag GmbH, Heidelberg, 2017.

[28] A. Frishman and P. Ronceray. Learning force fields from stochastic trajectories. 2018.

[29] S. Fürthauer, B. Lemma, P. J. Foster, S. C. Ems-McClung, C. E. Walczak, Z. Dogic, D. J. Needleman, and M. J. Shelley. Actively crosslinked microtubule networks: mechanics, dynamics and filament sliding. pages 15–17, 2018.

[30] C. Gardiner. Stochastic methods. 1985.

[31] A. Ghanta, J. C. Neu, and S. Teitsworth. Fluctuation loops in noise-driven linear dynamical systems. Phys. Rev. E, 95(3):1–9, 2017.

[32] J. Gladrow, C. P. Broedersz, and C. F. Schmidt. Nonequilibrium dynamics of probe filaments in actin-myosin networks. Phys. Rev. E, 96(2):022408, aug 2017.

[33] J. Gladrow, N. Fakhri, F. C. MacKintosh, C. F. Schmidt, and C. P. Broedersz. Broken Detailed Balance of Filament Dynamics in Active Networks. Phys. Rev. Lett., 116(24):248301, jun 2016.

[34] F. S. Gnesotto, F. Mura, J. Gladrow, and C. P. Broedersz. Broken detailed balance and non-equilibrium dynamics in living systems: a review. Reports Prog. Phys., 81(6):066601, jun 2018.

[35] F. S. Gnesotto, B. M. Remlein, and C. P. Broedersz. Non-equilibrium dynamics of isostatic spring networks. 2018.

[36] D. Goldstein, S. Ramaswamy, and B. Chakraborty. Stress Fluctuations in Transient Active Networks. Soft Matter, 15:3520–3526, 2019.

[37] R. Golestanian. Enhanced Diffusion of Enzymes that Catalyze Exothermic Reactions. Phys. Rev. Lett., 115(10):1–5, 2015.

[38] J. P. Gonzalez, J. C. Neu, and S. W. Teitsworth. Experimental metrics for detection of detailed balance violation. Phys. Rev. E, 99(2):22143, 2019.

[39] N. Gov and S. Safran. Red Blood Cell Membrane Fluctuations and Shape Controlled by ATP-Induced Cytoskeletal Defects. Biophys. J., 88(3):1859–1874, 2005.

[40] G. Gradziuk, F. Mura, and C. P. Broedersz. Scaling behavior of non-equilibrium measures in internally driven elastic assemblies. Arxiv, 2019.

[41] M. Guo, A. J. Ehrlicher, M. H. Jensen, M. Renz, J. R. Moore, R. D. Goldman, J. Lippincott-Schwartz, F. C. Mackintosh, and D. A. Weitz. Probing the stochastic, motor-driven properties of the cytoplasm using force spectrum microscopy. Cell, 158(4):822–832, 2014.

[42] O. Hachet, M. Berthelot-Grosjean, K. Kokkoris, V. Vincenzetti, J. Moosbrugger, and S. G. Martin. A phosphorylation cycle shapes gradients of the DYRK family kinase pom1 at the plasma membrane. Cell, 145(7):1116–1128, 2011.

[43] V. Hakim and P. Silberzan. Collective cell migration: A physics perspective. Reports Prog. Phys., 80(7):aa65ef, 2017.

[44] K. C. Holmes, D. Popp, W. Gebhard, and W. Kabsch. actin.pdf. Nature, 347:44–49, 1990.

[45] A.-Y. Jee, Y.-K. Cho, S. Granick, and T. Tlusty. Catalytic enzymes are active matter. Proc. Natl. Acad. Sci. U.S.A., 115(46):E10812–E10821, 2018.

[46] J. F. Joanny and J. Prost. Active gels as a description of the actin-myosin cytoskeleton. HFSP J., 3(2):94–104, 2009.

[47] F. Jülicher, K. Kruse, J. Prost, and J. F. Joanny. Active behavior of the Cytoskeleton. Phys. Rep., 449(1-3):3–28, 2007.

[48] E. F. Keller. Active matter, then and now. Hist. Philos. Life Sci., 38(3):1–11, 2016.

[49] J. Kim, J. Feng, C. A. Jones, X. Mao, L. M. Sander, H. Levine, and B. Sun. Stress-induced plasticity of dynamic collagen networks /639/766/747 /631/57/2266 article. Nat. Commun., 8(1):–, 2017.

[50] R. Kubo. The fluctuation-dissipation theorem. Reports Prog. Phys., 29(1):255, 1966.

[51] A. W. C. Lau, B. D. Hoffman, A. Davies, J. C. Crocker, and T. C. Lubensky. Microrheology, Stress Fluctuations, and Active Behavior of Living Cells. Phys. Rev. Lett., 91(19):198101, nov 2003.

[52] J. Li, J. M. Horowitz, T. R. Gingrich, and N. Fakhri. Quantifying dissipation using fluctuating currents. Nat. Commun., 10(1):–, 2019.

[53] F. C. MacKintosh and A. J. Levine. Nonequilibrium Mechanics and Dynamics of Motor-Activated Gels. Phys. Rev. Lett., 100(1):18104, jan 2008.

[54] X. Mao and T. C. Lubensky. Maxwell Lattices and Topological Mechanics. Annu. Rev. Condens. Matter Phys., 9(1):413–433, 2018.

[55] M. C. Marchetti, J. F. Joanny, S. Ramaswamy, T. B. Liverpool, J. Prost, M. Rao, and R. A. Simha. Hydrodynamics of soft active matter. Rev. Mod. Phys., 85(3):1143–1189, 2013.

[56] M. Melak, M. Plessner, and R. Grosse. Correction: Actin visualization at a glance. J. Cell Sci., 130(9):1688–1688, 2017.

[57] A. Melbinger, L. Reese, and E. Frey. Microtubule length regulation by molecular motors. Phys. Rev. Lett., 108(25):1–5, 2012.

[58] A. S. Mikhailov and R. Kapral. Hydrodynamic collective effects of active protein machines in solution and lipid bilayers. Proc. Natl. Acad. Sci. U.S.A., 112(28):E3639–E3644, 2015.

[59] D. Mizuno, C. Tardin, C. F. Schmidt, and F. C. MacKintosh. Nonequilibrium Mechanics of Active Cytoskeletal Networks. Science., 315(5810):370–373, 2007.

[60] F. Mura, G. Gradziuk, and C. P. Broedersz. Nonequilibrium Scaling Behavior in Driven Soft Biological Assemblies. Phys. Rev. Lett., 121(3):38002, 2018.

[61] F. Mura, G. Gradziuk, and C. P. Broedersz. Mesoscopic non-equilibrium measures can reveal intrinsic features of the active driving. 2019.

[62] S. Ornes. Core Concept: How nonequilibrium thermodynamics speaks to the mystery of life. Proc. Natl. Acad. Sci. U.S.A., 114(3):423–424, 2017.

[63] D. Osmanović and Y. Rabin. Dynamics of active Rouse chains. Soft Matter, 13(5):963–968, 2017.

[64] C. D. Paul, P. Mistriotis, and K. Konstantopoulos. Cancer cell motility: Lessons from migration in confined spaces. Nat. Rev. Cancer, 17(2):131–140, 2017.

[65] M. Polettini and M. Esposito. Effective Thermodynamics for a Marginal Observer. Phys. Rev. Lett., 119(24):240601, 2017.

[66] M. Polin, K. Ladavac, S.-H. Lee, Y. Roichman, and D. G. Grier. Optimized holographic optical traps. 13(15):4129–4135, 2005.

[67] J. Prost, F. Julicher, and J.-F. F. Joanny. Active gel physics. Nat. Phys., 11(2):111–117, 2015.

[68] C. Riedel, R. Gabizon, C. A. Wilson, K. Hamadani, K. Tsekouras, S. Marqusee, S. Pressé, and C. Bustamante. The heat released during catalytic turnover enhances the diffusion of an enzyme. Nature, 517(7533):227–230, 2015.

[69] H. Risken. The Fokker-Planck equation. Berlin, 1996.

[70] P. Ronceray, C. P. Broedersz, and M. Lenz. Fiber networks amplify active stress. Proc. Natl. Acad. Sci. U.S.A., 113(11):2827–2832, 2016.

[71] D. L. Schmitt and S. An. Spatial Organization of Metabolic Enzyme Complexes in Cells. Biochemistry, 56(25):3184–3196, 2017.

[72] U. S. Schwarz and S. A. Safran. Physics of adherent cells. Rev. Mod. Phys., 85(3):1327–1381, 2013.

[73] U. Seifert. Entropy Production along a Stochastic Trajectory and an Integral Fluctuaction Theorem. Phys. Rev. Lett., 95(040602):14380–14385, 2005.

[74] U. Seifert. Stochastic thermodynamics, fluctuation theorems and molecular machines. Reports Prog. Phys., 75(12):126001, dec 2012.

[75] M. J. Shelley. The Dynamics of Microtubule/Motor-Protein Assemblies in Biology and Physics. Annu. Rev. Fluid Mech., 48(1):487–506, 2015.

[76] A. Sonn-Segev, A. Bernheim-Groswasser, and Y. Roichman. Extracting the dynamic correlation length of actin networks from microrheology experiments. Soft Matter, 10(41):8324–8329, 2014.

[77] A. Sonn-Segev, A. Bernheim-Groswasser, and Y. Roichman. Scale dependence of the mechanics of active gels with increasing motor concentration. Soft Matter, 13(40):7352–7359, 2017.

[78] H. Sutherland and W. A. Bickmore. Transcription factories: Gene expression in unions? Nat. Rev. Genet., 10(7):457–466, 2009.

[79] H. Turlier, D. A. Fedosov, B. Audoly, T. Auth, N. S. Gov, C. Sylkes, J.-F. Joanny, G. Gompper, and T. Betz. Equilibrium physics breakdown reveals the active nature of red blood cell flickering. Nat. Phys., 12(5):513–519, jan 2016.

[80] M. Vahabi, A. Sharma, A. J. Licup, A. S. Van Oosten, P. A. Galie, P. A. Janmey, and F. C. Mackintosh. Elasticity of fibrous networks under uniaxial prestress. Soft Matter, 12(22):5050–5060, 2016.

[81] S. C. Weber, A. J. Spakowitz, and J. A. Theriot. Nonthermal ATP-dependent fluctuations contribute to the in vivo motion of chromosomal loci. Proc. Natl. Acad. Sci. U.S.A., 109(19):7338–7343, may 2012.

[82] J. B. Weiss. Coordinate invariance in stochastic dynamical systems. Tellus A, 55(3):208–218, may 2003.

[83] K. Yasuda, R. Okamoto, and S. Komura. Anomalous diffusion in viscoelastic media with active force dipoles. Phys. Rev. E, 95(3):1–14, 2017.

[84] M. G. Yucht, M. Sheinman, and C. P. Broedersz. Dynamical behavior of disordered spring networks. Soft Matter, 9(29):7000–7006, 2013.

[85] Y. Zhang and H. Hess. Enhanced Diffusion of Catalytically Active Enzymes. ACS Cent. Sci., page acscentsci.9b00228, 2019.

[86] X. Zhao, K. K. Dey, S. Jeganathan, P. J. Butler, U. M. Córdova-Figueroa, and A. Sen. Enhanced Diffusion of Passive Tracers in Active Enzyme Solutions. Nano Lett., 17(8):4807–4812, 2017.

Acknowledgements

During these years I never felt alone and always knew that I could count on the invaluable support of Chase Broedersz. I am extremely grateful for your guidance, trust, and the enormous amount of enthusiasm and time that you invested in this project. This is a moment when I really wish I could have your energy and liveliness to express my gratitude to you and all the people that supported me along the way.
A huge thank You to Grześ Gradziuk, now definitely a friend, but also the best working partner I could ever ask for. It has been a great fun and joy to share with You the best 3/4 of this journey.
A special thanks to Federico Gnesotto, for being a friend and a great discussion partner. And of course, for making the coffee breaks always enjoyable: thanks to you, coffee and sometimes physics, tasted less bitter.
Many thanks also to Stefano Ceolin, Karsten Miermans, Karl Wienand, Nanni Giunta, Grześ Gradziuk, David Brückner, Isabella Graf, Silke Bergeler, Joris Messelink, Federico Gnesotto and Felix Kempf for your precious suggestions and the time spent to proofread this thesis.
I am extremely grateful to my graduate school "Quantitative Biosciences Munich" for creating an always supportive and stimulating environment.
I am also indebted to Alessio Zaccone, thanks for welcoming me in your group at my arrival in Munich. It has been a short, yet intense and successful collaboration, I have learned a lot from it.
Thanks to everyone at LS Frey-Broedersz for being part of a fantastic group and making such a relaxed and friendly atmosphere. Special thanks to Manon Wigbers for the company in the office and sometimes in the Cyber Cycling-Raum.
I would like to thank all my friends, simply for their friendship, and in particular a huge thanks to Karl and Carmen, Federico and Lolo, Karsten, Isabella, Silke, Felix, Luca and clearly Nanni for making me love life in Munich.
Of course, thanks to my family in Oristano and Pordenone.
Finally, heartfelt thanks go to Ste, for your love, help and encouragement every day and in everything I do. I am sure that I never would have made it without you.